Engineering Fluidic Tools for Translational Science:
Developing In Vitro Tissues and Remote Sampling Platforms

Lauren G. Brown

A dissertation
submitted in partial fulfillment of the
requirements for the degree of

Doctor of Philosophy

University of Washington
2025

Reading Committee:
Ashleigh B. Theberge, Chair
Alshakim Nelson
Joshua C. Vaughan

Program Authorized to Offer Degree:

Department of Chemistry

University of Washington

Abstract

Engineering Fluidic Tools for Translational Science:
Developing In Vitro Tissues and Remote Sampling Platforms

Lauren G. Brown

Chair of the Supervisory Committee:
Ashleigh B. Theberge
Department of Chemistry

This dissertation discusses the development and optimization of various open microfluidic inspired tools for translational science applications in studying human health and the environment. Chapter 1 introduces the field of open microfluidics and provides background into open microfluidic hydrogel patterning for tissue engineering and at-home blood sampling for downstream transcriptomic analysis. Chapter 2 describes a novel removable suspended open microfluidic platform for patterning hydrogel-based tissue constructs suspended between two posts. This platform uses microfluidic principles such as surface tension and capillary pinning to control the flow and shape of hydrogels in a suspended format to generate engineered tissue constructs with defined interfacial regions for disease and tissue junction modeling. Chapter 3 explores the use of homeRNA, a previously established kit for at-home user-based blood collection and stabilization, in high temperature settings via two pilot studies conducted in the hot summer months in the Western and South Central United States and Doha, Qatar. These pilot studies yielded RNA from homeRNA-stabilized samples of sufficient quality for use in downstream transcriptomic analysis despite exposure to temperatures greater than 37°C. Chapter 4 further establishes the robustness of homeRNA by systematically testing RNA quality from homeRNA-stabilized samples after short-term (<2 days) and long-term exposure (>2 days) to a range of temperatures above 37°C via in-lab testing and a real-world controlled shipping experiment. These samples were then sequenced using 3' mRNA-sequencing technology, which showed little to no preferential transcript degradation of isolated RNA from homeRNA-stabilized samples due to high temperatures or extended shipping times. Chapter 5 then outlines the first

use of homeRNA with bulk RNA-sequencing, in which we demonstrated that homeRNA can successfully capture an LPS-induced inflammatory response that was comparable to that of stabilized venous blood. This work establishes the compatibility of homeRNA with bulk RNA-sequencing, demonstrating its potential as a useful tool for monitoring immune response via remote sampling. Lastly, Chapter 6 describes a yearlong homeRNA-based remote study to probe immune response to wildfire smoke exposure in the Western and South Central United States. This demonstrates the ability of homeRNA to be used in a fully remote and flexible study design for user-based blood collection in challenging environments. Ongoing work with this study includes investigating the gene expression profile of homeRNA-stabilized samples from 32 unique participants to elucidate the transcriptomic immune response to wildfire smoke. This dissertation presents two bioanalytical platforms that advance translational medicine by enabling more targeted biological and health-related investigations. Combined, STOMP and homeRNA collectively expand the scope of translational research in tissue engineering and remote sampling applications, thus supporting more targeted investigations into disease mechanisms, therapeutic efficacy, and environmental health impacts.

Table of Contents

List of Figures

Additional figures in appendices A-E

List of Tables

Acknowledgements

I have been so lucky to not only have the opportunity to complete a PhD (a goal that I have had since high school), but also to have gathered a large community of supporters along the way. All of the cliches about completing a PhD is true ("it takes a village," "it's a marathon not a sprint," "nothing occurs in isolation," etc.) and I am lucky to have a vast village, cheerleaders at every mile marker, and a large network of brilliant scientists, family members, and close friends who have kept me company and helped me grow. This acknowledgments section is by far the most challenging part of my dissertation to write, not for lack of gratitude, but because of the overwhelming abundance of it. To everyone who has supported me along the way, please know how deeply thankful I am, and please bear with me as I attempt to capture even a fraction of what your support has meant.

To all the Theberge lab members past and present, thank you for helping me grow both as a person and as a scientist. The lab was always a fun, welcoming, and interactive environment, and it made me look forward to coming to work every day mostly so I could talk to everyone (and yes, talk while doing my work, and sometimes instead of doing my work). Thank you to Filip and Jodie, the dream bean team, who started this journey with me, kept me in check, kept me sane, and became some of my closest friends in a new city. I couldn't have asked for better people with whom to start this journey. Thank you to Amanda for being a valuable mentor, co-author, and friend, even if you drive me insane at times. Thank you to Yuting for the coffee talks, the advice, and for letting me spend time with Sesame. Thank you to Jamison, who tolerated sitting across from me for years and who always listened to me (even if you did not want to). Your friendship inside and outside the lab were essential to me staying sane over the years and I promise to try to listen to you more in the future. Thank you to Ariel, who was so patient with me and my teaching skills and kept the lab a joy to be in every day. Thank you to starting so many traditions in our lab, from karaoke nights to exam banners. To both Jamison and Ariel, you have blossomed into independent and brilliant scientists, and I know the STOMP/SNaP/STEAM/Hydrogel Patterning (whatever we want to call it now) team are in good hands. To Laura, thank you for traveling all the way from Australia just to help me with my project. You came at a time I not only really needed help with the project, but also at a time when I

really needed a friend. I am so glad to have met you during this journey and I cannot wait to visit you in Australia. To Hannah, Serena, Ella, Asha, and Liam, your drive and enthusiasm for research inspired me daily. Each of you has grown into an impressively thoughtful and talented scientist, and I cannot wait to see what you do next. To TJ, Yunos, and Xiaofu, the future of the lab is bright with you three. Thank you for the laughs, the coffee and tea outings, the bowling competitions, and the help with countless projects and tasks. I am excited to see how the lab continues to grow with you in it.

To Ashleigh, thank you for being a mentor to me throughout my PhD. You taught me to go after every opportunity and helped me build my confidence over the last 4.5 years. To the Tapscott lab, who let me crash their group meetings every week so I could try to learn more molecular biology (and who stayed patient even as I continued to get terms wrong after two years), thank you for your endless support and your tolerance of my constant questions. To the Allbritton lab, where I began my research journey and first discovered my love for science, thank you for your guidance, advice, and mentorship throughout my undergraduate years and into my graduate career. To Sam, Sebastian, Johanna, and Hannah, thank you for showing me what great scientists look like (and show me how to have fun when the trials and tribulations of graduate school get me down).

To my closest friends in the cohort, Sahiti, Tori, and Jayden, thank you for the laughter, the office visits, and all of our shenanigans inside and outside of Bagley Hall. The fourth floor never felt lonely with the three of you nearby. Over the last four years, you three made Seattle feel like my home, so much so that it made me want to stay. To Wes, thank you for watching my cat, helping me eat all the candy and sweets I make, taking care of all the spiders in the house, and being a much-needed friend when I came home after long days in lab. I will miss our avatar weekends, Love is Blind nights, and crochet evenings, but you and Ethan will always be invited over to reminisce on the good ole days with me and Milo.

Outside of the lab, thank you to all of the people in Seattle who helped me destress after lab and made sure I was well socialized in society. To Jacie and Wren, thank you for the mahjong and the fabulous home-cooked meals. Also, an extra special thank you to Jacie for living with me for the first two years and for being one of the first friends I made in Seattle. To Erica, thank you for going on Ballard walks with me, for

the airport pickups, and for being so easy to talk to about anything. I am so glad that you are back in Seattle to hang out with me again.

To my friends back home, thank you for continuing to love and support me from across the country. To Hope, thank you for the long phone calls, for going on new hikes with me, visiting me, letting me use your flight benefits, and for your endless love. You helped me stay grounded and heard through some of the hardest moments of my life. To Danelle, thank you for always checking in with me, for visiting me when I first moved here and being an old friend to me in a new city, for letting me crash on your floor when I had Covid, and for always being someone I can be open and honest to. To Annie, thank you for the voice memos (even if we both became very sporadic with them in the end), for coming to visit me in Seattle, and for always being someone I can rely on. To Eli, thank you for supporting me throughout my PhD (even though you always dared me to drop out) and for letting me assimilate myself into your family while you were gone. To Kieran, thank you for letting me visit you in Chicago and San Francisco and for being there for me since high school. To Devin, thank you for being my best friend since 5th grade. Even though we haven't seen each other as much recently, you will always be the person I can fully be myself with and someone I know I can always rely on.

To my family, thank you for supporting me throughout this journey. Even if you didn't want me to move across the country, you always supported me and made me feel at home away from home. To Mom and Dad, thank you for raising me to be an independent woman and thinker, for instilling into me the importance of reading (to mom) and staying active (to dad), and for teaching me to be hard-working and to never give up (a talent I learned from both of you). To Anastasia, thank you for being my best friend through the ups and the downs and for being my number one supporter no matter what. Some of my best memories over the last few years have been when I was able to see you again, whether it was Christmas, New Years, my visits to Charlotte, or your visits to Seattle. To Michael, thank you for always making an effort to see me when I come back to North Carolina. It always makes me so happy to see you and even with the distance I am always thinking of you.

To my partner, Milomir, thank you for being there since day one of my PhD. From randomly meeting you in your office during my first visit to Seattle to our long drives all across Washington to moving you to Ohio to having you come back to Seattle, you have been my rock throughout this entire process. Words cannot express enough how much your love and support have helped me crossed the finish line. You taught me so much about hunting (against my will), camping (mainly how to come out of the woods alive when I go camping with you), the joy of long car rides (even if sometimes I push back and constantly want snacks), and how to do good science (even if sometimes unsolicited). Most importantly, you taught me what it feels like to be truly supported in every version of myself, from tired to overwhelmed, from excited to stubborn, from dramatic to hopeful, and everything in between. You have brought so much laughter, stability, and warmth into my life, and you've made this wild PhD journey feel like an adventure we were on together. Thank you for loving me so steadily and so generously. I would choose every long drive, every long-distance phone call, every long-awaited reunion, and all the stress of long lab days again if it meant finding you at the end of it.

In the end, this PhD has been as much a personal journey as an academic one. It taught me how to fail (again and again and again) and how to get back up with more resilience than I ever believed I had. It taught me discipline on the days I wanted to quit, patience on the days nothing worked, and confidence on the days when no one but me really cared if an experiment worked or not. It pushed me through long nights, failed experiments, unexpected (and often unwelcomed) detours, and the strange reality that no one truly understands a PhD except the people who have lived one. But it also carried me across the country and across the world, introducing me to people from countless backgrounds and creating experiences I will hold onto forever. I am grateful for the science I learned, but even more grateful for the person I became along the way. And though the PhD path often felt solitary, I never walked it alone; for everyone who walked beside me, whether for a moment or for the entire journey, thank you. You helped make this long, winding path not only possible, but meaningful. And now that I've finished, I'm hoping real life is significantly less dramatic than a PhD (but I'm not holding my breath).

Dedication

For my mom and dad, Lisa and David, who always supported me no matter what; for my brother and sister, Michael and Anastasia, who cheered me on; for my partner, Milomir, who was there since the beginning of it all; for all of my friends near and far, who kept me sane, loved, and endlessly fulfilled.

Chapter 1 | Introduction

Portions of this introduction have been excerpted or paraphrased from Chapters 2-6 of this dissertation.

1.1 Introduction to open microfluidics

Microfluidics is an interdisciplinary field that has developed significantly in the last two decades. Microfluidic systems can be broadly defined as the study and manipulation of small liquid volumes within channels with at least one dimension on the micron scale[1]. These systems integrate techniques and principles from physics, chemistry, engineering, and biology to develop total analysis systems (i.e., lab-on-a-chip systems) for a wide range of applications, such as chemical synthesis, biological analysis, microscopy, and diagnostic analysis[1–4]. Microfluidic systems are particularly useful because they allow for automated workflows, high-throughput processing, and low consumption of reagents or materials (e.g., primary cells, synthetic hydrogels, decellularized extracellular matrices from primary tissues). Additionally, microfluidic systems can manipulate fluid flow via active or passive pumping mechanisms, which enables precise spatial control over fluid and material placement within fabricated microchannels[5].

Microfluidic systems are often categorized into closed and open systems. In closed microfluidic systems, fluid flow occurs within fully enclosed structures (i.e., a channel with four borders). In traditional closed systems, specialized pumps (e.g., syringe pumps) at the channel inlet and outlet control fluid flow throughout the system, often referred to as active pumping[5]. As a result, the fluid is not accessible to the user throughout the closed channel system. In contrast, open microfluidic systems lack one or more channel borders, which creates an air-liquid interface along the length of the channel design[6,7]. This open channel design enables access throughout the channel using standard laboratory tools (e.g., a micropipette) to add, remove, or manipulate fluid or materials. Flow in open microfluidic systems is governed by capillary forces and surface tension, thus eliminating the need for specialized fluidic pumping equipment and reducing cost and complexity of microfluidic systems[7–9]. Consequently, these combined advantages of reduced channel complexity, enhanced fluid accessibility, and simplified fluid manipulation make open microfluidic

systems particularly well-suited for translational applications in biomimetic tissue engineering, cellular analysis, and molecular analysis[10–12].

Since open microfluidic systems are broadly defined as lacking at least one channel boundary (and therefore containing at least one air-liquid interface), this structural flexibility allows for a wide array of channel configurations to be designed according to specific application requirements. These configurations include: simple channels devoid of a ceiling (referred to as "u-shaped" channels), rail-based channels containing a ceiling and a floor border but lacking two side walls (generating two air-liquid interfaces), suspended channels that lack a ceiling and a floor but contain two wall borders, or enclosed channels with an open inlet and outlet (often referred to as semi-open systems)[6–8,13,14]. However, when designing an open microfluidic system, both the channel geometry and the surface chemistry must be carefully considered, as fluid flow is governed by surface tension and capillary forces. A key mechanism enabling this flow control is spontaneous capillary flow (SCF). A simplified equation has been described[8] that indicates the conditions for whether SCF will occur and can be summarized in equation (1.1):

$$\frac{p_f}{p_w} < cos(\theta) \qquad \text{(Eq. 1.1)}$$

where p_f refers to the free perimeter of a cross-section of a channel, or the portion of the perimeter that contains an air-liquid interface, p_w refers to the wetted perimeter, or the portion of the perimeter where liquid is in contact with a surface, and θ refers to the contact angle of the fluid on that surface. By manipulating these parameters to satisfy the inequality, researchers can design open microfluidic systems with predictable, SCF-driven fluid flow.

1.2 Engineering tissues through open microfluidic hydrogel patterning

Patterning refers to a category of techniques that facilitate the precise arrangement of materials in a user-specified geometry or pattern. In three-dimensional (3D) cell culture, patterning refers to the precise arrangement of cells, hydrogels, or molecules to generate physiologically relevant tissue-like structures. Hydrogels, both native-derived and synthetic, are widely used in 3D cell culture techniques due to their ability to mimic the structural and biochemical properties present in native extracellular matrix (ECM)

networks[15]. Conventional methods for 3D cell culture involve embedding cells homogeneously within a hydrogel scaffold to increase cell-cell and cell-ECM interactions *in vitro*[16,17]; these cultures often consist solely of one combination of cell and hydrogel type[18–20] or two or more cell types homogeneously mixed within a single culture[21–24]. Incorporating patterning within conventional 3D cell-laden hydrogel systems allows for multiple cell types, ECM types, and/or ECM compositions to be spatially arranged within a single 3D tissue construct. Hydrogel patterning in 3D systems thereby enables user-defined designs of tissue-level structures or interfacial regions between different tissue types in a controlled microenvironment. The tissue complexity mediated by 3D patterning allows for more physiologically relevant investigations into cell signaling behavior[25–27], tissue regeneration[28–30], and drug or other small molecule interactions[25,31–33].

Cell-embedded hydrogel patterning techniques that enable spatially and geometrically controlled tissue structures include photolithography, soft lithography (e.g., micromolding), 3D bioprinting, and microfluidics.[34–37] In photolithography, light is used to activate photo-crosslinkable moieties in a cell-laden hydrogel.[38,39] By defining the area that is exposed to light through the use of photomasks or laser irradiation, the geometry and composition of the resulting tissue structure can be controlled. Soft lithography uses a mold or stamp to dictate the shape and pattern of cells/proteins in a cell-laden hydrogel.[40,41] Lastly, extrusion-based 3D bioprinting uses bioink to print 3D structures in a controlled layer-by-layer approach to include different regions of cells and ECMs.[42,43] Comparatively, microfluidic systems utilize manipulation of fluid flow to enable precise spatial control over hydrogel placement within fabricated microchannels. By changing the channel dimensions and/or surface properties to favor fluid advancement or impediment, fluid movement and placement can be controlled within the channels.[44,45] These modifications enable the precise shaping of hydrogels to create patterned tissue constructs.

Building upon the principles of microfluidic hydrogel patterning, this dissertation introduces an open microfluidic approach for controlling hydrogel placement to generate 3D suspended and patterned cell-ECM constructs for tissue engineering applications. Taking advantage of surface tension, capillary pinning features can be incorporated into open channels to stop fluid advancement and control fluid front placement

(Figure 1.1). In this work, a suspended open channel (i.e., a channel with two walls but no ceiling or floor) with capillary pinning features is used to pattern multiple regions within a single suspended tissue construct (Chapter 2). Since open channels are accessible via pipette across the channel geometry, distinct regions of cell-ECM liquid precursors can be patterned along the channel length; the number of distinct regions depends on the number of capillary pinning feature sets positioned along the channel. With this open microfluidic patterning method, open microfluidic channels control tissue deposition but can be subsequently removed to reveal free-standing engineered tissue models for downstream applications (e.g., mechanical loading, further patterning, staining, and imaging).

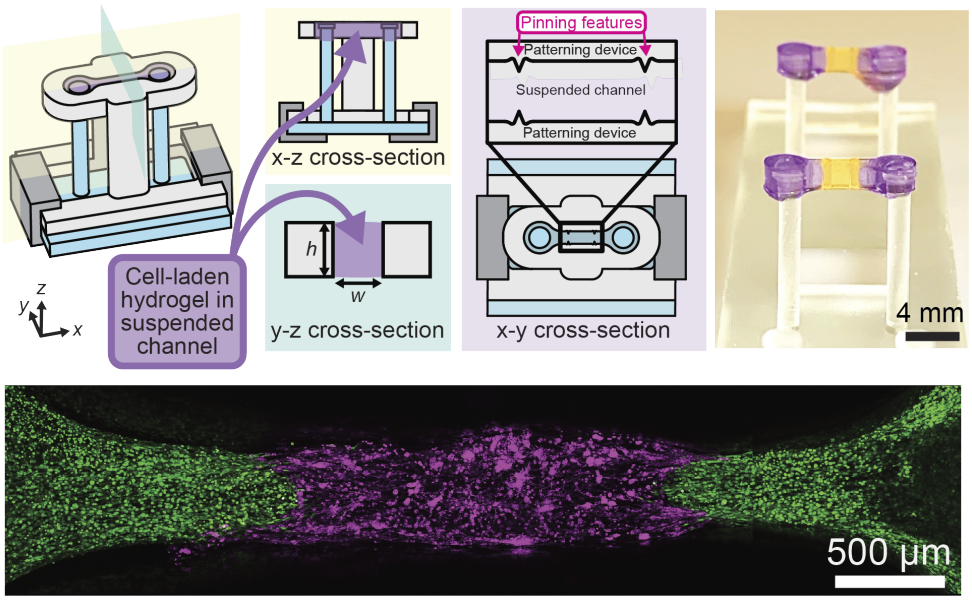

Figure 1.1. Suspended tissue open microfluidic patterning for tissue engineering. Schematic demonstrating suspended tissue open microfluidic patterning with the incorporation of capillary pinning features to pattern distinct regions within a single tissue construct. Example images were generated by patterning three regions of purple- and yellow-colored agarose gels (top right) and mouse fibroblast cells dyed by CellTracker Green (green) and CellTracker Red (magenta) laden in fibrin.

1.2.1 Suspended tissue open microfluidic patterning

While suspended tissue models offer advantages for studying mechanical cues in 3D cell culture[46–48], current methods for generating these constructs are limited in their ability to create regional heterogeneity within a single tissue. Traditional casting methods, which involve pouring a precursor cell-ECM liquid solution into a mold[49,50], lack precise geometric and cellular distribution control, while 3D bioprinting

approaches coupled with sacrificial suspension baths require specialized equipment, which limits accessibility and scalability, and is often limited by the type of cells and ECMs that can be used due to the shear-thinning nature of 3D bioprinting[51–53]. Although previous open microfluidic work has demonstrated the ability to pattern multiple cell types or ECMs in various configurations[54–57], suspended open microfluidic systems have been limited to generating tissues with uniform cell-ECM compositions[58,59]. To address these limitations, Chapter 2 presents the development of Suspended Tissue on Open Microfluidic Patterning (STOMP), a novel approach that combines the accessibility of open microfluidics with capillary pinning features to generate regionally heterogeneous suspended tissue constructs. STOMP uses a removable open microfluidic patterning device that interfaces two suspended posts, thus generating a suspended hydrogel over an open space without the use of a sacrificial material (Figure 1.1). Utilizing surface tension to drive flow and capillary pinning to stop flow, STOMP can control the spatial placement of tissue components within a single suspended construct. Additionally, STOMP employs two complementary approaches for device removal: leveraging cellular contractile forces to pull tissues away from the STOMP channel walls or incorporating degradable wall materials that dissolve to release the patterned tissue construct. In this work (Chapter 2), we demonstrate STOMP's utility by modeling a fibrotic region within engineered heart tissue and a bone-ligament interface in periodontal tissue constructs. This work demonstrates that STOMP has the potential to model diverse biological structures and border regions for physiological tissue engineering and preclinical drug screening applications.

1.3 Remote blood sampling for translational transcriptomic studies

Blood transcriptomic profiling is widely used in translational research to investigate gene expression signatures and biomarkers across diverse immune states, including disease onset and progression, response to environmental exposures, and therapeutic interventions[60–65]. To better capture these dynamic immune responses, remote blood sampling has emerged as a valuable technology, enabling participant-initiated sample collection outside traditional clinical facility settings[66–68]. By eliminating the need for centralized clinic locations and trained phlebotomy staff, remote blood sampling enables researchers to achieve (1) greater inclusion of participants who would otherwise be excluded due to logistical or personal constraints

(e.g., work schedules, caregiver responsibilities, mobility challenges)[69], (2) enhanced ability to capture immediate physiological responses to acute exposures (e.g., environmental, vaccine or medication response, autoimmune flares)[70], (3) simplified frequent collection of samples for longitudinal studies without the burden of repeated clinic visits[71,72], and (4) expanded geographical sampling locations, including rural settings with limited access to hospitals or clinics[73].

1.3.1 Current remote blood sampling methods and challenges

Blood transcriptomic profiling methods rely on well-preserved RNA samples, as low-quality or highly degraded RNA can introduce biases in gene expression profiles that reduce the accuracy and reproducibility of transcriptomic analyses[74–76]. However, the inherent instability of whole blood RNA ex vivo presents a significant challenge for transcriptomic profiling. Blood contains high amounts of ribonucleases (known as RNases) that can activate degradation pathways, compromising the integrity of intracellular RNA transcripts and altering measured gene expression levels[76,77]. Therefore, studies that do not include immediate extraction of RNA from collected blood samples require a method of RNA stabilization[78]. In clinic-based studies, commercially available RNA stabilization solutions such as PAXgene and Tempus are commonly used; these solutions can come packaged in vacutainer tubes which make it easy to directly collect blood into the stabilizer solution from a phlebotomy draw. RNAlater is another available stabilization solution which has been used to preserve RNA in both blood and tissue samples.

The established need for RNA stabilization in clinic-based studies becomes even more critical when samples need to be collected remotely and shipped to centralized laboratories. Remotely collected samples must withstand extended shipping times, temperature fluctuations that can occur during transit, and handling variations that can further compromise RNA stability. Current remote sampling approaches have attempted to address these challenges through two primary strategies: dried blood spot (DBS) sampling and liquid blood collection with stabilization. DBS-based sampling, which typically uses a lancet on a fingertip to collect a drop of blood on a piece of paper, relies on drying of the blood to stabilize RNA[79,80]. While several studies have demonstrated successful RNA sequencing from DBS samples[81–83], this approach faces

significant limitations including inconsistent RNA yields, lack of standardized processing protocols, and frequent requirement for pre-amplification steps that can introduce bias into transcriptomic data[84–87]. Additionally, the small volume of blood collected (typically <100 μL) limits the scope of analyses that can be performed. To overcome volume limitations, newer remote collection devices utilize a lancet that collects blood from the upper arm (e.g., Tasso, YourBio) that can draw larger blood volumes (up to 1 mL)[88,89]. However, these increased volumes are incompatible with drying-based stabilization, necessitating liquid stabilization approaches to maintain RNA integrity in transit.

1.3.2 homeRNA for remote self-administered blood collection and stabilization

To address the need for a remote blood sampling method that combines larger blood volumes with robust RNA stabilization, we developed the homeRNA kit. The homeRNA kit is an at-home blood self-collection and RNA stabilization platform that combines the commercially available Tasso-SST upper-arm collection device with a custom stabilizer tube containing RNAlater[90]. Figure 1.2 illustrates the homeRNA workflow for conducting remote blood transcriptomic studies, including the workflow of blood self-collection and stabilization process with homeRNA. Using homeRNA, participants collect up to 0.5 mL of whole blood from their upper arm, immediately stabilize the collected blood sample with RNAlater, and ship it back to the laboratory for further processing and analysis. We previously demonstrated the feasibility and usability of homeRNA in a pilot study involving 47 participants across 10 US states. These remotely collected samples yielded RNA of sufficient quantity and quality for downstream transcriptomic analysis, establishing the potential of homeRNA for use in large-scale remote research.[90]. However, several critical questions remained regarding the validation and demonstration of homeRNA for downstream transcriptomic analysis. Building on this foundation, the research presented in this dissertation addresses three key areas: (1) validating RNA stability and quality under high temperature shipping conditions, (2) demonstrating comparable immune response detection to traditional venous sampling, and (3) applying homeRNA to a large-scale environmental health study to capture immune responses to wildfire smoke exposure.

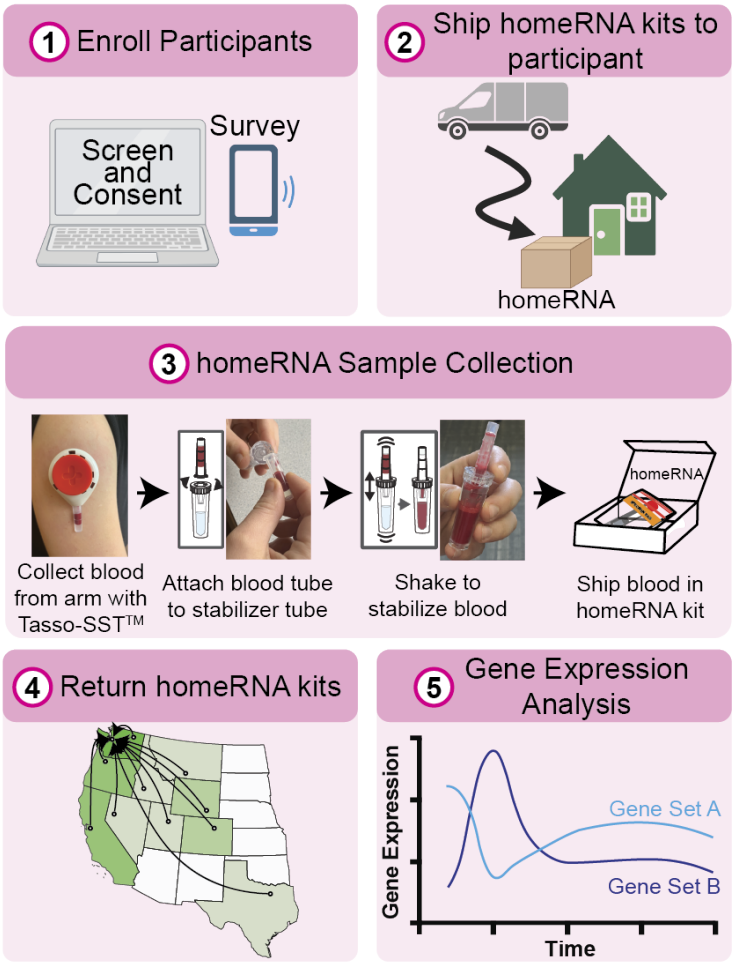

Figure 1.2. Workflow for remote blood sampling with homeRNA, a self-blood collection and stabilization kit.

1.3.3 Stability of homeRNA in high temperature settings

Validating remote blood sampling methods under high temperature shipping conditions has important implications for expanding clinical research applications to tropical disease studies (e.g., dengue fever, malaria) or seasonal environmental exposures (e.g., wildfire events during hot summer months). Specifically, it is critical to determine whether blood samples exposed to elevated temperatures during shipping experience preferential degradation of specific RNA transcripts, which could adversely affect RNA quality or systematically bias transcriptomic analyses. The existing body of research has primarily investigated the effects of cold and ambient temperatures on RNA integrity prior to isolation from whole blood samples, as well as stability of RNA following extraction[91–94]. However, few studies to date have

systematically investigated exposure of blood to high temperatures (>37°C) and its effect on the resulting isolated RNA quality or transcriptomic results.

In Chapters 3 and 4 of this dissertation, I describe additional investigations into validating homeRNA for use in high temperature settings. In Chapter 3, I describe two small pilot studies that investigate RNA quality of homeRNA-stabilized samples exposed to high external temperatures during sample collection and shipment[95]. The first pilot study took place in Doha, Qatar (known for its dry desert climate) and the second pilot study took place in Western and South Central US States during hot summer months (including a record heat wave during June 2021 in the Pacific Northwest). For samples collected from both studies, we examined quality control metrics typical to determining suitability of isolated RNA for downstream RNA transcript analysis, including the RNA integrity number (RIN) and total cellular RNA yield. In Chapter 4, we expanded upon the work done in Chapter 3 to design a set of temperature-controlled experiments on RNAlater-stabilized whole blood samples exposed to temperatures up to 50°C for up to 8 days. Additionally, we conducted a real-world shipping experiment with homeRNA-stabilized samples and sequenced a subset of these samples using 3' mRNA sequencing (3' mRNA-seq) to better understand how variable exposure to different temperatures and shipping times can affect the quality of the transcriptomic data[96]. Overall, these combined chapters support that homeRNA can be used in elevated temperature conditions and experience limited preferential degradation of transcripts as a result of different shipping times, temperatures, and regions.

1.3.4 Capturing controlled immune response via lipopolysaccharide stimulation with homeRNA

Previous studies have demonstrated that homeRNA robustly stabilizes blood during remote self-sampling, user-stabilization, and shipping processes[90,95,96]. A recent study also showed that homeRNA can capture a biological immune response to SARS-CoV-2 using a targeted Nanostring gene panel, which is a mRNA-barcoding technology that directly quantifies specific gene transcripts[71,97]. However, homeRNA had not yet been validated for genome-wide transcriptomic profiling using bulk RNA sequencing and direct comparison of homeRNA to traditional clinical sampling methods remained unexplored. To address this need, Chapter 5 demonstrates the applicability of homeRNA for detecting biological responses through

bulk RNA sequencing analysis. Specifically, we leveraged the comprehensive read depth of RNA sequencing to identify pathway and gene-level alterations that homeRNA can capture compared to standard phlebotomy blood draws. We measured induced immune responses to LPS stimulation in blood collected with homeRNA compared to venous blood stabilized with either RNAlater (the same solution used in homeRNA) or PAXgene (a common stabilization solution for phlebotomy draws). This comparative study validates homeRNA as a remote sampling method capable of generating transcriptomic data comparable to traditional clinic-based blood sampling approaches.

1.3.5 Real-world application of homeRNA: Probing immune response to wildfire smoke exposure

Wildfire incidence and severity are increasing globally, with longer fire seasons and higher intensity expected to continue in a warming climate[98–100]. Particularly in the western US, wildfire frequency and resulting burned area have dramatically increased over the last two decades[101,102]. Beyond environmental damage, wildfire smoke exposure causes acute respiratory symptoms[103,104] and exacerbates chronic conditions including COPD[105,106], asthma[107], and cardiovascular disease[108,109]. Understanding the biological mechanisms underlying these health impacts, particularly related to immune and inflammatory responses, could enable biomarker discovery, targeted therapies, and improved risk assessment tools.

Despite growing interest in wildfire smoke health effects, few studies have investigated transcriptomic immune responses to smoke exposure in humans. Traditional clinic-based studies face significant logistical challenges due to wildfires' unpredictable nature and occurrence in rural areas with limited healthcare infrastructure. Researchers must either rely on historical data to predict fire-prone locations with adequate clinical facilities[110], establish expensive multi-site studies, or depend on retrospective analyses[111–113]. These factors limit the ability to capture acute immune responses during active smoke events.

Chapter 6 details a large-scale longitudinal study that utilized homeRNA to collect samples in response to wildfire smoke throughout the western United States. The primary objective of this study was to (1) evaluate the feasibility of a flexible study design in response to disasters and (2) assess the immediate and longitudinal effects of wildfire smoke exposure on blood transcriptomics in an initial cohort. This study

demonstrates the utility of homeRNA for responsive, fully remote study designs that can be rapidly deployed during unpredictable environmental events, enabling real-time capture of immune responses to wildfire smoke exposure.

1.4 Dissertation Summary

This dissertation presents two bioanalytical platforms that advance translational medicine by enabling more targeted biological and health-related investigations. First, I developed Suspended Tissue on Open Microfluidic Patterning (STOMP), a novel microfluidic approach that utilizes capillary pinning features to generate heterogeneous, multi-region 3D tissue constructs with precise spatial control over cellular and extracellular matrix composition. STOMP enables the modeling of complex tissue interfaces and pathological regions, as demonstrated through cardiac fibrosis models and periodontal bone-ligament constructs, thereby facilitating targeted investigations of disease mechanisms and therapeutic interventions. Second, I developed and optimized homeRNA, a remote blood self-collection and RNA stabilization platform that enables downstream transcriptomic studies in diverse populations and settings. I validated homeRNA's robustness through high-temperature stability testing, demonstrated its capability for immune response detection via lipopolysaccharide stimulation, and applied it in a real-world study capturing immune responses to wildfire smoke exposure across the western United States. Critically, homeRNA-stabilized samples were shown to be compatible with downstream RNA sequencing analysis (3' mRNA-sequencing and bulk RNA-sequencing) and were able to maintain RNA integrity across diverse environmental conditions and extended shipping periods. Combined, STOMP and homeRNA collectively expand the scope of translational research in tissue engineering and remote sampling applications, thus supporting more targeted investigations into disease mechanisms, therapeutic efficacy, and environmental health impacts.

1.5 References

1. Whitesides, G. M. The origins and the future of microfluidics. *Nature* **442**, 368–373 (2006).
2. Ge, T. *et al.* Open and closed microfluidics for biosensing. *Mater. Today Bio* **26**, 101048 (2024).
3. Lei, K. F. Microfluidic Systems for Diagnostic Applications: A Review. *SLAS Technol.* **17**, 330–347 (2012).
4. Trinh, T. N. D. *et al.* Droplet-Based Microfluidics: Applications in Pharmaceuticals. *Pharmaceuticals*

16, 937 (2023).
5. Iakovlev, A. P., Erofeev, A. S. & Gorelkin, P. V. Novel Pumping Methods for Microfluidic Devices: A Comprehensive Review. *Biosensors* **12**, 956 (2022).
6. Oliveira, N. M., Vilabril, S., Oliveira, M. B., Reis, R. L. & Mano, J. F. Recent advances on open fluidic systems for biomedical applications: A review. *Mater. Sci. Eng. C* **97**, 851–863 (2019).
7. Berthier, E., Dostie, A. M., Lee, U. N., Berthier, J. & Theberge, A. B. Open Microfluidic Capillary Systems. *Anal. Chem.* **91**, 8739–8750 (2019).
8. Casavant, B. P. *et al.* Suspended microfluidics. *Proc. Natl. Acad. Sci.* **110**, 10111–10116 (2013).
9. Berthier, J., Brakke, K. A. & Berthier, E. *Open Microfluidics*. (Scrivener Publishing ; Wiley, Beverly, Massachusetts : Hoboken, New Jersey, 2016).
10. Kaigala, G. V., Lovchik, R. D. & Delamarche, E. Microfluidics in the "Open Space" for Performing Localized Chemistry on Biological Interfaces. *Angew. Chem. Int. Ed.* **51**, 11224–11240 (2012).
11. Liu, Z., Han, X. & Qin, L. Recent Progress of Microfluidics in Translational Applications. *Adv. Healthc. Mater.* **5**, 871–888 (2016).
12. Sun, S., Xue, X. & Fu, J. Modeling development using microfluidics: bridging gaps to foster fundamental and translational research. *Curr. Opin. Genet. Dev.* **82**, 102097 (2023).
13. Bischel, L. L., Lee, S.-H. & Beebe, D. J. A Practical Method for Patterning Lumens through ECM Hydrogels via Viscous Finger Patterning. *SLAS Technol.* **17**, 96–103 (2012).
14. Park, D. *et al.* Aspiration-mediated hydrogel micropatterning using rail-based open microfluidic devices for high-throughput 3D cell culture. *Sci. Rep.* **11**, (2021).
15. Tibbitt, M. W. & Anseth, K. S. Hydrogels as extracellular matrix mimics for 3D cell culture. *Biotechnol. Bioeng.* **103**, 655–663 (2009).
16. Lee, S.-Y., Koo, I.-S., Hwang, H. J. & Lee, D. W. In Vitro three-dimensional (3D) cell culture tools for spheroid and organoid models. *SLAS Discov.* **28**, 119–137 (2023).
17. Abuwatfa, W. H., Pitt, W. G. & Husseini, G. A. Scaffold-based 3D cell culture models in cancer research. *J. Biomed. Sci.* **31**, 7 (2024).
18. Sugimoto, S. & Sato, T. Establishment of 3D Intestinal Organoid Cultures from Intestinal Stem Cells. in *3D Cell Culture* (ed. Koledova, Z.) vol. 1612 97–105 (Springer New York, New York, NY, 2017).
19. Herreros-Pomares, A. *et al.* 3D printing novel in vitro cancer cell culture model systems for lung cancer stem cell study. *Mater. Sci. Eng. C* **122**, 111914 (2021).
20. Smith, A. S. *et al.* High-throughput, real-time monitoring of engineered skeletal muscle function using magnetic sensing. *J. Tissue Eng.* **13**, 20417314221122127 (2022).
21. Norberg, K. J. *et al.* A novel pancreatic tumour and stellate cell 3D co-culture spheroid model. *BMC Cancer* **20**, 475 (2020).
22. Lazzari, G. *et al.* Multicellular spheroid based on a triple co-culture: A novel 3D model to mimic pancreatic tumor complexity. *Acta Biomater.* **78**, 296–307 (2018).
23. Yakavets, I. *et al.* Advanced co-culture 3D breast cancer model for investigation of fibrosis induced by external stimuli: optimization study. *Sci. Rep.* **10**, 21273 (2020).
24. Moghimi, N. *et al.* Controlled tumor heterogeneity in a co-culture system by 3D bio-printed tumor-on-chip model. *Sci. Rep.* **13**, 13648 (2023).
25. Zhong, H. *et al.* Generation of a co-culture cell micropattern model to simulate lung cancer bone metastasis for anti-cancer drug evaluation. *RSC Adv.* **7**, 21837–21847 (2017).
26. Piard, C. *et al.* 3D printed HUVECs/MSCs cocultures impact cellular interactions and angiogenesis depending on cell-cell distance. *Biomaterials* **222**, 119423 (2019).
27. Sugiura, S. *et al.* Dynamic three-dimensional micropatterned cell co-cultures within photocurable and chemically degradable hydrogels: Dynamic 3D micropatterned co-cultures. *J. Tissue Eng. Regen. Med.* **10**, 690–699 (2016).
28. Kazemzadeh-Narbat, M. *et al.* Engineering Photocrosslinkable Bicomponent Hydrogel Constructs for Creating 3D Vascularized Bone. *Adv. Healthc. Mater.* **6**, 1601122 (2017).
29. Kim, S., Lee, H., Chung, M. & Jeon, N. L. Engineering of functional, perfusable 3D microvascular networks on a chip. *Lab. Chip* **13**, 1489 (2013).

30. Gegg, C. & Yang, F. Spatially patterned microribbon-based hydrogels induce zonally-organized cartilage regeneration by stem cells in 3D. *Acta Biomater.* **101**, 196–205 (2020).
31. Biju, T. S., Priya, V. V. & Francis, A. P. Role of three-dimensional cell culture in therapeutics and diagnostics: an updated review. *Drug Deliv. Transl. Res.* **13**, 2239–2253 (2023).
32. Liu, Y., Xia, T., Wei, J., Liu, Q. & Li, X. Micropatterned co-culture of cardiac myocytes on fibrous scaffolds for predictive screening of drug cardiotoxicities. *Nanoscale* **9**, 4950–4962 (2017).
33. Liu, Y. *et al.* Micropatterned coculture of hepatocytes on electrospun fibers as a potential in vitro model for predictive drug metabolism. *Mater. Sci. Eng. C* **63**, 475–484 (2016).
34. Tenje, M. *et al.* A practical guide to microfabrication and patterning of hydrogels for biomimetic cell culture scaffolds. *Organs---Chip* **2**, 100003 (2020).
35. Primo, G. A. & Mata, A. 3D Patterning within Hydrogels for the Recreation of Functional Biological Environments. *Adv. Funct. Mater.* **31**, 2009574 (2021).
36. Weigel, N., Li, Y., Thiele, J. & Fery, A. From microfluidics to hierarchical hydrogel materials. *Curr. Opin. Colloid Interface Sci.* **64**, 101673 (2023).
37. Khetan, S. & Burdick, J. A. Patterning hydrogels in three dimensions towards controlling cellular interactions. *Soft Matter* **7**, 830–838 (2011).
38. Lee, M., Rizzo, R., Surman, F. & Zenobi-Wong, M. Guiding Lights: Tissue Bioprinting Using Photoactivated Materials. *Chem. Rev.* **120**, 10950–11027 (2020).
39. Francis, R. M. & DeForest, C. A. 4D Biochemical Photocustomization of Hydrogel Scaffolds for Biomimetic Tissue Engineering. *Acc. Mater. Res.* **4**, 704–715 (2023).
40. Lima, M. J., Correlo, V. M. & Reis, R. L. Micro/nano replication and 3D assembling techniques for scaffold fabrication. *Mater. Sci. Eng. C* **42**, 615–621 (2014).
41. Moeinzadeh, S. & Jabbari, E. 3D Cell Culture in Micropatterned Hydrogels Prepared by Photomask, Microneedle, or Soft Lithography Techniques. in *3D Cell Culture* (ed. Koledova, Z.) vol. 1612 239–252 (Springer New York, New York, NY, 2017).
42. Chae, S., Ha, D.-H. & Lee, H. 3D bioprinting strategy for engineering vascularized tissue models. *Int. J. Bioprinting* **9**, 748 (2023).
43. Hull, S. M., Brunel, L. G. & Heilshorn, S. C. 3D Bioprinting of Cell-Laden Hydrogels for Improved Biological Functionality. *Adv. Mater.* **34**, 2103691 (2022).
44. Chiu, D. T. *et al.* Patterned deposition of cells and proteins onto surfaces by using three-dimensional microfluidic systems. *Proc. Natl. Acad. Sci.* **97**, 2408–2413 (2000).
45. Choi, N. W. *et al.* Microfluidic scaffolds for tissue engineering. *Nat. Mater.* **6**, 908–915 (2007).
46. Legant, W. R. *et al.* Microfabricated tissue gauges to measure and manipulate forces from 3D microtissues. *Proc. Natl. Acad. Sci.* **106**, 10097–10102 (2009).
47. Eyckmans, J. & Chen, C. S. 3D culture models of tissues under tension. *J. Cell Sci.* (2016) doi:10.1242/jcs.198630.
48. Ribeiro, A. J. S., Denisin, A. K., Wilson, R. E. & Pruitt, B. L. For whom the cells pull: Hydrogel and micropost devices for measuring traction forces. *Methods* **94**, 51–64 (2016).
49. Iuliano, A. *et al.* Coupling 3D Printing and Novel Replica Molding for In House Fabrication of Skeletal Muscle Tissue Engineering Devices. *Adv. Mater. Technol.* **5**, (2020).
50. Leonard, A. *et al.* Afterload promotes maturation of human induced pluripotent stem cell derived cardiomyocytes in engineered heart tissues. *J. Mol. Cell. Cardiol.* **118**, 147–158 (2018).
51. Gill, E. L. *et al.* Fabrication of Designable and Suspended Microfibers via Low-Voltage 3D Micropatterning. *ACS Appl. Mater. Interfaces* **11**, 19679–19690 (2019).
52. Shiwarski, D. J., Hudson, A. R., Tashman, J. W. & Feinberg, A. W. Emergence of FRESH 3D printing as a platform for advanced tissue biofabrication. *APL Bioeng.* **5**, (2021).
53. Riffe, M. B. *et al.* Multi-Material Volumetric Additive Manufacturing of Hydrogels using Gelatin as a Sacrificial Network and 3D Suspension Bath. *Adv. Mater.* **36**, (2024).
54. Lee, U. N. *et al.* Layer-by-layer fabrication of 3D hydrogel structures using open microfluidics. *Lab. Chip* **20**, 525–536 (2020).
55. Berry, S. B. *et al.* Upgrading well plates using open microfluidic patterning. *Lab. Chip* **17**, 4253–

4264 (2017).
56. Park, S. E. *et al.* Geometric engineering of organoid culture for enhanced organogenesis in a dish. *Nat. Methods* **19**, 1449–1460 (2022).
57. Lee, S. H. *et al.* Capillary Based Patterning of Cellular Communities in Laterally Open Channels. *Anal. Chem.* **82**, 2900–2906 (2010).
58. Yu, J. *et al.* Reconfigurable open microfluidics for studying the spatiotemporal dynamics of paracrine signalling. *Nat. Biomed. Eng.* **3**, 830–841 (2019).
59. Humayun, M., Chow, C.-W. & Young, E. W. K. Microfluidic lung airway-on-a-chip with arrayable suspended gels for studying epithelial and smooth muscle cell interactions. *Lab. Chip* **18**, 1298–1309 (2018).
60. Wang, H. *et al.* Blood transcriptome profiling as potential biomarkers of suboptimal health status: potential utility of novel biomarkers for predictive, preventive, and personalized medicine strategy. *EPMA J.* **12**, 103–115 (2021).
61. Nath, M. *et al.* Whole blood transcriptomic profiling identifies molecular pathways related to cardiovascular mortality in heart failure. *Eur. J. Heart Fail.* **24**, 1009–1019 (2022).
62. Riemann, L. *et al.* Blood transcriptome profiling reveals distinct gene networks induced by mRNA vaccination against COVID-19. *Eur. J. Immunol.* **54**, 2451236 (2024).
63. Rinchai, D. *et al.* High–temporal resolution profiling reveals distinct immune trajectories following the first and second doses of COVID-19 mRNA vaccines. *Sci. Adv.* **8**, eabp9961 (2022).
64. Rehman, M. Y. A. *et al.* Transcriptome responses in blood reveal distinct biological pathways associated with arsenic exposure through drinking water in rural settings of Punjab, Pakistan. *Environ. Int.* **135**, 105403 (2020).
65. Chaussabel, D. Assessment of immune status using blood transcriptomics and potential implications for global health. *Semin. Immunol.* **27**, 58–66 (2015).
66. Baillargeon, K. R. & Mace, C. R. Microsampling tools for collecting, processing, and storing blood at the point-of-care. *Bioeng. Transl. Med.* **8**, e10476 (2023).
67. Thangavelu, M. U., Wouters, B., Kindt, A., Reiss, I. K. M. & Hankemeier, T. Blood microsampling technologies: Innovations and applications in 2022. *Anal. Sci. Adv.* **4**, 154–180 (2023).
68. Maass, K. F. *et al.* Leveraging patient-centric sampling for clinical drug development and decentralized clinical trials: Promise to reality. *Clin. Transl. Sci.* **15**, 2785–2795 (2022).
69. Krasowski, M. D. Remote Blood Collection Devices Improve Study Participation from Hard to Reach Populations. *J. Appl. Lab. Med.* **9**, 874–876 (2024).
70. Carignan, C. C. *et al.* Self-Collection Blood Test for PFASs: Comparing Volumetric Microsamplers with a Traditional Serum Approach. *Environ. Sci. Technol.* **57**, 7950–7957 (2023).
71. Lim, F. Y. *et al.* High-frequency home self-collection of capillary blood correlates IFI27 expression kinetics with SARS-CoV-2 viral clearance. *J. Clin. Invest.* **133**, e173715 (2023).
72. Al-Uzri, A. *et al.* Longitudinal study on the use of dried blood spots for home monitoring in children after kidney transplantation. *Pediatr. Transplant.* **21**, e12983 (2017).
73. Byström, J. W. *et al.* At-home sampling to meet geographical challenges for serological assessment of SARS-CoV-2 exposure in a rural region of northern Sweden, March to May 2021: a retrospective cohort study. *Eurosurveillance* **28**, (2023).
74. Lu, W., Zhou, Q. & Chen, Y. Impact of RNA degradation on next-generation sequencing transcriptome data. *Genomics* **114**, 110429 (2022).
75. Kukurba, K. R. & Montgomery, S. B. RNA Sequencing and Analysis. *Cold Spring Harb. Protoc.* **2015**, pdb.top084970 (2015).
76. Gallego Romero, I., Pai, A. A., Tung, J. & Gilad, Y. RNA-seq: impact of RNA degradation on transcript quantification. *BMC Biol.* **12**, 42 (2014).
77. Houseley, J. & Tollervey, D. The Many Pathways of RNA Degradation. *Cell* **136**, 763–776 (2009).
78. Bender, A. T., Sullivan, B. P., Lillis, L. & Posner, J. D. Enzymatic and Chemical-Based Methods to Inactivate Endogenous Blood Ribonucleases for Nucleic Acid Diagnostics. *J. Mol. Diagn.* **22**, 1030–1040 (2020).

79. Delahaye, L. *et al.* Alternative Sampling Devices to Collect Dried Blood Microsamples: State-of-the-Art. *Ther. Drug Monit.* **43**, 310–321 (2021).
80. Malsagova, K. *et al.* Dried Blood Spot in Laboratory: Directions and Prospects. *Diagnostics* **10**, 248 (2020).
81. Bybjerg-Grauholm, J. *et al.* RNA sequencing of archived neonatal dried blood spots. *Mol. Genet. Metab. Rep.* **10**, 33–37 (2017).
82. Reust, M. J. *et al.* Dried Blood Spot RNA Transcriptomes Correlate with Transcriptomes Derived from Whole Blood RNA. *Am. J. Trop. Med. Hyg.* **98**, 1541–1546 (2018).
83. Bertoli-Avella, A. M. *et al.* Beyond genomics: using RNA-seq from dried blood spots to unlock the clinical relevance of splicing variation in a diagnostic setting. *Eur. J. Hum. Genet.* **33**, 614–623 (2025).
84. Kalikiri, M. K. R. *et al.* Technical assessment of different extraction methods and transcriptome profiling of RNA isolated from small volumes of blood. *Sci. Rep.* **13**, 3598 (2023).
85. Morgunova, A. *et al.* Preparation and processing of dried blood spots for microRNA sequencing. *Biol. Methods Protoc.* **8**, bpad020 (2023).
86. McDade, T. W. *et al.* Genome-Wide Profiling of RNA from Dried Blood Spots: Convergence with Bioinformatic Results Derived from Whole Venous Blood and Peripheral Blood Mononuclear Cells. *Biodemography Soc. Biol.* **62**, 182–197 (2016).
87. Demirev, P. A. Dried Blood Spots: Analysis and Applications. *Anal. Chem.* **85**, 779–789 (2013).
88. Zarbl, J. *et al.* Remote self-collection of capillary blood using upper arm devices for autoantibody analysis in patients with immune-mediated inflammatory rheumatic diseases. *RMD Open* **8**, e002641 (2022).
89. Dasari, H., Smyrnova, A., Leng, J. & Ducharme, F. M. Feasibility, acceptability, and safety of a novel device for self-collecting capillary blood samples in clinical trials in the context of the pandemic and beyond. *PLOS ONE* **19**, e0304155 (2024).
90. Haack, A. J. *et al.* homeRNA: A Self-Sampling Kit for the Collection of Peripheral Blood and Stabilization of RNA. *Anal. Chem.* **93**, 13196–13203 (2021).
91. Huang, L.-H. *et al.* The effects of storage temperature and duration of blood samples on DNA and RNA qualities. *PLOS ONE* **12**, e0184692 (2017).
92. Kim, S. J. *et al.* Effects of Storage, RNA Extraction, Genechip Type, and Donor Sex on Gene Expression Profiling of Human Whole Blood. *Clin. Chem.* **53**, 1038–1045 (2007).
93. Koh, E. J. *et al.* Understanding Confounding Effects of Blood Handling Strategies on RNA Quality and Transcriptomic Alteration Using RNA Sequencing. *BioChip J.* **15**, 187–194 (2021).
94. Jiang, Z. *et al.* Effects of storage temperature, storage time, and hemolysis on the RNA quality of blood specimens: A systematic quantitative assessment. *Heliyon* **9**, e16234 (2023).
95. Brown, L. G. *et al.* At-home blood collection and stabilization in high temperature climates using homeRNA. *Front. Digit. Health* **4**, 903153–903153 (2022).
96. Stefanovic, F. *et al.* Your Blood is Out for Delivery: Considerations of Shipping Time and Temperature on Degradation of RNA from Stabilized Whole Blood. *Anal. Chem.* **97**, 1635–1644 (2025).
97. Lim, F. Y. *et al.* homeRNA self-blood collection enables high-frequency temporal profiling of presymptomatic host immune kinetics to respiratory viral infection: a prospective cohort study. *eBioMedicine* **112**, 105531 (2025).
98. Senande-Rivera, M., Insua-Costa, D. & Miguez-Macho, G. Spatial and temporal expansion of global wildland fire activity in response to climate change. *Nat. Commun.* **13**, 1208 (2022).
99. Doerr, S. H. & Santín, C. Global trends in wildfire and its impacts: perceptions versus realities in a changing world. *Philos. Trans. R. Soc. B Biol. Sci.* **371**, 20150345 (2016).
100. Jones, M. W. *et al.* Global and Regional Trends and Drivers of Fire Under Climate Change. *Rev. Geophys.* **60**, e2020RG000726 (2022).
101. Parks, S. A. & Abatzoglou, J. T. Warmer and Drier Fire Seasons Contribute to Increases in Area Burned at High Severity in Western US Forests From 1985 to 2017. *Geophys. Res. Lett.* **47**,

e2020GL089858 (2020).
102. Juang, C. S. *et al.* Rapid Growth of Large Forest Fires Drives the Exponential Response of Annual Forest-Fire Area to Aridity in the Western United States. *Geophys. Res. Lett.* **49**, e2021GL097131 (2022).
103. Reid, C. E. *et al.* Critical Review of Health Impacts of Wildfire Smoke Exposure. *Environ. Health Perspect.* **124**, 1334–1343 (2016).
104. Ma, Y. *et al.* Long-term exposure to wildland fire smoke $PM_{2.5}$ and mortality in the contiguous United States. *Proc. Natl. Acad. Sci.* **121**, e2403960121 (2024).
105. Wilgus, M.-L. & Merchant, M. Clearing the Air: Understanding the Impact of Wildfire Smoke on Asthma and COPD. *Healthcare* **12**, 307 (2024).
106. Zhao, J. *et al.* Role of PM2.5 in the development and progression of COPD and its mechanisms. *Respir. Res.* **20**, 1–13 (2019).
107. Noah, T. L., Worden, C. P., Rebuli, M. E. & Jaspers, I. The Effects of Wildfire Smoke on Asthma and Allergy. *Curr. Allergy Asthma Rep.* **23**, 375–387 (2023).
108. Chen, H., Samet, J. M., Bromberg, P. A. & Tong, H. Cardiovascular health impacts of wildfire smoke exposure. *Part. Fibre Toxicol.* **18**, 2 (2021).
109. Williams, V. A. *et al.* Impact of Wildfires on Cardiovascular Health. *Circ. Res.* **134**, 1061–1082 (2024).
110. Aguilera, J. *et al.* Granzymes, IL-16, and poly(ADP-ribose) polymerase 1 increase during wildfire smoke exposure. *J. Allergy Clin. Immunol. Glob.* **2**, 100093 (2023).
111. Parenteau, A. M. *et al.* Associations of air pollution with peripheral inflammation and cardiac autonomic physiology in children. *New Dir. Child Adolesc. Dev.* **2022**, 125–154 (2022).
112. Xu, R. *et al.* Wildfire-related PM2.5 and DNA methylation: An Australian twin and family study. *Environ. Int.* **171**, (2023).
113. Sanghar, G. K. *et al.* Real-life observation of wildfire smoke–impaired COVID-19 vaccine immunity. *J. Allergy Clin. Immunol.* **155**, 1371-1377.e6 (2025).

Chapter 2 | Suspended Tissue Open Microfluidic Patterning (STOMP)

Reproduced in part from A. J. Haack, L. G. Brown*, A. J. Goldstein, P. Mulimani, J. Berthier, A. R. Viswanathan, I. Kopyeva, J. M. Whitten, A. Lin, S. N. Nguyen, T. P. Leahy, E. E. Bouker, R. M. Padgett, N. A. Mazzawi, J. C. Tokihiro, R. C. Bretherton, A. Wu, S. J. Tapscott, C. A. DeForest, T. E. Popowics, E. Berthier, N. J. Sniadecki[#], A. B. Theberge[#]. "Suspended Tissue Open Microfluidic Patterning (STOMP)." Advanced Science, 2025, 2501148.*

**Equal contribution*

[#]Co-corresponding authors

AJH, LGB, NJS, and ABT conceived the project. NJS and ABT supervised the project. AJH and LGB designed and fabricated the device with process inputs from JB, RB, AW, EB, and ABT. AG, PM and NM fabricated the PDMS posts with process inputs from NJS. JB performed the theoretical analysis and derivations of the Laplace pressure at the pinning features. LGB and AJH performed the experimental pinning of collagen in the different pinning features. AG designed and conducted the engineered heart tissue experiments with design inputs from LGB, AJH, and NJS. AG performed the data analysis for the engineered heart tissue experiments. PM designed and PM and NM conducted the periodontal tissue construct experiments with design inputs from AJH, LGB, TEP, and NJS. PM performed the fluorescent staining and data analysis of the periodontal tissue constructs with NM and TL. SN designed the suspended core devices with design inputs from AJH. AV designed the degradable wall devices with design inputs from AJH and IK. IK synthesized the degradable PEG components and assisted in experimental design with input from CAD. AJH, LGB, AG, PM, JMW, AL, SN, AV, EEB, RP, JCT and NM assisted with cell culture. JMW and AL performed the contact angle measurements. AJH and LGB wrote the manuscript with significant inputs from AG, PM, JB, SJT, CAD, TEP, EB, NJS, and ABT.

Abstract: Free-standing tissue structures tethered between pillars are powerful mechanobiology tools for studying cell contraction. To model interfaces ubiquitous in natural tissues and upgrade existing single-region suspended constructs, we developed Suspended Tissue Open Microfluidic Patterning (STOMP), a method to create multi-regional suspended tissues. STOMP uses open microfluidics and capillary pinning to pattern subregions within free-standing tissues, facilitating the study of complex tissue interfaces, such as diseased-healthy boundaries (e.g., fibrotic-healthy) and tissue-type interfaces (e.g., bone-ligament). We observed altered contractile dynamics in fibrotic-healthy engineered heart tissues compared to single-region tissues and differing contractility in bone-ligament enthesis constructs compared to single-tissue periodontal ligament models. STOMP is a versatile platform – surface tension-driven patterning removes material requirements common with other patterning methods (e.g., shear-thinning, photopolymerizable) allowing tissue generation in multiple geometries with native extracellular matrices and advanced 4D materials. STOMP combines the contractile functionality of suspended tissues with precise patterning, enabling dynamic and spatially controlled studies.

2.1 Introduction

Developing methods to generate more physiologically relevant three-dimensional (3D) tissue models is important for a wide range of applications, from modeling tissue development to realizing clinical applications in tissue regeneration[1,2]. To recapitulate *in vivo* tissue architecture, traditional 3D cell cultures embed cells within a hydrogel consisting of natural or synthetic compositions of the extracellular matrix (ECM). However, in traditional 3D cell culture models (e.g., attached to the bottom of a well plate or in a hanging drop spheroid), it is often difficult to control mechanical cues that play a crucial role in cell morphology, alignment, proliferation, and differentiation[3,4]**.** To address this limitation, flexible cantilevers and pillars can serve as scaffolds for suspended 3D tissue structures that experience tensile forces[5-9]; these platforms have been used to develop engineered heart[10], musculoskeletal[11,12], and lung[13-15] tissues, as well as wound healing skin models[16]. However, suspended models typically consist of a single cell type or ECM composition, lacking the regional heterogeneity seen in natural tissues. This heterogeneity is reflected not only in the distinct junctions seen in healthy tissues (e.g., bone-ligament interfaces), but also disease processes (e.g., fibrosis) can locally alter cell types and ECM composition. Having control over the precise cellular and ECM composition within a single tissue construct increases the physiological relevance and opens new applications for modeling complex disease processes.

To achieve geometric control in 3D tissue constructs, many biofabrication techniques, such as casting[17-19], photopatterning[20,21], and 3D bioprinting[22-24], have been developed to recapitulate the complex structural and cellular composition of native tissues[25]. Of these biofabrication techniques, the casting method is widely used to generate free-standing suspended tissues (e.g., a tissue suspended between two posts in culture)[26,27]. However, the casting method is limited in geometric and cellular distribution control. Recently, 3D bioprinting has been used to generate suspended microfibers[28] via low-voltage electrospinning, and freeform structures via a sacrificial suspension bath[29-33]. These bioprinting methods require custom-engineered 3D bioprinted systems, which limit their accessibility and scalability. Microfluidic-based technologies are also widely used for their ability to introduce dynamic or perfusable

flow to complex culture systems, where active flow can be used to pattern cells or cell-laden hydrogels within a microfluidic device[34-39].

It is also possible to use surface tension to drive passive flow; this type of flow has been used extensively in open microfluidic systems, eliminating the need for complex off-chip pumping systems. Open microfluidic systems are defined as having at least one channel boundary that confines the fluid flow open to the air[40-45]. Open channels can exist in multiple configurations and can be defined within solid boundaries to pattern distinct regions[40,46-49] or within fluid boundaries to pattern aqueous circuits[50]. Open-to-air channels allow for easy accessibility and manipulation of cell-ECM solutions via a simple pipetting step. Recently, open microfluidic-based 3D cell culture platforms have been realized to pattern multiple cell types or ECMs in layered 3D structures[46,51,52], for generating rail-based (i.e., a channel without walls) regional culture systems[47-49,53-56], and for patterning regions of degradable gels for temporal and spatial control of the cellular microenvironment[46,57,58]. Suspended open microfluidic systems that are devoid of a ceiling and floor have been used to generate suspended tissues composed of a uniform cell-ECM composition[51,52].

Here, we utilize suspended open microfluidics and capillary pinning to pattern 3D free-standing suspended tissues; we call this method Suspended Tissue Open Microfluidic Patterning (STOMP). STOMP interfaces with our previously described platform in which a tissue is suspended between two posts such that the tissue construct forms a bridge between these posts[26,59-62]. Previously, tissues formed using this post platform were generated with a casting method to form a tissue that is uniform in composition. In contrast, the STOMP platform uses a removable 3D-printed patterning device containing an open microfluidic channel that interfaces around the two posts. This method offers the unique advantage of spatially controlled material and cell composition by employing capillary pinning features along the open channel. Using surface tension to drive flow and capillary pinning to stop flow, we can achieve control over the placement of tissue components to pattern multiple regions within a single suspended tissue. After patterning, we either take advantage of cell compaction allowing for the tissue to pull away from the patterning walls, or employ a degradable poly(ethylene glycol) (PEG)-based hydrogel patterned in an open microfluidic

channel within the STOMP channel walls to dissolve the channel wall, allowing for gentle removal of the STOMP device and revealing a suspended tissue. This system provides the capability to model complex biological features, such as border regions between tissues (e.g., disease and healthy tissue borders) and tissue junctions (e.g., bone-ligament interfaces).

2.2 STOMP is a versatile tool for achieving geometric, volumetric, and compositional control over a diverse set of materials and tissues

Free-standing engineered tissues suspended between two posts are commonly generated using a casting technique where posts are placed upside down within a well plate that contains a mold where a cell-laden hydrogel precursor solution is pipetted[62]. STOMP adds upon these existing techniques, enabling spatial control over tissue composition. To achieve this control, STOMP uses a pinning technique, where a geometric discontinuity acts as a pinning feature that opposes the driving capillary forces that advance the fluid front, thereby immobilizing the capillary flow at a predefined location[63-67] (Figure 2.1). Further, the use of an open channel (i.e., a channel without a ceiling and floor) allows for access so different combinations of cell-hydrogel precursors can be pipetted into different regions. The fluid fronts on either side of a pair of pinning features come together to form a contiguous tissue with distinctly different regions. The pinning features of STOMP can be placed anywhere along the length of the open channel. Moreover, multiple pinning features can be placed in one tissue, generating more than two regions. To illustrate the versatility of possible geometries, we show patterning of one, two, and three regions with colored agarose (Figure 2.1).

STOMP uses three components: (1) two vertical posts that suspend the final tissue as a bridge between them, (2) a removable patterning device containing an open microfluidic suspended channel designed to surround the two posts, and (3) holding clips to secure the assembly together (Figure 2.1a-b). Once assembled, we pipette a cell-laden hydrogel precursor into the open channel (Figure 2.1d). The solution flows throughout the open channel via spontaneous capillary flow. Once the cell-laden hydrogel solidifies and the traction forces of the embedded cells cause the construct to pull away from the walls of the

patterning device, we remove the patterning device and the construct is cultured as a free-standing suspended tissue.

The precursor solution is held suspended between the walls of the open channel of the patterning device via surface tension as the solution transitions from liquid to gel state[40]. After gelation, the entire assembled patterning device is placed in a 24-well plate with media (Figure 2.1c). To prevent the tissue from sticking to the walls, we incubate the channel with 1% bovine serum albumin (BSA) prior to pipetting the precursor solution. T-shaped caps on each of the posts anchor the tissue such that it stays suspended between the tips of the posts. After visible compaction, the patterning device is gently lifted, thereby releasing the tissue while it stays suspended between the two posts. In this work, we have generated suspended tissues with STOMP composed of multiple hydrogel and ECM types including type I collagen, fibrin, Matrigel, agarose and custom-engineered enzymatically degradable poly(ethylene glycol) (PEG). We have also used multiple cell types including fibroblasts, periodontal ligament cells, and cardiomyocytes. We demonstrate using two sets of pinning features (Figure 2.1e) with 3T3 mouse fibroblast cells dyed by CellTracker Green CMFDA and CellTracker Red CMTPX patterned to make a three-region configuration (Figure 2.1f). This workflow requires three pipetting steps, where different precursor solutions on either side of the pinning feature will meet (Figure 2.1g). We further demonstrate this spatial patterning of three separate regions in a free-standing tissue with colored agarose (Figure 2.1h).

By adding this regional control we enable in vitro models to investigate heterogeneity within a single tissue (e.g., diseased adjacent to healthy tissue), or even the investigation of multiple tissue interfaces within a single construct (e.g., bone adjacent to ligament tissue). STOMP also offers volumetric control in tissue size. In open microfluidic systems, surface tension is the main driving force of flow[40-43,68]. By changing the dimensions of the patterning channel, we can change the shape of the generated tissue as long as the cross-sectional dimensions of the channel follow the equation necessary for spontaneous capillary flow (Eq. 2.1), where pf is the free perimeter and pw is the wetted perimeter of the cross section[40]. Equation (2.1) can be simplified to equation (2.2) for a suspended channel geometry where w is the width (free perimeter) of the

channel, h is the height (wetted perimeter) of the channel, and θ is the contact angle of the hydrogel on the channel surface[40,46]. These dimensions can be visualized in the x-z cross-section in Figure 2.1B.

$$\frac{p_f}{p_w} < \cos(\theta) \tag{2.1}$$

$$\frac{w}{h} < \cos(\theta) \tag{2.2}$$

With STOMP, dimensions smaller than the capillary length of a fluid – where surface tension dominates over gravity – are preferred to maintain a uniform cross-section of the hydrogel fluid front along the channel. At larger geometrical dimensions, droplets can form within the channel, thereby preventing the complete filling of the open channel (i.e., wetting of the hydrogel along channel walls). Therefore, by maintaining the conditions for spontaneous capillary flow in a suspended channel (Eq. 2.2), we scaled our current STOMP design to achieve tissue volumes between 30-100 μL of hydrogel precursor, depending on channel dimensions. With customizable channel geometries, STOMP can be used to generate tissues of various sizes. For instance, a smaller volume may be advantageous when using precious cells or designer hydrogel material, and a larger volume may be advantageous for longer culture periods in tissues that compact and remodel their matrix.

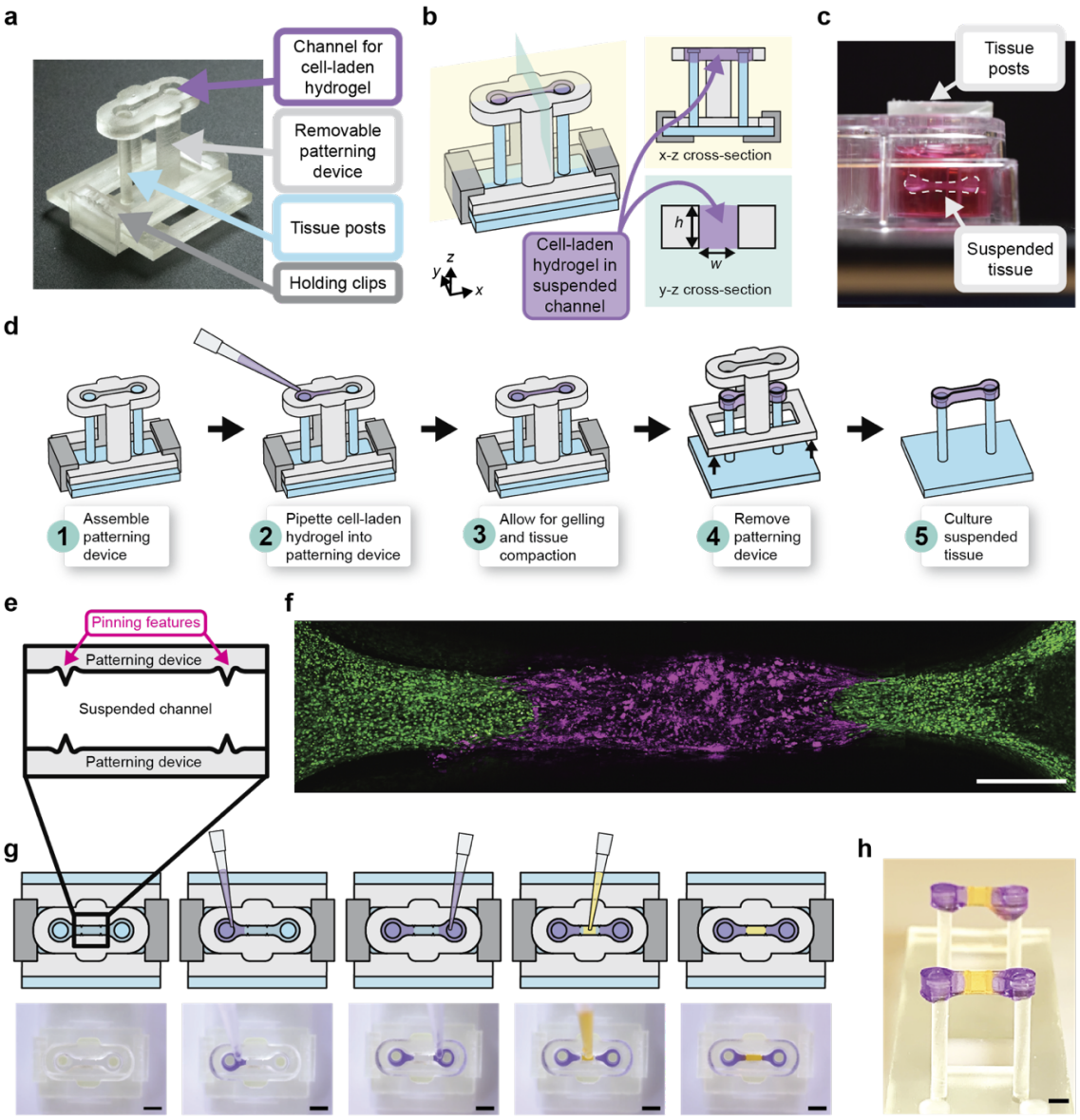

Figure 2.1. Workflow of generating single and multi-region suspended tissues using the STOMP platform. **(a)** Image of the STOMP platform, which includes a removable patterning device containing an open channel that interfaces with a pair of vertical posts. The patterning device is held in place to the base for the posts with holding clips. **(b)** Schematic of the STOMP platform. A cell-laden hydrogel is pipetted into the open channel, where it flows via surface-tension driven forces across the open channel and anchors onto the suspended posts, thus generating a free-standing suspended tissue. **(c)** Side view of the resulting suspended tissue cultured in a 24-well plate. **(d)** Workflow of patterning a tissue composed of a single region, where the composition is the same across the tissue. **(e)** Top-down view of the capillary pinning features along the open channel that are used to pin the fluid front. **(f)**Fluorescent image of patterned 3T3 mouse fibroblast cells laden in a fibrin hydrogel using STOMP. The outer region of 3T3 cells were dyed by CellTracker Green (green) and were pipetted first. The middle region of 3T3 cells were dyed by CellTracker Red (magenta). Scale bar is 500 μm. **(g)**Workflow of patterning tissues comprising three distinct regions. Corresponding video stills show patterning of purple-colored agarose in the outer regions first, followed by patterning yellow-colored agarose in the middle region. All scale bars are 2 mm. **(h)** Side view image of multi-region agarose suspended hydrogel construct. Scale bar is 2 mm.

2.3 Theoretical modeling of capillary pinning features for control over 3D geometry within a suspended tissue construct

To pattern distinct regions, we use pinning features to stop the fluid front, thus creating a defined border region. However, when a second solution is pipetted into the channel on the other side of the pinning feature, the pinning must intentionally be broken, allowing the two fluid fronts to meet to form a continuous tissue. Here, we analyze two pinning feature designs we refer to as convex "vampire" or concave "cavity" pins. The convex "vampire" pinning feature design comprises opposing reliefs resembling "teeth", with the reliefs extending along the height of the channel (Figure 2.2a). We note that α is the angle formed by the triangular shaped relief, θ is the contact angle of the hydrogel with the channel wall, and w_1 is the distance between the two opposing reliefs of the convex "vampire" pins (Figure 2.2a). If γ denotes the surface tension of the liquid, the Laplace pressure, P, of the liquid is given below (Eq. 2.3), where r is the curvature radius of the pinned interface.

$$\Delta P = \frac{\gamma}{r} \tag{2.3}$$

At the pinning limit (i.e., the maximum interface the fluid bulges before pinning is broken), the interface forms the angle θ with the triangular edge[64-67,69] (Figure 2.2a). At this pinning limit, the relationship between the geometry of the convex "vampire" pins (Figure 2.2a) and the contact angle θ is described by equation (2.4); a more detailed derivation is located in Appendix A, and geometric considerations are illustrated in Supplementary Figure A4.

$$\sin\left(\theta - \frac{\alpha}{2}\right) = \frac{w_1}{2r} \tag{2.4}$$

Substituting equation (2.4) into equation (2.3) yields the threshold Laplace pinning pressure, above which pinning is lost in the convex "vampire" pinning feature design (Eq. 2.5).

$$\Delta P = \frac{\gamma}{r} = \frac{2\gamma \sin\left(\theta - \frac{\alpha}{2}\right)}{w_1} \tag{2.5}$$

The concave "cavity" pinning feature comprises two facing cuts into the open channel resembling circular cavities, with the cut extending along the height of the channel (Figure 2.2b). We note that β is the

angle formed by the line tangent to the circular cavity and the wall of the channel, θ is the contact angle of the hydrogel with the channel wall, and w2 is the width of the open channel (Figure 2.2b). Equation (2.6) describes the geometric relations of the concave "cavity" pinning feature and the contact angle at the pinning limit. A more detailed derivation is located in Appendix A and geometric considerations are illustrated in Supplementary Figures A5-6.

$$\cos(\theta - \beta) = \frac{w_2}{2r} \tag{2.6}$$

Substituting equation (2.6) into equation (2.3) yields the threshold Laplace pinning pressure, above which pinning is lost in the concave "cavity" pinning feature design (Eq. 2.7).

$$\Delta P = \frac{\gamma}{r} = \frac{2\gamma\cos(\theta - \beta)}{w_2} \tag{2.7}$$

Because gravity has a small, but non-negligible effect, we must also consider hydrostatic pressure at the pinning interface. For both pinning feature designs, hydrostatic pressure at the bottom of the channel is given below in equation (2.8), where ρ is the density of the hydrogel, g is the gravitational constant, and h is the height of the channel. The effect of gravity on our system is further described in Appendix A and Supplementary Figure A7.

$$\Delta P = \rho g h \tag{2.8}$$

The pinning is determined by the fluid pressure at the pinning site. Pinning remains stable if the fluid pressure is lower than the threshold Laplace pinning pressure. The highest pressure occurs at the bottom of the channel where hydrostatic pressure is maximum. Therefore, the stability of pinning is dictated by the conditions at the bottom of the device. If pinning is lost at the bottom, it leads to a gradual loss of pinning along the entire vertical ridge. Figure 2.2g depicts a representative illustration of what the fluid front looks when pinning of the first pipetted region fails.

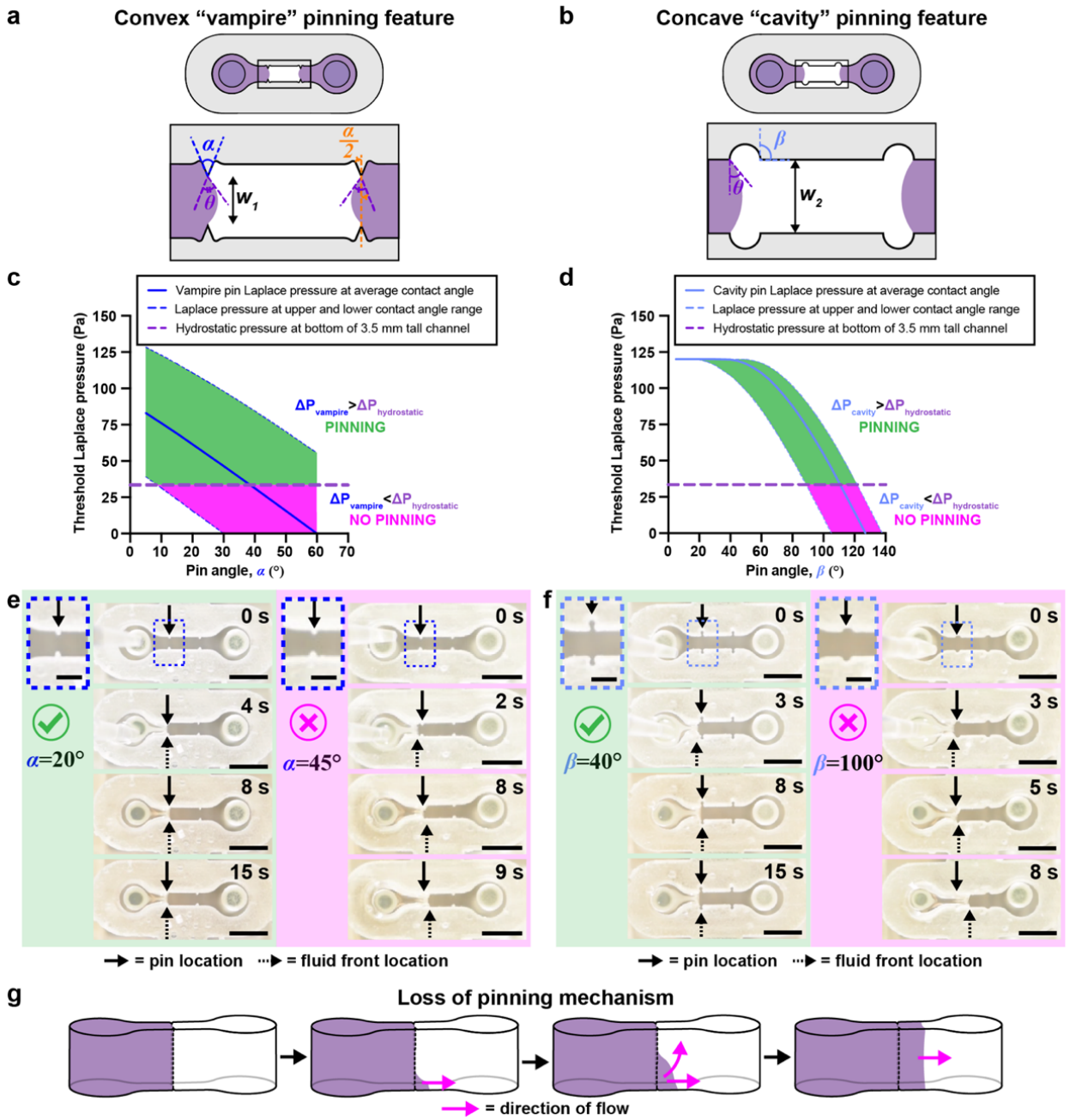

Figure 2.2. Characterization of capillary pinning features used in STOMP to generate multi-region suspended tissues. Geometric considerations of **(a)** vampire and **(b)** cavity pinning feature designs. Graphs of maximum Laplace pinning pressure plotted against **(c)** α, pin angle of the vampire feature and **(d)** β, pin angle of the cavity feature. Solid lines represent a Laplace pinning pressure ($\Delta P_{vampire}$ or ΔP_{cavity}) for a contact angle of Θ = 30°, which is the average contact angle for 5 mg/mL collagen on 3D-printed resin treated with 1% BSA at room temperature for one hour. Upper and lower bounds of the Laplace pinning pressure is calculated based on the largest measured contact angle (Θ = 48°) and the smallest measured contact angle (Θ = 15°) on 1% BSA-treated 3D-printed resin. If the Laplace pinning pressure is greater than that of the hydrostatic pressure ($\Delta P_{hydrostatic}$ = 33.5 Pa) then pinning is predicted to occur (shaded in green). If the Laplace pinning pressure is less than $\Delta P_{hydrostatic}$, then pinning will not occur (shaded in magenta). **(e)** Representative video still images of 23 µL of a 5 mg/mL precursor collagen solution pipetted into two different 1% BSA treated STOMP devices containing the vampire pinning features; left four

images use devices with α = 20° and right four images use devices α = 45°. **(f)** Representative video still images of 23 μL of a 5 mg/mL precursor collagen solution pipetted into two different 1% BSA treated STOMP devices containing the cavity pinning features; left four images uses devices with β = 40° and right four images use devices with β = 100°. Scale bars on insets are 1 mm. All other scale bars are 3 mm. **(g)** Visualization for the loss of pinning mechanism, where a pink arrow indicates the direction of flow of the purple hydrogel, with pinning first lost at the bottom of the channel.

According to equations (2.5) and (2.7), the angles α and β of the convex "vampire" and concave "cavity" pins, respectively, affect whether pinning is maintained or lost (Figure 2.2a-b). We plotted a range of these angles to generate a theoretical prediction of the threshold Laplace pinning pressure using the parameters for 5 mg/mL collagen, with a 1% BSA treated 3D printed resin surface (Figure 2.2c-d). The contact angle was found to be 30°±2° (n=20). We also considered how the range of the contact angle (15-48°) affects the theoretical modeling (see Supplementary Table A1). Using the values of the different parameters in Supplementary Table A3, we plot the threshold Laplace pinning pressure for different pinning angles (α and β) for the convex "vampire" (Figure 2.2c) and concave "cavity" design (Figure 2.2d), respectively.

Considering the average contact angle found for type I collagen on 1% BSA treated resin (30°), the pinning angle above which pinning is lost is when α is 35° for the convex "vampire" pinning feature; this is when Eq (2.5) is equal to Eq (2.8). For the concave "cavity" pinning features, pinning is lost when the pinning angle β is between 100° and 105°; this is when Eq (2.7) is equal to Eq (2.8). These angles are where the Laplace pinning threshold line crosses the hydrostatic pressure line (Figure 2.2c-d). When the maximum hydrostatic pressure is greater than the threshold Laplace pinning, pinning in the first pipetted region will likely fail. Loss of pinning will occur if the pressure at the fluid front exceeds the threshold Laplace pinning. The hydrostatic pressure at the bottom of the device is constant and does not depend on the geometry of the pinning features. Therefore, when the threshold Laplace pinning curve crosses below the hydrostatic pressure line, pinning will fail because the total pressure, which is dictated by the hydrostatic pressure, exceeds the threshold Laplace pressure.

When tested experimentally, we found that the success of pinning reflects these theoretical predictions while also demonstrating the variability in the system, i.e., success varies due to the large range of possible

contact angles (Supplementary Figure A2). The large range of the contact angles are due to multiple factors, including the variability of the BSA coating and local changes in surface roughness and defects on the 3D printed resin surface. With both pinning geometries, the smaller angles pinned more consistently, while the larger angles (particularly those that are above where the hydrostatic pressure is greater than that of the threshold Laplace pinning pressure) failed to pin. In some cases, the average contact angle line predicted that pinning would occur, but it did not in all cases. However, when considering the range of possible contact angles, the lower bound lines on the graphs actually predicted failure, therefore we can assume the contact angle was smaller in those particular devices. A detailed description of these results is found in Appendix A. Additionally, we found that pipetting 1 μL of additional volume can change the bulging angle of the pinned fluid front's vertical interface (see additional results and discussion in Appendix A, Supplementary Table A2, and Supplementary Figures A8-10 for detailed derivation). This phenomenon can help explain why experimentally we observed changes in successful pinning of the fluid front at different pipetted volumes. It should be noted that the theoretical conditions tested here are specific to parameters associated with a 5 mg/mL collagen solution. The specific cutoff values for pinning with the different features will change with different materials and with different channel and pinning geometries.

2.4 Spatially heterogeneous engineered heart tissues (EHTs) generated with STOMP model cardiac fibrotic pathology

Fibrotic remodeling is an innate component of almost all acute and chronic cardiac pathologies, including hypertension, myocardial infarction, inherited cardiomyopathies, and end-stage heart failure [70]. This remodeling is characterized by an increase in the myocardial extracellular matrix, proliferation of stromal cells, and often a loss of cardiomyocytes[71]. Fibrotic progression is typically associated with an enhanced risk of arrhythmias and cardiac dysfunction[72]. Despite the near ubiquitous presence of fibrotic progression in cardiac disease, there are currently no clinical therapies available that directly address fibrosis[73]. While numerous investigators have developed various engineered heart tissue (EHT) platforms to model cardiac fibrosis, these systems are primarily homogeneous in cell type and ECM composition and fail to recreate the focal remodeling seen *in vivo*. Currently, the most advanced systems for modeling cardiac

fibrosis using hiPSC-derived cardiomyocytes consist of a cardiac microtissue model utilizing a laser induced injury[74] and the Biowire II platform with two heteropolar healthy and fibrotic myocardial regions[75].

Using STOMP, we sought to develop an *in vitro* model of a cardiac tissue with a fibrotic interface, by creating spatially heterogeneous EHTs with a middle "fibrotic" region containing a localized excess of stromal cells and collagen, and deficit of cardiomyocytes, bordered on both sides by a "healthy" myocardial section (Figure 2.3a). Stromal cells used in the outer or middle regions were fluorescent HS5-GFP or HS5-mCherry cells, respectively, to delineate the regional boundaries and HS27A stromal cells were seeded throughout all regions (Figure 2.3a-b). To measure functional outputs of the patterned EHTs, both the control and fibrotic tissues were paced under 1.5 Hz frequency, resulting in the average twitch force waveforms seen in Figure 2.3c. Both control and fibrotic EHTs formed effective cardiac syncytia, as shown by their ability to follow the pacing frequency (Figure 2.3d). We next looked at the unpaced, spontaneous beat frequency of the EHTs, representative of a resting heart rate. Compared to control tissues, fibrotic tissues showed an elevated beat frequency, a response similar to that seen in patients with heart failure downstream of cardiomyopathy[76-78] (Figure 2.3e). Additionally, measurement of tissue contractions revealed that fibrotic EHTs presented with altered kinetics as they returned to diastole, or the phase where the heart chambers relax and refill with blood in preparation for the next contraction. This diastolic alteration in fibrotic EHTs was seen as a faster time to 50% relaxation (Figure 2.3f), but this difference is no longer evident at 90% relaxation (Figure 2.3g), suggesting that the fibrotic heart tissues initially relaxed faster but then slowed relaxation, compared to the control tissues. In patients with dilated cardiomyopathy, total relaxation time tends to be increased[79], therefore it is notable that in our model time to 50% relaxation was decreased. The increased stromal cells in the fibrotic tissue model may also partially explain the quicker time to 50% relaxation, a result that has been noted in previous *in vitro* models[80]. Finally, despite no differences in the twitch force (Figure 2.3h), specific force (Figure 2.3i), or shortening velocity (Figure 2.3j) compared to control tissues, fibrotic EHTs did display altered systole, or the contractile phase of cardiac cycle, as shown by a lower time to peak (Figure 2.3k).

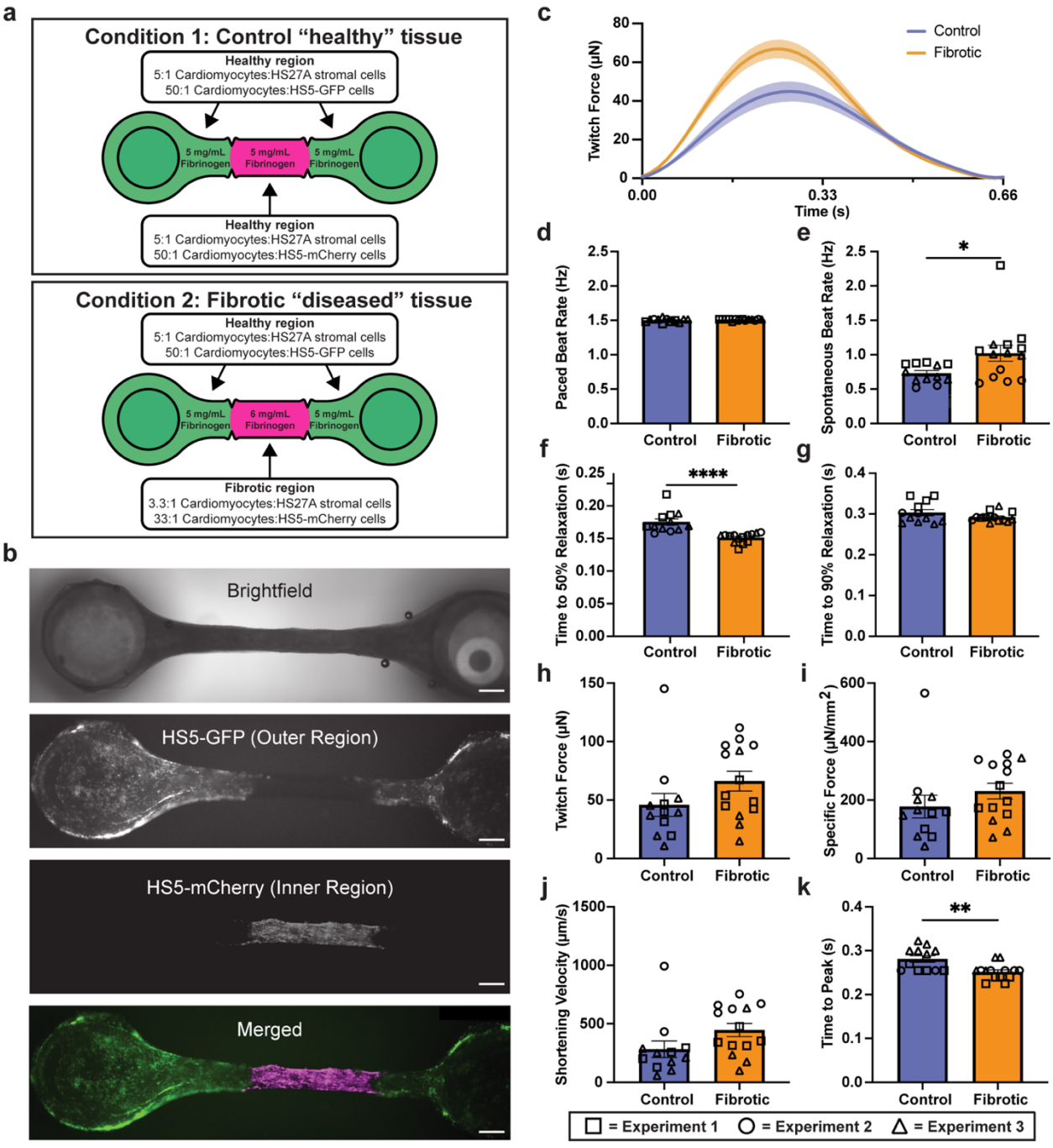

Figure 2.3. Patterned engineered heart tissues (EHTs). **(a)** Conditions tested for modeling a fibrotic region in an EHT using STOMP, where the middle region has a higher fibrin content and lower cardiomyocyte density than the regions at either end. **(a)** Representative brightfield and fluorescent images of a control EHT seeded with HS5-GFP human bone marrow stromal cells (green) on the two outer regions near the flexible and rigid posts, and HS5-mCherry cells (magenta) in the center region. All scale bars are 500 μm. **(c)** Average twitch force traces of patterned control and fibrotic EHTs under 1.5 Hz pacing. **(d)** Paced beat rate of patterned control and fibrotic EHTs. **(e)** Spontaneous unpaced beat rate of patterned control and fibrotic EHTs. While all EHTs developed effective electromechanical coupling and were able to follow a pacing frequency of 1.5 Hz, fibrotic EHTs showed an elevated spontaneous beat rate when pacing was not

applied. Diastolic function of control and fibrotic EHTs under 1.5 Hz pacing for **(f)** time to 50% relaxation and **(g)** time to 90% relaxation. Fibrotic EHTs show a delay in time to 50% relaxation and no change in the time to 90% relaxation. Systolic function of control and fibrotic EHTs under 1.5 Hz pacing, where fibrotic EHTs showed no differences in **(h)** maximum twitch force, **(i)** specific force, or **(j)** shortening velocity, but they did have a reduced **(k)** time to peak as compared to controls. Each shape (triangle, circle, square) represents an independent experiment for control EHTs (n = 12) and fibrotic EHTs (n = 14). Each data point is a separate tissue, with lines representing mean ± SEM. Statistical analysis was performed using unpaired t-test with two tails. *p≤0.05, **p≤ 0.01, ****≤0.0001.

Here we were able to demonstrate a defined border region between fibrotic and non-fibrotic tissue in an EHT model with STOMP. The ability to create this border region using STOMP will allow for further investigation of cardiac fibrotic pathology in longer-term cultures. In particular, having a healthy and fibrotic region within a single tissue will allow for investigation into pathological cardiac remodeling. However, further studies are required to validate STOMP as a platform for recapitulating pathological cardiac remodeling, such as investigations into cell-cell electrical and morphological couplings at the interface.

2.5 STOMP enables a multi-tissue periodontal model with distinct regions and cellular enthesis

Periodontal ligament (PDL) attachment to alveolar bone is a key structural element that determines PDL function and behavior. The bone-ligament junction, or enthesis, in periodontal tissue constitutes a critical transition zone for stress distribution and functional adaptation to repeated cyclic mechanical loads that arise from oral functions like chewing. We have previously developed a 3D periodontal tissue construct (PTC) to investigate biomechanical behavior of PDL under tensile loads, however it is constituted of only PDL cells and lacks spatial patterning with different cell types[81]. Because the PTC model lacks the inclusion of the enthesis region, further investigations into periodontal health, disease, and regeneration at this interface are limited[82-84]. Here, we use STOMP to create a PTC model that incorporates spatially patterned regions of mineralization.

Specifically, we patterned osteogenic PDL cells in a collagen hydrogel on the outer regions connected by PDL cells in the center (referred to as OPO), mimicking the bone-PDL-bone arrangement found in vivo (Figure 2.4a). OPO PTCs were found to maintain these two cell populations in their specific locations as seen in bright field imaging (Figure 2.4b) along with corresponding spatial deposition of calcium deposits

stained with alizarin red in the osteogenic outer regions (Figure 2.4c). Importantly, the PTCs had a distinct suture-like demarcation where the pinning features were located, transitioning from one tissue type to another. This border region indicates formation of a cellular enthesis representative of the fibrous union between PDL and alveolar bone in vivo[85].

Due to the suspended configuration, we were able to measure contractile forces in the patterned OPO, and the tissues containing only PDL cells (referred to as PPP) or only osteogenic PDL cells (referred to as OOO). Cells in the PTCs contract the ECM, pulling the flexible post towards the center. Patterned OPO tissues exhibited similar contractile forces to the tissues patterned solely with osteogenic PDL cells (OOO) (Figure 2.4e). However, both the OPO and OOO tissues exhibited significantly lower contractility and greater tissue length as compared to tissues patterned solely with periodontal ligament cells (PPP) (Figure 2.4d-e). This data indicates a change in biomechanical properties of tissues based on the function of constituent cells within the patterned regions. This observation is a valuable property recapitulated by PTCs made using STOMP, which can facilitate exploration of the biomechanical behaviors within and interactions between the multiple cell-layers of the PDL.

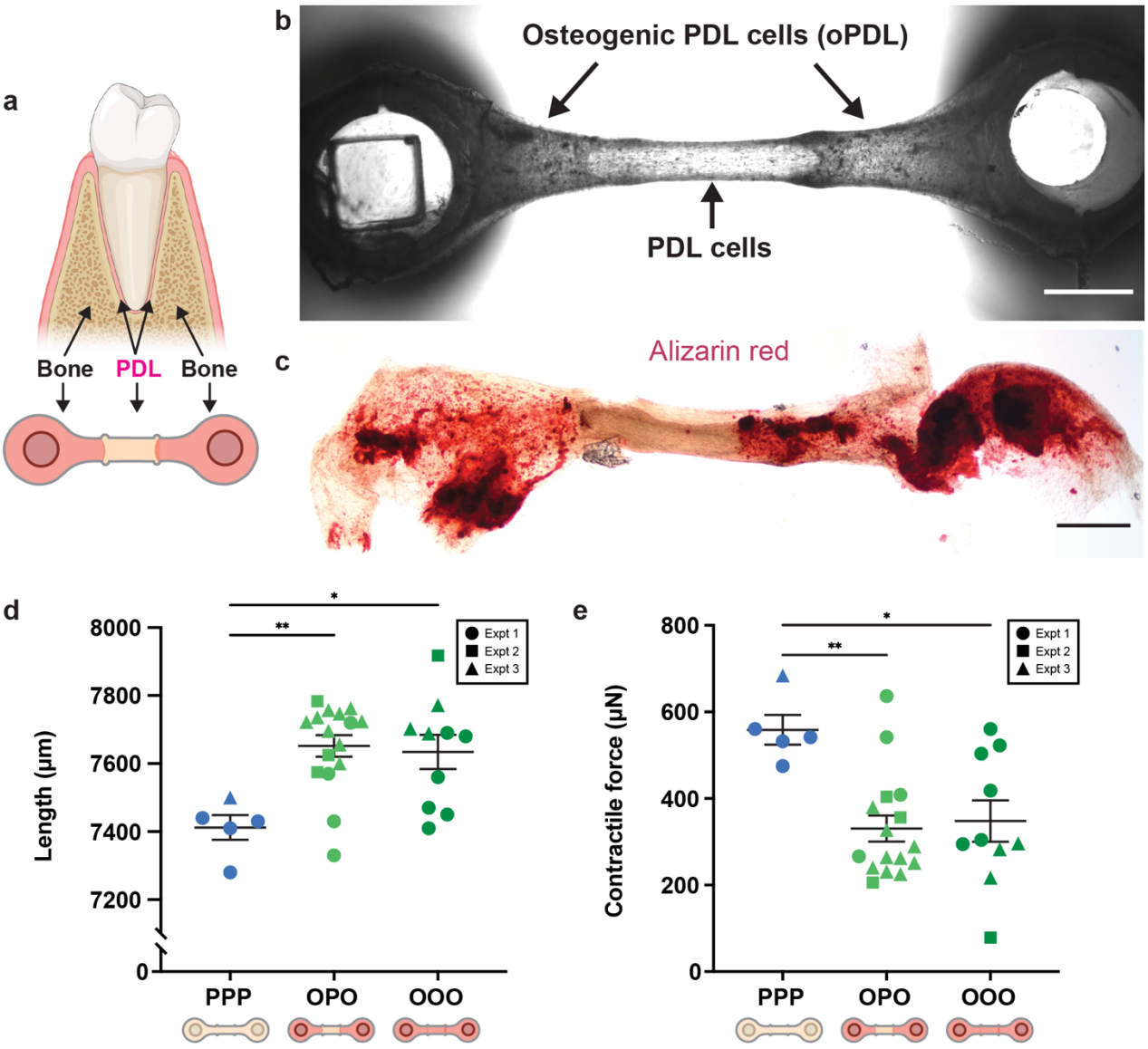

Figure 2.4. Patterned periodontal tissue constructs (PTCs) with a bone-periodontal ligament (PDL) border region. (a) Visual representation of the bone-PDL junction observed in the human tooth with corresponding schematic of how this junction was patterned using STOMP. **(b)** Representative brightfield image of the cellular entheses between osteogenic PDL cells (oPDL) in the outer regions and PDL cells in the inner region. Scale bar is 1 mm. **(c)** Representative brightfield image of alizarin red assay showing mineralized calcium deposits (red) located in the outer regions containing oPDL cells. Scale bar is 1 mm. **(d)** Final tissue length measurements of patterned oPDL-PDL-oPDL (OPO) tissues and control all periodontal (PPP) and all osteogenic PDL (OOO) tissues. **(e)** Contractile force measurements of patterned OPO tissues and control PPP and OOO tissues. OPO tissues have contractile forces that are similar to OOO tissues and significantly lower than PPP tissues. Each shape (circle, square, triangle) represents an independent experiment for control PPP (n = 5), control OOO (n=10), and patterned OPO (n=16) tissues. Each data point is a separate tissue, with lines representing mean ± SEM. Statistical analysis was performed using a one-way ANOVA with Tukey's multiple comparisons *post hoc* test. *p≤0.05, **p≤0.01.

2.6 STOMP enables versatile tissue geometries and expanded patterning capabilities from suspended cores to patterning non-compactable cell-ECM combinations and designer materials

In all patterning implementations described thus far, we show a geometry where we are changing the region along one axis. However, we expand upon the geometric versatility capabilities of STOMP by creating a tissue with an inner core region fully surrounded by a second outer region, which enables patterning along the z-axis in addition to the x-y axes (Figure 2.5a-c). The process for generating a core region is shown in Figure 2.5a. After patterning an inner core region with any configuration of STOMP (e.g., one, two, or three regions), a second patterning device is added that has an open channel that is larger in length, width, and height than that of the first patterning device; this outer region can then be patterned around the first hydrogel, generating a suspended tissue that is completely encapsulated by another cell-laden hydrogel (Figure 2.5a). We demonstrate this ability with an inner core composed of a single region of 3T3 cells dyed by CellTracker Red CMTPX laden in fibrin and an outer core composed of 3T3 cells dyed by CellTracker Green CMFDA laden in fibrin (Figure 2.5b). Further, we show multiple combinations of the inner core containing one, two, and three-patterning regions that are then completely encapsulated by an outer region with colored agarose (Figure 2.5c). In future implementations, the outer region could also contain multiple regions by adding pinning features to the outer region patterning device.

In addition to expanding upon the geometric capabilities of STOMP, we also implement strategies to expand the types of hydrogels that can be used in the STOMP system. The requirement of the tissue pulling away from the channel walls of the patterning device limits STOMP to cell-ECM combinations that allow for sufficient tissue compaction or materials that do not adhere strongly to channel walls (such as in the case for agarose). To address this limitation, we designed a STOMP device with a v-shaped channel carved into the walls of the patterning channel (Figure 2.5d). We pipetted a degradable hydrogel into this channel (for demonstration we use a sortase-degradable PEG, although any degradable hydrogel can be used); after gelation, this degradable hydrogel becomes the STOMP channel walls. We could then pipette a second solution into the middle tissue region. After patterning, the channel wall can be exogenously triggered to degrade, thus allowing for facile release of tissue from the patterning device without a

requirement for tissue compaction. A schematic for the patterning process of the degradable "wall" region and tissue region is shown in Supplementary Figure A13, and a still image from a video with colored agarose for visualization is shown in Figure 2.5e. Using this method, we successfully patterned a second PEG-based designer material laden with 3T3 fibroblast cells that otherwise cannot be removed from the STOMP device after patterning (Figure 2.5f). After the cell-ECM PEG tissue region was gelled, the entire assembly was placed in a solution containing sortase specifically engineered to recognize and cleave the cross-linker in the PEG pipetted into the v-shaped channel walls. After degradation of the PEG hydrogel in the v-shaped channel, the tissue patterned in the center tissue region was released as the channel "walls" degraded. Adding the new degradable wall feature allows STOMP to be used for synthetic materials that do not compact readily (e.g., stimuli responsive or "4D" PEG-based materials that can be patterned in space and triggered in time)[57,86-88] or for cell types that do not readily remodel ECM and compact (e.g., nerve cells in a neuromuscular junction). This addition extends STOMP to virtually any tissue or material, opening a frontier in 4D suspended multiregion tissues.

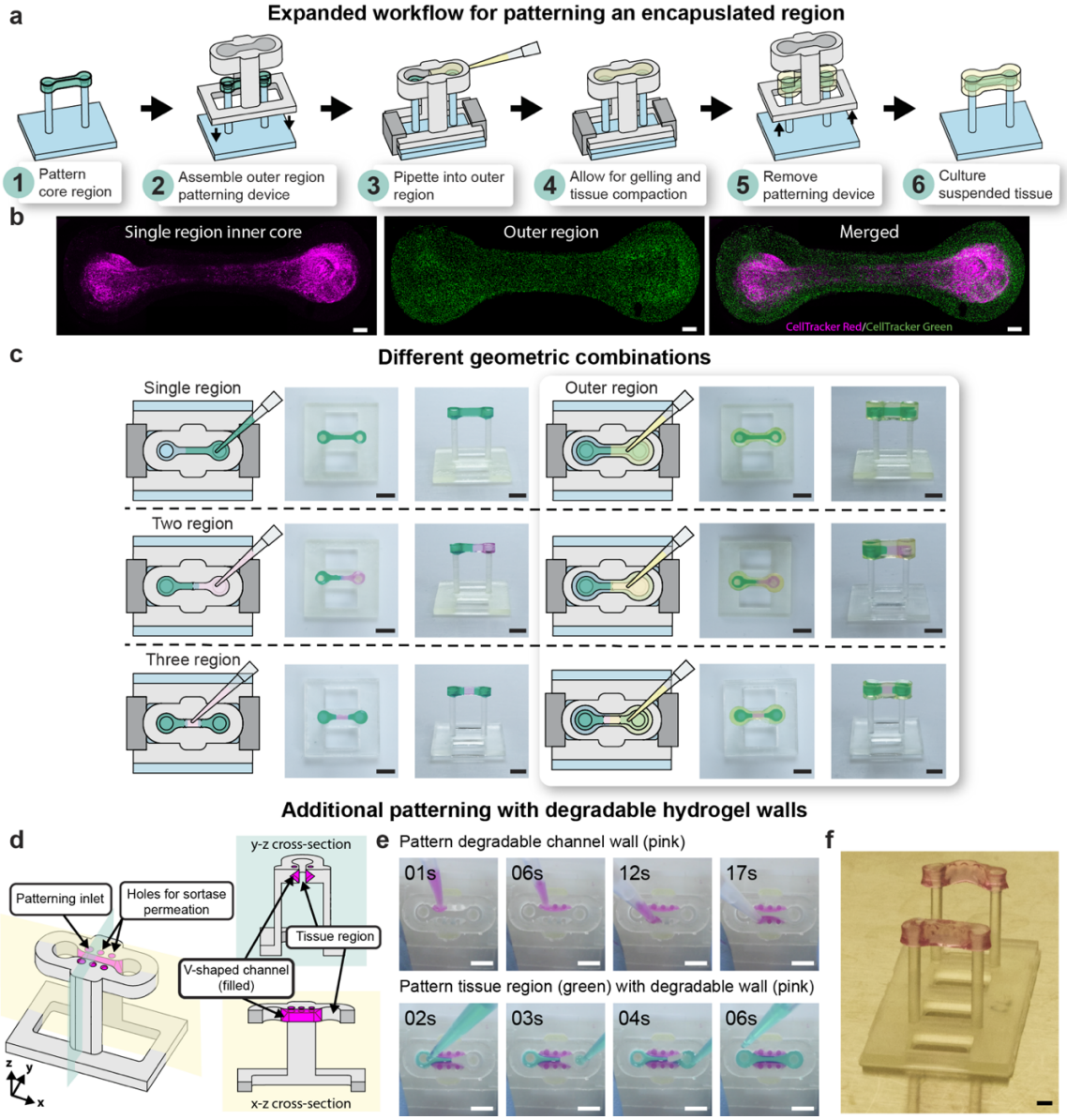

Figure 2.5. Expansive geometric and patterning capabilities of STOMP. (a) Workflow of patterning an inner core region completely encapsulated by an outer region, thus patterning suspended tissues in the z-direction. **(b)** Representative fluorescent images of patterned 3T3 mouse fibroblast cells laden in fibrin to generate a suspended tissue with an inner region and outer region. The inner region tissue was generated with the single region STOMP configuration; 3T3 cells were dyed by CellTracker Red CMTPX (magenta). The outer region contains 3T3 cells dyed by CellTracker Green CMFDA (green). All scale bars are 500 μm. **(c)** Demonstration of patterning single region, two region, and three region suspended tissue constructs using colored 1.5% agarose; additionally, these patterned tissues can be completely encapsulated by placing a patterning device larger in width, height, and length around the previously patterned tissue to generate an encapsulated core. All scale bars are 4 mm. **(d)** Schematic of a STOMP patterning device containing a v-shaped channel within the walls of the patterning device tissue region's open channel. This geometry can be used to pattern non-compactable synthetic hydrogels, such as poly-ethylene glycol (PEG), where a degradable PEG hydrogel can be patterned in the v-shaped channel and degraded after patterning in the tissue region. **(e)** Representative video still images of colored agarose patterned in the v-shaped channel wall region (pink hydrogel) and tissue region (green hydrogel). All scale bars are 2 mm. **(f)** Representative image of resulting suspended PEG hydrogel laden with 3T3 mouse fibroblast cells. Scale bar is 2 mm.

2.7 Discussion

The STOMP platform is an open microfluidic approach for generating spatially controlled suspended tissue models. Precise spatial patterning can be achieved in the STOMP system via capillary pinning in the x-y direction (i.e., within a single tissue) or along the z-direction (i.e., generating encapsulated tissue structures). With STOMP we can achieve a wide range of geometrical combinations, including structures that are difficult to pattern with existing fabrication methods such as the fully encapsulated suspended tissue. In this initial proof-of-concept demonstration of STOMP, we show that STOMP can be used to model tissue interfaces (e.g., periodontal ligament-bone) and intra-tissue heterogeneity (e.g., fibrotic and healthy tissue co-culture), thus establishing the versatility and board applicability of STOMP for modeling complex multiregional suspended architectures. Lastly, we demonstrated the use of degradable PEG-based hydrogels, a material that may not meet requirements for other 3D suspended patterning methods. The ability to pattern stimuli-responsive synthetic hydrogels opens a fourth dimension (i.e., time) of control to the suspended patterned tissues, allowing for STOMP to be used in 4D suspended tissue engineering applications. STOMP is designed to complement existing post-based suspended culture systems; its strength lies in its ability to integrate easily into these tissue fabrication workflows while adding regional control via open microfluidic principles.

Existing post-based suspended tissues protocols utilize a casting method, where a cell-ECM liquid precursor solution is pipetted into a mold made of agarose or PDMS that surrounds the suspended posts[17,18,26,27]. Because there are no features to compartmentalize these molds, regional control has not previously been demonstrated, limiting studies to a homogenous singular region. Other methods, such as 3D bioprinting and photopatterning, allow for the additional fabrication complexity of patterning multiple regions within a single tissue. However, these methods typically require highly viscous, extrudable materials or photoactive moieties, making it difficult to pattern unmodified native ECMs. Recently, there have been advancements in 3D bioprinting techniques to mitigate these limitations on materials by printing cell-laden hydrogels into a sacrificial gelatin suspension bath[29,32,33]. These approaches enable the 3D printing and spatial patterning of natural polymers, such as alginate, collagen, fibrin, and hyaluronic acid.

While suspended biofabrication methods allow for the generation of large-scale structures (millimeter- to centimeter-scale), these methods typically require large volumes (milliliter to tens of milliliters) of hydrogel material—both for the sacrificial support and the final suspended structure—which can limit the use of precious biomaterials. Additionally, these techniques often rely on custom-engineered 3D bioprinting systems, restricting scalability and accessibility. In comparison to other suspended biofabrication methods, STOMP offers finer volumetric control at smaller scales (30 μL - 100 μL), making it a more efficient and scalable alternative for applications requiring precise hydrogel patterning without excessive material consumption. Taken together, STOMP fills an important niche for simple, microliter-scale, and multi-region in vitro modeling; other methods such as 3D bioprinting will remain important for large-scale, high resolution organ modeling.

In the STOMP system, material limitation is governed by the removal process. While surface tension-driven flow allows virtually any hydrogel that transitions from a liquid to a solid state to flow in the STOMP channel, some hydrogel materials can adhere to the STOMP channel during the removal process. Therefore, when adapting the STOMP workflow to a new tissue model, it is important to consider material and tissue type compatibility with the STOMP device. For example, we experienced significant challenges while using the PEG-based degradable hydrogels in the original implementation of STOMP (i.e., without the degradable walls), because the material did not allow for sufficient compaction of the tissue to facilitate successful removal of the STOMP device. This issue would be similar in other cases using compactable ECMs (e.g., fibrin or collagen) with a cell line that typically does not remodel ECM or contract (e.g., neuronal cells without supporting fibroblasts). While we do present a work-around to this issue with degradable channel walls, the degradable walls add complexity, require the use of more expensive degradable materials, and limit the addition of pinning features due to the difficulty of patterning.

Once a hydrogel is determined to be compatible with the removal of the STOMP device, there are two additional practical considerations for patterning multi-region tissues: first, determining the best pinning feature shape and angle and second, determining if two regions at the defined interface can integrate to form a contiguous tissue. In this work, we provide general equations for users to insert their specific

hydrogel density and contact angle to determine the relationship between hydrostatic pressure and maximum Laplace pinning pressure in the STOMP device (Eq. 2.5, 2.7, and 2.8). To demonstrate the workflow, we specifically calculate these relationships using the density and contact angle of a 5 mg/mL precursor collagen solution on a 1% BSA treated 3D printed surface (the same treatment done to the STOMP device before patterning), allowing us to determine the best pinning feature and angle for workflows involving collagen (i.e., 90° concave "cavity" pinning features). However, when working with fibrin, we found that the convex "vampire" pinning features resulted in better patterning (i.e., pinning and subsequent de-pinning to connect two regions at the defined interface). If using a different hydrogel other than collagen and fibrin, the user would benefit from utilizing the equations detailed in the work as well as experimentally testing the best pinning feature shape and angle that will result in the most reproducible patterning for their tissue. After optimizing the pinning geometry, it must next be determined if two regions at an interface can form a functional, contiguous tissue. Two regions will more easily form a contiguous tissue if each region utilizes similar ECM and cell compositions, such as two separate cell types with similar propensity to contract ECM or two different ECMs (e.g., collagen and Matrigel) that have similar components and can bind together. However, collagen and fibrin are two common ECMs for 3D tissue modeling, and while these two ECMs are compositionally different, in preliminary experiments we have patterned cell-laden tissues with a collagen-fibrin interface, which successfully formed a contiguous tissue. This example illustrates the importance of testing each new ECM and cell-type for patterning compatibility. If the desired interface requires materials that are incompatible, STOMP would not be a suitable platform.

In addition to material considerations, there are also dimensional considerations when adapting the STOMP platform to specific experimental needs. It may be desired to have a smaller tissue volume (micrometer-wide channels with millimeter-scale separation between the two posts) when using precious cells or materials or increasing the throughput of an experiment. In this case, the principles of surface tension-driven flow would make flow in the STOMP system (i.e., a channel without a ceiling or floor) more desirable since there would be less of an effect due to gravity at smaller scales, resulting in less bulging of the liquid underneath the channel. Since the hydrostatic pressure at the bottom of the channel would be

decreased in a smaller channel design (e.g., a channel 0.2 mm in width and 1.0 mm in height) compared to a larger channel design (e.g., a channel 0.8 mm in width and 3.5 mm in height as detailed in this work), the pinning in smaller channel dimensions would be more stable. Therefore, the smaller channels would also be less sensitive to changes in volume due to increased maximum Laplace pinning pressure (Eq. 2.5 and Eq. 2.7) and decreased hydrostatic pressure (Eq. 2.8) observed in channels with decreased w and h values. However, at smaller dimensions, the tolerance of the 3D printer used will have a greater effect on the channel dimensions and therefore also on the total volume that would completely fill the channel; a tolerance of 20 μm would have a larger effect on the volume of a channel that is 200 μm wide than a channel that is 800 μm wide. This potential variability could be mitigated by using a higher resolution printer with tighter tolerances or with a different fabrication technique (e.g., CNC milling or injection molding). Smaller channel length dimensions also limit the number of different regions that can be generated within a single tissue since it is practically challenging to pipette accurate volumes into small regions.

For larger tissue volumes (millimeter-wide channels with centimeter-scale separation between the two posts), which could be desired for longer-term tissue cultures that are highly contractile and more prone to breaking over time, there are additional limitations and challenges. When increasing the width of the channel, the height of the channel must also be increased to fulfill the equation for spontaneous capillary flow in the STOMP system (Eq. 2.2). Increasing the volume will cause a greater effect due to gravity which will exacerbate non-uniform filling of the channel cross-section, with more liquid bulging at the bottom of the channel. Since hydrostatic pressure increases and maximum Laplace pinning pressure decreases in larger channels, pinning is less stable overall. Therefore, de-pinning events, which typically occur at the bottom of the channel where hydrostatic pressure is the greatest, in larger channels would be more sensitive to changes in volume pipetted.

While optimizing STOMP for a specific workflow requires careful consideration of materials, dimensions, and interface integration, once established, it enables seamless spatial patterning in a suspended system with just a few pipetting steps. This adaptability makes STOMP a powerful and flexible tool for advancing complex suspended tissue engineering applications. Our ability to pattern multiple regions

within the tissue enhances integration of different cell types and ECMs, enabling complex studies of tissue interactions, maturation, and disease progression. These benefits can be combined with the suspended nature of the tissue, which provides axial stretching and mechanical cues, and the use of flexible PDMS posts for controlled manipulations and functional measurements. STOMP's versatility in integrating different cell types and ECMs, coupled with the mechanical benefits of suspended tissues, opens new experimental possibilities and advances our understanding of tissue behavior in both healthy and diseased states.

2.8 Materials and methods

Device Design, Fabrication, and Sterilization

Post arrays made from polydimethylsiloxane (PDMS) were fabricated as described in Bielawski et al[59]. Briefly, uncured PDMS was poured into a four-part acrylic mold to fabricate an array that contains six pairs of posts and that fits in a row of a 24-well plate. Glass capillary tubes were cut to the appropriate length and inserted into one side of the mold prior to curing such that each pair contained one rigid post. The posts were baked overnight at 65°C and then removed from the molds. Fabricated posts were 8 mm apart in spacing, 12 mm in length, and 1.5 mm in diameter with a cap structure (0.5 mm thick and 2.0 mm diameter) to aid in attachment of the cell-laden hydrogel of interest.

For STOMP, the open microfluidic patterning device and clips were designed in Solidworks and 3D printed out of Formlabs clear resin V4 using a Form 3B+ 3D printer (Formlabs Inc.). Dimensions of the open channel were designed to fit around the PDMS posts; dimensions of the three open channel designs used in this work are depicted in Supplementary Figure A1. Clips were designed to hold the patterning device in place during the tissue patterning process. The patterning devices and clips were cleaned in two separate FormWash units (Formlabs Inc.) with isopropyl alcohol (IPA) for 20 minutes and then another 10 minutes to remove excess uncured resin. The devices were dried with compressed air and cured under UV light at 60°C for 15 minutes in a FormCure (Formlabs Inc.).

To sterilize the PDMS posts, patterning devices, and clips for cell culture, all parts were first placed within a biosafety cabinet and UV sterilized for 20 minutes. The PDMS posts were additionally sterilized

with 70% ethanol for five minutes by placing the tips of the posts in a 24-well plate, where each well contained 2 mL of 70% ethanol. The PDMS posts were then rinsed with sterile DI water twice for five minutes each.

After sterilization, the patterning devices that were to be used with a cell-laden hydrogel or ECM were incubated in a solution of 1% bovine serum albumin (BSA) for 1 hour at room temperature. After incubation, the 1% BSA solution was aspirated, and the patterning devices were allowed to fully dry prior to assembling the suspended tissue open microfluidic patterning devices. The open microfluidic patterning device was placed such that it surrounded the ends of each post, and the clips were used to hold the patterning device in place at the base of the PDMS post array.

Experimental Pinning Analysis

Measuring contact angle of 5 mg/mL collagen on BSA treated resin: 3D printed resin squares were utilized to provide a flat surface for contact angle measurements. Each square was treated with 1% BSA for 1 hour at room temperature. A Drop Shape Analyzer DSA25 (Krüss) was utilized on the sessile drop mode to measure contact angle. A SY3601 disposable 1 mL syringe with Luer connector (Krüss) was filled with DI water and then fitted with a NE94 steel needle with a 0.51 mm diameter (Krüss). The DSA25 was calibrated to the image of the needle. A collagen solution was prepared by mixing a stock of rat tail collagen type I (Corning) in 0.02 N acetic acid with sterile deionized water, 10X PBS, and 1N NaOH to achieve a final collagen density of 5 mg/mL and kept on ice to prevent gelation. A BSA treated resin square was placed on the platform below the needle and a 2 µL droplet of the collagen solution was dispensed via pipetting. The contact angle of each drop was measured using multiple images of the collagen sessile drop at the points of intersection (three-phase contact points) between the drop contour and the projection of the surface baseline using ADVANCE software (Krüss). Twenty different drops were measured on 20 different BSA treated resin squares (one drop per resin square); the mean contact angle and standard deviation of each drop were calculated by the Krüss Drop Shape Analyzer based on the number of measured technical replicates, which are multiple images of the same droplet (see raw data in Supplementary Table A1). The experiment number indicated in Supplementary Table AI (Experiment 1-3) indicates which experiment

number a particular resin part belongs to (i.e., we performed these contact angle measurements on three different days with different batches of 3D printed surfaces and 1% BSA solutions). The overall average contact angle of the 20 drops and the minimum and maximum contact angle measurement were used for theoretical modeling of the pinning of collagen in STOMP.

Measuring success or failure of collagen pinning in STOMP system: The STOMP devices with a channel height of 3.5 mm and a width of 1.2 mm were used for the pinning experiment. All STOMP patterning devices were treated with 1% BSA for 1 hour. A collagen precursor hydrogel solution was prepared as described above. Pipettes were set to 23, 25, 26 or 27 μL to dispense collagen precursor slowly at the circular outer section of the STOMP channel, stopping at the first stop of the pipette to avoid bubble introduction. The pipette set to 23, 25, 26, and 27 μL dispensed actual volumes of 20, 22, 23, and 24 μL, respectively, as measured by weight in triplicate and using the density of 5 mg/mL precursor collagen solution (958 kg/m3). Throughout the text, the actual volumes dispensed for the pinning experiments will be referenced. The flow was observed for 10s. If the flow moved past the pinning feature, then the replicate was considered a "failure" of pinning. If the fluid front remained pinned at the pinning feature at the end of 10 s then it was deemed a "success" of pinning. Each pinning feature, angle, and volume was done in triplicate. Figure 6.2e-f shows representative images of examples of successful pinning and no pinning in both pinning feature designs; the volume of collagen used in these pictures was 23 μL. The complete dataset is visualized in Supplementary Figure A2.

Cell Culture and Maintenance

3T3 mouse fibroblasts: Initial optimization experiments were conducted with NIH/3T3 mouse embryonic fibroblast cell line obtained from ATCC. The cells were maintained in a tissue culture flask containing Dulbecco's Modified Eagle Medium (DMEM) supplemented with 10% fetal bovine serum (FBS) and 1% penicillin-streptomycin at 37°C, 5% CO2. Culture medium was changed every other day until cells reached around 80-90% confluency, whereupon the culture was rinsed with 1X PBS, followed by addition of TrypLE Express (Gibco). After incubation for 3 minutes at 37°C, the TrypLE was inactivated by diluting with cell culture medium. The fluid volume was centrifuged at 300 RCF for 3 minutes. The cells were

resuspended in cell culture medium for further passaging or used for hydrogel encapsulation, as described below.

Human induced pluripotent stem cell (hiPSC) derived cardiomyocytes: WTC11 hiPSCs were differentiated using a modified small molecule Wnt-modulating protocol as previously described[26,89-91]. Cells were seeded at a density of 1.6-5.8 x 104 cells/cm2 on plates coated with a 1:30 dilution of Matrigel in mTeSR+ (STEMCELL Technologies) supplemented with 100 U/mL penicillin-streptomycin and 5 μM ROCK inhibitor Y-27632. Upon reaching 50-80% confluency (Day -1), cells were washed with 1X PBS and the media was changed to mTeSR+ supplemented with 1 μM CHIR-99021 (Cayman Chemical). After 24 hours (Day 0), cells were washed with 1X PBS and media was replaced with RBA (RPMI 1640, 500 μg/mL BSA, 220 μg/mL ascorbic acid, 100 U/mL penicillin-streptomycin) supplemented with 3-5 μM CHIR-99021. After 48 hours (Day 2), cells were washed with 1X PBS and media was replaced with RBA supplemented with 2 μM Wnt-C59 (SelleckChem). After 48 hours (Day 4), cells were washed with 1X PBS and the media was replaced with RBA without supplementation. After 48 hours (Day 6), cells were washed with 1X PBS and media was replaced with cardiomyocyte media (RPMI 1640, B27 plus insulin, 100 U/mL penicillin-streptomycin) and replaced every other day until cells began beating on Day 10-11. hiPSC-CMs were then washed with 1X PBS and metabolically enriched by culturing in DMEM without glucose supplemented with 4 mM sodium L-lactate for 4 days. hiPSC-CMs were then returned to cardiomyocyte media for 48 hours. hiPSC-CMs were then replated at a density of 1.5-1.8 x 105 cells/cm2 on plates coated in a 1:60 dilution of Matrigel in cardiomyocyte media supplemented with 5% FBS and 5 μM ROCK inhibitor Y-27632. After 24 hours, the media was replaced with standard cardiomyocyte media. After 24 hours, hiPSC-CMs washed with 1X PBS and again metabolically enriched by culturing in DMEM without glucose supplemented with 4 mM sodium L-lactate for 4 days. hiPSC-CMs were then returned to cardiomyocyte media with the media replaced every other day until Day 35-40 when used for EHT casting.

WTC11 hiPSCs were cultured in mTeSR+ supplemented with 100 U/mL penicillin-streptomycin on plates coated with a 1:30 dilution of Matrigel. Cells were fed every other day. Media was supplemented with 5 μM ROCK inhibitor Y-27632 for the first 24 hours after passing.

Human periodontal ligament (PDL) cells: PDL cells were harvested from the roots of healthy premolars extracted for orthodontic purposes, using pre-established protocols[92]. Briefly, PDL tissue was gently dissected from the middle third of the tooth root surface in a culture dish containing wash buffer [Hanks' balanced salt solution (HBSS; Gibco) supplemented with 5% (v/v) FBS (HyClone) and 50 U/mL penicillin and 50 μg/mL streptomycin]. The suspension was centrifuged at 400 RCF for 10 min at 4 oC. After aspirating the supernatant, PDL tissue was digested in collagenase I (3 mg/mL, Sigma-Aldrich) and dispase II (4 mg/mL; Sigma-Aldrich) for 1 hour at 37 oC. After digestion, the suspension was passed through a 70 μm strainer to obtain a suspension of isolated cells.

The population of cells was expanded by seeding them in 24-well plates. Cells were grown in DMEM supplemented with 10% FBS (HyClone) and 1% penicillin-streptomycin at 37 oC with 5% CO2. On reaching confluence, cells were washed with PBS, trypsinized with 0.25% trypsin-EDTA (Gibco), and passaged progressively into T-75 and T-175 flasks. Cells at passage numbers 1 to 3 were stored in freezing media Cryostor (1 mL per 10 million cells) in a liquid nitrogen freezer then thawed, plated, and expanded as needed in T-75 and T-175 flasks. PDL cells between passage numbers 3 and 8 were used for the patterning experiments.

Osteogenic differentiation of PDL cells: To induce osteogenic differentiation, a sub-population of PDL cells between passages 3 to 6 was transferred to a T-75 flask and cultured in DMEM media with 10% FBS and 1% penicillin-streptomycin. The cells were left to grow up to 80-90% confluence with culture medium changes every 3 days before adding osteogenic induction medium (culture medium supplemented with 50 μM ascorbic acid-2-phosphate, 10 mM β-glycerophosphate, and 10 nM dexamethasone) for 2 weeks. After 2 weeks, these cells were trypsinized and lifted to be used for hydrogel encapsulation.

STOMP Tissue Preparation

Patterning with agarose: Low gelling temperature agarose (MilliporeSigma) was dissolved in deionized water to a concentration of 15 mg/mL and dyed for visual aid with food dye (Spice Supreme) or India ink (Dr. Ph. Martin's). Prior to patterning, the agarose solution was heated to a liquid state (95°C) and then pipetted into STOMP devices. To generate Figure 2.1g-h, agarose was pipetted into a STOMP device with

a channel height of 2 mm and width of 1 mm and the three region 60° convex "vampire" pinning features. For generating agarose structures seen in Figure 2.5, the STOMP devices used to generate the inner core had a channel height of 2 mm and width of 1 mm and either the two or three region 20° convex "vampire" pinning features. For the outer core patterning, a STOMP device with a channel height of 4 mm and width of 1.9 mm was used. Agarose structures were allowed to gel at room temperature for 5-10 minutes. All agarose structures used 1.5% wt/v gel.

Patterning 3T3 mouse fibroblast cells with fibrin: Fibrinogen stock solutions were prepared at 50 mg/mL by dissolving 250 mg of powdered fibrinogen from human plasma (Sigma-Aldrich) in 5 mL of warmed 0.9% NaCl in deionized water. The fibrinogen solution was then filter-sterilized with a 0.22 mm syringe filter. Thrombin stock solutions were prepared at 100 U/mL by dissolving 100 units of powder thrombin from human plasma (Sigma-Aldrich) in 1 mL of warmed 0.9% NaCl in deionized water. Fibrinogen and thrombin stock solutions were aliquoted and stored at -20°C until ready for use.

After dissociating the 3T3 cells, two aliquots of the cells were dyed by either CellTracker Green CMFDA or CellTracker Red CMTPX at a final concentration of 25 μM in DMEM for 30 minutes at 37°C. After dying, the cells were pelleted and resuspended at a final concentration of 5 x 10^6 cells/mL in DMEM with 5 mg/mL bovine fibrinogen and 3 U/mL thrombin. For patterning in Figure 2.1f, the STOMP device with a channel height of 3.5 mm and width of 1.2 mm and the three region 60° convex "vampire" pinning features was used. For patterning in Fig 6.5b, the inner core was patterned with a STOMP device containing a channel height of 2 mm and width of 1 mm and the outer core was patterned with a STOMP device containing a channel height of 4 mm and width of 1.9 mm. After patterning, the 3D printed posts with the patterning device and clips assembled were placed in a 24-well plate and allowed to gel for 30 minutes at 37°C. After gelling, 2 mL of growth media supplemented with 5 mg/mL 6-aminocaproic acid (Sigma-Aldrich) was added to each well. After two days in culture, the STOMP devices were removed from the 3D printed posts and fresh media was added to the wells. Tissues were cultured for one day after the STOMP patterning device was removed then fixed with 4% paraformaldehyde (PFA) for one hour at 4°C. Tissues were rinsed twice with 1X PBS and stored at 4°C until ready for imaging. Tissue samples were imaged by

placing the tissue directly on a coverslip without removing from the posts. All tissues were imaged on a Leica SP8 confocal microscope at 10X magnification.

Patterning engineered heart tissues (EHTs) with fibrin: Fibrinogen stock solutions were prepared at 50 mg/mL by dissolving 1 g of fibrinogen from bovine plasma (Sigma-Aldrich) in 20 mL of warmed cardiomyocyte media. Thrombin stock solutions were prepared at 100 U/mL by dissolving 1000 U of thrombin from bovine plasma (Sigma-Aldrich) in 10 mL of a 3:2 ratio of PBS to H20. EHTs were cast on PDMS posts using a modification of our previously described protocol[59,60,90]. For generating the EHTs, STOMP devices with a channel height of 3.5 mm and width of 1.2 mm and the three region 60° convex "vampire" pinning features were used. The two outer regions of all tissues were patterned using a solution of 27 µL volume consisting of 1.35 x 10^5 hiPSC-CMs (5 x 10^6 cells/mL), 2.7 x 10^4 HS27a human bone marrow stromal cells (1 x 10^6 cells/mL), and 2.7 x 103 HS5-GFP human bone marrow stromal cells (1 x 10^5 cells/mL) in cardiomyocyte media with 5 mg/mL bovine fibrinogen and 3 U/mL thrombin. The center region of control tissues was patterned using a solution of 12 µL volume consisting of 6.0 x 10^4 hiPSC-CMs (5 x 10^6 cells/mL), 1.2 x 10^4 HS27a human bone marrow stromal cells (1 x 10^6 cells/mL), and 1.2 x 10^3 HS5-mCherry human bone marrow stromal cells (1 x 10^5 cells/mL) in cardiomyocyte media with 5 mg/mL bovine fibrinogen and 3 U/mL thrombin. The center region of fibrotic tissues was patterned using a solution of 12 µL volume consisting of 4.8 x 10^4 hiPSC-CMs (4 x 10^6 cells/mL), 1.44 x 10^4 HS27a human bone marrow stromal cells (1.2 x 10^6 cells/mL), and 1.44 x 10^3 HS5-mCherry human bone marrow stromal cells (1.2 x 10^5 cells/mL) in cardiomyocyte media with 6 mg/mL bovine fibrinogen and 3.6 U/mL thrombin. After the tissues were patterned, the PDMS post array with the patterning device and clips assembled were placed in a 24-well plate and allowed to gel for 60 minutes at 37°C. After gelation, the tissues were transferred to wells containing cardiomyocyte media supplemented with 5% DMEM, 5% FBS, 1% non-essential amino acid (NEAA), and 5 mg/mL aminocaproic acid. After 48 hours, the media was replaced with cardiomyocyte media supplemented with 5% FBS, 1% NEAA supplement, and 5 mg/mL aminocaproic acid. After 24 hours, the patterning devices were removed from the EHTs and the tissues

were transferred to EHT media (cardiomyocyte media supplemented with 5 mg/mL aminocaproic acid). EHT media was replaced every 2-3 days for 18 days until subsequent analysis.

Patterning periodontal tissue constructs (PTCs) with type I collagen: Following sterilization, PDMS posts were treated with 0.1% polyethylenimine (PEI) for 10 minutes and rinsed with sterile deionized water for 5 minutes. Next, the PDMS posts were treated for 30 minutes with 0.01% glutaraldehyde and then rinsed twice with sterile deionized water for 5 minutes each. For each treatment step, 2.5 mL/well of the respective solution was placed in a 24-well plate so that the tips of each PDMS post were in contact with the solution.

For generating PTCs, STOMP devices with a channel height of 2 mm and width of 1 mm and the three region 90° concave "cavity" pinning features were used. To pattern the tissues, two different cell-collagen mixtures were prepared with the PDL cells and osteogenic PDL (oPDL) cells. To prepare the cell-collagen mixtures, each cell type was mixed with type I rat tail collagen such that a 100 μL cell-collagen mixture was composed of 1:4 ratio of cell solution (20 μL culture media containing 300,000 cells) and collagen mixture [80 μL of 9 parts of collagen (4 mg/mL; Advanced Biomatrix) mixed with 1 part of neutralization solution (Advanced Biomatrix)]. Each cell-collagen mixed had a final concentration of $3x10^6$ cells/mL.

First, 13 μL of the oPDL cell-collagen mixture was pipetted on one of the circular ends of the STOMP channel that surround the PDMS posts and then the other. Then, 3-4 μL of PDL cell-collagen mixture was pipetted in the center region of the STOMP channel. The PDMS posts, with the patterning rail and cell-ECM precursor solution, were then placed upside down in a 24-well plate. The assembly was transferred to the incubator at 37°C with 5% CO2. After 90 min, 2.5 mL of culture media was gently added to the wells containing the PTCs and then incubated again at 37°C. After 48 hours, the clips and patterning rails were removed to reveal a suspended tissue between the PDMS posts. These patterned PTCs (referred to as OPO) were then transferred to a fresh 24-well plate with 2.5 mL/well of culture medium, which was changed every 2 to 3 days. Similarly, patterned control tissues consisting of oPDL cells in all 3 regions (referred to as OOO) and periodontal cells in all 3 regions (referred to as PPP) were also generated.

Patterning poly(ethylene glycol) (PEG) in modified STOMP: To pattern tissues with enzymatically degradable PEG as the ECM, we used PEG-tetraBCN (a four-arm PEG end-capped with reactive bicyclononyne groups) with two different sortase-degradable and bis(azide)-modified peptide crosslinkers. These materials are described in detail in previous work[57,86,93]. The synthesis of the PEG-tetraBCN and crosslinkers are described in detail in Appendix A. The LPESG crosslinker is cleaved by the eSrtA(4S9) sortase, and the LAETG is cleaved by the eSrtA(2A9) sortase. Briefly, PEG was prepared by combining the peptide crosslinker with a final concentration of 8mM, PEG-tetraBCN with a final concentration of 4mM. Components were vortexed together to ensure homogeneity. The PEG that served as the degradable "channel wall" was pipetted into the v-shaped channel. In this case, we used the eSrtA(2A9)-sensitive LAETG crosslinker in the v-shaped channel. There were no cells in the outside channel, therefore the PEG-BCN was suspended in 1X PBS. We used the eSrtA(4S9)-sensitive LPESG crosslinker in the tissue region that made up the final tissue, although we did not degrade this region. Because this region was laden with NIH 3T3 mouse fibroblasts at a final concentration of 5 x 10^6 cells/mL, RGDS peptide, the adhesion motif from fibronectin, was added at a final concentration of 1 mM, and the mixture was resuspended in cell culture media. For the tissue region, the height of the channel was 2 mm and the width of the channel (measured as the distance between the degradable channel walls) was 1 mm.

We observed that the PEG hydrogel made with the LAETG crosslinker would swell more when left in media than the PEG hydrogel made with the LPESG crosslinker. We therefore decided to use the LPESG crosslinker as the region that made up the final tissue, since this needed to be removed from the STOMP patterning device, and the swelling made this more difficult. The v-shaped degradable channel wall regions were patterned with 15 µl of hydrogel precursor each and filled until the liquid bulged slightly out of the channel. Devices with the patterned PEG in the v-shaped channels were incubated at 37ºC for 30 minutes to allow for gelling. Sacrificial 1X PBS was used to prevent drying out of the hydrogel. After 30 minutes, devices were removed from the incubator and the cylindrical region of the patterning rails that surround the posts were treated with 1% BSA for one hour to prevent the tissue in contact with the circular walls from sticking upon removal of the patterning device. BSA was aspirated and devices were allowed

time to dry for 5 to 10 minutes. Some absorption of the BSA by the hydrogel in the v-shaped degradable channel was observed, but swelling caused by this absorption resolved after 5 to 10 minutes of drying in open air. The center tissue region of the device was patterned with 50 µL of hydrogel precursor, then placed in the 37ºC incubator to gel for 30 minutes. Sacrificial 1X PBS was added to the bottom of the well plates, beneath the patterning device, to prevent gels from drying out during gelation.

Once gelled, the hydrogel devices were inverted and completely submerged in 3 mL of eSrt(2A9) sortase solution. This sortase cleaves the peptide LAETG, which was used to pattern the degradable channel wall region in the v-shaped channels. The eSrt(2A9) sortase solution was prepared to a final concentration of 50 µM eSrt(2A9), 18 mM triglycine (GGG) (ChemImpex; Wood Dale, IL), and 1.8 mM CaCl2. GGG and CaCl2 were resuspended in cell culture media and adjusted to pH 7 using a 6 N solution of NaOH. Media was added to the final volume and the solution was sterile filtered with a 0.2 µm syringe filter. The devices were incubated in the eSrt(2A9) sortase working solution for 16 hours to degrade the PEG patterned in the v-shaped channel walls. Holes were added to the design to aid in permeation of the sortase solution into this region. After incubation, the clips and patterning device that now had a degraded channel wall were gently removed, releasing the PEG-based suspended hydrogel. Removal of the STOMP patterning device was performed while the hydrogel was submerged in a media.

EHT analysis

Force measurements: EHTs were placed in a Tyrode's buffer (1.8 mM CaCl2, 1 mM MgCl2, 5.4 mM KCl, 140 mM NaCl, 0.33 mM NaH2PO4, 5 mM glucose, pH 7.35) at 37°C for contractile analysis. Biphasic field stimulation at 1.5 Hz (5 V/cm for 10 ms duration) during imaging was provided by a custom pacing device incorporating carbon electrodes designed to fit in a 24-well plate and an electrical stimulator (Astro Med Grass Stimulator, Model S88X) as previously described[26,60,91]. Brightfield videos of EHT contraction were taken at 66.7 fps for 7.5 seconds for stimulated contractile measurements and 15 seconds for spontaneous contractile measurements. A custom MATLAB script was used to track the deflection of the flexible post and calculate the twitch force, shortening velocity, time to peak, time to 50% relaxation, time

to 90% relaxation, beat frequency, and cross-sectional area. Specific force was calculated by dividing the twitch force of each tissue by its cross-sectional area.

Immunofluorescent Imaging: To visualize HS5-cells expressing GFP or mCherry which were seeded in the EHT outer or center regions respectively, EHTs were placed in a Tyrode's buffer and imaged at 20 fps on an ORCA-Flash4.0 C13440 CMOS camera (Hamamatsu) on a Nikon TEi epifluorescent microscope with a FITC or TRITC filter cube. Images were processed using ImageJ.

Periodontal tissue analysis

Calculation of PTC contractile force: Contractile force generated by PTCs was calculated by quantifying the magnitude of deflection they caused in the post pairs they were suspended between. Based on a modulus of elasticity of 2.5 MPa for PDMS, the bending stiffness (Kpost) of the flexible posts was calculated to be 0.95 μN/μm, as done previously[59]. Contractile force was calculated by multiplying the bending stiffness by the deflection of the post (initial length of tissue, L_0, minus the final length of tissue, L_F) (see Supplementary Figure E11).

Alizarin red staining: PTCs on posts were fixed in 4% PFA at room temperature for 1 hour and then removed from the posts. PTCs were then washed with DH2O, and incubated in alizarin red solution (pH 4.1 to 4.3) (Sigma-Aldrich) for 45 min at room temperature and washed 4x with DH2O on a shaker at room temperature. Whole PTCs were then coverslipped in VECTASHIELD mounting medium and allowed to dry overnight. The next day, brightfield microscope images at 4X were taken. Images were processed using the FIJI image analysis software.

Statistical analysis: Data from both the EHT and PTC work represents tissues collected from three independent experiments. All data points in the figures designate values for a single tissue. All values shown are reported as the mean ± standard error of mean. For the EHT work, results were compared by using an unpaired t-test with two tails. For the PTC work, results were compared using one-way ANOVA with post-hoc comparisons using GraphPad Prism. Differences with p-values ≤ 0.05 were considered statistically significant and denoted with an asterisk.

2.9 References

1. Elson, E. L. & Genin, G. M. Tissue constructs: platforms for basic research and drug discovery. *Interface Focus* **6**, (2016).
2. Park, Y., Huh, K. M. & Kang, S. W. Applications of Biomaterials in 3D Cell Culture and Contributions of 3D Cell Culture to Drug Development and Basic Biomedical Research. *Int. J. Mol. Sci. 2021 Vol 22 Page 2491* **22**, 2491 (2021).
3. Zhang, W., Huang, G. & Xu, F. Engineering Biomaterials and Approaches for Mechanical Stretching of Cells in Three Dimensions. *Front. Bioeng. Biotechnol.* **8**, 1151 (2020).
4. Riehl, B. D., Park, J. H., Kwon, I. K. & Lim, J. Y. Mechanical stretching for tissue engineering: Two-dimensional and three-dimensional constructs. *Tissue Eng. - Part B Rev.* **18**, 288–300 (2012).
5. Legant, W. R. *et al.* Microfabricated tissue gauges to measure and manipulate forces from 3D microtissues. *Proc. Natl. Acad. Sci. U. S. A.* **106**, 10097–10102 (2009).
6. Christensen, R. K., Laier, C. V. H., Kiziltay, A., Wilson, S. & Larsen, N. B. 3D Printed Hydrogel Multiassay Platforms for Robust Generation of Engineered Contractile Tissues. *Biomacromolecules* **21**, 356–365 (2020).
7. Gaio, N. *et al.* Cytostretch, an Organ-on-Chip Platform. *Micromachines 2016 Vol 7 Page 120* **7**, 120 (2016).
8. Eyckmans, J. & Chen, C. S. 3D culture models of tissues under tension. *J. Cell Sci.* **130**, 63–70 (2017).
9. Ribeiro, A. J. S., Denisin, A. K., Wilson, R. E. & Pruitt, B. L. For whom the cells pull: Hydrogel and micropost devices for measuring traction forces. *Methods* **94**, 51–64 (2016).
10. Rogozinski, N., Yanez, A., Bhoi, R., Lee, M.-Y. & Yang, H. Current methods for fabricating 3D cardiac engineered constructs. *iScience* **25**, 104330 (2022).
11. Bramson, M. T. K., Van Houten, S. K. & Corr, D. T. Mechanobiology in Tendon, Ligament, and Skeletal Muscle Tissue Engineering. *J. Biomech. Eng.* **143**, 070801 (2021).
12. Fernández-Costa, J. M., Fernández-Garibay, X., Velasco-Mallorquí, F. & Ramón-Azcón, J. Bioengineered *in vitro* skeletal muscles as new tools for muscular dystrophies preclinical studies. *J. Tissue Eng.* **12**, 204173142098133 (2021).
13. Chen, Z. *et al.* Lung Microtissue Array to Screen the Fibrogenic Potential of Carbon Nanotubes. *Sci. Rep. 2016 61* **6**, 1–11 (2016).
14. West, A. R. *et al.* Development and characterization of a 3D multicell microtissue culture model of airway smooth muscle. *Am. J. Physiol. - Lung Cell. Mol. Physiol.* **304**, 4–16 (2013).
15. Asmani, M. *et al.* Fibrotic microtissue array to predict anti-fibrosis drug efficacy. *Nat. Commun.* **9**, 2066 (2018).
16. Sakar, M. S. *et al.* Cellular forces and matrix assembly coordinate fibrous tissue repair. *Nat. Commun. 2016 71* **7**, 1–8 (2016).
17. Miller, J. S. *et al.* Rapid casting of patterned vascular networks for perfusable engineered three-dimensional tissues. *Nat. Mater. 2012 119* **11**, 768–774 (2012).
18. Velthoven, M. J. J. V. *et al.* Gel Casting as an Approach for Tissue Engineering of Multilayered Tubular Structures. *Tissue Eng. - Part C Methods* **26**, 190–198 (2020).
19. Ling, Y. *et al.* A cell-laden microfluidic hydrogel. *Lab. Chip* **7**, 756–762 (2007).
20. Chan, V., Zorlutuna, P., Jeong, J. H., Kong, H. & Bashir, R. Three-dimensional photopatterning of hydrogels using stereolithography for long-term cell encapsulation. *Lab. Chip* **10**, 2062 (2010).
21. Batalov, I., Stevens, K. R. & DeForest, C. A. Photopatterned biomolecule immobilization to guide three-dimensional cell fate in natural protein-based hydrogels. *Proc. Natl. Acad. Sci.* **118**, e2014194118 (2021).
22. Adhikari, J. *et al.* Effects of surface patterning and topography on the cellular functions of tissue engineered scaffolds with special reference to 3D bioprinting. *Biomaterials Science* vol. 11 1236–1269 (2022).

23. Murphy, S. V. & Atala, A. 3D bioprinting of tissues and organs. *Nat. Biotechnol. 2014 328* **32**, 773–785 (2014).
24. Lee, A. *et al.* 3D bioprinting of collagen to rebuild components of the human heart. *Science* **365**, 482–487 (2019).
25. Pedde, R. D. *et al.* Emerging Biofabrication Strategies for Engineering Complex Tissue Constructs. *Adv. Mater.* **29**, 1606061 (2017).
26. Leonard, A. *et al.* Afterload promotes maturation of human induced pluripotent stem cell derived cardiomyocytes in engineered heart tissues. *J. Mol. Cell. Cardiol.* **118**, 147–158 (2018).
27. Iuliano, A. *et al.* Coupling 3D Printing and Novel Replica Molding for In House Fabrication of Skeletal Muscle Tissue Engineering Devices. *Adv. Mater. Technol.* **5**, 2000344 (2020).
28. Gill, E. L. *et al.* Fabrication of Designable and Suspended Microfibers via Low-Voltage 3D Micropatterning. *ACS Appl. Mater. Interfaces* **11**, 19679–19690 (2019).
29. Hinton, T. J. *et al.* Three-dimensional printing of complex biological structures by freeform reversible embedding of suspended hydrogels. *Sci. Adv.* **1**, e1500758 (2015).
30. Mirdamadi, E., Tashman, J. W., Shiwarski, D. J., Palchesko, R. N. & Feinberg, A. W. FRESH 3D Bioprinting a Full-Size Model of the Human Heart. *ACS Biomater. Sci. Eng.* **6**, 6453–6459 (2020).
31. Shiwarski, D. J., Hudson, A. R., Tashman, J. W. & Feinberg, A. W. Emergence of FRESH 3D printing as a platform for advanced tissue biofabrication. *APL Bioeng.* **5**, 010904 (2021).
32. Riffe, M. B. *et al.* Multi-Material Volumetric Additive Manufacturing of Hydrogels using Gelatin as a Sacrificial Network and 3D Suspension Bath. *Adv. Mater.* **36**, 2309026 (2024).
33. Moxon, S. R. *et al.* Suspended Manufacture of Biological Structures. *Adv. Mater.* **29**, 1605594 (2017).
34. Filippi, M. *et al.* Microfluidic Tissue Engineering and Bio-Actuation. *Adv. Mater.* **34**, 2108427 (2022).
35. Su, C. *et al.* A facile and scalable hydrogel patterning method for microfluidic 3D cell culture and spheroid-in-gel culture array. *Biosensors* **11**, 509 (2021).
36. Tu, C. *et al.* A Microfluidic Chip for Cell Patterning Utilizing Paired Microwells and Protein Patterns. *Micromachines 2017 Vol 8 Page 1* **8**, 1 (2016).
37. Torisawa, Y. S. *et al.* Microfluidic hydrodynamic cellular patterning for systematic formation of co-culture spheroids. *Integr. Biol.* **1**, 649–654 (2009).
38. Ong, L. J. Y. *et al.* Localized Oxygen Control in a Microfluidic Osteochondral Interface Model Recapitulates Bone–Cartilage Crosstalk During Osteoarthritis. *Adv. Funct. Mater.* **34**, 2315608 (2024).
39. Nguyen, M.-L. *et al.* Studying the impact of geometrical and cellular cues on myogenesis with a skeletal muscle-on-chip. *Lab. Chip* **24**, 4147–4160 (2024).
40. Casavant, B. P. *et al.* Suspended microfluidics. *Proc. Natl. Acad. Sci. U. S. A.* **110**, 10111–10116 (2013).
41. Oliveira, N. M., Vilabril, S., Oliveira, M. B., Reis, R. L. & Mano, J. F. Recent advances on open fluidic systems for biomedical applications: A review. *Mater. Sci. Eng. C* **97**, 851–863 (2019).
42. Berthier, E., Dostie, A. M., Lee, U. N., Berthier, J. & Theberge, A. B. Open Microfluidic Capillary Systems. *Anal. Chem.* **91**, 8739–8750 (2019).
43. Berthier, J., Brakke, K. A. & Berthier, E. *Open Microfluidics*. (Scrivener-Wiley Publishing, 2016).
44. Zhang, Q., Feng, S., Lin, L., Mao, S. & Lin, J.-M. Emerging open microfluidics for cell manipulation. *Chem. Soc. Rev.* **50**, 5333–5348 (2021).
45. Deroy, C., Nebuloni, F., Cook, P. R. & Walsh, E. J. Microfluidics on Standard Petri Dishes for Bioscientists. *Small Methods* **5**, 2100724 (2021).
46. Lee, U. N. *et al.* Layer-by-layer fabrication of 3D hydrogel structures using open microfluidics. *Lab. Chip* **20**, 525–536 (2020).
47. Berry, S. B. *et al.* Upgrading well plates using open microfluidic patterning. *Lab. Chip* **17**, 4253–4264 (2017).

48. Park, D. *et al.* Aspiration-mediated hydrogel micropatterning using rail-based open microfluidic devices for high-throughput 3D cell culture. *Sci. Rep.* **11**, 19986 (2021).
49. Lee, Y. *et al.* Microfluidics within a well: an injection-molded plastic array 3D culture platform. *Lab. Chip* **18**, 2433–2440 (2018).
50. Walsh, E. J. *et al.* Microfluidics with fluid walls. *Nat. Commun.* **8**, 816 (2017).
51. Yu, J. *et al.* Reconfigurable open microfluidics for studying the spatiotemporal dynamics of paracrine signalling. *Nat. Biomed. Eng.* **3**, 830–841 (2019).
52. Humayun, M., Chow, C.-W. & Young, E. W. K. Microfluidic lung airway-on-a-chip with arrayable suspended gels for studying epithelial and smooth muscle cell interactions. *Lab. Chip* **18**, 1298–1309 (2018).
53. Lee, S.-R. *et al.* U-IMPACT: a universal 3D microfluidic cell culture platform. *Microsyst. Nanoeng.* **8**, 126 (2022).
54. Li, Q., Niu, K., Wang, D., Xuan, L. & Wang, X. Low-cost rapid prototyping and assembly of an open microfluidic device for a 3D vascularized organ-on-a-chip. *Lab. Chip* **22**, 2682–2694 (2022).
55. Park, S. E. *et al.* Geometric engineering of organoid culture for enhanced organogenesis in a dish. *Nat. Methods* **19**, 1449–1460 (2022).
56. Lee, S. H. *et al.* Capillary Based Patterning of Cellular Communities in Laterally Open Channels. *Anal. Chem.* **82**, 2900–2906 (2010).
57. Bretherton, R. C. *et al.* User-Controlled 4D Biomaterial Degradation with Substrate-Selective Sortase Transpeptidases for Single-Cell Biology. *Adv. Mater.* **35**, 2209904 (2023).
58. Rapp, T. L. & DeForest, C. A. Tricolor visible wavelength-selective photodegradable hydrogel biomaterials. *Nat. Commun.* **14**, 5250 (2023).
59. Bielawski, K. S., Leonard, A., Bhandari, S., Murry, C. E. & Sniadecki, N. J. Real-Time Force and Frequency Analysis of Engineered Human Heart Tissue Derived from Induced Pluripotent Stem Cells Using Magnetic Sensing. *Tissue Eng. Part C Methods* **22**, 932–940 (2016).
60. Bremner, S., Goldstein, A. J., Higashi, T. & Sniadecki, N. J. Engineered Heart Tissues for Contractile, Structural, and Transcriptional Assessment of Human Pluripotent Stem Cell-Derived Cardiomyocytes in a Three-Dimensional, Auxotonic Environment. *Methods Mol. Biol.* **2485**, 87–97 (2022).
61. Stoehr, A. *et al.* Automated analysis of contractile force and Ca2+ transients in engineered heart tissue. *Am. J. Physiol.-Heart Circ. Physiol.* **306**, H1353–H1363 (2014).
62. Schaaf, S. *et al.* Human Engineered Heart Tissue as a Versatile Tool in Basic Research and Preclinical Toxicology. *PLOS ONE* **6**, e26397 (2011).
63. Olanrewaju, A., Beaugrand, M., Yafia, M. & Juncker, D. Capillary microfluidics in microchannels: from microfluidic networks to capillaric circuits. *Lab. Chip* **18**, 2323–2347 (2018).
64. Buguin, A., Talini, L. & Silberzan, P. Ratchet-like topological structures for the control of microdrops. *Appl. Phys. A* **75**, 207–212 (2002).
65. Bico, J., Marzolin, C. & Quéré, D. Pearl drops. *Europhys. Lett. EPL* **47**, 220–226 (1999).
66. Bico, J., Tordeux, C. & Quéré, D. Rough wetting. *Europhys. Lett. EPL* **55**, 214–220 (2001).
67. Berthier, J. & Brakke, K. A. Sessile Droplets. in *The Physics of Microdroplets* 105–142 (Wiley, 2012). doi:10.1002/9781118401323.
68. Berthier, J., Theberge, A. B. & Berthier, E. *Open-Channel Microfluidics; Fundamentals and Applications*. (IOP Publishing, 2024).
69. Ondarçuhu, T. Total or Partial Pinning of a Droplet on a Surface with a Chemical Discontinuity. *J. Phys. II* **5**, 227–241 (1995).
70. Eijgenraam, T. R., Silljé, H. H. W. & De Boer, R. A. Current understanding of fibrosis in genetic cardiomyopathies. *Trends Cardiovasc. Med.* **30**, 353–361 (2020).
71. Li, L., Zhao, Q. & Kong, W. Extracellular matrix remodeling and cardiac fibrosis. *Matrix Biol.* **68–69**, 490–506 (2018).
72. Mainardi, A. *et al.* A dynamic microscale mid-throughput fibrosis model to investigate the effects of different ratios of cardiomyocytes and fibroblasts. *Lab. Chip* **21**, 4177–4195 (2021).

73. Bracco Gartner, T. C. L. *et al.* Pirfenidone Has Anti-fibrotic Effects in a Tissue-Engineered Model of Human Cardiac Fibrosis. *Front. Cardiovasc. Med.* **9**, 854314 (2022).
74. Das, S. L., Sutherland, B. P., Lejeune, E., Eyckmans, J. & Chen, C. S. Mechanical response of cardiac microtissues to acute localized injury. *Am. J. Physiol.-Heart Circ. Physiol.* **323**, H738–H748 (2022).
75. Wang, E. Y. *et al.* Biowire Model of Interstitial and Focal Cardiac Fibrosis. *ACS Cent. Sci.* **5**, 1146–1158 (2019).
76. Graf, L., Iwata, M. & Torok-Storb, B. Gene expression profiling of the functionally distinct human bone marrow stromal cell lines HS-5 and HS-27a. *Blood* **100**, 1509–1511 (2002).
77. Torok-Storb, B. *et al.* Dissecting the Marrow Microenvironment. *Ann. N. Y. Acad. Sci.* **872**, 164–170 (1999).
78. Roberts, M. A. *et al.* Stromal Cells in Dense Collagen Promote Cardiomyocyte and Microvascular Patterning in Engineered Human Heart Tissue. *Tissue Eng. Part A* **22**, 633–644 (2016).
79. Yotti, R., Seidman, C. E. & Seidman, J. G. Advances in the Genetic Basis and Pathogenesis of Sarcomere Cardiomyopathies. *Annu. Rev. Genomics Hum. Genet.* **20**, 129–153 (2019).
80. Rupert, C. E., Kim, T. Y., Choi, B.-R. & Coulombe, K. L. K. Human Cardiac Fibroblast Number and Activation State Modulate Electromechanical Function of hiPSC-Cardiomyocytes in Engineered Myocardium. *Stem Cells Int.* **2020**, 1–16 (2020).
81. Mulimani, P. *et al.* Engineered 3D Periodontal Ligament Model with Magnetic Tensile Loading. *J. Dent. Res.* 00220345241264792 (2024) doi:10.1177/00220345241264792.
82. Yang, L., Yang, Y., Wang, S., Li, Y. & Zhao, Z. In vitro mechanical loading models for periodontal ligament cells: From two-dimensional to three-dimensional models. *Arch. Oral Biol.* **60**, 416–424 (2015).
83. Aveic, S., Craveiro, R. B., Wolf, M. & Fischer, H. Current Trends in In Vitro Modeling to Mimic Cellular Crosstalk in Periodontal Tissue. *Adv. Healthc. Mater.* **10**, 2001269 (2021).
84. Huang, C. *et al.* The Application of Organs-on-a-Chip in Dental, Oral, and Craniofacial Research. *J. Dent. Res.* **102**, 364–375 (2023).
85. Lin, J. D. *et al.* Periodontal ligament entheses and their adaptive role in the context of dentoalveolar joint function. *Dent. Mater.* **33**, 650–666 (2017).
86. Kopyeva, I. *et al.* Stepwise Stiffening/Softening of and Cell Recovery from Reversibly Formulated Hydrogel Interpenetrating Networks. *Adv. Mater.* 2404880 (2024) doi:10.1002/adma.202404880.
87. Neumann, M. *et al.* Stimuli-Responsive Hydrogels: The Dynamic Smart Biomaterials of Tomorrow. *Macromolecules* **56**, 8377–8392 (2023).
88. Ifkovits, J. L. & Burdick, J. A. Review: Photopolymerizable and Degradable Biomaterials for Tissue Engineering Applications. *Tissue Eng.* **13**, 2369–2385 (2007).
89. Lian, X. *et al.* Directed cardiomyocyte differentiation from human pluripotent stem cells by modulating Wnt/β-catenin signaling under fully defined conditions. *Nat. Protoc.* **8**, 162–175 (2013).
90. Bremner, S. B. *et al.* Full-length dystrophin deficiency leads to contractile and calcium transient defects in human engineered heart tissues. *J. Tissue Eng.* **13**, 204173142211196 (2022).
91. Loiben, A. M. *et al.* Cardiomyocyte Apoptosis Is Associated with Contractile Dysfunction in Stem Cell Model of MYH7 E848G Hypertrophic Cardiomyopathy. *Int. J. Mol. Sci.* **24**, 4909 (2023).
92. Somermen, M. J., Foster, R. A., Vorsteg, G. M., Progebin, K. & Wynn, R. L. Effects of minocycline on fibroblast attachment and spreading. *J. Periodontal Res.* **23**, 154–159 (1988).
93. DeForest, C. A. & Tirrell, D. A. A photoreversible protein-patterning approach for guiding stem cell fate in three-dimensional gels. *Nat. Mater.* **14**, 523–531 (2015).

Chapter 3 | At-home blood collection and stabilization in high temperature climates using homeRNA

Reproduced in part from L.G. Brown, A. J. Haack*, D. S. Kennedy, K. N. Adams, J. E. Stolarczuk, M. G. Takezawa, E. Berthier, S. Thongpang, F. Y. Lim, D. Chaussabel[#], M. Garand[#], and A. B. Theberge[#], "At-home blood collection and stabilization in high temperature climates using homeRNA" Frontiers in Digital Health, 2022, 4, 903153.*
** Equal contribution*
[#]Co-corresponding authors

LGB, AJH, EB, ST, DC, MG, and ABT contributed to the conception and design of the study. AJH, DSK, FYL, EB, and ABT developed homeRNA and the protocols implemented in home sampling in this manuscript. AJH, DSK, KNA, JS, and MGT conducted/contributed to the human subjects research with participants in the Western and South Central USA. DC and MG conducted the human subjects research with participants in Doha, Qatar. LGB, AJH, and MG performed the RNA extractions on samples and collected the RIN and yield data. LGB, AJH, JS, MGT, FYL, EB, ST, DC, MG, and ABT analyzed/interpreted the data. LGB, AJH, MG, and ABT prepared the figures and wrote the manuscript. All authors contributed to the article and approved the submitted version.

Abstract: Expanding whole blood sample collection for transcriptome analysis beyond traditional phlebotomy clinics will open new frontiers for remote immune research and telemedicine. Determining the stability of RNA in blood samples exposed to high ambient temperatures (>30°C) is necessary for deploying home-sampling in settings with elevated temperatures (e.g., studying physiological response to natural disasters that occur in warm locations or in the summer). Recently, we have developed homeRNA, a technology that allows for self-blood sampling and RNA stabilization remotely. homeRNA consists of a lancet-based blood collection device, the Tasso-SST™ which collects up to 0.5 mL of blood from the upper arm, and a custom-built stabilization transfer tube containing RNAlater™. In this study, we investigated the robustness of our homeRNA kit in high temperature settings via two small pilot studies in Doha, Qatar (no. participants = 8), and the Western and South Central USA during the summer of 2021, which included a heatwave of unusually high temperatures in some locations (no. participants = 11). Samples collected from participants in Doha were subjected to rapid external temperature fluctuations from being moved to and from air-conditioned areas and extreme heat environments (up to 41°C external temperature during brief temperature spikes). In the USA pilot study, regions varied in outdoor temperature highs (between 25°C and 43.4°C). All samples that returned a RNA integrity number (RIN) value from the Doha, Qatar group had a RIN ≥7.0, a typical integrity threshold for downstream transcriptomics analysis. RIN values

for the Western and South Central USA samples (n=12 samples) ranged from 6.9-8.7 with 9 out of 12 samples reporting RINs ≥7.0. Overall, our pilot data suggest that homeRNA can be used in some regions that experience elevated temperatures, opening up new geographical frontiers in disseminated transcriptome analysis for applications critical to telemedicine, global health, and expanded clinical research. Further studies, including our ongoing work in Qatar, USA, and Thailand, will continue to test the robustness of homeRNA.

3.1 Introduction

Blood is a useful biofluid for transcriptome analysis, as it is relatively non-invasive to obtain and provides ample information for biomarker identification and analysis [1]. Consequently, whole blood RNA transcript analysis has emerged as an avenue for realizing the goals of personalized medicine [2, 3]. Key biomarkers discovered through blood transcriptomic studies have potential applications in novel therapeutics and diagnostics [4–8] and have provided new avenues for disease monitoring of chronic [9, 10], autoimmune [11, 12], and infectious diseases [13]. By combining home-sampling technologies and transcriptomics, one can further expand upon these applications, opening up both biomarker discovery through discovery-based research studies, and bring applications such as gene expression-based disease monitoring and diagnostics to home-based tests. Further, a technology that allows for remote blood transcriptomics would be enabling for increasing access to rural, remote, or underserved communities, for both research studies and telemedicine, and could be a powerful technology for enhancing global health efforts [2].

Conducting remote blood transcriptomics research presents several challenges. For example, while blood is relatively non- invasive to collect, conventional blood collection is limited to phlebotomy. Logistically, relying on phlebotomy for collection geographically confines blood collections to clinic/lab locations or research institutes. Several self-blood collection technologies have been developed for remote use, including fingersticks [8], dried blood spots [14–16], and lancet-based technologies that collect blood from the upper arm [17–21], such as the Tasso-SST device that we use in our home- sampling and RNA

stabilization kits (including the work in this manuscript). Another major challenge of remote blood transcriptomics is stabilization of whole blood RNA to minimize RNA degradation due to spontaneous degradation via autohydrolysis or degradation due to the presence of ribonucleases [22]. Toma et al. developed an at-home blood collection kit that collects 50µl of capillary blood via fingerstick and mixes with a proprietary RNA preservative solution at a 1:4 ratio [8]. To test the ability of the RNA preservative solution to preserve blood transcriptome, Toma et al. collected blood samples from participants (n = 3) and stored at ambient temperature (22°C) or −80°C for 0, 7, 14, and 28 days, with and without shipping. They found high correlation coefficients between gene expression levels from the samples in all conditions, demonstrating the efficacy of the RNA stabilization solution to preserve RNA integrity over 28 days [8].

To address this burgeoning need and develop technology for higher blood volumes than are possible with fingersticks, we have recently developed homeRNA, a kit for the self-collection and stabilization of whole blood RNA, for use in disseminated whole blood transcriptome applications [23]. homeRNA uses a blood collection device, the Tasso-SST, that collects capillary blood from the upper arm via a lancet; the blood collection tube from the Tasso system then interfaces with a custom engineered stabilizer tube that holds liquid stabilizer solution (RNAlater) [23]. Previously, we demonstrated successful stabilization of RNA extracted from samples collected with homeRNA in 47 participants in 10 USA states in a pilot feasibility study for validation of homeRNA for remote blood collection and RNA stabilization. However, most of these samples were collected in regions with relatively moderate summer temperatures or during the fall/winter and thus we sought to test the homeRNA sampling kit in regions with elevated temperatures. Our present study builds on a small body of prior work examining the effects of blood storage temperature on RNA quality; prior work largely focused on the effects of cold storage and did not examine temperatures above 25°C [24–26].

Establishing means to remotely probe the human whole blood transcriptome in elevated temperature settings has important implications, including enabling clinical research or personalized medicine applications in areas with high temperature and studying diseases/events that are specific to warm climates or warm times of year. For example, regions more highly burdened by tropical diseases would benefit from

a better understanding of the stability of RNA because many of these areas often have persistently elevated temperatures. Further, even in regions with more moderate climates for part of the year, researchers may wish to conduct remote sampling studies in the summer months, particularly when tied to a specific seasonal event. For example, a study aiming to understand wildfire smoke exposure in the Western and South Central USA would necessitate sampling in the summer months where temperatures are elevated, as these months are when wildfires occur. Overall, the ability to reliably stabilize RNA with homeRNA in high temperature settings will open up remote transcriptome studies to regions with a warmer climate, whether seasonally or permanently.

We present here two small pilot studies exploring the application of homeRNA in high temperature settings. In the first pilot study, homeRNA was used by a small group in the city of Doha, Qatar before the sample was exposed to simulated shipping conditions of fluctuating temperatures. In the second study, homeRNA was used at a regional scale, where participants used homeRNA in their own homes during the summer months in several Western and South Central USA states, which included regions that are typically very hot [e.g., Reno, Nevada and Southern California) as well as the Pacific Northwest during the June 2021 heat wave. For samples collected from both studies, we examine quality control metrics typical to determining suitability of isolated RNA for downstream RNA transcript analysis, including the RNA integrity number (RIN) and total cellular RNA yield. In both the small pilot study in Qatar, and the small pilot study in the Western and South Central USA, we found satisfactory RIN values (RIN $\geq$7) in the majority of samples (84%, 16 out of 19 samples), with a RIN of 6.9 in the remaining 3 samples. Overall, our data demonstrate successful RNA stabilization as a function of yield and RIN values using homeRNA in high temperature settings.

3.2 homeRNA at high temperatures: An overview of two pilot studies

In this work, we tested the robustness of the homeRNA kit by evaluating the stability of RNA transcripts in blood collected using the homeRNA kits during high temperatures in the summer months (July-August) in two different regions: Doha, Qatar (in-lab collection with homeRNA, followed by in-field sample exposure in a hot car to simulate conditions in a courier service) and the Western and South Central

USA (remote collection with homeRNA by participants in their home, shipped back to the lab). A typical logistical process of collecting, stabilizing, shipping, and processing homeRNA blood samples is outlined in Figure 3.1, including a schematic of how a user can collect and stabilize blood with homeRNA. In each case, our study design was chosen based on how at-home clinical research studies would be performed in that region (i.e., a 3-hour car ride to simulate a courier service in Doha and overnight shipping via UPS in the USA). Specifically, in the Qatar pilot study we were interested in understanding if stabilized blood samples exposed to high temperature fluctuations in a region of the world that regularly experiences high temperatures would affect the quality of isolated blood RNA. The Qatar samples were collected in a laboratory setting which was air conditioned (to model the air-conditioned home environment typical in Qatar) and deliberately stressed in different temperature environments (i.e., collection at air-conditioned ambient temperature, exposure to external outdoor high temperatures, transportation conditions, etc. (Table B1)) to simulate shipping conditions that typically occur between remote blood collection and shipment back to the lab for analysis in Qatar. In Qatar, air conditioning is prevalent, and therefore samples may go from air-conditioned areas to extreme heat during shipping. Further, in Doha courier services (such as Uber) are a common method of moving packages around the city. The conditions we employed (Table B1) were chosen to mimic a typical car ride that the samples would experience in a courier service for shipments within the city itself; the length of the car ride (3h) is shorter than the time required to ship packages in the USA with UPS, but is relevant for courier services in Doha. Subsequently, the Western and South Central USA pilot study experienced real-world shipping conditions, in which participants were mailed homeRNA kits from Seattle, WA to various states in the Western region of the USA during the summer (Table 3.1), yielding data from participants in a range of regions and temperatures to further test the applicability of homeRNA in multiple high temperature environments.

The robustness of the homeRNA kit to elevated ambient temperature exposures was validated by assessing isolated blood RNA quality with RNA integrity number (RIN) values. RIN values range between 1 and 10, with 1 referring to a completely degraded sample and 10 referring to an intact sample [27]. RIN

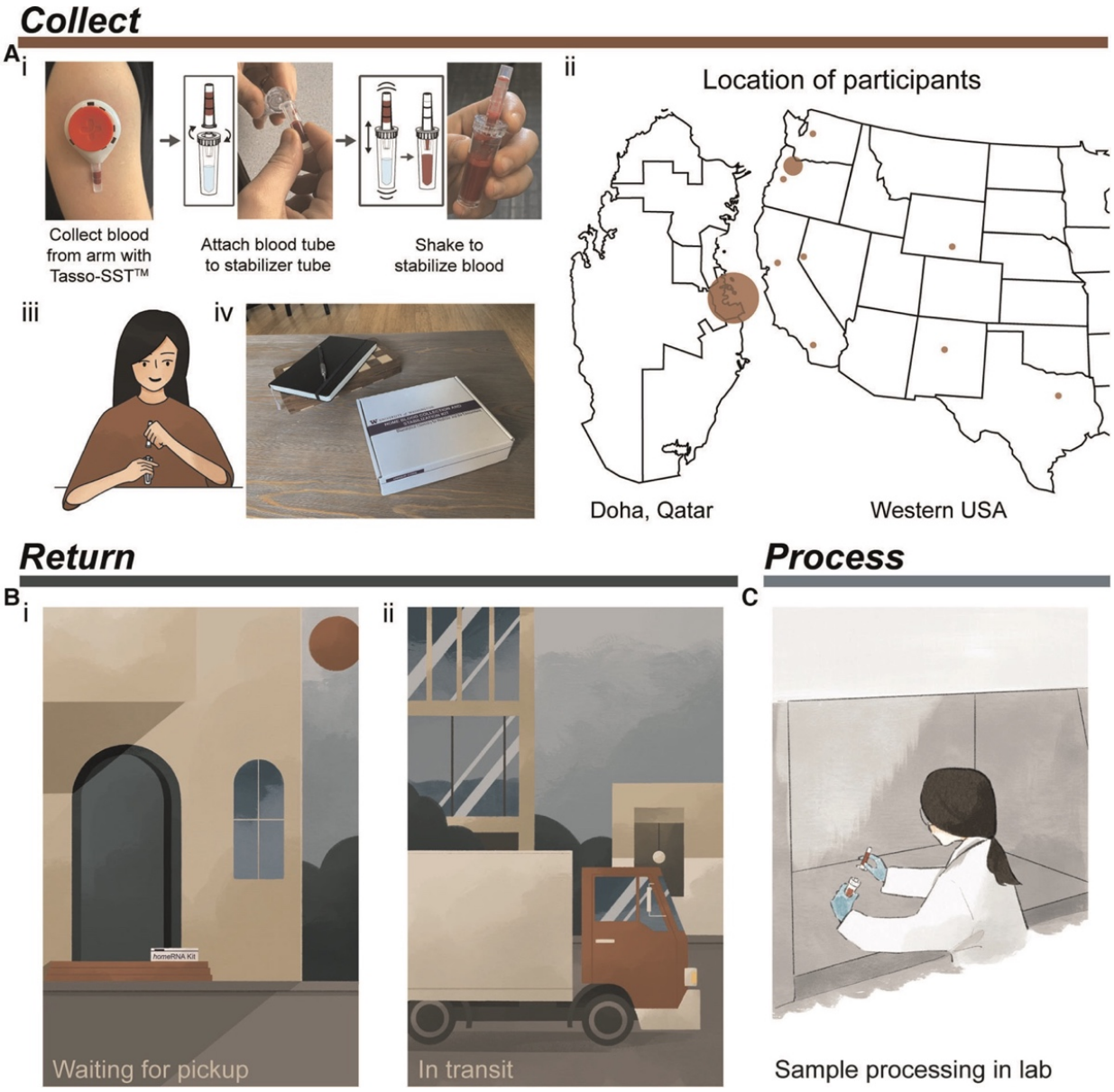

Figure 3.1. Typical process for using *home*RNA from collection to processing of samples. (A) Collection and stabilization of blood using *home*RNA. (i) Process of collecting blood from the upper arm with Tasso device and stabilizing the sample with the *home*RNA custom stabilizer tube. Image was reprinted with permission from Haack, Lim, et al. *home*RNA: A Self-Sampling Kit for the Collection of Peripheral Blood and Stabilization of RNA. Anal. Chem. 2021, 93, 39, 13196–13203. Copyright 2021 American Chemical Society [23]. (ii) Map depicting locations of participants in the small pilot studies conducted in Qatar and the Western and South Central USA. Note, participants in Qatar collected samples themselves in a lab setting. (iii) illustration demonstrating a participant connecting the Tasso blood tube and the *home*RNA stabilizer tube, (iv) *home*RNA kit on a coffee table, depicting a home setting for blood collection. (B) Illustration demonstrating two possible locations where samples may be exposed to high temperatures including (i) located on a front porch waiting to be picked up (which was the pickup location for many participants in the Western and South Central USA pilot study) and (ii) in transit in a delivery truck or courier service. (C) final step of sample processing for downstream analysis in a laboratory setting.

values ≥7.0 are standard QC cut-offs for genome wide transcriptional profiling [28]. However, useful RNA sequencing data can still be obtained from more degraded samples (RIN values between 4 and 7) [29].

Table 3.1: Participant and sampling information for the Western USA pilot study

Participant	Self-Reported Blood Volume (µL)	Indoor Temperature at Sampling (°C)	Outdoor Temperature High on Pickup Day (°C)	Location of Sampling	Month of Sampling	Total Yield (ug)	RIN
1A	200	25.0	42.3	Albany, OR	Late June	0.7	6.9
1B	300	26.3	35.6	Albany, OR	Early July	0.8	6.9
2	400	25.8	36.8	Davis, CA	Late July	1.1	7.1
3	300	23.2	28.7	Seattle, WA	Early August	0.8	7.4
4	300	24.0	33.4	Dallas, TX	Early July	0.7	7.3
5	200	23.1	35.3	Laramie, WY	Late July	0.5	7.6
6	200	24.5	34.8	Pasadena CA	Mid July	0.8	6.9
7	300	26.9	43.4	Portland, OR	Late June	0.5	7.4
8	400	27.2	32.3	Reno, NV	Early August	1.0	7.3
9	300	21.2	25.0	Albuquerque, NM	Late June	1.9	8.2
10	400	25.0	35.4	Portland, OR	Late July	1.8	7.6
11	400	23.0	25.5	Portland, OR	Late July	1.6	8.7

3.3 homeRNA for high temperature regions: a pilot study in Doha, Qatar

To understand the robustness of the *home*RNA device for use in clinical studies performed in Doha, Qatar, 8 participants in Doha, Qatar collected and stabilized their own blood in late August 2021. After blood collection and stabilization with the *home*RNA kit, each sample was incubated at room temperature (21°C) for 27 h, simulating time between remote blood collection and next-day sample pick up for shipment. After sitting out at room temperature, the stabilized blood samples were then exposed to fluctuating external temperatures in air-conditioned, indoor, and outdoor environments, as outlined in Figure 3.2A and Table B1, by driving the samples around Doha in a car. This setup mimics the change in environment and temperatures that the stabilized blood samples would experience in transit using a typical courier service (see rationale for design described at the beginning of the Results and Discussion). The samples underwent external changes in temperature between 21°C and 41°C over the course of three hours before storage at −80°C until the time of analysis (Figure 3.2A). Of the 8 participants, stabilized blood

samples from 7 of the donors were exposed to these high environmental temperature spikes. Samples 1 and 2a (from participant 2 who was sampled twice: 2a for control and 2b for temperature stress) were frozen after overnight incubation at room temperature to serve as controls.

The quality of isolated RNA from all 9 blood samples (from 8 participants) was assessed to observe if the high external temperature spikes had adverse effects on the RNA stability in the *home*RNA platform. Of the 9 samples, 7 yielded scorable RIN values (Figure 3.2C). The two that did not yield a RIN value (participants 6 and 8) both reported collected blood volumes of ~100 µl. We note that blood volume does not necessarily correlate with RNA yield (see Figure B5) and that variability in blood volume could result from device-to-device variability in the Tasso blood collection system and inaccuracy in participant reporting of the volume of collected blood. These two samples had low RNA concentrations beneath the limit of detection of the RNA 6000 Nano Kit (<5 ng/µl), but distinct 18S and 28S rRNA bands are noted in the digital gel (Figure 3.2B). The scorable RNA samples had RIN values between 7.6–8.7, demonstrating a sample quality suitable for downstream transcriptome (e.g., RNA-seq) analysis. Electropherograms obtained from the bioanalyzer can be found in Appendix B (Figure B1). RNA concentrations for the first 50 µl elution were also obtained with the bioanalyzer (Figure B2). For the 5 samples that were exposed to temperature fluctuations and yielded a scorable RIN value, the RNA concentrations from the first 50 µl elution ranged from 21 ng/µl to 40 ng/µl (1,050–2,000 ng total cellular RNA in the first 50µl elution). The two samples that yielded a concentration less than the qualitative range (5 ng/µl) of the Nano 6000 kit (participant 6 and 8) both measured a concentration of 4 ng/µl (200 ng total cellular RNA in the first 50µl elution). Therefore, all samples, including the low concentration samples (participant 6 and 8), likely had at least 200 ng total yield of RNA in the first elution. In general, 500 ng is a comfortable minimal cutoff value for large-scale transcriptomics analyses such as standard RNA-Seq (with many facilities accepting lower amounts of RNA), and 100 ng is a comfortable minimal cutoff value for expression analyses of a small panel of targeted genes. For RNA-Seq, we note that different cutoff values exist (for example as low as 10–30 ng) depending on the method and whether cDNA amplification is performed.

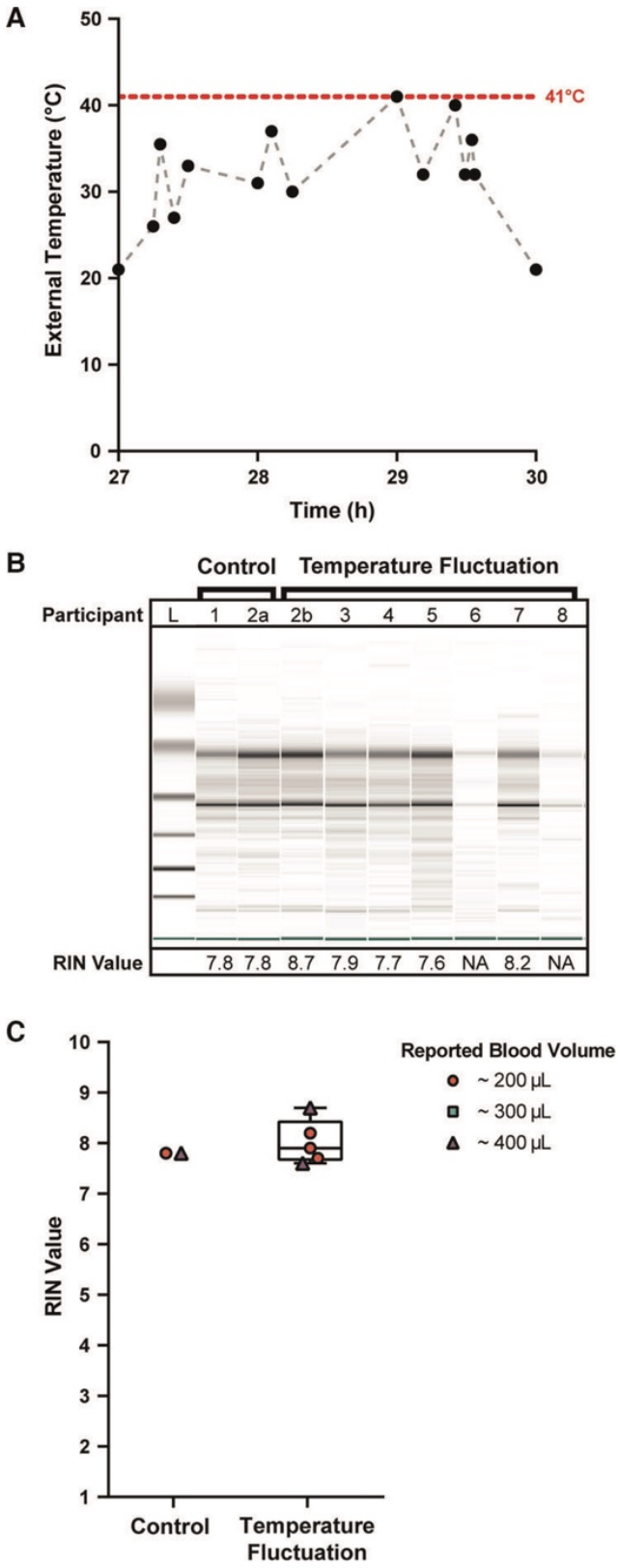

Figure 3.2. Quality of isolated RNA from stabilized *home*RNA samples exposed to high external temperature spikes in Doha, Qatar. (A) External temperature fluctuation experienced by self-collected and stabilized blood samples after storage at ambient temperature (21° C) for 27 h. External temperature reached a maximum of 41°C. Black data points indicate the measured temperature; gray dashed lines are included to connect the points to guide the eye only (transitions between temperatures may not be linear). (B) Digital gel image of RNA isolated from *home*RNA blood samples with corresponding RIN values. Samples 2a and 2b were from the same participant. Samples 1 and 2a did not undergo temperature fluctuations (they were frozen down at −80°C after overnight ambient temperature incubation to use as controls). (C) Scorable RIN values for each blood sample not exposed (control) and exposed (temperature fluctuation) to high temperature spikes along with the reported approximate blood volume collected by each participant. Participants 6 and 8 yielded too low of a RNA concentration to be detected using the RNA 6000 Nano kit.

The successful isolation and high quality of RNA from blood samples collected, stabilized, and analyzed in Doha suggests that the *home*RNA platform can be used for at-home clinical studies in Doha or places similar to Doha, a hot climate where air conditioning is commonplace in buildings and vehicles and fast courier services are available. In this setting, samples experience exposure to short term, high temperature fluctuations in external environmental conditions. Perhaps some researchers would assume that rapid temperature spikes would not affect the quality of RNA*later*TM- stabilized RNA, but we felt that it was necessary to conduct this field testing before using *home*RNA for clinical research in Doha. One important note regarding the experimental setup for this small pilot study is that the reported temperatures (Figure 3.2A, Table B1) are that of the local external environment (i.e., temperature inside the car, ambient outdoor temperature, etc.) rather than the temperature of the blood sample itself. It is possible that even though the external temperatures fluctuated markedly over the course of three hours with intervals of rapid but short increases or decreases in ambient temperatures, the blood sample itself may not have fully equilibrated to these observed external temperatures. Further experimentation, such as in-lab controlled temperature stress experiments, could further determine how spikes in external temperature affect the temperature of the blood sample itself.

3.4 homeRNA for high temperature seasons: a pilot study in Western and South Central USA

To further assess the robustness of the *home*RNA kit in high temperature settings, 11 participants in various regions throughout the Western and South Central USA collected and stabilized their own blood and shipped it back to our lab for analysis. These samples were collected during the summer of 2021, which involved unusually high temperatures in some locations, and 2 of these samples were collected during the June 2021 heatwave in the Pacific Northwest region. Samples were collected at indoor ambient temperatures ranging between 21°C and 27°C (Table 3.1, Figure 3.3Bi). Typically, stabilized blood samples were shipped back the same day or the following day with overnight shipping. The logistics of the study were such that participants left their package in a designated pickup area; all participants chose to have their samples picked up from outside their homes; therefore, all the stabilized blood samples were also exposed to the outdoor ambient temperatures following indoor collection and stabilization (See Table 3.1 for pickup

location). The duration of post-collection specimen storage prior to transit back to the lab (turnover duration) can be highly variable; this ranges from immediate transit (direct package handover a courier service driver) to overnight storage, in which these specimens can experience prolonged exposure to high ambient temperatures. This turnover duration is an important variable in temperature-dependent specimen stability and our data reflects the cumulative effect of variations in turnover duration experienced during real-world transits.

According to the day that each sample was collected and stabilized, the maximum outdoor temperature ("daily high") reported for the corresponding location of each participant (based on local weather reports found at Weather Underground) is included in Table 3.1. These outdoor temperatures spanned between 25°C and 44°C (Table 3.1, Figure 3.3Bii). We note that we do not know if the sample was outside during the daily high and further note that it is possible that the package was exposed to temperatures higher than the daily high, such as if it was placed in direct sunlight or if the temperature inside the pickup vehicle exceeded the daily high. Thus, the daily high is simply provided as a reference. In addition to the above, as noted in the Doha pilot study, the temperature of the blood sample may be different from the temperature of the external environment.

The quality of isolated RNA from 12 blood samples (from 11 participants) was assessed to observe how various temperature exposures (indoor, outdoor, shipping conditions, etc.) affected *home*RNA stability in a field test. 75% of the samples (9 out of 12 samples) yielded a RIN ≥7.0 (7.1–8.7) and the remaining yielded a RIN of 6.9 (Figure 3.3A). The RIN values demonstrate sufficient RNA quality for downstream transcriptomic analysis.

To observe how temperature at the time of collection and shipment affected the RNA integrity, RIN values were plotted against the respective indoor temperature at the time of collection and stabilization (Figure 3.3Bi) along with the local weather reports maximum outdoor temperature (Figure 3.3Bii). Indoor temperatures reported for the 12 samples range from 21.2–27.2°C. Indoor temperature at the time of collection (at least across the temperature range and small sample size used in this study) does not have a clear influence on the RIN value. Notably, there is overlap between the indoor temperatures reported here

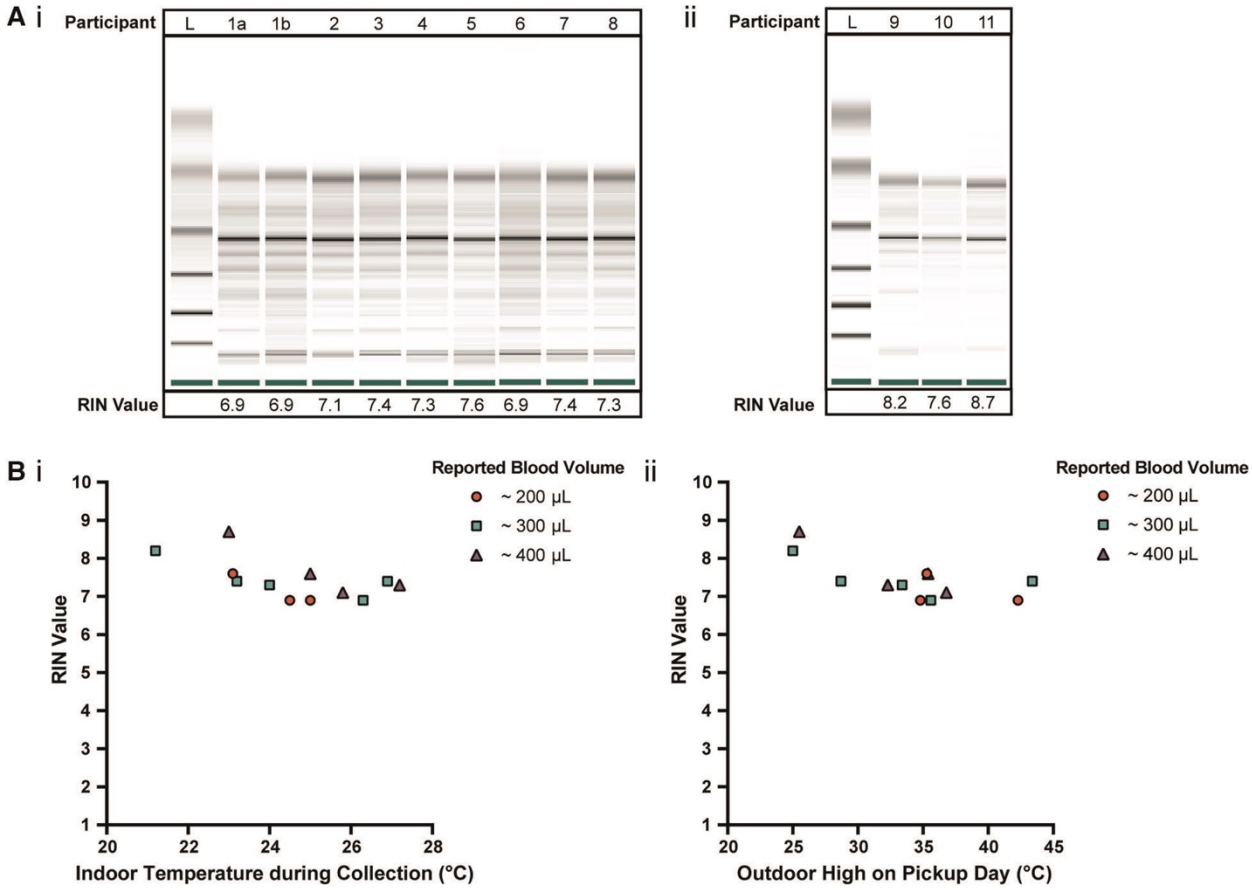

Figure 3.3. Quality of isolated RNA from stabilized *home*RNA samples collected during the summer in the Western and South Central USA. (A) Digital gel image of RNA isolated from *home*RNA stabilized blood samples with corresponding RIN values, with (i) samples diluted 1:5 with nuclease-free water and run with a RNA 6000 Pico kit and (ii) samples run with a RNA 6000 Nano kit without dilution. Participant 1 contributed two samples, 1a and 1b, that were collected and stabilized on different days and at different temperatures. (B) (i) RIN values from blood collected and stabilized at different indoor ambient temperatures during summer and (ii) RIN values according to the outdoor temperature high reported on the day of collection. Each participant was asked to report the approximate blood volume collected before stabilization based on Figure A6 in the collection survey.

(Figure 3.3B) and in our initial *home*RNA feasibility study [23]. In our previous pilot study conducted in 2020 [23], the majority of the samples were collected with an ambient indoor temperature between 18–25°C (n=43/53 analyzed returned samples where participants completed their surveys and provided indoor temperature data), with the other 9 samples ranging from 26–28°C, with 5 at 26°C, 1 at 27°C and 3 at 28°C. The results from the present study conducted in 2021 with respect to indoor temperature are plotted together with the results from our 2020 pilot study [23] with regards to RIN (Figure B5Ai) and total RNA yield (Figure B5Bi), in the Appendix B. There is also some overlap in the range of outdoor highs on pickup day

in this study and our previous study conducted in 2020, but the samples collected in the 2021 study described here in the Western and South Central USA were picked up on days with a warmer outdoor high, on average. For the 2020 pilot study, the outdoor highs on pickup day ranged from 9–34.8°C, with a median outdoor high of 21.4°C, and only 7/60 total samples (collected from 47 total participants) had an outdoor high on the pickup day >30°C [23]. In contrast, the median and range of the outdoor high on pickup day was higher for the present 2021 study, ranging between 25–43.4°C, with a median of 35.1°C. The RIN (Figure B5Aii) and total RNA yield (Figure B5Bii) from the 2020 and 2021 studies are plotted together with respect to outdoor high on pickup day in Figure A5. All but one of the samples where a RIN was obtained in our 2020 pilot study yielded a RIN ≥7.0; the one sample with a RIN <7 was evaluated to a RIN of 6.8 [23]. With regards to the relationship between the outdoor high and RIN in the present study, the three samples with the lowest RIN (RIN of 6.9) correspond to outdoor daily high temperatures ≥34°C; however, four other samples corresponding to outdoor daily high temperatures ≥35°C returned RIN values ≥7.0.

Although RIN values were indicated as the main performance metric in this study, we acknowledge that other performance metrics (e.g., total yield and RNA concentration) may be used concurrently to guide sample selection for downstream analysis. In longitudinal studies with multiple collection time points, extremely low yields either due to low blood volume or low circulating WBCs can lead to exclusion of specific time points in the longitudinal data series. These missing-at-random (MAR) samples can be problematic in longitudinal studies as they create unbalanced data and biased estimates [30]. However, additional statistical approaches such as time-course gene set analysis (TcGSA) can be used to account for such heterogeneity in the dataset [30].

In studies where sampling is done in high temperature climates and samples are susceptible to variable levels of temperature-induced degradation, it is crucial that initial analysis of the genes of interest is performed to determine how their transcript levels change with respect to post- stabilization temperature stress as degradation may not occur uniformly within the sample [29]. Prior to complete sample stabilization, multiple RNA decay pathways may influence rate of decay for distinct transcript sets [31]. In

such studies, alternative normalization strategies (e.g. using linear model framework to control for effects of RIN values) may be used to enable identification of biological meaningful expression signatures [29].

3.5 Conclusion

The ability to remotely collect and stabilize blood will expand future applications in the field of personalized medicine, particularly for analyzing blood transcriptomes that can give insight to disease progression/therapy response, immune response, and biomarker discovery. However, in order to establish the capability to do this, it is important to examine how exposure to various temperature conditions affects RNA stability. In this work, we conducted two small pilot studies to test the robustness of our *home*RNA at-home self-collection and stabilization blood kit to successfully preserve RNA integrity in high ambient temperature environments (>30°C) in two different study designs. These two pilot studies can inform clinical studies that could be run in places similar to Doha, Qatar (where samples are only exposed to short temperature spikes in transit) and the Western and South Central USA (where samples are in transit overnight given the regional nature of the study). We demonstrated that the majority of these blood samples yielded sufficient RIN (≥7.0), which suggests the usability of these samples for downstream transcriptome analyses. Important limitations of the present work include relatively small sample sizes, although we note that this work follows on our larger study with 47 participants across the USA. [23] Further, we have several ongoing clinical studies in the USA, with >1,000 samples collected over the past year; these studies will eventually add to the literature on the robustness of *home*RNA across the USA through different seasons. It is also important to study the performance of *home*RNA in tropical climates where samples will undergo longer transit times and longer periods of sustained high temperatures than those expected in Doha; to this end, we have ongoing studies utilizing *home*RNA in urban and rural Thailand. As *home*RNA is applied to diagnosis and monitoring of specific diseases, it will be important to analyze the expression of genes of interest that could be affected by elevated temperatures (i.e., transcriptional levels of inflammatory genes or disease- specific genes) using controlled in-lab experiments prior to personalized medicine applications. To our knowledge, this is the first study to establish use of *home*RNA in sampling regions experiencing

higher ambient temperatures, representing an initial validation study to extend the use of *home*RNA to warm environments.

3.6 Materials and methods

_home_RNA for the collection and stabilization of whole blood cellular RNA

***Design and assembly of home*RNA:** The fabrication of the RNA stabilizer tube as an interface to the Tasso-SST blood tube has been described previously [23]. Briefly, the RNA stabilizer tube was designed to hold the RNA*later*TM stabilization solution and connect to the Tasso-SST blood collection tube for remote self-blood collection and RNA stabilization. The Tasso-SST blood collection tube does not contain an anticoagulant. We previously showed that Tasso-SST-mediated capillary blood collection, despite not having an anticoagulant, did not result in major compromise of RNA quality as measured by RIN values [23]. At the time of the development of the *home*RNA kit, the Tasso-SST was the only commercially available Tasso product for collecting liquid samples; we note that we do not use the serum separator tube (SST) feature. The stabilizer tube was injection molded out of polycarbonate (PC: Makrolon 2407) by Protolabs, Inc (Maple Plain, MN). Details of the stabilizer tube components and design files can be found in Haack, Lim, et al. [23]. Prior to assembly of the stabilizer tube, all components were first cleaned via sonication in 70% ethanol (v/v) for 30 min and air dried. The stabilizer tube was filled with 1.3 ml RNA*later* (Thermo Fisher) stabilization solution and capped. The stabilizer tube insert was designed to hold the stabilizer tube containing blood in a 50 ml conical tube during transport. The insert also allows for facile centrifugation of the sample in the 50 ml standard conical tube when it arrives in a laboratory setting, as it centers and immobilizes the *home*RNA sample tube relative to the 50ml tube. The insert was injection molded out of polycarbonate (PC: Makrolon 2407) by Protolabs, Inc (Maple Plain, MN). All other components included in the *home*RNA blood kit and the Instruction for Use (IFU) are listed previously [23] and included in Appendix B of this chapter for easy reference. All kit components were placed in a rigid custom design mailer box fabricated via die-cutting (The BoxMaker, Inc.) [23].

High temperature fluctuations in *home*RNA collected samples: A small pilot study in Doha, Qatar

Participant recruitment and demographics: Healthy adult volunteers (18 years or older) were recruited in Doha, Qatar via word of mouth under a protocol approved by Sidra Medicine Institutional Review Board study number 1609004823. Written informed consent was obtained from all participants. In total, the study enrolled 8 participants between the ages of 29 and 53 (7 male and 1 female).

Temperature fluctuations of* home*RNA collected and stabilized blood samples: Participants were asked to collect and stabilize 1–2 whole blood samples using *home*RNA in a laboratory setting. The stabilizer vial containing the stabilized blood was placed in the 50ml conical tube with the insert provided in the *home*RNA kits (see design and assembly of *home*RNA above). Next the 50 ml tube containing the stabilized blood samples was placed in a sealed bag (provided in the kit) inside the *home*RNA cardboard package, and then incubated at ambient temperature (21°C) for 27 h to simulate the amount of time that might pass between blood collection at home and a scheduled pickup time from a courier service. Samples 1a (from participant 1 who was sampled twice) and 2 were frozen at −80°C after incubation at ambient room temperature for 27 h. The remaining 6 samples, after 27 h incubation at ambient temperature, underwent 3h of exposure to cycling temperatures in air-conditioned, indoor, and outdoor environments to simulate shipping conditions of the *home*RNA kit from remote site to lab. Each sample was exposed to a low of 21°C and a high of 41°C (with the elevated temperatures occurring as brief temperature spikes, see Table A1 and rationale for this temperature exposure/study design provided in the Results and Discussion) over the course of 27–30h after blood collection and stabilization.

***home*RNA collection during summer months: A small pilot study in the Western and South Central USA**

Participant recruitment and demographics: Healthy adult volunteers (18 years or older) were recruited from US states that historically experience wildfire smoke (i.e., the Western USA) via word of mouth under a protocol approved by University of Washington Institutional Review Board (STUDY00012463). 11 participants between the ages of 20 and 56 years old were enrolled (4 male and 7 female) and collected samples used in this study. Note: these samples were collected as part of a larger ongoing study our research

group is performing to investigate the effects of wildfire smoke exposure on inflammation. These 12 samples (from 11 participants) were chosen to capture a range of temperatures including the warmest temperatures experienced by our participants in summer 2021. Written informed consent was obtained from all participants. Participants were located in 7 states, including California, Nevada, New Mexico, Texas, Oregon, Washington, and Wyoming. Samples were collected between June and July of 2021, including samples (n = 2) that were collected during the June 2021 heat wave in the Pacific Northwest.

***Participant blood self-collection and stabilization**:* Participants were asked to self-collect and stabilize blood from their upper arm using the *home*RNA blood collection and stabilization kit. Each participant was also asked to complete a survey with each collection that included information about the ambient temperature during collection and the approximate blood level (see Figure B6). Participants were asked to package their stabilized blood samples to be returned to the lab for analysis using the provided return mailer bag (per instructions including containment in a 50 ml conical tube, plastic bag, and the *home*RNA kit cardboard box). Participants left their sample outside for pickup between the hours of 12:00 PM and 3:00 PM. All stabilized blood samples were mailed using next day delivery courier services (United Parcel Service, UPS). Returned samples were delivered to a −20°C freezer and subsequently stored at −80°C prior to RNA extraction.

***Temperature data collection**:* Participants were provided with a temperature monitor (ThermPro) and were asked to record the temperature at the time of sampling to obtain the indoor temperature data (Figure 3.3Bi). We collected the maximum temperature from the day the sample was picked up as the outdoor high on pickup day (Figure 3.3Bii). Temperature data was obtained from the daily high reported from the closest weather station on the day of the pickup. The weather station data was obtained from Weather Underground.

RNA isolation and assessment of RNA integrity from *home*RNA-stabilized whole blood

RNA isolation: For both small pilot studies in Doha, Qatar and the Western and South Central USA, total cellular RNA was isolated using the RibopureTM - Blood RNA Isolation Kit (Thermo Fisher) according to manufacturer's protocol and eluted in two 50 µl aliquots. Prior to removing the stabilized blood from the

collection tube, the 50 ml conical tube holding the *home*RNA device was briefly centrifuged 10 s at 50 g. Isolated RNA was stored at −80°C until ready for further analysis.

Assessment of yield and RNA integrity of total cellular RNA in the Western and South Central USA: For the pilot study in the USA, RIN values of the first 50 µl elution were obtained on a Bioanalyzer 2100 (Agilent). The Agilent 2100 Bioanalyzer uses proprietary, built-in software to calculate RIN values, which is based on the relative peak height and shape of the 18S and 28S rRNA fragments in the resulting electropherogram after separation. All samples were assessed using the RNA 6000 Nano Kit. Samples with returned concentrations below the quantitative range (<25 ng/µl) of the RNA 6000 Nano Kit were further analyzed using the RNA 6000 Pico kit. For these low concentration samples, only values provided by the Pico kit were used in the data analysis. Samples 9–11 had sufficient RNA concentration to be within the quantitative range of the RNA 6000 Nano Kit (25–500 ng/µl), whereas RNA concentration from the first elution from samples 1–8 were below this threshold and were therefore diluted 1:5 with nuclease free water to be within the quantitative range for the RNA 6000 Pico Kit (50–5,000 pg/µl). RNA concentration was measured for both isolated RNA aliquots using a Cytation 5 Multi-Mode Reader (Agilent Biotek Instruments) with a Take3 Micro-Volume Plate at the wavelengths of 260, 280, and 320 nm (Figure B4).

Assessment of yield and RNA integrity of total cellular RNA in Qatar: For the pilot study in Qatar, RNA integrity number (RIN) values and RNA concentration of the first 50 µl elution were obtained on a Bioanalyzer 2100 (Agilent) using the RNA 6000 Nano Kit (Agilent) for all samples. For samples analyzed in Qatar, additional assays on the Pico kit were not performed on samples with concentrations below the qualitative range of the Nano kit. The bioanalyzer was used to obtain the RNA concentration from the first 50 µl elution of the RNA isolation protocol (Figure B2).

3.7 References

1. Mohr, S. & Liew, C.-C. The peripheral-blood transcriptome: new insights into disease and risk assessment. *Trends in Molecular Medicine* **13**, 422–432 (2007).
2. Chaussabel, D. Assessment of immune status using blood transcriptomics and potential implications for global health. *Seminars in Immunology* **27**, 58–66 (2015).
3. Heidecker, B. & Hare, J. M. The use of transcriptomic biomarkers for personalized medicine. *Heart Failure Reviews* **12**, 1–11 (2007).

4. Runne, H. *et al.* Analysis of potential transcriptomic biomarkers for Huntington's disease in peripheral blood. *Proceedings of the National Academy of Sciences* **104**, 14424–14429 (2007).
5. Li, C.-x. *et al.* Whole-Transcriptome RNA Sequencing Reveals Significant Differentially Expressed mRNAs, miRNAs, and lncRNAs and Related Regulating Biological Pathways in the Peripheral Blood of COVID-19 Patients. *Mediators of Inflammation* **2021**, 1–22 (2021).
6. Liew, C.-C., Ma, J., Tang, H.-C., Zheng, R. & Dempsey, A. A. The peripheral blood transcriptome dynamically reflects system wide biology: a potential diagnostic tool. *Journal of Laboratory and Clinical Medicine* **147**, 126–132 (2006).
7. Byron, S. A., Van Keuren-Jensen, K. R., Engelthaler, D. M., Carpten, J. D. & Craig, D. W. Translating RNA sequencing into clinical diagnostics: opportunities and challenges. *Nature Reviews Genetics* **17**, 257–271 (2016).
8. Toma, R. *et al.* A Clinically Validated Human Capillary Blood Transcriptome Test For Global Systems Biology Studies. *BioTechniques* **69**, 289–301 (2020).
9. Ahmad, T., Fiuzat, M., Felker, G. M. & O'Connor, C. Novel biomarkers in chronic heart failure. *Nature Reviews Cardiology* **9**, 347–359 (2012).
10. Yang, I. V. *et al.* The Peripheral Blood Transcriptome Identifies the Presence and Extent of Disease in Idiopathic Pulmonary Fibrosis. *PLoS ONE* **7**, e37708 (2012).
11. Burbelo, P. D., Iadarola, M. J., Alevizos, I. & Sapio, M. R. Transcriptomic Segregation of Human Autoantigens Useful for the Diagnosis of Autoimmune Diseases. *Molecular Diagnosis & Therapy* **20**, 415–427 (2016).
12. Mesko, B., Poliska, S. & Nagy, L. Gene expression profiles in peripheral blood for the diagnosis of autoimmune diseases. *Trends in Molecular Medicine* **17**, 223–233 (2011).
13. Bayaa, R. *et al.* Multi-country evaluation of RISK6, a 6-gene blood transcriptomic signature, for tuberculosis diagnosis and treatment monitoring. *Scientific Reports* **11**, 13646 (2021).
14. Martinez, P. & Zemore, S. E. Feasibility of a mail-in, self-administered dried blood spot collection method in national, population-based alcohol surveys in the United States. *Addiction* **114**, 1303–1308 (2019).
15. Hicks, J. *et al.* Serologic Cross-Reactivity of SARS-CoV-2 with Endemic and Seasonal Betacoronaviruses. *Journal of Clinical Immunology* **41**, 906–913 (2021).
16. Li, K., Naviaux, J. C., Monk, J. M., Wang, L. & Naviaux, R. K. Improved Dried Blood Spot-Based Metabolomics: A Targeted, Broad-Spectrum, Single-Injection Method. *Metabolites* **10**, 82 (2020).
17. Catala, A., Culp-Hill, R., Nemkov, T. & D'Alessandro, A. Quantitative metabolomics comparison of traditional blood draws and TAP capillary blood collection. *Metabolomics* **14**, 100 (2018).
18. Blicharz, T. M. *et al.* Microneedle-based device for the one-step painless collection of capillary blood samples. *Nature Biomedical Engineering* **2**, 151–157 (2018).
19. Fedoruk, M. N. Virtual Drug Testing: Redefining Sample Collection in a Global Pandemic. *Bioanalysis* **12**, 715–718 (2020).
20. Vusirikala, A. *et al.* Seroprevalence of SARS-CoV-2 antibodies in university students: Crosssectional study, December 2020, England. *Journal of Infection* **83**, 104–111 (2021).
21. Williams, K. J., Lutman, J., McCaughey, C. & Fischer, S. K. Assessment of Low Volume Sampling Technologies: Utility in Nonclinical and Clinical Studies. *Bioanalysis* **13**, 679–691 (2021).
22. Tenhunen, J. Hydrolysis of single-stranded RNA in aqueous solutions—effect on quantitative hybridizations. *Molecular and Cellular Probes* **3**, 391–396 (1989).

23. Haack, A. J. *et al. home* RNA: A Self-Sampling Kit for the Collection of Peripheral Blood and Stabilization of RNA. *Analytical Chemistry* **93**, 13196–13203 (2021).
24. Huang, L.-H. *et al.* The effects of storage temperature and duration of blood samples on DNA and RNA qualities. *PLOS ONE* **12**, e0184692 (2017).
25. Duale, N. *et al.* Long-term storage of blood RNA collected in RNA stabilizing Tempus tubes in a large biobank – evaluation of RNA quality and stability. *BMC Research Notes* **7**, 633 (2014).
26. Shen, Y. *et al.* Impact of RNA integrity and blood sample storage conditions on the gene expression analysis. *OncoTargets and Therapy* **Volume 11**, 3573–3581 (2018).
27. Schroeder, A. *et al.* The RIN: an RNA integrity number for assigning integrity values to RNA measurements. *BMC Molecular Biology* **7**, 3 (2006).
28. Kukurba, K. R. & Montgomery, S. B. RNA Sequencing and Analysis. *Cold Spring Harbor Protocols* **2015**, pdb.top084970 (2015).
29. Gallego Romero, I., Pai, A. A., Tung, J. & Gilad, Y. RNA-seq: impact of RNA degradation on transcript quantification. *BMC Biology* **12**, 42 (2014).
30. Hejblum, B. P., Skinner, J. & Thi´ebaut, R. Time-Course Gene Set Analysis for Longitudinal Gene Expression Data. *PLOS Computational Biology* **11**, e1004310 (2015).
31. Tuck, A. C. *et al.* Mammalian RNA Decay Pathways are Highly Specialized and Widely Linked to Translation. *Moelcular Cell* **77**, 1222-1236, e13 (2020).

Chapter 4 │ Your Blood is Out for Delivery: Considerations of Shipping Time and Temperature on Degradation of RNA from Stabilized Whole Blood

Reproduced in part from F. Stefanovic, L.G. Brown*, J. MacDonald, T. Bammler, D. Rinchai, S. Nguyen, Y. Zeng, V. Shinkawa, K. Adams, D. Chaussabel, E. Berthier, A.J. Haack[#], and A.B. Theberge[#], "Your Blood is Out for Delivery: Considerations of Shipping Time and Temperature on Degradation of RNA from Stabilized Whole Blood." Anal Chem. 2025 Jan 28;97(3):1635-1644.*
** Equal contribution*
[#]Co-corresponding authors

FS, LGB, EB, AJH, and ABT contributed to the conception and design of the study. FS, LGB, SN, VS, and AJH conducted the experiments. FS, LGB, SN, YZ, and VS performed the RNA extractions on samples and collected the RIN and yield data. FS, LGB, JM, TB, DR, DC, EB, AJH, and ABT analyzed/interpreted the data. FS, LGB, DR, AJH, and ABT prepared the figures and wrote the manuscript. All authors contributed to the article and approved the submitted version.

Abstract: Remote research studies are an invaluable tool for reaching populations with limited access to large medical centers or universities. To expand the remote study toolkit, we previously developed homeRNA, which allows for at-home self-collection and stabilization of blood and demonstrated the feasibility of using homeRNA in high temperature climates. Here, we expand upon this work through a systematic study exploring the effects of high temperature on RNA integrity (represented as RNA Integrity Number, RIN) through in-lab and field experiments. Compared to the frozen controls (overall mean RIN of 8.2, n = 8), samples kept at 37°C for 2, 4, and 8 days had mean RINs of 7.6, 5.9, and 5.2 (n = 3), respectively, indicating that typical shipping conditions (~2 days) yield samples suitable for downstream RNA sequencing. Shorter time intervals (6 hours) resulted in minimal RNA degradation (median RIN of 6.4, n = 3) even at higher temperatures (50°C) compared to the frozen control (mean RIN of 7.8, n = 3). Additionally, we shipped homeRNA-stabilized blood from a single donor to 14 states and back during the summer with continuous temperature probes (7.1 median RIN, n = 42). Samples from all locations were analyzed with 3' mRNA-seq to assess differences in gene counts, with the data suggesting that there was no preferential degradation of transcripts as a result of different shipping times, temperatures, and regions. Overall, our data support that homeRNA can be used in elevated temperature conditions, enabling decentralized sample collection for telemedicine, global health, and clinical research.

4.1 Introduction

Remote self-sampling studies have become more prevalent in the wake of the COVID-19 pandemic; however, their utility goes far beyond the convenience of at-home sampling in a pandemic setting [1–5]. Fully remote studies circumvent many logistical barriers that preclude underserved and rural populations from participating in clinical research. These barriers include access to clinics or study sites that can perform blood draws, need for trained phlebotomists, suitable transportation, and sufficient time outside of typical work schedules. Additionally, remote sampling is compatible with collection of time-sensitive and longitudinal samples, making it an invaluable tool for human health research [6–11].

Devices for remote blood sampling (such as lancet-based devices from Tasso (Seattle, WA), YourBio Health (Medford, MA), etc.) offer a user-friendly way to self-collect blood samples. To enable analysis of many blood analytes, remote sample stabilization is necessary, particularly for whole blood RNA. Without stabilization, RNAses in whole blood can trigger intracellular RNA transcript degradation pathways ex vivo that can alter gene expression levels [12–15]. To address this aspect of RNA degradation, our lab has developed the homeRNA kit which consists of a commercially available Tasso-SST upper-arm blood collection device (which collects up to 0.5 mL of blood) and a custom-engineered stabilizer tube containing RNAlater [9]. RNAlater is a commercially available RNA stabilization agent commonly used with biological tissue samples that inhibits RNase activity and stabilizes cellular RNA [16–19]. In previous homeRNA studies, we have demonstrated that RNAlater effectively stabilizes self-collected blood and yields RNA of sufficient quality (represented by RNA Integrity Number, RIN) and quantity for downstream transcriptome analyses [9–11, 20]. In these studies, samples experience variable shipping times and often are not stored in the freezer until >48 h after collection. In ongoing work, we use homeRNA to study the inflammatory response to wildfire smoke exposure, which includes sampling during hot summer months across Western and Central U.S., and acute immune response to COVID-19 infection with nationwide sampling during all seasons [10, 11]. Since the US has vastly different climates depending on the time of year and location, it is important to consider how the shipping process may affect the integrity of RNA in remotely collected and stabilized blood samples. For example, our wildfire smoke exposure study took

place over a 10-month period (before, during, and after wildfire smoke exposure) and many samples were collected during the summer months. Further, we have previously conducted a preliminary examination of homeRNA in the Western and Central U.S. and Qatar with the goal of validating its utility in high temperature settings [20].

While the majority of samples collected in our previous and ongoing studies have sufficient RNA quality and yield for transcriptomic analysis, it is important to further investigate if transcripts are preferentially degraded and could bias the interpretation of these results. A potential concern based on past remote study experiences is that rural communities experience longer shipping times which could adversely affect RNA quality. Similarly, there is a concern that remote studies investigating immune response in tropical climates or during summer months could suffer from heat-induced RNA degradation.

The existing body of research has primarily investigated the effects of cold and ambient temperatures on RNA integrity prior to isolation from whole blood samples, as well as stability of RNA following extraction [21–24]. However, few studies to date have systematically investigated exposure of blood to high temperatures (>37°C) and its effect on the resulting isolated RNA quality; one study from Sarathkumara et al. investigated the effect of exposing Tempus- and PAXgene-stabilized blood samples up to 40°C and found a decrease in RIN with prolonged exposure (up to 10 days) [25]. Additionally, Heneghan et al. observed a 5-10 fold increase in the rate of RNA transcript degradation from dried blood spots stored at 37°C, suggesting that higher temperatures may compromise the integrity of the transcriptome in dried blood spots [26]. Drawing on our past experiences with homeRNA and remote studies, we designed a set of temperature-controlled experiments on RNAlater-stabilized whole blood samples exposed to temperatures up to 50°C for up to 8 days. Additionally, we conducted a real-world shipping experiment and sequenced a subset of these samples using 3’ mRNA sequencing (3’ mRNA-seq) to better understand how variable exposure to different temperatures and shipping times can affect the quality of the transcriptomic data. This work serves as a roadmap for developing future remote transcriptomic studies that take place in elevated temperatures (e.g., tropical climates, summer months) and lays the groundwork for understanding the role temperature degradation plays in the interpretation of these data.

4.2 Investigating RNA Integrity of RNAlater Stabilized Blood Samples in Temperature Controlled Experiments

To validate the utility of the homeRNA kit for preservation of RNA, we conducted a set of experiments to systematically probe the effects of storage conditions (time, temperature, repeat exposure). We chose times and temperatures to replicate scenarios similar to what samples would experience in a remote study conducted with the homeRNA platform [9-11, 20]. In a typical homeRNA study, participants are given instructions for self-collection and blood stabilization. Participants then package their stabilized samples for next- or same-day courier pickup. Many study participants opt to leave the samples on their front porch for a pickup window of 2 – 4 hours. Based on the location and time of year, samples may experience multiple hours outdoors in hot temperatures (>37℃). After pickup, packages typically take 1 – 2 days to be returned to the lab, depending on the participant's location; but in rare cases it has taken up to 2 weeks for a package to be returned [9]. Additionally, while in transit, samples may experience fluctuations in temperatures (e.g., prior to pickup, during transit, or in storage facilities) (Figure C2) that could affect the stability of the RNA and cause differential degradation of RNA transcripts. In this work, we aim to elucidate (1) if exposure to longer shipping times and higher temperatures results in increased degradation of RNA and (2) if the variable conditions in the shipping process result in preferential degradation of specific transcripts.

To model shipping times and temperatures that homeRNA samples may experience, we exposed RNAlater-stabilized venous blood samples to various temperatures (25℃, 37℃, 40℃, 45℃, or 50℃) and varying lengths of time (6 h, 1 day, 2 days, 4 days, or 8 days) in the lab. We place emphasis on the effects of higher temperature conditions (>37°C) since some of our ongoing homeRNA studies take place in hot climates or during the summer months. Remote studies can also take place in winter months or colder climates and may experience freezing with subsequent thawing prior to processing. Although some literature reports adverse effects of freeze-thaw cycles on RNA integrity from whole blood samples, we have found that RNAlater-stabilized whole blood samples are minimally affected by a freeze-thaw cycle (Figure C3) [21, 27, 28].

4.3 Longer Term (2, 4, and 8 day) Exposure to High Temperatures (>37°C)

Our first experiment was set up to understand the effect of "longer-term" exposure to various temperatures and storage times (2, 4, or 8 days) of the stabilized blood samples and the resulting effects on RNA integrity. These time points were chosen to recapitulate potential scenarios we have seen with homeRNA. While we have opted for overnight shipping with private companies (UPS, FedEx) to minimize time samples spend in transit, we recognize that these are not available to all researchers who may want to use the homeRNA platform. As such, the longer time points (4 and 8 days) are valuable for an array of scenarios where samples spend extended periods in transit such as overseas shipping, or shipping from rural areas. Additionally, we chose to hold the samples at steady temperatures to understand temperature-dependent degradation of RNA. For this experiment, we chose three conditions to represent three different scenarios: (condition 1) the sample is left out on the porch for pickup immediately after collection, (condition 2) the sample is kept in a fridge prior to being left on the porch for pickup, and (condition 3) the sample is kept indoors (not refrigerated) overnight prior to being left outside for pickup. All samples were stored at -20°C until being extracted, which is known to be stable for prolonged periods of time per the manufacturer's information.

RNA Integrity Number (RIN) is a common metric used to measure the quality of RNA samples; RIN values are found using Agilent's 2100 Bioanalyzer which calculates the RIN through a proprietary algorithm, taking into account the relative peak height and shape of the 18S and 28S ribosomal RNA subunits in a given sample, as well as other features of the resulting electropherograms [29, 30]. There are some discrepancies in the literature about a cutoff RIN value that is suitable for sequencing, with values of 7 or 8 often cited [14, 31–33]. However, newer sequencing technologies such as 3' mRNA-seq and post-sequencing computational processing methods make possible the sequencing of samples with RINs as low as 3 [14, 32, 34–36]. Our data show that increasing temperatures results in greater RNA degradation (lower RIN values) in RNAlater-stabilized blood samples as compared to samples immediately frozen after stabilization (Figure 4.1). Longer exposures resulted in additional degradation; for example, the mean RIN

for the 50°C condition changed from 5.5 to 4.0 to 1.8 for the samples at 2, 4, and 8 days, respectively. When incubated for two days at any temperature, all samples had RINs that were suitable for downstream transcriptomic analysis (from 7.9 at 25°C to 5.5 at 50°C). Although notable degradation was observed for samples that were kept at 45°C and 50°C for 8 days, it is also important to note that samples in a remote study will be subject to variable temperatures and not a constant exposure to the high temperatures over several days. For example, it is highly unlikely that a sample would be exposed to 8 days at 50°C, the highest and longest condition that we tested. Moreover, samples that were kept at 25°C had a mean RIN of at least 7 across all time points, suggesting that RNAlater-stabilized samples at lower temperatures undergo limited degradation even at longer time scales (up to 8 days). Further, samples in condition 2 (refrigerated prior to shipment) gave similar RIN values as samples in condition 3 (kept at room temperature overnight). Taken together, these results suggest that the additional refrigeration step prior to sample shipping is not strictly necessary.

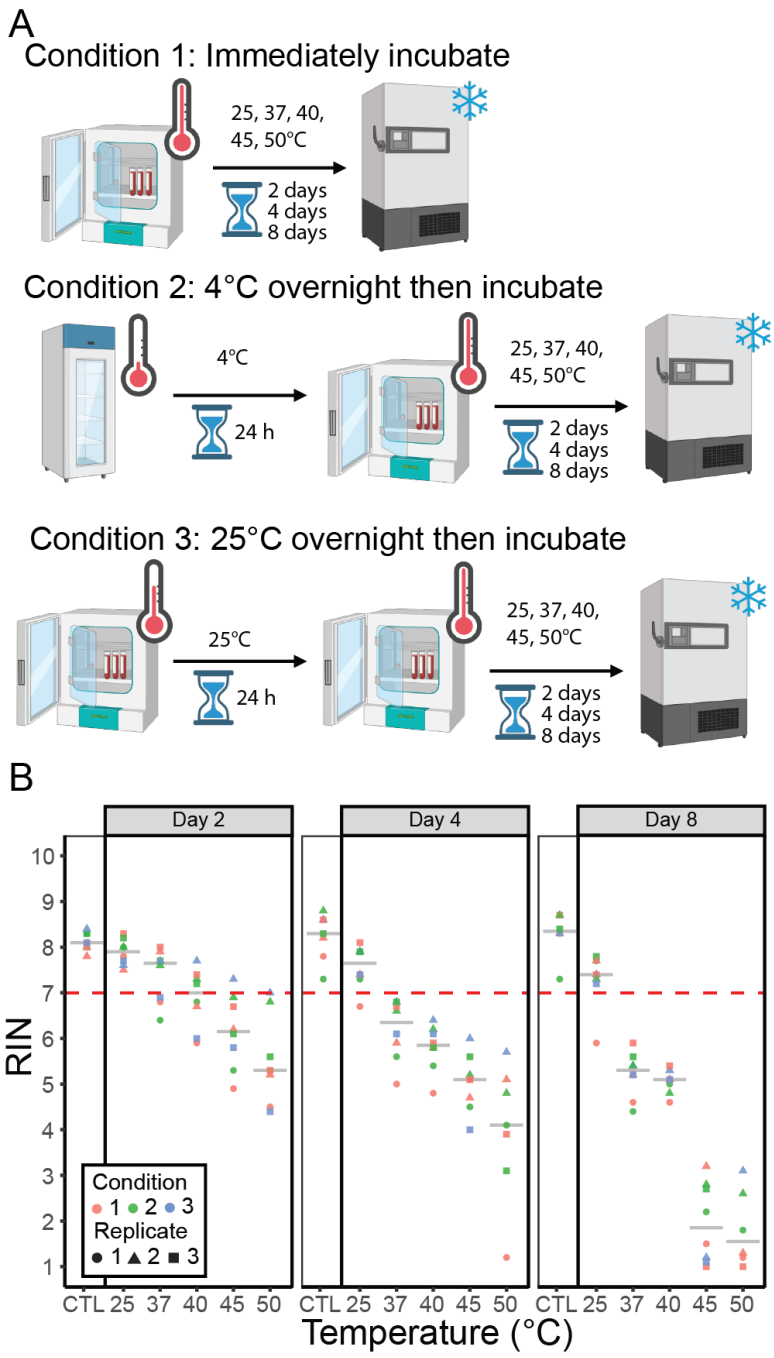

Figure 4.1. Exposure of RNAlater-stabilized whole blood samples to longer term (2, 4, and 8 day) high temperatures (>37°C). (A) Outline of experimental conditions. Condition 1, samples were immediately incubated at 25°C, 37°C, 40°C, 45°C, and 50°C for 2, 4, and 8 days. One sample was frozen at -20°C immediately after stabilizing with RNAlater; Condition 2, samples were incubated at 4°C for 24 hours then exposed to the same set of temperatures and times as condition 1. One sample was frozen at -20°C after incubation for 24 hours at 4°C; and condition 3, samples were incubated at 25°C for 24 hours prior to exposure to the same set of temperatures and times as condition 1. One sample was frozen at -20°C after incubation for 24 hours at 25°C. After each timepoint, one sample from every temperature was immediately frozen and kept at -20°C until ready for RNA extraction. Created with BioRender.com. (B) RNA quality of each extracted sample from each condition. For each condition, samples were extracted based on timepoints, resulting in three total extraction batches (day 2, 4, and 8) with 6 samples in each batch (condition control (CTL), 25°C, 37°C, 40°C, 45°C, and 50°C). Each condition was performed in triplicate. The gray crossbars signify the mean RIN at each time and temperature across all conditions and replicates.

4.4 Shorter Term (<2 days) Exposure to High Temperatures (>37°C)

Beyond investigating longer times samples may experience at high temperatures (>37°C) during shipping, we were also interested in shorter durations (within hours) of high temperature exposure. In homeRNA studies, participants will often opt to have the sample picked up by a courier service by leaving

the sample on their front porch. Depending on location and time of year, the sample may be exposed to very high temperatures for several hours.

To better mimic the conditions homeRNA samples may experience, we replicated conditions from different scenarios prior to shipment. All experimental samples were kept at room temperature (25°C) overnight (16 hours) to emulate a study participant collecting their sample and leaving it at home until pickup. After this initial incubation, the experimental samples were either frozen or exposed to the same set of temperatures established in our previous longer-term experiment (25°C, 37°C, 40°C, 45°C, and 50°C) for 6 hours. The samples that were frozen after incubation at room temperature overnight (Condition 1, Figure 4.2) represent degradation prior to pickup. We tested this condition because in many of our remote studies participants collect their samples the day before the pickup is scheduled, with the stabilized blood kept at room temperature overnight. The data show that there was effectively no difference between these samples and the control frozen at -20° immediately after stabilization, suggesting that there is little-to-no degradation of RNA during overnight ambient temperature storage in remote studies. The next set of samples were exposed to varying temperatures following the initial incubation for 6 hours (Condition 2, Figure 4.2). Samples from this condition simulate stabilized blood that sits at a participant's front door prior to pickup. The mean RIN scores ranged from 6.4 to 7.2 across the different temperatures and only one sample at 25°C yielded a RIN of 4.9 and one at 50°C had a RIN of 5.2. We include 25°C as one of the temperature conditions for incubation to capture study participants who either leave their sample to be picked up indoors in an apartment lounge or mail room or choose to drop their sample off at a UPS store. Finally, condition 3 had an additional overnight room temperature incubation as a representation of specimens that do not get picked up the day after sampling These samples matched closely to condition 2, further indicating that additional storage at room temperature (up to 38 hours) results in negligible degradation of RNA in homeRNA samples.

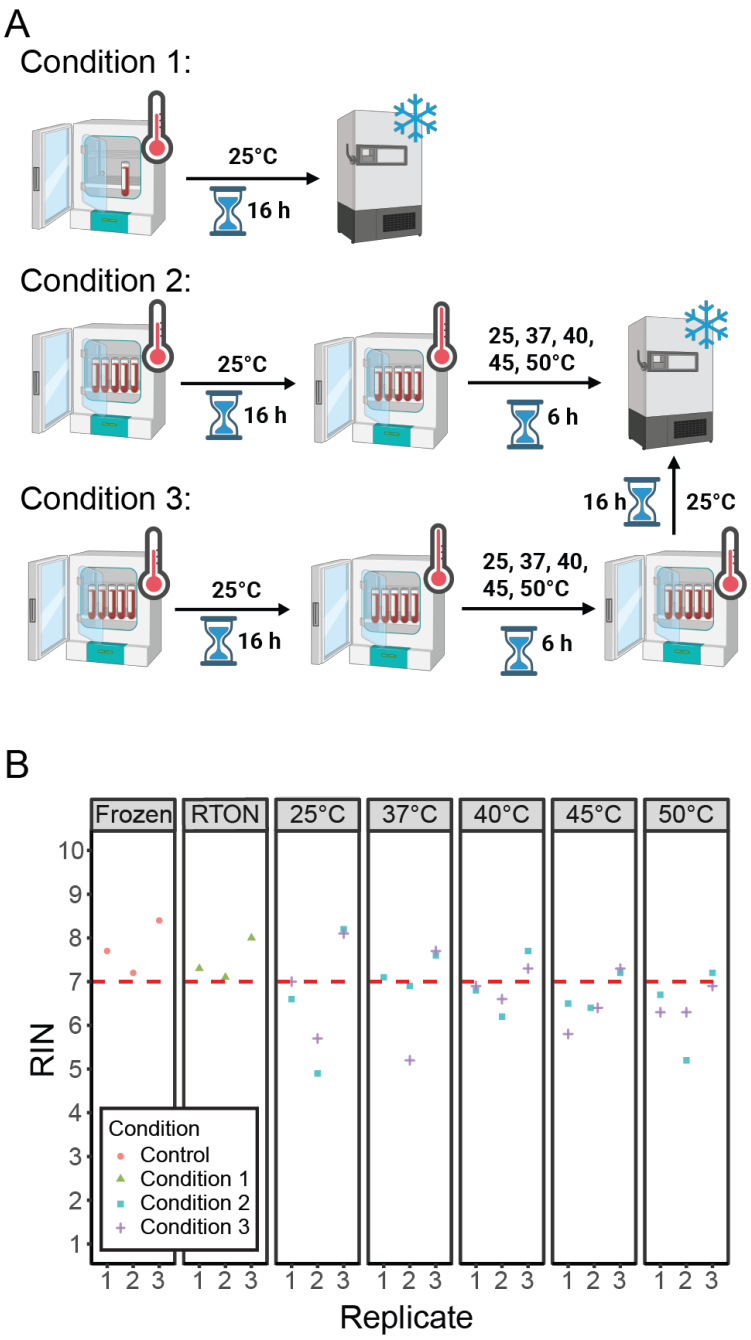

Figure 4.2. Exposure of RNAlater-stabilized whole blood samples to shorter term (<2 days) high temperatures (>37°C). (A) Outline of experimental conditions. One sample was frozen at -20°C immediately after stabilizing with RNAlater to be used as a baseline control. Condition 1 kept one sample at 25°C for 16 hours and then frozen at -20°C; this is referred to as room temperature overnight (RTON). Condition 2 incubated samples at 25°C for 16 hours and then exposed one sample each to 25°C, 37°C, 40°C, 45°C, and 50°C for 6 hours. Condition 3 incubated samples at 25°C for 16 hours and then exposed one sample each to 25°C, 37°C, 40°C, 45°C, and 50°C for 6 hours. After incubation at the different temperatures, all samples were incubated at 25°C for 16 hours then frozen at -20°C. Created with BioRender.com. (B) Resulting RNA quality of each extracted sample from each condition. Each condition was performed in triplicate. Amongst each replicate, all samples across all conditions were extracted in the same batch, resulting in an extraction batch with 12 samples (immediately frozen, one sample from condition 1, 5 samples from condition 2, and 5 samples from condition 3).

4.5 Shipping of RNAlater-Stabilized Blood Across United States with Continuous Temperature Monitoring

While the in-lab temperature-controlled experiments capture a large range of time scales, we were interested in monitoring continuous temperature fluctuations that would be experienced in real shipping conditions (e.g., packages moving from doorstep to shipping vehicle, samples moving between air-

conditioned areas to areas without air conditioning, etc.). To this end, we designed an experiment where blood aliquots from a single venous draw were stabilized using the homeRNA kit and shipped out to volunteers across 14 different states. These states are colored green in Figure 4.3A and include Washington (WA), New Mexico (NM), North Carolina (NC), Minnesota (MN), Maine (ME), Massachusetts (MA), Kansas (KS), Illinois (IL), Georgia (GA), Colorado (CO), California (CA), Arizona (AZ), Hawaii (HI), and Nebraska (NE). Samples were shipped during the summer in August of 2022. We aimed to include a diverse set of states reaching most regions of the U.S. including those located in regions with warm summers (HI, CA, AZ, GA, and NC). The locations include both urban and rural locations, reflected by the Rural-Urban Commuting Area (RUCA) codes (Table C1). Additionally, our samples were also shipped to an island in Hawaii, which requires longer shipping times to and from Seattle, Washington (location of study lab) than locations within the contiguous U.S.

Each package also included an Elitech RC-5+ continuous temperature probe (Figure C1) that recorded the temperature from the moment the samples were prepared for shipment in the lab, through the shipping process to the volunteer, to the samples being returned to our lab. These temperature data are plotted in Figure C2 and summarized in Table C1. The maximum temperature spike we observed was 45.1°C in the sample shipped to NE, which was the most rural of our shipping locations (highest RUCA score) and took 7 days to be returned to the lab. Although HI did not have as high of a RUCA score, the samples shipped to this location took the longest to return to the lab (8 days). Most shipping locations (10 out of the 14 states) took 3 days to return to the lab.

Further, the RIN values from different locations followed a similar trend as the stabilized blood in the temperature-controlled experiments, where longer times and exposure to higher temperatures resulted in lower RIN values. Notably, AZ, NE, and HI had the lowest mean RINs (6.1, 5.5, and 6.2, respectively) and were the locations that took the longest to be returned to the lab. In addition, all three of these states reached temperatures greater than 40°C and spent the longest time above 30°C, with the samples sent to NE spending 55 h above 30°C. Conversely, locations such as CA had similar exposure to a maximum temperature of 44.4°C but had a RIN of 7.0. Even though the maximum temperatures were the same, the

longer times in transit and higher median temperatures are the likely causes for the lower RIN from the NE samples.

It is also worth noting that long-term storage at room temperature results in some RNA degradation. The In-Lab sample, which was kept in a 25ºC incubator for the duration of the experiment (8 days), exhibited RINs similar to those of AZ, HI, and NE (that took 7 – 8 days to return). The In-Lab sample also had lower RINs than the other samples from shipped locations (e.g., WA, NM, NC, MN) that were returned within 4 days. This result indicates that RNAlater-stabilized blood samples will undergo some RNA degradation even at room temperature after prolonged periods of time and also that short-term temperature spikes do not markedly affect RIN.

In the context of remote studies, the data obtained from the real-world shipping experiment is both encouraging and informative. Even the most degraded sample (NE, RIN = 5.5) had RNA of sufficient quality for 3'RNA sequencing (see 3' mRNA-seq section below). Additionally, all samples were shipped in two directions (to the participant and back to the lab), whereas samples collected in remote studies using homeRNA are only shipped from the participants back to the lab. As such, we expect less degradation to occur in other homeRNA studies since the samples will only be shipped in one direction.

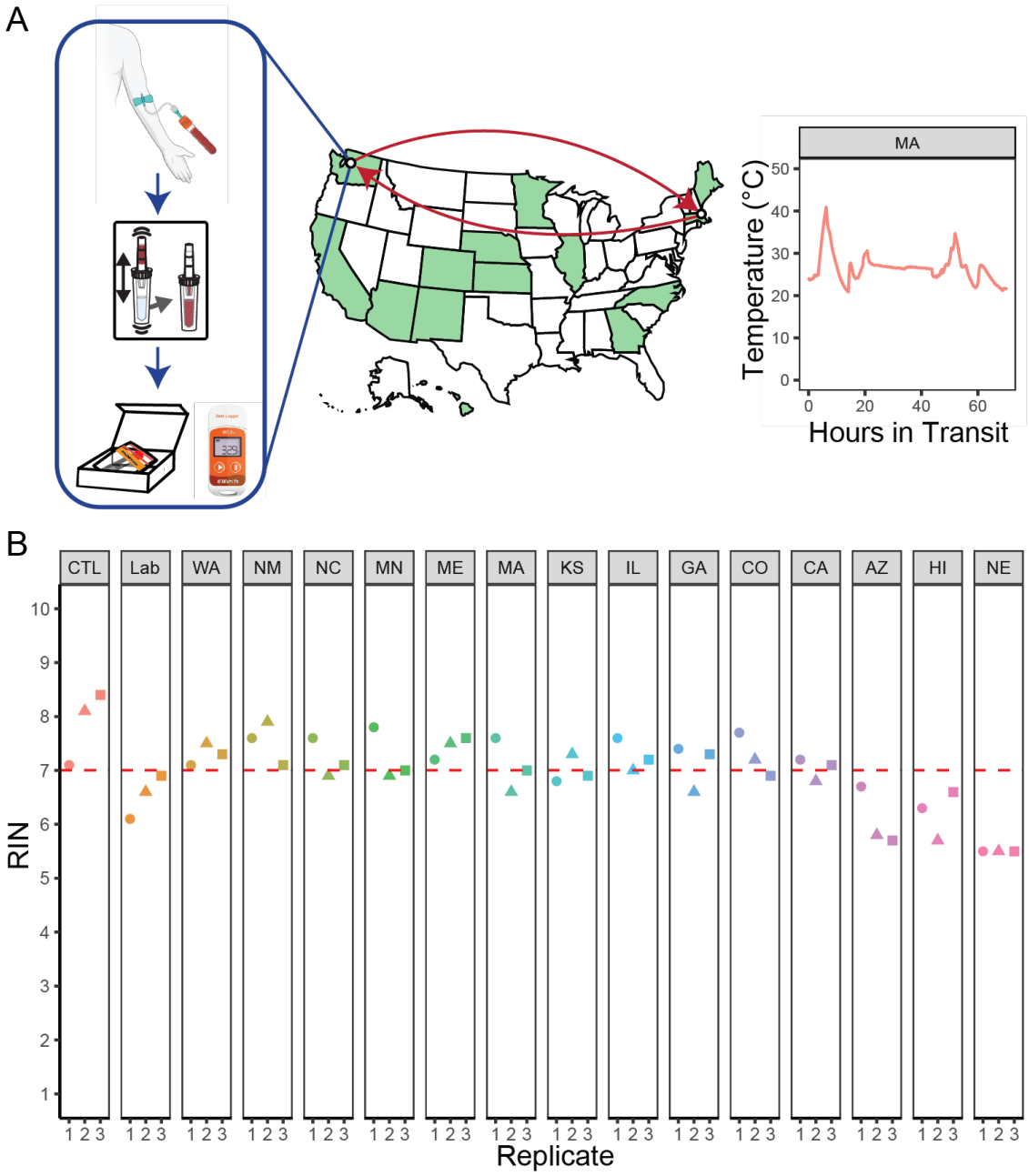

Figure 4.3. All samples across different shipping locations had RINs suitable for RNA sequencing. (A) Blood from a venous draw from a single participant was aliquoted into the Tasso blood collection tube and stabilized using the homeRNA kit in triplicates and shipped to 14 different U.S. states. The homeRNA kits were packaged as in our other homeRNA studies within a cardboard box and mailer bag, and a continuous temperature probe was directly attached to the samples [9–11, 20]. Once returned to the lab, the samples were kept frozen until ready for further processing. The RNA was extracted from the blood and tested for integrity. Created with BioRender.com. (B) The resulting RINs are plotted categorized by shipping location. The twoletter abbreviations in the figure correspond to U.S. state abbreviations (see text above). The shape of the data point (circle, triangle, square) corresponds to the extraction batch. Control condition (CTL) was immediately frozen after stabilization, while the in-lab condition (Lab) was kept in a 25°C incubator until frozen at -20°C at the time the last sample (Hawaii, HI) was received (8 days).

4.6 3' mRNA Sequencing of Real-World Shipping Experiment

Finally, we look for selective degradation of RNA fragments from 3'mRNA-seq data. Since all samples in the shipping experiment came from a single blood draw, we can assume that any differences in the measured transcriptome can be attributed to shipping-related degradation. To probe this question further, we selected 20 samples to perform 3' mRNA-seq analysis, including all samples from extraction batch 3. Additionally, we chose to sequence all three control samples to establish a baseline as well as all three samples from the location with the most degraded samples (NE).

Our first approach is to reference the sequencing data of the samples against a well-characterized immune response signature from the BloodGen3 module repertoire [37, 38]. Each BloodGen3 module consists of a set of genes ranging from 12 to 169 with an average of 37.1 genes per module; these modules have been previously associated with responses to immune-modifying therapies or pathogenic processes [37]. By calculating enrichment scores (which summarizes the prevalence of a given gene in a module) using the gene set variation analysis (GSVA) method for each of the 382 modules across all samples, we aimed to break down the results and provide a more granular understanding of the immune response landscape [39]. Principal component analysis (PCA) of these scores revealed minimal clustering patterns based on shipping location (Figure 4.4A), indicating a lack of significant variability within the shipped samples. While the In-Lab samples (kept at 25ºC incubator for the duration of the experiment, 8 days) did exhibit some clustering, the Control sample (immediately frozen) clustered with the rest of the shipping locations. It is possible that the clustering of the In-Lab samples can be attributed to the fact that they experienced no temperature fluctuations nor agitation (Figure C2B). However, it is important to note that the overall variability captured by the PC1 is only 16.25% and PC2 is 8.97% and that the distribution of the points is relatively tight. The proximity of the Control to the rest of the samples also indicates that there is very little variability arising from the shipping process. The heatmap visualization of enrichment scores across various modules and samples (Figure 4.4B) and the focused analysis of three key module groups (module aggregates A28, A35, and A37, corresponding to interferon, inflammation and circulating erythroid cells signatures, respectively) (Figure 4.4C) further supported this observation, with only minor

variations in enrichment scores across individual samples. These findings highlight the relative homogeneity of our samples and indicate little variation depending on the sample location.

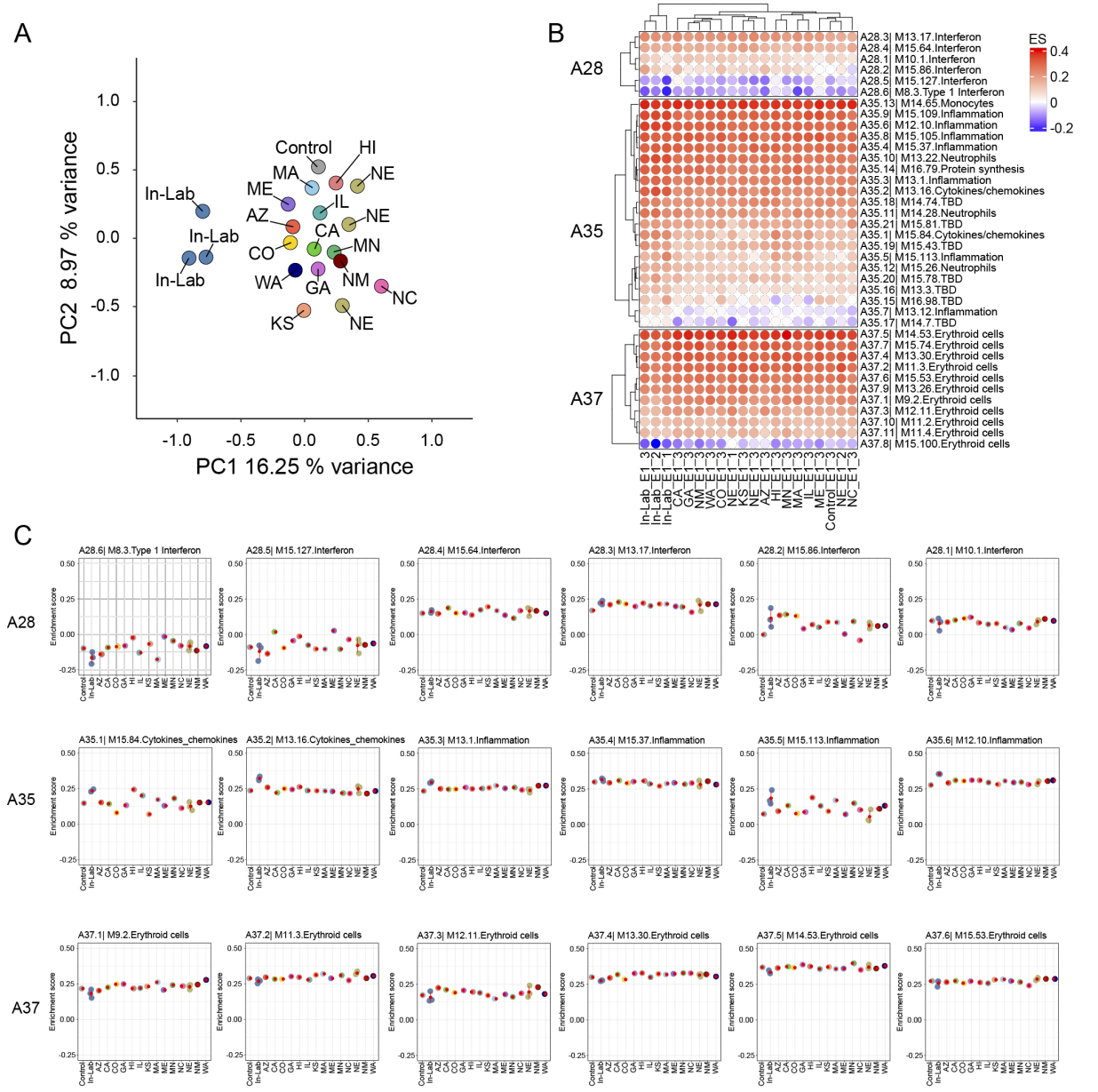

Figure 4.4. Analysis of Module Enrichment Scores in Samples. (A) PCA of sample data by location. This PCA plot provides a visualization of the data variance, with each point representing a sample's projection on the two principal components labeled based on sample condition (shipping location, control (frozen immediately), or in-lab sample (stored at 25°C for 8 days)). (B) Heatmap of enrichment scores across conditions. Enrichment scores for various biological modules are depicted in a heatmap format, with rows representing different modules (e.g., interferon response, inflammation) and columns representing individual samples. The color gradient indicates the level of enrichment from decreased (blue) to increased (red). (C) Detailed module enrichment scores for groups A28, A35, and A37. The dot plots show the enrichment scores for selected modules within the three groups. Individual sample scores are plotted on the x-axis against their corresponding enrichment score on the y-axis.

Further, to contextualize the observed variation in gene expression in our samples, we include results from a previously published COVAX study, which investigated the immune response to COVID-19 mRNA vaccine [42]. By comparing the enrichment scores of six interferon response modules (M8.3, M10.1, M13.17, M15.64, M15.86, and M15.127, comprised in the module aggregate A28) at different timepoints before and after vaccination, we can observe the differences in signal variability occurring due to a well-controlled biological signal. The dot plot in the supporting information (Figure C4) demonstrates a clear increase in interferon module enrichment scores following vaccination, with peak responses observed at days 2 and 3. This distinct pattern of vaccine-induced immune activation serves as a reference point for interpreting the variability observed in our samples (labeled as UW in Figure C4). Assuming that the stabilized blood exhibits minimal DNA transcription ex vivo, any large difference in transcript counts can be attributed to degradation during the shipping process. The tight clustering of our samples compared to the large differences in the COVAX data suggests that the variability introduced by temperature exposure during shipping is much smaller in magnitude than the changes induced by a biological signal, such as an immune response elicited by vaccination. Taken together, this indicates that there is minimal RNA degradation of homeRNA-stabilized samples owing to variable exposure to temperature and shipping times. We performed additional analyses that confirmed that there was minimal differential degradation barring two genes (MMP9 and ADGRG3, Figure B5). We also considered how time in transit and time spent above 30ºC impact RIN (Figures C6 and C7) and found minimal effects on RNA integrity (see Supplementary Text in Appendix C for more details).

In summary, based on our 3’ mRNA-seq dataset, there is little evidence that differences in shipping conditions result in consistent changes in the measured mRNA expression levels in blood RNA from a single donor. We expect that samples in other remote studies using homeRNA that have similar RINs will also exhibit negligible transcript-specific degradation from variable shipping conditions as measured by 3’ mRNA-seq. It is important to note that traditional RNA-seq methods may yield different results owing to differences in read depth and genes detected. Further work is needed to conclusively determine if the

homeRNA system is completely resilient to preferential degradation of transcripts when exposed to variable shipping conditions, however, the current work shows promising results.

4.7 Conclusion

We expand upon existing literature on RNA stability in cold storage conditions and dried blood spots by investigating the effects of variable time and temperature exposure on RNAlater-stabilized samples, with a systematic study on the effects of high temperature exposure and shipping time on liquid blood samples. In the temperature-controlled experiments, we found that longer storage times (4 and 8 days) at high temperatures (>37°C) resulted in lower RIN values, while shorter exposures (<6 hours) to high temperatures resulted in minimal RNA degradation. We also used homeRNA-stabilized blood samples in a real-world shipping experiment. All shipped samples were sequenced using Lexogen's QuantSeq 3' mRNA technology, with minimal differences in the transcriptome measured.

This study illustrates the utility of the homeRNA platform in high temperature settings. It also serves as a guide for other researchers who aim to conduct remote sampling studies that use RNA as a readout and rely on shipping via courier service for sample retrieval. Our findings strongly suggest that there is limited preferential degradation of transcripts in the shipping process and, as such, give us confidence in interpreting transcriptomic data from homeRNA-stabilized whole blood samples. These results will inform ongoing homeRNA studies and will be critical for future study design. Future work will use larger sample sizes, longer read depth sequencing such as total RNA-seq to further substantiate these findings, and work in low- and middle-income countries (LMICs) with different courier methods and climates.

4.8 Materials and methods

Participant Recruitment and Demographics

Healthy adult volunteers (18 years or older) were recruited in Seattle, Washington via word of mouth under a protocol approved by the University of Washington Institutional Review Board study number STUDY00014133. Written informed consent was obtained from all participants.

Investigating RNA Integrity of RNAlater-Stabilized Blood Samples in Temperature Controlled Experiments

Exposure to Longer Term (2, 4, and 8 days) High Temperatures (>37°C): A venous blood draw was performed and promptly stabilized with RNAlater at the manufacturer's recommended ratio (2.6 mL RNAlater per 1 mL blood). For the first biological replicate, blood was acquired via venipuncture from Bloodworks and stabilized within 1-2 hours. For the second and third replicate, blood was collected via venipuncture in lab under study number STUDY00014133. After stabilization with RNAlater, the stabilized blood was aliquoted in 1.8 mL samples to replicate the maximum volume of homeRNA (0.5 mL blood and 1.3 mL RNAlater). After stabilization, each sample was stored according to the following conditions: (1) immediately incubated at set temperatures (25°C, 37°C, 40°C, 45°C, and 50°C) for 2, 4, and 8 days, (2) kept at 4°C for 24 hours then incubated at set temperatures (25°C, 37°C, 40°C, 45°C, 50°C) for 2, 4, and 8 days, and (3) kept at 25°C for 24 hours then incubated at set temperatures (25°C, 37°C, 40°C, 45°C, 50°C) for 2, 4, and 8 days. Each condition had a corresponding control: (1) frozen immediately at -20°C, (2) incubated at 4°C for 24 hours then frozen at -20°C, (3) incubated at 25°C for 24 h then frozen at -20°C. One sample at each temperature and condition was removed after 2, 4, and 8 days such that there was a single replicate for each temperature and condition on each day of removal. At these timepoints, the blood was moved from the incubators to the -20°C freezer until ready for RNA isolation. For each condition, RNA from the stabilized blood samples was extracted based on timepoints, resulting in three total extraction batches based on day removed after high temperature exposure (day 2, 4, and 8) with six samples in each batch (condition control, 25°C, 37°C, 40°C, 45°C, and 50°C). The experiment was repeated two more times for a total of three replicates from two donors (replicate 2 and 3 from the same donor, with the blood drawn on separate days).

Exposure to Shorter Term (<2 days) High Temperatures (>37°C): A venous blood draw was performed in lab under study number STUDY00014133 and promptly stabilized with RNAlater at the manufacturer's recommended ratio (2.6 mL RNAlater per 1 mL blood). The stabilized blood was then aliquoted to 1.8 mL samples. One sample was immediately frozen at -20°C as the control. The rest of the samples were then treated according to the following conditions: (1) one sample kept at room temperature (25°C) overnight (16 h), then frozen (-20°C), (2) five samples kept at room temperature (25°C) overnight (16 h), moved to

incubators of corresponding temperatures (25℃, 37℃, 40℃, 45℃, 50℃) for 6 h, then frozen (-20℃), (3) five samples kept at room temperature (25℃) overnight (16 h), moved to incubators of corresponding temperatures (25℃, 37℃, 40℃, 45℃, 50℃) for 6 h, moved back to room temp (25℃) for 24 h, then frozen (-20℃). This resulted in a total of one replicate for each temperature and condition combination. The stabilized blood samples were stored at -20℃ until ready for RNA isolation and assessment. All 12 samples from each replicate were extracted in one batch. The experiment was repeated two more times for a total of three replicates from three separate blood draws from one donor.

Effects of a Freeze-Thaw Cycle on RNA Stability: For this experiment, blood from a venous blood draw is stabilized using RNAlater according to manufacturer instructions. The blood is then aliquoted into 9 samples which are separated into three conditions: (1) control which is immediately frozen, (2) room temperature (25°C) for 24 h (room temperature overnight, RTON) then frozen, and (3) freeze-thaw (FT) where the samples were frozen immediately after stabilization for 24 h, then kept at room temperature for 24 h before being frozen again. The samples were frozen at -20°C for the duration of the experiment then moved to -80°C until further processing. The experiment was performed two more times for a total of three replicates. Once the RNA was extracted the samples were tested for RNA integrity using the Agilent 2100 Bioanalyzer.

Investigating RNA Integrity of RNAlater-Stabilized Blood Samples in Real World Setting with homeRNA

Shipping of RNAlater-Stabilized Blood Across United States with Continuous Temperature Monitoring:

A venous blood draw was performed in the lab under study number STUDY00014133. The blood sample was aliquoted into 48 Tasso-SST tubes at 0.5 mL each. The blood was then stabilized by attaching the Tasso-SST tubes to a custom-designed stabilizer tube with 1.3 mL RNAlater and shaken to mimic blood stabilization in homeRNA kits. The remaining blood was stabilized in bulk (2.6 mL RNA later per 1 mL blood), aliquoted into 1.8 mL samples, and immediately frozen at -20℃ as controls. The 48 homeRNA-stabilized samples were then placed in 50 mL conical tubes fitted with custom adapters as described in Haack et al. [9]. The 50 mL tubes were then adhered together using tape in sets of three such that three

technical replicates would be sent to each shipped location. Each set had an RC-5+ continuous temperature monitor (Elitech) directly attached with lab tape (see Figure B1A), with temperatures being recorded every 2 minutes.

These constructs were then placed in a biohazard bag and into the box used for homeRNA kits (see Haack et al., 2021) prior to being packaged into a UPS LabPak. The full setup is shown in Figure C1. The complete packages were shipped to volunteers in 14 different states across the United States via UPS. The states included: Washington (WA), New Mexico (NM), North Carolina (NC), Minnesota (MN), Maine (ME), Massachusetts (MA), Kansas (KS), Illinois (IL), Georgia (GA), Colorado (CO), California (CA), Arizona (AZ), Hawaii (HI), and Nebraska (NE). One additional package was kept in a 25°C incubator (In-Lab/Lab). Upon delivery, the volunteers were instructed to keep the packages inside overnight at room temperature and adhere the return labels to the package. For pickup, most volunteers left the package outside on the front porch, two volunteers left the package indoors in a mailroom, and one volunteer directly handed the package to the UPS courier. Most samples were picked up within 1 – 2 days from the volunteer and shipped back to the lab. Shipping return times ranged from overnight to 4 days after pickup. Upon return to the lab, the packages were immediately placed into a -20°C freezer. Once all the packages were returned, the samples that were kept in the lab in a 25°C incubator were also frozen at -20°C. All samples were stored at -20°C until ready for RNA isolation. RNA was extracted from all shipped homeRNA-stabilized blood samples in three extraction batches, with one technical replicate from each shipping location and in-lab baseline samples (immediately frozen and constant 25°C sample), resulting in 16 samples extracted in each batch.

Visualization of Temperature Over Time Across Shipping Locations: The data from the temperature probe directly attached to the samples is assumed to have readings closest to the "true" temperature the samples would experience in transit and only the data from this probe are visualized and used for downstream analysis. Since the temperature probes were not stopped until all packages arrived, the data needed to be filtered prior to graphing. The data were filtered using the R dplyr package such that the time did not exceed 200 hours (close to the maximum time for the last sample returned to lab) and was above 10°C given that

the lowest temperature reading prior to being frozen was closer to 20°C for all samples. The temperature was then plotted against time (hours) to illustrate the variability in shipping process and temperature fluctuations.

RNA Isolation and Assessment of total cellular RNA integrity and yield

For all samples, total cellular RNA was isolated using the Ribopure Blood RNA Isolation Kit (Thermo Fisher) according to manufacturer's protocol and eluted in two 50 µl aliquots. Isolated RNA was stored at -80°C until ready for further analysis. RNA Integrity number (RIN) values were obtained on a Bioanalyzer 2100 (Agilent) from the first 50 µl elution. The Agilent 2100 Bioanalyzer uses proprietary, built-in software to calculate RIN values, which is based on the relative peak height and shape of the 18S and 28S rRNA fragments in the resulting electropherogram after separation. All samples were assessed using the RNA 6000 Nano Kit (Agilent). For the in lab temperature-controlled experiments, RNA concentration was measured from the first 50 µl elution aliquot using a Cytation 5 Multi-Mode Reader (Agilent Biotek Instruments) with a Take3 Micro-Volume Plate at the wavelengths of 260, 280, and 320 nm. For the field experiments, RNA concentration was measured from the first 50 µl elution using a Qubit 4 Fluorometer using the RNA High Sensitivity (HS) Assay kit (Invitrogen).

RNA Sequencing and Analysis

3' mRNA-seq of Real-World Shipping Experiment: After isolation the samples were tested for RIN scores on the Agilent 2100 Bioanalyzer (see Assessment of total cellular RNA integrity and yield section above and Figure C8 for resulting electropherograms). A 100 ng of total RNA from 20 selected samples were sequenced by the Lexogen facility (Vienna, Austria) using 3' mRNA-sequencing technology (Lexogen QuantSeq 3' mRNA-seq V2 Library Prep Kit FWD with UDI) on an Illumina NextSeq 2000 instrument according to the manufacturers' standard instructions. The 16 samples from the third batch were selected for sequencing as the third batch had the greatest proportion of the median RIN values amongst the three replicates from each location. Additionally, all three replicates from the baseline sample (frozen immediately after stabilization) and all three replicates from the location with the lowest RIN (NE, mean RIN of 5.5) were sent for sequencing. In total, 20 samples (16 from batch 3, 2 additional from NE, 2

additional from In-Lab) were sent for 3' mRNA sequencing. Prior to library preparation, all samples were treated with Ambion DNase I (Invitrogen) for 10 minutes at 37°C followed by heat inactivation with EDTA at 75C for 10 minutes. Libraries were prepared using 17 ng of RNA as input. Libraries were amplified for 18 cycles and were quality controlled on a Fragment Analyzer device using the DNF-474 HS NGS Fragment kit (1-6000 bp) (Agilent). The samples were sequenced to a read depth of 5 million reads.

Transcriptomic Analysis of Individual Gene Expression Counts: Summarized counts/genes were imported into R and analyzed using the limma-voom pipeline, which uses conventional weighted linear regression to model the data [40]. The matrix of gene counts was filtered to remove those genes with consistently low expression, and then converted to log counts/million counts, using estimated library sizes calculated using the trimmed mean of M-values (TMM) method [41]. The logCPM values have a dependence between the mean and variance which is estimated as part of the limma-voom pipeline and used to estimate observation-level weights. These weights are used as part of the weighted line regression to adjust for heteroskedasticity. We fit a model that includes time ¿30°C for each sample, the RIN (to adjust for RNA quality), and five surrogate variables computed using the Bioconductor sva package. The surrogate variables are intended to adjust for unobserved variability and have been shown to increase power to detect differences [43]. We then tested for any apparent changes in gene expression that correlate with exposure to high temperatures.

Module Enrichment Score Calculation: Enrichment scores were calculated using the gene set variation analysis (GSVA) method for each of the 382 transcriptional modules from the BloodGen3 repertoire across all samples [37–39].

Principal Component Analysis: Principal component analysis (PCA) was performed on the module enrichment scores to visualize the variance among samples, labeled by their condition (shipping location, in-lab sample, or control).

Heatmap Visualization: Module enrichment scores were represented in a heatmap format, with rows corresponding to different modules associated with biological processes such as interferon response and

inflammation, and columns representing individual samples. The color gradient of the heatmap indicates the level of enrichment, ranging from decreased (blue) to increased (red).

Dot Plot Visualization: For a more detailed analysis, we focused on specific module groups (A28, A35, and A37) and plotted their enrichment scores using dot plots. The x-axis represents individual samples, while the y-axis denotes the corresponding enrichment score for each sample within the selected modules.

Interferon Response Kinetics Analysis: We used data from the COVAX study (Rinchai et al [42]), to illustrate the kinetics of six interferon response modules (M8.3, M10.1, M13.17, M15.64, M15.86, and M15.127) at different timepoints before and after administration of COVID-19 mRNA vaccine [42]. Enrichment scores for these modules were plotted for each sample across the various timepoints.

4.9 References

1. Maass, K. F. *et al.* Leveraging patient-centric sampling for clinical drug development and decentralized clinical trials: Promise to reality. *Clinical and Translational Science* **15**, 2785–2795 (2022).
2. Harahap, Y., Diptasaadya, R. & Purwanto, D. J. Volumetric Absorptive Microsampling as a Sampling Alternative in Clinical Trials and Therapeutic Drug Monitoring During the COVID19 Pandemic: A Review. *Drug Design, Development and Therapy* **14**, 5757–5771 (2020).
3. Fuller, G. *et al.* Feasibility of Patient-Centric Remote Dried Blood Sampling: The Prediction, Risk, and Evaluation of Major Adverse Cardiac Events (PREMACE) Study. *Biodemography and Social Biology* **65**, 313–322 (2020).
4. Weiner, M. W. *et al.* Increasing participant diversity in AD research: Plans for digital screening, blood testing, and a community-engaged approach in the Alzheimer's Disease Neuroimaging Initiative 4. *Alzheimer's & Dementia* **19**, 307–317 (2023).
5. Koulman, A. *et al.* The development, validation and application of remote blood sample collection in telehealth programmes. *Journal of Telemedicine and Telecare* **30**, 731–738 (2024).
6. Buck Louis, G. M. *et al.* Designing prospective cohort studies for assessing reproductive and developmental toxicity during sensitive windows of human reproduction and development – the LIFE Study. *Paediatric and Perinatal Epidemiology* **25**, 413–424 (2011).
7. Garcia-Beltran, W. F. *et al.* Remote Fingerstick Blood Collection for Severe Acute Respiratory Syndrome Coronavirus 2 (SARS-CoV-2) Antibody Testing. *Archives of Pathology & Laboratory Medicine* **145**, 415–418 (2020).
8. Laven-Law, G. *et al.* Hot Mail: Temperature Exposure during Mail Return of an Immunochemical Fecal Occult Blood Test. *Clinical Chemistry* **69**, 615–626 (2023).
9. Haack, A. J. *et al.* homeRNA: A Self-Sampling Kit for the Collection of Peripheral Blood and Stabilization of RNA. *Analytical Chemistry* **93**, 13196–13203 (2021).
10. Lim, F. Y. *et al.* Longitudinal home self-collection of capillary blood using homeRNA correlates interferon and innate viral defense pathways with SARS-CoV-2 viral clearance (2023).
11. Lim, F. Y. *et al.* homeRNA self-blood collection by exposed close contacts enables high-frequency temporal profiling of the pre-symptomatic host immune kinetics to respiratory viral infection (2023).
12. Donohue, D. E. *et al.* Gene expression profiling of whole blood: A comparative assessment of RNA-stabilizing collection methods. *PLOS ONE* **14**, e0223065 (2019).

13. Opitz, L. *et al.* Impact of RNA degradation on gene expression profiling. *BMC Medical Genomics* **3**, 36 (2010).
14. Gallego Romero, I., Pai, A. A., Tung, J. & Gilad, Y. RNA-seq: impact of RNA degradation on transcript quantification. *BMC Biology* **12**, 42 (2014).
15. Houseley, J. & Tollervey, D. The Many Pathways of RNA Degradation. *Cell* **136**, 763–776 (2009).
16. Micke, P. *et al.* Biobanking of fresh frozen tissue: RNA is stable in nonfixed surgical specimens. *Laboratory Investigation* **86**, 202–211 (2006).
17. Florell, S. R. *et al.* Preservation of RNA for Functional Genomic Studies: A Multidisciplinary Tumor Bank Protocol. *Modern Pathology* **14**, 116–128 (2001).
18. Chowdary, D. *et al.* Prognostic gene expression signatures can be measured in tissues collected in RNAlater preservative. *The Journal of molecular diagnostics: JMD* **8**, 31–39 (2006).
19. Kruse, C. P. S., Basu, P., Luesse, D. R. & Wyatt, S. E. Transcriptome and proteome responses in RNAlater preserved tissue of Arabidopsis thaliana. *PLOS ONE* **12**, e0175943 (2017).
20. Brown, L. G. *et al.* At-home blood collection and stabilization in high temperature climates using homeRNA. *Frontiers in Digital Health* **4**, 903153 (2022).
21. Huang, L.-H. *et al.* The effects of storage temperature and duration of blood samples on DNA and RNA qualities. *PLOS ONE* **12**, e0184692 (2017).
22. Das, K. *et al.* Stabilization of Cellular RNA in Blood During Storage at Room Temperature: A Comparison of Cell-Free RNA BCT® with K3EDTA Tubes. *Molecular Diagnosis & Therapy* **18**, 647–653 (2014).
23. Tsui, N. B., Ng, E. K. & Lo, Y. D. Stability of Endogenous and Added RNA in Blood Specimens, Serum, and Plasma. *Clinical Chemistry* **48**, 1647–1653 (2002).
24. Kim, S. J. *et al.* Effects of Storage, RNA Extraction, Genechip Type, and Donor Sex on Gene Expression Profiling of Human Whole Blood. *Clinical Chemistry* **53**, 1038–1045 (2007).
25. Sarathkumara, Y. D. *et al.* The Effect of Tropical Temperatures on the Quality of RNA Extracted from Stabilized Whole-Blood Samples. *International Journal of Molecular Sciences* **23**, 10609 (2022).
26. Heneghan, N., Fu, J., Pritchard, J., Payton, M. & Allen, R. W. The effect of environmental conditions on the rate of RNA degradation in dried blood stains. *Forensic Science International: Genetics* **51**, 102456 (2021).
27. Beekman, J. M. *et al.* Recovery of microarray-quality RNA from frozen EDTA blood samples. *Journal of Pharmacological and Toxicological Methods* **59**, 44–49 (2009).
28. Muth, D. C., Powell, B. H., Zhao, Z. & Witwer, K. W. miRNAs in platelet-poor blood plasma and purified RNA are highly stable: a confirmatory study. *BMC Research Notes* **11**, 273 (2018).
29. Mueller, O., Lightfoot, S. & Schroeder, A. RNA integrity number (RIN)–standardization of RNA quality control. (2016).
30. Schroeder, A. *et al.* The RIN: an RNA integrity number for assigning integrity values to RNA measurements. *BMC Molecular Biology* **7**, 3 (2006).
31. Jahn, C. E., Charkowski, A. O. & Willis, D. K. Evaluation of isolation methods and RNA integrity for bacterial RNA quantitation. *Journal of Microbiological Methods* **75**, 318–324 (2008).
32. Sigurgeirsson, B., Emanuelsson, O. & Lundeberg, J. Sequencing Degraded RNA Addressed by 3' Tag Counting. *PLoS ONE* **9**, e91851 (2014).
33. Hitzemann, R. *et al.* Genes, behavior and next-generation RNA sequencing. *Genes, Brain and Behavior* **12**, 1–12 (2013).
34. Puchta, M., Boczkowska, M. & Groszyk, J. Low RIN Value for RNA-Seq Library Construction from Long-Term Stored Seeds: A Case Study of Barley Seeds. *Genes* **11**, 1190 (2020).
35. Johnson, M. T. J. *et al.* Evaluating Methods for Isolating Total RNA and Predicting the Success of Sequencing Phylogenetically Diverse Plant Transcriptomes. *PLOS ONE* **7**, e50226 (2012).
36. Li, S. *et al.* Multi-platform assessment of transcriptome profiling using RNA-seq in the ABRF next-generation sequencing study. *Nature Biotechnology* **32**, 915–925 (2014).
37. Altman, M. C. *et al.* Development of a fixed module repertoire for the analysis and interpretation of blood transcriptome data. *Nature Communications* **12**, 4385 (2021).

38. Rinchai, D. *et al.* BloodGen3Module: blood transcriptional module repertoire analysis and visualization using R. *Bioinformatics* **37**, 2382–2389 (2021).
39. H¨anzelmann, S., Castelo, R. & Guinney, J. GSVA: gene set variation analysis for microarray and RNA-Seq data. *BMC Bioinformatics* **14**, 7 (2013).
40. Law, C. W., Chen, Y., Shi, W. & Smyth, G. K. voom: precision weights unlock linear model analysis tools for RNA-seq read counts. *Genome Biology* **15**, R29 (2014).
41. Robinson, M. D. & Oshlack, A. A scaling normalization method for differential expression analysis of RNA-seq data. *Genome Biology* **11**, R25 (2010).
42. Rinchai, D. *et al.* High–temporal resolution profiling reveals distinct immune trajectories following the first and second doses of COVID-19 mRNA vaccines. *Science Advances* **8**, eabp9961 (2022).
43. Leek, J. T. & Storey, J. D. Capturing Heterogeneity in Gene Expression Studies by Surrogate Variable Analysis. PLOS Genetics 3, e161 (2007).

Chapter 5 | From Home to Transcriptome: Comparing the transcriptomic profile of induced immune response via lipopolysaccharide stimulation in homeRNA and venous blood

Reproduced in part from Lauren G. Brown, Xiaofu Wei, Laura A. Milton, M. Yunos Alizai, James W. MacDonald, Theo K. Bammler, Yuting Zeng, Ingrid H. Robertson, Karen N. Adams, Damien Chaussabel, Erwin Berthier, Amanda J. Haack[#], and Ashleigh B. Theberge[#], "From Home to Transcriptome: Comparing the transcriptomic profile of induced immune response via lipopolysaccharide stimulation in homeRNA and venous blood" In preparation.
[#]Co-corresponding authors

LGB, YZ, DC, EB, AJH, and ABT contributed to the conception and design of the study. IHR and KNA assisted with the human subject portion of this study. LGB conducted the experiments, performed the RNA extractions, and prepared all samples for sequencing. LGB, XW, LAM, MYA, JWM, TKB, EB, AJH, and ABT analyzed/interpreted the data. LGB, XW, LAM, MYA, AJH, and ABT prepared the figures and wrote the manuscript.

Abstract: Remote blood sampling offers multiple advantages over traditional clinic-based blood sampling studies, including greater patient inclusion, more frequent sampling, and broader geographical reach. Combining remote blood sampling with transcriptomic analysis opens potential in translational applications for capturing acute and dynamic immune responses to various exposures. In this study, we establish the feasibility of homeRNA, a capillary blood collection and RNA*later*-based stabilization kit, for use in downstream bulk RNA-sequencing applications via capturing a lipopolysaccharide (LPS)-induced inflammatory response. We also compared the baseline gene expression profiles and induced inflammatory response following LPS stimulation between homeRNA-stabilized samples and venous blood stabilized with RNA*later* or PAXgene. We found that homeRNA was successfully able to capture an inflammatory response to LPS, specifically targeting various cytokines (e.g., *IL6, IL12B, IL1B*), chemokines (e.g., *CCL3, CXCL10, CCL4*), and other transcriptional factors in the toll-like receptor pathway, the primary pathway activated during LPS stimulation. Importantly, we also found that homeRNA captured a LPS-induced inflammatory response comparable to that of venous blood samples stabilized with either RNA*later* or PAXgene. Overall, this work demonstrates that the homeRNA platform is compatible with downstream bulk RNA-sequencing analysis and can capture transcriptomic immune responses to a known stimulus which are analogous to results in traditional stabilized venous blood samples.

5.1 Introduction

The convergence of remote blood sampling technologies and transcriptomic analyses enables large-scale, longitudinal gene expression studies that capture transient immune responses outside of the constraints of clinical settings. By eliminating the need for centralized clinic locations and trained phlebotomy staff, remote blood sampling not only increases geographical sampling locations, but also facilitates greater inclusion of participants who would otherwise be excluded due to logistical or personal constraints[1–5]. Further, with a remote study design, researchers can track immune responses to real-world exposures and collect frequent longitudinal samples without the burden of repeated clinic visits[6,7].

Among the various molecular readouts possible from blood samples, RNA expression profiling is of particular value for capturing dynamic immune responses[8–10]. However, the inherent instability of whole blood RNA presents a significant challenge for *ex vivo* transcriptomic profiling; endogenous RNases can activate degradation pathways that compromise the integrity of intracellular transcripts, which can alter gene expression levels[11,12]. Therefore, studies that do not include immediate extraction of RNA from collected blood samples require a method of RNA stabilization. In clinic-based studies, commercially available RNA stabilization solutions such as PAXgene® and Tempus™ are commonly used; these solutions can come packaged in vacutainer tubes which make it easy to directly collect blood into the stabilizer solution from a phlebotomy draw. RNA*later*™ is another available stabilization solution which has been used to stabilize RNA in both blood and tissue samples[13,14].

The need for RNA stabilization becomes even more critical when samples must be collected remotely and shipped to centralized laboratories. A commonly used method for remote sampling is dried blood spot (DBS)-based sampling, which typically uses a lancet on a fingertip to collect a drop of blood on a piece of paper[15,16]. DBS sampling relies on the drying of the blood sample to stabilize RNA. Many studies have successfully used RNA-sequencing on DBS samples[17–19], but there is no standardized protocol for processing RNA from these samples[20–22] and a pre-amplification step is often required prior to sequencing due to low RNA yield[17,23,24]. To increase RNA yield from remotely collected blood, there have been additional blood collection devices that utilize a lancet that collects blood from the upper arm (e.g., Tasso,

YourBio)[25,26]. These collection methods will typically draw up to 1 mL of blood, which is incompatible with drying, so liquid stabilization is required to preserve RNA integrity in transit.

To address this need, we developed the homeRNA kit, an at-home blood self-collection and RNA stabilization kit that uses the commercially available Tasso-SST device, an upper-arm blood collection device, and a custom stabilizer tube containing RNA*later*[27]. Blood samples collected with homeRNA have demonstrated sufficient RNA integrity number (RIN) value cutoffs for typical requirements for RNA sequencing analysis, suggesting that homeRNA allows for sufficient stabilization during the remote self-sampling, user-stabilization, and shipping processes[27]. Further, we demonstrated that homeRNA was robust during the shipping process (i.e., shipping time and exposure to high temperatures), in which we found negligible effects on subsequent gene expression using 3' mRNA-sequencing[28,29]. Critically, we also demonstrated that homeRNA can effectively capture a biological immune response to SARS-CoV-2 using a targeted Nanostring gene panel[6,30].

In this work, we demonstrate the applicability of homeRNA to detect a biological response with bulk RNA-sequencing transcriptomic analysis to build on our prior work with 3' mRNA-sequencing[29] and Nanostring analysis[6,30]. Specifically, we are interested in leveraging the larger read depth of bulk RNA-sequencing technologies in comparison to that of 3' mRNA-sequencing and Nanostring analysis to investigate gene expression signatures in homeRNA-collected samples and standard phlebotomy blood draws. In this study, we measure an induced immune response to lipopolysaccharide (LPS)—a well established immune stimulation model[31–33]—in homeRNA-collected and stabilized blood compared to RNA*later*-stabilized or PAXgene-stabilized venous blood. By comparing the gene expression profiles between homeRNA-stabilized capillary blood and traditional phlebotomy-drawn venous blood, this study establishes the compatibility of homeRNA with bulk RNA-sequencing technologies and demonstrates that homeRNA can capture a LPS-induced inflammatory response similar to that of venous blood. This study aims to provide critical guidance for researchers implementing homeRNA-based remote blood collection in studies investigating immune activation.

5.2 Comparison of LPS-induced gene expression across homeRNA and venous blood collection methods

In this study, we sought to assess the ability of the homeRNA kit to capture a biological response through bulk RNA-sequencing methods. To accomplish this, we induced a known biological response via bacterial lipopolysaccharide (LPS) stimulation, a well-established immune *ex vivo* whole blood stimulation model that activates a targeted inflammatory response[31–33]. To further establish homeRNA as a remote sampling tool that can be used to probe transcriptomic immune responses, we also compared the LPS-stimulated response of homeRNA-stabilized samples to that of RNA*later*-stabilized or PAXgene-stabilized venous blood. These stabilizers were chosen as RNA*later* is the stabilizer used in homeRNA, allowing for direct comparison of homeRNA-collected and stabilized samples with phlebotomy drawn and stabilized blood. PAXgene was chosen as it is a commonly used stabilization solution for clinic-based phlebotomy draws since it comes already packaged in vacutainer tubes. To properly compare these different collection and stabilization methods with a LPS-stimulated response, we designed an experiment where venous blood (via phlebotomy draw) and capillary blood (using the lancet-based Tasso-SST included in the homeRNA kit that draws blood from the upper arm) were collected from a participant during the same visit. All collected blood samples (Tasso-collected blood and phlebotomy-drawn blood) were either stimulated with 100 ng/mL LPS or left unstimulated prior to stabilization (Figure 5.1A). Venous blood samples were stabilized with either RNA*later* or PAXgene (Figure 5.1A). Tasso-collected blood samples were stabilized by attaching the Tasso tube to a custom engineered stabilizer tube containing RNA*later* and shaking per the instructions of the homeRNA kit (Figure 5.1A)[6,27–30].

First, to illustrate the overall gene expression response of the three different collection and stabilization methods, we generated a heatmap of differentially expressed genes associated with response to LPS (Figure 5.1B). The heatmap reveals that all three collection/stabilization methods captured the expected changes in gene expression following LPS stimulation, with clear differential up-regulation and down-regulation of genes in response to LPS. However, some donor-to-donor variability is evident, particularly within donor 3 in the homeRNA and Venous PAXgene samples (Figure 5.1B). This variability likely reflects a combination of biological differences in individual immune responses to LPS stimulation,

technical variations inherent to each collection and stabilization protocol, and in the case of homeRNA, potential differences between capillary and venous blood composition. Despite this donor variability, a differential LPS-induced response is still observed across the different collection and stabilization methods.

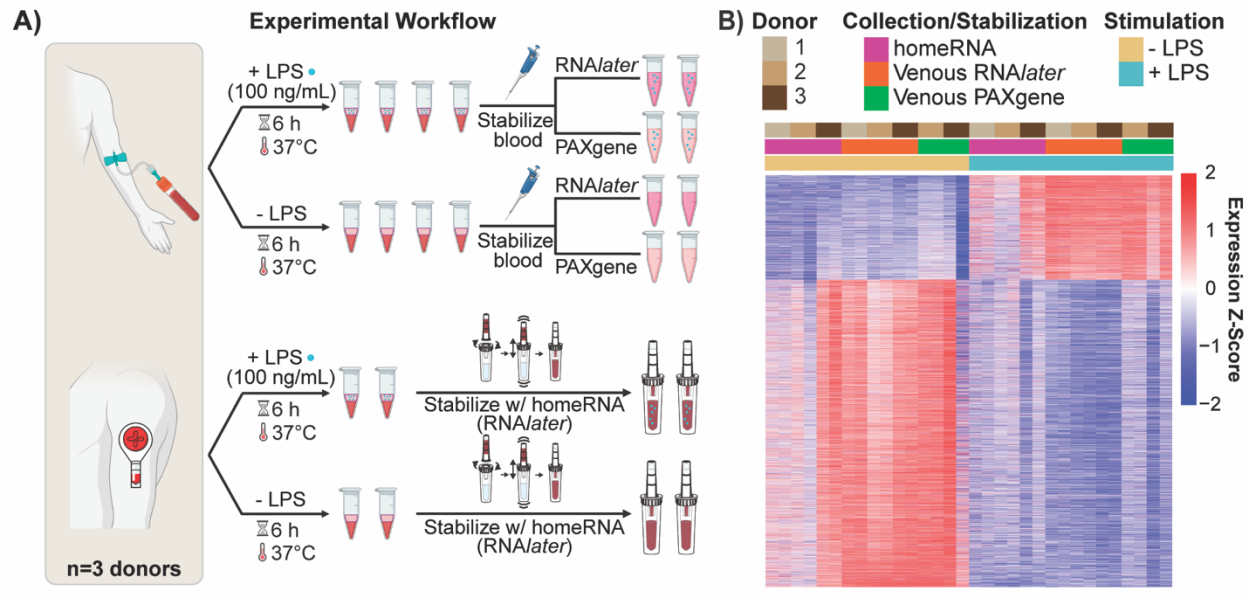

Figure 5.1. Comparison of response to lipopolysaccharide (LPS) in venous blood and homeRNA-stabilized blood. A) Workflow of stimulating blood with LPS in venous blood and Tasso-collected blood. Each donor (n=3 donors) had blood drawn from a phlebotomy draw and from the upper arm using the Tasso-SST device on the same day. The blood samples were then aliquoted and incubated in media supplemented with 100 ng/mL LPS or in control media (without LPS). After incubation, blood samples collected from the Tasso device were then stabilized with homeRNA, and blood samples collected from the phlebotomy draw were stabilized with either RNAlater or PAXgene. Created using Biorender.com. B) Unsupervised heatmap of differentially expressed genes (30% change in expression, FDR $\leq$ 0.05) between LPS-stimulated and unstimulated blood samples across different collection and stabilization methods after removing the batch effect from different donors. Each column represents an individual sample (each donor had two replicates), and each row represents a gene (7777 genes in total). The homeRNA and Venous RNAlater samples had three donors (n=6 samples) and Venous PAXgene had two donors (n=4 samples). Colors represent standardized expression values (z-scores) for each gene across all samples, with red indicating higher expression and blue indicating lower expression relative to each gene's mean across all experimental conditions.

5.3 homeRNA captured LPS-induced biological response

We next interrogated the ability of homeRNA to capture an induced biological response via LPS stimulation. We identified 943 differentially expressed genes (DEGs) with LPS stimulation in the homeRNA-stabilized samples. Figure 5.2A summarizes the identified DEGs, with the top 10 most significantly up- and down-regulated genes in response to LPS stimulation in Tasso-collected and

homeRNA-stabilized blood samples labeled. A number of these genes are associated with inflammatory responses and have been shown previously to be expressed in LPS-stimulated blood. These genes include: *IL6* and *IL12B*, both of which are cytokines activated downstream of LPS-induced toll-like receptor 4 (TLR4) pathway[42,43]; *IL36G* and *CSF3*, cytokines present in regulating innate inflammatory responses mediated by IL-1 and IL-6, respectively[44–47]; and *CFB* and *ACOD1*, which are regulators in LPS-activated immune response pathways[48,49].

Further, gene ontology enrichment analysis was performed to identify the top six biological processes and the top 10 overrepresented genes within each process (Figure 5.2B). These top gene ontology (GO)-derived biological processes are related to defense responses to pathogens, peptides, and other stimuli. Overrepresentation of these biological processes is expected as LPS is a molecule present on the surface of gram-negative bacteria and thus stimulates a host-like response. Notably, cytokines (*IL6*, *IL36G*, *IL12B*), complement components (*CFB*), and chemokines (*CCL3*, *CXCL10*) were strongly linked to immune defense pathways, suggesting an overall innate immune activation due to LPS.

Lastly, we further interrogated the alterations in gene expression related to the toll-like receptor signaling (Figure 5.2C). Toll-like receptor signaling is the primary pathway activated in an LPS response; LPS binds TLR4 in immune cells, transducing signals across the plasma membrane[50]. TLR4 activation then initiates key downstream inflammatory pathways including mitogen-activated protein kinase (MAPK) signalling and nuclear factor kappa (NF-kB) signalling, resulting in an inflammatory response[51–53]. When we probed the toll-like receptor signaling pathway, we observed an upregulation in cytokines (*IL6*, *IL12B*, *IL1B*, and *TNF*), chemokines (*CXCL10*, *CCL3*, *CCL3L1*, *CCL4*, *CCL4L1*, *CCL4L2*), and interferon related genes (*IFNB1*, *IRF7*) that is consistent in LPS-induced immune response in the literature (Figure 5.2C)[32,42,54–56]. Similarly, we observed similar LPS-induction of genes associated with the NF-kB and MAPK signaling pathways, such as *IL1A*, *IL1B*, and *ICAM1*, demonstrating the full inflammatory response captured in LPS-induced, homeRNA-stabilized samples (Supplementary Figure D1).

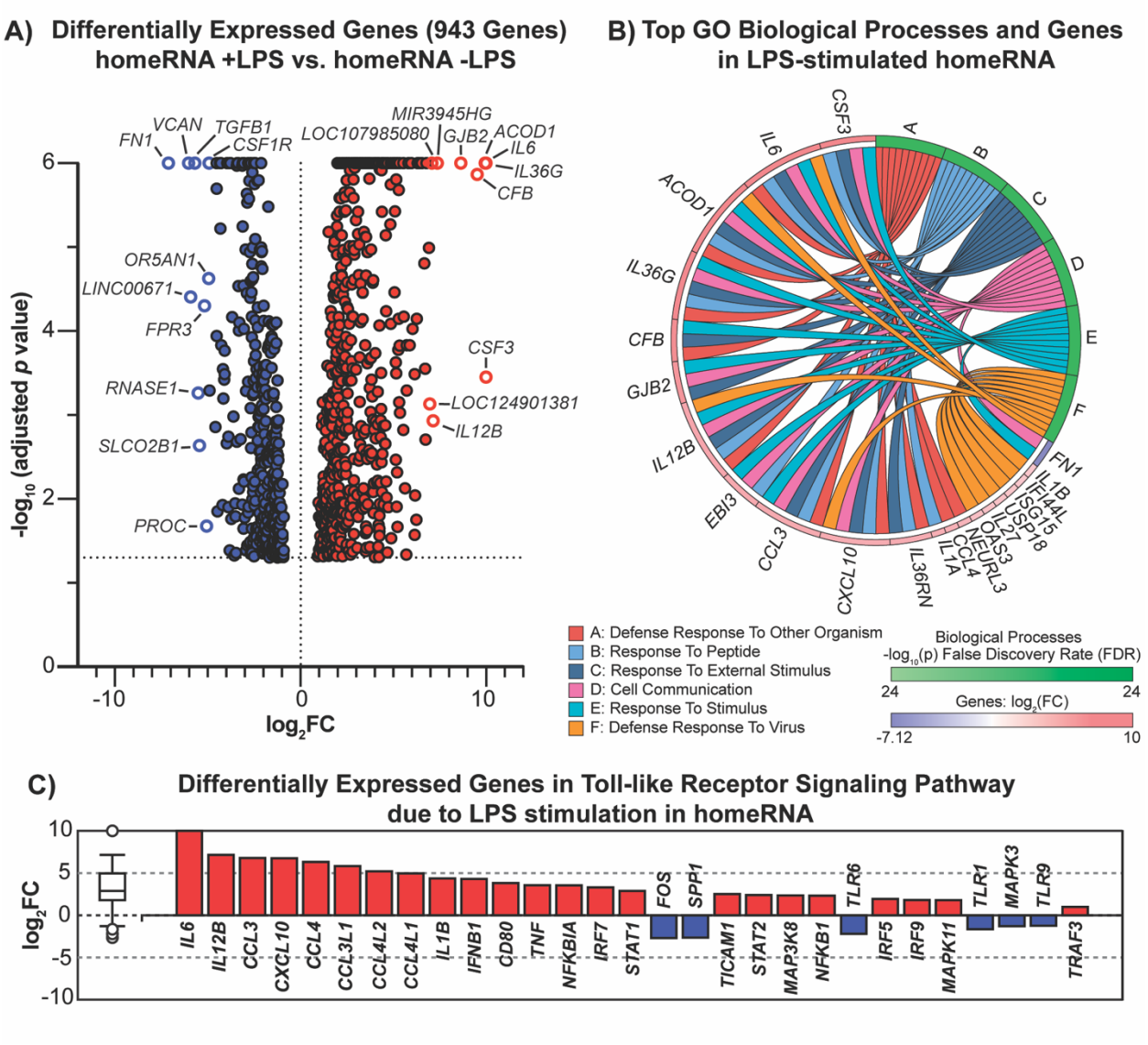

Figure 5.2. homeRNA captures LPS-induced immune response. A) Volcano plot of differentially expressed genes (DEGs) between LPS-stimulated and unstimulated homeRNA-stabilized samples. The measured 943 DEGs (30% change in expression, FDR ≤ 0.05) are represented by the negative log10 of the adjusted p-value on the y-axis and log2 fold change on the x-axis. Red points represent up-regulated genes and blue points represent down-regulated genes with LPS stimulation. The top 10 highly expressed up-regulated and down-regulated genes are labeled. B) Gene ontology (GO) enrichment chord diagram visualizing the top 10 DEGs present in each of the top six biological processes. Genes are positioned around the circle and colored by their log2 fold change (red for up-regulated, blue for down-regulated). Biological processes are labeled A-F around the outer ring. Connecting ribbons link genes to their associated biological processes, with ribbon colors corresponding to a biological process. C) All up- and down-regulated DEGs (n=29 DEGs) in the toll-like receptor signaling pathway (KEGG: 04060) ranked based on their absolute value of log2 fold change. Up-regulated genes are shown in red; down-regulated genes are shown in blue. The box and whisker plot on the left summarizes the distribution of all DEGs in this pathway with outliers represented by circles. p-values were adjusted for multiple comparisons by controlling for the false discovery rate (FDR) using the Benjamini-Hochberg (BH) procedure[41].

5.4 homeRNA-stabilized samples capture a similar LPS-induced inflammatory response to that of venous blood stabilized with RNAlater or PAXgene

Having demonstrated that homeRNA can effectively capture biological responses via LPS stimulation, we next sought to directly compare the induced immune response in homeRNA-stabilized capillary blood with that of traditional phlebotomy-drawn venous blood. The primary aim of this comparative analysis was to characterize differences in gene expression profiles between these two collection methods to inform the feasibility of using homeRNA in future transcriptomic studies. This comparison is particularly relevant for determining whether homeRNA could enable the transition of clinic-based immune response studies to remote sampling applications. By comparing the similarities and differences between homeRNA (capillary) and venous blood transcriptomic responses to LPS stimulation, we aim to provide critical guidance for researchers considering the implementation of homeRNA-based remote blood collection in studies investigating immune activation and inflammatory pathways.

Towards this aim, we first identified DEGs in LPS-stimulated and unstimulated blood samples within our three collection/stabilization methods: Tasso-collected blood stabilized with RNA*later* (i.e., homeRNA-stabilized samples), venous blood stabilized with RNA*later*, and venous blood stabilized with PAXgene. We found 682 DEGs to be common between all three groups (Figure 5.3A), suggesting some alignment between the LPS-induced response from each collection and stabilization method. In addition, each method captured unique DEGs, suggesting that some components of the response may be method-specific (i.e., collection method or stabilization method), potentially reflecting differences in sample type (i.e., capillary vs. venous). GO-derived biological processes and KEGG pathway analysis on the DEGs of each group also found 41 overlapping biological processes (Figure 5.3B) and 68 overlapping pathways (Figure 5.3C).

To examine these differences in more detail, we focused on the toll-like receptor signaling pathway, a key mediator of LPS-induced immune responses. We identified 33 up-regulated DEGs in the toll-like receptor signaling pathway induced by LPS stimulation across the three collection/stabilization groups (Figure 5.3D). The majority of these up-regulated DEGs were consistently present in all three groups,

including key LPS-induced cytokines (*IL6*, *IL12B*, *IL1B*, *TNF*) and chemokines (*CXCL10*, *CCL3*, *CCL4*) as previously described. However, we observed a notable difference in the expression of the two chemokines *CXCL9* and *CXCL11*, which showed significant up-regulation in both venous blood groups (RNA*later* and PAXgene) following LPS stimulation, but were absent from the stimulated homeRNA blood samples (Figure 5.3D). This difference appears to be linked to interferon-gamma (IFN-γ) signaling, as CXCL9 and CXCL11 are specifically IFN-γ-inducible chemokines while CXCL10, which is present in all three groups, can be induced by LPS or TNF-α as well as IFN-γ[57–59]. Consistent with this IFN-γ signaling, we observed significant up-regulation of *IFNγ* in both LPS-stimulated venous groups while no significant change was observed in stimulated homeRNA samples (Figure 5.3E). The absence of *IFNγ* induction in homeRNA samples may explain why *CXCL9* and *CXCL11* were not differentially expressed in these samples. This is further supported by previous studies demonstrating that LPS and IFN-γ act synergistically to induce CXCL9 and CXCL11 expression in various cell types[60–63], providing a potential mechanistic basis for the robust up-regulation of these chemokines observed specifically in the venous blood samples where both LPS stimulation and *IFNγ* induction occurred. It should be noted that other studies found that LPS stimulation did not induce IFN-γ protein in either capillary blood collected via a microneedle in the upper arm or venous blood[64], but yet other studies have found that LPS can induce IFN-γ in natural killer cells and monocytes[65,66]. Taken together, there is variation observed in the literature in LPS-induced IFN-γ levels across blood types; the observed differences in transcriptional *IFNγ* induction between capillary and venous blood in our study could be a result of physiological differences between capillary and venous blood. Given our limited sample size, future studies with larger cohorts would be needed to provide greater statistical power and more definitive insights into IFN-γ-mediated differences between these sampling methods.

We also compared the baseline gene expression profiles between unstimulated homeRNA-stabilized blood (capillary) and RNA*later*-stabilized venous blood (Supplementary Figures D2, D3, and D4 and associated discussion). We identified a baseline inflammatory signature present in capillary samples and absent in venous samples that likely reflects methodological differences in blood collection completed in this study; specifically, the Tasso-SST blood collection tubes used for the homeRNA samples contain no

anticoagulant, whereas the venous blood samples were collected in EDTA-coated vacutainers. The lack of anticoagulant in the Tasso-collected samples may have promoted clotting activation, contributing to the observed inflammatory signature. Additionally, in this study the collected blood samples were incubated for six hours prior to stabilization so that they could serve as controls for LPS-stimulated samples, which were also incubated for six hours. However, in typical homeRNA-based studies, collected capillary blood samples would be immediately stabilized by the participant after collection. Therefore, the increased gene expression response observed in some inflammatory genes between homeRNA and RNA*later*-stabilized venous samples in this study does not necessarily translate to typical conditions used in homeRNA studies. Despite some of the inflammatory genes being up-regulated in homeRNA-stabilized, unstimulated samples, when we probed the bulk gene expression profile (19,751 genes total), we observed high correlation between the unstimulated homeRNA and venous RNA*later* samples (Pearson correlation r=0.95) (Supplementary Figure D2). This correlation is consistent with other comparisons on the gene and protein expression between capillary blood and venous blood observed in other studies[67–71], supporting the potential of homeRNA to be used in remote transcriptomic studies in place of clinic-based phlebotomy draws.

Despite differences in *IFNγ* induction and baseline inflammatory signature between the homeRNA and RNA*later*-stabilized venous samples, we were still able to capture a similar inflammatory response to LPS stimulation across all blood collection and stabilization conditions. These similarities in LPS response are further seen in the top 20 overlapping overrepresented biological processes (Figure 5.3F) and pathways (Figure 5.3G) across all three groups. Here, as expected, we observe significant enrichment of biological processes and pathways related to inflammation and host immune response across all groups due to LPS stimulation. Overall, the primary LPS-driven immune response signature remains well-aligned across the collection and stabilization methods, suggesting that homeRNA can capture a similar inflammatory response to that of venous blood sampling.

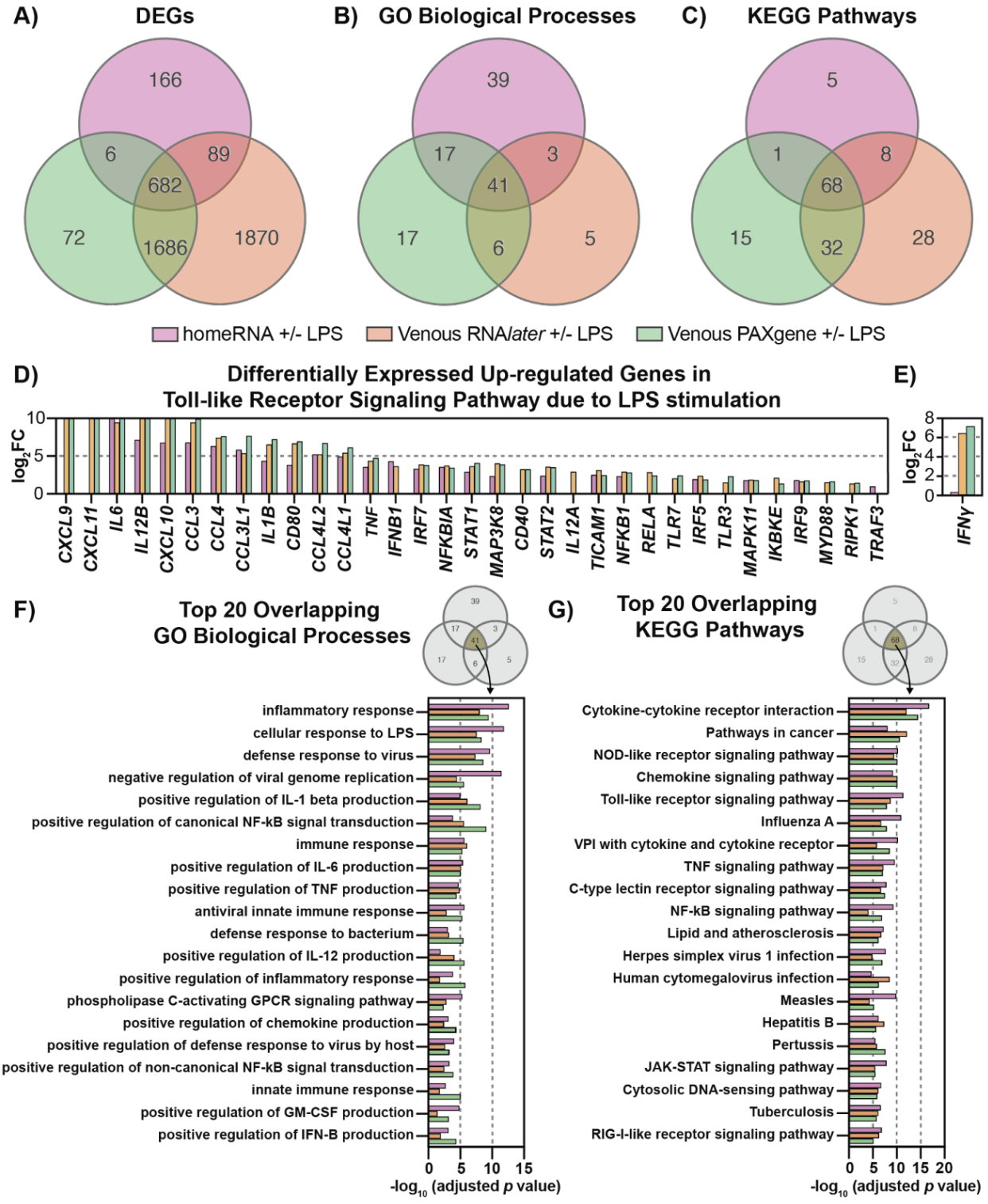

Figure 5.3. homeRNA-stabilized samples capture a similar LPS-induced inflammatory response to that of venous blood stabilized with RNA*later* or PAXgene. Overlapping A) differentially expressed genes (DEGs) between the LPS stimulated and unstimulated conditions of the homeRNA-stabilized, RNA*later*-stabilized venous blood, and PAXgene-stabilized venous blood samples. B) Enriched gene ontology (GO)-derived biological processes and C) KEGG pathways from the DEGs. D) All up-regulated DEGs (n=33 DEGs) in the toll-like receptor signaling pathway (KEGG: 04060) from each LPS-stimulated and unstimulated

comparison. DEGs are ranked based on their average log_2 fold change across all three groups. E) LPS-stimulated response of *IFNγ* in each comparison. F) Top 20 overlapping GO-derived biological processes pathways between all three LPS-stimulated collection/stabilization groups. Biological processes are ranked based on their average adjusted p-value across all three groups. G) Top 20 overlapping KEGG pathways between all three LPS-stimulated collection/stabilization groups. Pathways are ranked based on their average adjusted p-value across all three groups. VPI stands for viral protein interaction. p-values were adjusted for multiple comparisons by controlling for the false discovery rate (FDR) using the Benjamini-Hochberg (BH) procedure[41].

5.5 Conclusion

In this study, we demonstrate the feasibility of homeRNA for transcriptomic studies by comparing the gene expression profile and LPS-induced biological response between homeRNA sampling and traditional venous sampling. We found that homeRNA successfully captured a LPS-induced inflammatory response that was comparable to that of venous blood samples stabilized with either RNA*later* or PAXgene. Further, we observed strong correlation in baseline gene expression profiles between the two collection methods (capillary blood from the upper arm and venous blood) and the two stabilization methods in venous blood (RNA*later* and PAXgene). This work establishes the compatibility of homeRNA with bulk RNA-sequencing, demonstrating its potential as a useful tool for monitoring of immune response via remote sampling.

Overall, this study aims to provide guidance for other researchers seeking to combine remote blood collection studies with downstream RNA-sequencing analysis. Future work with larger sample sizes will be required to further validate the biological reproducibility of homeRNA and to establish which genes and pathways can most accurately be quantified using homeRNA. To date, we have already demonstrated the use of homeRNA to capture dynamic immune response signatures during SARS-CoV-2 infection, including both the presymptomatic and acute phases, via a targeted Nanostring gene panel[6,30]. This current work adds to the body of literature that characterizes the biological and analytical factors that contribute to transcriptomic differences between capillary and venous blood sampling that is crucial to properly interpret results in remote, capillary-blood based studies compared to clinic-based venipuncture studies.

5.6 Materials and methods

Participant Recruitment and Demographics

Healthy adult volunteers (18 years or older) were recruited in Seattle, Washington via word of mouth under a protocol approved by the University of Washington Institutional Review Board study number STUDY00007868. Written informed consent was obtained from all participants (n=3). Each participant had 10 mL of venous blood collected into an EDTA-coated BD vacutainer (Becton Dickenson) as well as 0.6 mL to 1.5 mL of blood collected from the upper arm using two to three Tasso-SST devices, which was pooled together. The authors note that the serum separator tube (SST) gel (included in the Tasso-SST collection tube) is not necessary for RNA stabilization and analysis. At the time of the study, the Tasso-SST was the only available Tasso device for purchase.

LPS stimulation and blood stabilization

Lipopolysaccharide from Escherichia coli O111:B4 (Sigma Aldrich) was reconstituted in RPMI culture media (Gibco) to make a 1 mg/mL stock solution. After blood collection, the blood collected from the two to three separate Tasso-SST™ devices used by a single participant was pooled into a microcentrifuge tube and mixed with a pipette until homogeneous. For each donor, 150 μL of venous blood and Tasso-collected blood was pipetted into separate replicates (n=2 replicates for each condition for a total of four samples for Tasso-collected blood and eight samples for venous blood per donor) within a 24-well plate. 150 μL of RPMI media containing LPS was added to each LPS stimulation replicate to achieve a final concentration of 100 ng/mL LPS. 150 μL of RPMI media (not containing any LPS) was added to each -LPS control replicate. Each sample was then incubated at 37°C for 6 h. Immediately after incubation, each venous blood sample (300 μL total including blood and added media volume) was transferred to microcentrifuge tube and stabilized according to manufacturer's protocol with either RNA*later*™ (1:2.6 mL blood:RNA*later*™) or PAXgene® (1:2.76 mL blood:PAXgene®). For the Tasso-collected samples, each blood sample (300 μL total including blood and added media volume) was transferred back into a fresh Tasso-SST blood collection tube which was then attached to a custom engineered stabilizer tube used in the homeRNA kit,

which contained 1.3 mL RNA*later*, and shaken to mimic blood stabilization in homeRNA kits[27]. After stabilization, blood samples were stored at -80°C until ready for RNA isolation.

RNA isolation

For all blood samples stabilized with RNA*later*, total cellular RNA was isolated using the Ribopure Blood RNA Isolation Kit (Thermo Fisher) according to the manufacturer's protocol without DNase treatment. Isolated RNA was stored at -80°C until ready for sequencing. For all blood samples stabilized with PAXgene, total cellular RNA was isolated using the PAXgene Blood RNA Kit (PreAnalytix) according to the manufacturer's protocol without DNase treatment. Due to procedural errors, one donor's PAXgene-stabilized samples were not usable.

RNA sequencing and analysis

Library preparation and sequencing: Total RNA samples were shipped to Psomagen for library preparation and sequencing. Prior to library preparation, all samples were treated with DNase I according to manufacturer's protocol. After DNase treatment, RNA quantity was measured using fluorescence-based quantification method Ribogreen (Life technologies) and RNA quality was assessed using Agilent RNA screentape (Agilent Technologies) on Agilent 4200 TapeStation system. All samples yielded RNA Quality Numbers (RQNs) ≥ 6.5. For each sample, 25ng of RNA was used as input for library preparation using Illumina Stranded Total RNA Prep with Ribo-Zero Plus kit. The resulting libraries were validated with D1000 Screen Tape (Agilent Technologies) and D1000 Reagents (Agilent Technologies) on 4200 TapeStation system (Agilent Technologies) to determine library size. Library quantification was measured with the Roche library quantification kit on LightCycler480 (Roche). Validated libraries were then normalized, diluted to the desired loading concentration and sequenced on the NovaSeq X Plus system using paired-end 151bp reads, targeting 15Gb per sample. Sequencing was performed using the NovaSeq X Plus system software. Real Time Analysis software was used to perform base calling from the raw images files generated by the Illumina sequencer. The resulting binary BCL/cBCL files were then converted to FASTQ files format using bcl2fastq, an Illumina provided package.

RNA sequencing quality control, alignment, and quantification: Quality of raw sequencing data was assessed using fastqc (https://www.bioinformatics.babraham.ac.uk/projects/fastqc/), and then reads were aligned to the NBCI GRCh38 transcriptome using the salmon aligner[34]. Transcript abundances were read into R and summarized at the gene level using the Bioconductor tximport package[35]. Genes with unreliably low expression were excluded, with 19,751 genes retained for analysis.

Identification of differentially expressed genes: Differentially expressed genes were identified using the limma-voom pipeline[33]. Briefly, gene counts were adjusted for library size by computing counts per million counts (CPM), and then taking logs (logCPM). The logCPM values have reduced right skew, but still have a dependence between the mean and variance, which violates a core assumption for linear regression. Observation-level weights were estimated from the trend between the mean and variance and used in a weighted linear regression to account for the heteroscedasticity. Between-group comparisons were made using empirical Bayes adjusted contrasts, selecting genes at a false discovery rate (FDR) < 0.05, and incorporating an additional 30% change criterion in our statistic[37].

Heatmap visualization: Heatmaps were generated in R (v4.5.1) using the pheatmap package (v1.0.13). Genes included in the heatmaps were selected as differentially expressed (FDR < 0.05) with at least 30% change in expression. Batch effects from donors were removed using the *removeBatchEffect* function in the limma package (v3.64.1)[38]. Z-scores, used for row scaling, were calculated from $\log_2$-transformed counts per million (logCPM) values generated using the edgeR (v4.6.2) package.

Volcano plot visualization: Volcano plots were generated using iPathwayGuide™ (AdvaitaBio Corporation, https://ipathwayguide.advaitabio.com/)[39,40].

Gene ontology enrichment and pathway analysis: Gene Ontology (GO) Term Enrichment analysis, chord diagrams, and multiple comparisons were generated using iPathwayGuide™ (AdvaitaBio Corporation, https://ipathwayguide.advaitabio.com/)[39,40]. p-values were adjusted for multiple comparisons controlling false discovery rate (FDR) using the Benjamini-Hochberg (BH) procedure[41]. Significant GO terms in the stimulated vs unstimulated homeRNA group (Fig 2B) were selected at an FDR<0.05. To perform multiple comparisons and determine overlapping GO biological processes between all three experimental stimulated

vs unstimulated conditions seen in Figure 3B and 3F, the high specificity pruning method was used to assess the significance of GO terms. KEGG pathways analysis was also performed using iPathwayGuide™ (AdvaitaBio Corporation, https://ipathwayguide.advaitabio.com/)[39,40]. Significant KEGG pathways between the stimulated vs unstimulated conditions across all three groups seen in Figure 5.3C and 5.3G were selected using an FDR<0.05.

5.7 References

1. Krasowski, M. D. Remote Blood Collection Devices Improve Study Participation from Hard to Reach Populations. J. Appl. Lab. Med. 2024, 9 (5), 874–876. https://doi.org/10.1093/jalm/jfae075.
2. Maass, K. F.; Barfield, M. D.; Ito, M.; James, C. A.; Kavetska, O.; Kozinn, M.; Kumar, P.; Lepak, M.; Leuthold, L. A.; Li, W.; Mikhailov, D.; Patel, S.; Perez, N. L.; Jackson Rudd, D.; Vakkalagadda, B.; Williams, T. M.; Zha, J.; Zhang, X.; Anderson, M. D. Leveraging Patient-centric Sampling for Clinical Drug Development and Decentralized Clinical Trials: Promise to Reality. Clin. Transl. Sci. 2022, 15 (12), 2785–2795. https://doi.org/10.1111/cts.13411.
3. Koulman, A.; Rennie, K. L.; Parkington, D.; Tyrrell, C. S.; Catt, M.; Gkrania-Klotsas, E.; Wareham, N. J. The Development, Validation and Application of Remote Blood Sample Collection in Telehealth Programmes. J. Telemed. Telecare 2024, 30 (4), 731–738. https://doi.org/10.1177/1357633X221093434.
4. Baillargeon, K. R.; Mace, C. R. Microsampling Tools for Collecting, Processing, and Storing Blood at the Point-of-care. Bioeng. Transl. Med. 2023, 8 (2), e10476. https://doi.org/10.1002/btm2.10476.
5. Thangavelu, M. U.; Wouters, B.; Kindt, A.; Reiss, I. K. M.; Hankemeier, T. Blood Microsampling Technologies: Innovations and Applications in 2022. Anal. Sci. Adv. 2023, 4 (5–6), 154–180. https://doi.org/10.1002/ansa.202300011.
6. Lim, F. Y.; Lea, H. G.; Dostie, A. M.; Kim, S.-Y.; Van Neel, T. L.; Hassan, G. W.; Takezawa, M. G.; Starita, L. M.; Adams, K. N.; Boeckh, M.; Schiffer, J. T.; Hyrien, O.; Waghmare, A.; Berthier, E.; Theberge, A. B. homeRNA Self-Blood Collection Enables High-Frequency Temporal Profiling of Presymptomatic Host Immune Kinetics to Respiratory Viral Infection: A Prospective Cohort Study. eBioMedicine 2025, 112, 105531. https://doi.org/10.1016/j.ebiom.2024.105531.
7. Al-Uzri, A.; Freeman, K. A.; Wade, J.; Clark, K.; Bleyle, L. A.; Munar, M.; Koop, D. R. Longitudinal Study on the Use of Dried Blood Spots for Home Monitoring in Children after Kidney Transplantation. Pediatr. Transplant. 2017, 21 (6), e12983. https://doi.org/10.1111/petr.12983.
8. Chaussabel, D. Assessment of Immune Status Using Blood Transcriptomics and Potential Implications for Global Health. Semin. Immunol. 2015, 27 (1), 58–66. https://doi.org/10.1016/j.smim.2015.03.002.
9. Ivanov, S. M.; Tarasova, O. A.; Poroikov, V. V. Transcriptome-Based Analysis of Human Peripheral Blood Reveals Regulators of Immune Response in Different Viral Infections. Front. Immunol. 2023, 14, 1199482. https://doi.org/10.3389/fimmu.2023.1199482.
10. Hoffmann, M.; Willruth, L.-L.; Dietrich, A.; Lee, H. K.; Knabl, L.; Trummer, N.; Baumbach, J.; Furth, P. A.; Hennighausen, L.; List, M. Blood Transcriptomics Analysis Offers Insights into Variant-Specific Immune Response to SARS-CoV-2. Sci. Rep. 2024, 14 (1), 2808. https://doi.org/10.1038/s41598-024-53117-w.
11. Houseley, J.; Tollervey, D. The Many Pathways of RNA Degradation. Cell 2009, 136 (4), 763–776. https://doi.org/10.1016/j.cell.2009.01.019.
12. Gallego Romero, I.; Pai, A. A.; Tung, J.; Gilad, Y. RNA-Seq: Impact of RNA Degradation on Transcript Quantification. BMC Biol. 2014, 12 (1), 42. https://doi.org/10.1186/1741-7007-12-42.
13. Weber, D. G.; Casjens, S.; Rozynek, P.; Lehnert, M.; Zilch-Schöneweis, S.; Bryk, O.; Taeger, D.; Gomolka, M.; Kreuzer, M.; Otten, H.; Pesch, B.; Johnen, G.; Brüning, T. Assessment of mRNA and

microRNA Stabilization in Peripheral Human Blood for Multicenter Studies and Biobanks. Biomark. Insights 2010, 5, BMI.S5522. https://doi.org/10.4137/BMI.S5522.
14. Wang, M.; Ji, X.; Wang, B.; Li, Q.; Zhou, J. Simultaneous Evaluation of the Preservative Effect of RNA Later on Different Tissues by Biomolecular and Histological Analysis. Biopreservation Biobanking 2018, 16 (6), 426–433. https://doi.org/10.1089/bio.2018.0055.
15. Delahaye, L.; Veenhof, H.; Koch, B. C. P.; Alffenaar, J.-W. C.; Linden, R.; Stove, C. Alternative Sampling Devices to Collect Dried Blood Microsamples: State-of-the-Art. Ther. Drug Monit. 2021, 43 (3), 310–321. https://doi.org/10.1097/FTD.0000000000000864.
16. Malsagova, K.; Kopylov, A.; Stepanov, A.; Butkova, T.; Izotov, A.; Kaysheva, A. Dried Blood Spot in Laboratory: Directions and Prospects. Diagnostics 2020, 10 (4), 248. https://doi.org/10.3390/diagnostics10040248.
17. Bybjerg-Grauholm, J.; Hagen, C. M.; Khoo, S. K.; Johannesen, M. L.; Hansen, C. S.; Bækvad-Hansen, M.; Christiansen, M.; Hougaard, D. M.; Hollegaard, M. V. RNA Sequencing of Archived Neonatal Dried Blood Spots. Mol. Genet. Metab. Rep. 2017, 10, 33–37. https://doi.org/10.1016/j.ymgmr.2016.12.004.
18. Reust, M. J.; Lee, M. H.; Xiang, J.; Zhang, W.; Xu, D.; Batson, T.; Zhang, T.; Downs, J. A.; Dupnik, K. M. Dried Blood Spot RNA Transcriptomes Correlate with Transcriptomes Derived from Whole Blood RNA. Am. J. Trop. Med. Hyg. 2018, 98 (5), 1541–1546. https://doi.org/10.4269/ajtmh.17-0653.
19. Bertoli-Avella, A. M.; Radefeldt, M.; Al-Ali, R.; Pardo, L. M.; Lemke, S.; Leubauer, A.; Polla, D. L.; Hörnicke, R.; Almeida, L. S.; Kandaswamy, K. K.; Beetz, C.; Pinto Basto, J.; Bauer, P. Beyond Genomics: Using RNA-Seq from Dried Blood Spots to Unlock the Clinical Relevance of Splicing Variation in a Diagnostic Setting. Eur. J. Hum. Genet. 2025, 33 (5), 614–623. https://doi.org/10.1038/s41431-025-01792-2.
20. Demirev, P. A. Dried Blood Spots: Analysis and Applications. Anal. Chem. 2013, 85 (2), 779–789. https://doi.org/10.1021/ac303205m.
21. Kalikiri, M. K. R.; Manjunath, H. S.; Vempalli, F. R.; Mathew, L. S.; Liu, L.; Wang, L.; Wang, G.; Wang, K.; Soloviov, O.; Lorenz, S.; Tomei, S. Technical Assessment of Different Extraction Methods and Transcriptome Profiling of RNA Isolated from Small Volumes of Blood. Sci. Rep. 2023, 13 (1), 3598. https://doi.org/10.1038/s41598-023-30629-5.
22. Morgunova, A.; Ibrahim, P.; Chen, G. G.; Coury, S. M.; Turecki, G.; Meaney, M. J.; Gifuni, A.; Gotlib, I. H.; Nagy, C.; Ho, T. C.; Flores, C. Preparation and Processing of Dried Blood Spots for microRNA Sequencing. Biol. Methods Protoc. 2023, 8 (1), bpad020. https://doi.org/10.1093/biomethods/bpad020.
23. Grauholm, J.; Khoo, S. K.; Nickolov, R. Z.; Poulsen, J. B.; Bækvad-Hansen, M.; Hansen, C. S.; Hougaard, D. M.; Hollegaard, M. V. Gene Expression Profiling of Archived Dried Blood Spot Samples from the Danish Neonatal Screening Biobank. Mol. Genet. Metab. 2015, 116 (3), 119–124. https://doi.org/10.1016/j.ymgme.2015.06.011.
24. McDade, T. W.; M. Ross, K.; L. Fried, R.; Arevalo, J. M. G.; Ma, J.; Miller, G. E.; Cole, S. W. Genome-Wide Profiling of RNA from Dried Blood Spots: Convergence with Bioinformatic Results Derived from Whole Venous Blood and Peripheral Blood Mononuclear Cells. Biodemography Soc. Biol. 2016, 62 (2), 182–197. https://doi.org/10.1080/19485565.2016.1185600.
25. Zarbl, J.; Eimer, E.; Gigg, C.; Bendzuck, G.; Korinth, M.; Elling-Audersch, C.; Kleyer, A.; Simon, D.; Boeltz, S.; Krusche, M.; Mucke, J.; Muehlensiepen, F.; Vuillerme, N.; Krönke, G.; Schett, G.; Knitza, J. Remote Self-Collection of Capillary Blood Using Upper Arm Devices for Autoantibody Analysis in Patients with Immune-Mediated Inflammatory Rheumatic Diseases. RMD Open 2022, 8 (2), e002641. https://doi.org/10.1136/rmdopen-2022-002641.
26. Dasari, H.; Smyrnova, A.; Leng, J.; Ducharme, F. M. Feasibility, Acceptability, and Safety of a Novel Device for Self-Collecting Capillary Blood Samples in Clinical Trials in the Context of the Pandemic and Beyond. PLOS ONE 2024, 19 (5), e0304155. https://doi.org/10.1371/journal.pone.0304155.
27. Haack, A. J.; Lim, F. Y.; Kennedy, D. S.; Day, J. H.; Adams, K. N.; Lee, J. J.; Berthier, E.; Theberge, A. B. Home RNA: A Self-Sampling Kit for the Collection of Peripheral Blood and Stabilization of RNA. Anal. Chem. 2021, 93 (39), 13196–13203. https://doi.org/10.1021/acs.analchem.1c02008.

28. Brown, L. G.; Haack, A. J.; Kennedy, D. S.; Adams, K. N.; Stolarczuk, J. E.; Takezawa, M. G.; Berthier, E.; Thongpang, S.; Lim, F. Y.; Chaussabel, D.; Garand, M.; Theberge, A. B. At-Home Blood Collection and Stabilization in High Temperature Climates Using homeRNA. Front. Digit. Health 2022, 4, 903153. https://doi.org/10.3389/fdgth.2022.903153.
29. Stefanovic, F.; Brown, L. G.; MacDonald, J.; Bammler, T.; Rinchai, D.; Nguyen, S.; Zeng, Y.; Shinkawa, V.; Adams, K.; Chaussabel, D.; Berthier, E.; Haack, A. J.; Theberge, A. B. Your Blood Is Out for Delivery: Considerations of Shipping Time and Temperature on Degradation of RNA from Stabilized Whole Blood. Anal. Chem. 2025, 97 (3), 1635–1644. https://doi.org/10.1021/acs.analchem.4c04591.
30. Lim, F. Y.; Kim, S.-Y.; Kulkarni, K. N.; Blazevic, R. L.; Kimball, L. E.; Lea, H. G.; Haack, A. J.; Gower, M. S.; Stevens-Ayers, T.; Starita, L. M.; Boeckh, M.; Hyrien, O.; Schiffer, J. T.; Theberge, A. B.; Waghmare, A. High-Frequency Home Self-Collection of Capillary Blood Correlates IFI27 Expression Kinetics with SARS-CoV-2 Viral Clearance. J. Clin. Invest. 2023, 133 (23), e173715. https://doi.org/10.1172/JCI173715.
31. Rosadini, C. V.; Kagan, J. C. Early Innate Immune Responses to Bacterial LPS. Curr. Opin. Immunol. 2017, 44, 14–19. https://doi.org/10.1016/j.coi.2016.10.005.
32. Jorda, A.; Eberl, S.; Nussbaumer-Pröll, A.; Sarhan, M.; Weber, M.; Tegrovsky, L.; Wahrmann, M.; Al Jalali, V.; Bergmann, F.; Pracher, L.; Leutzendorff, A.; Farlik, M.; Jilma, B.; Zeitlinger, M. Reproducibility of LPS-Induced Ex Vivo Cytokine Response of Healthy Volunteers Using a Whole Blood Assay. J. Inflamm. Res. 2024, Volume 17, 4781–4790. https://doi.org/10.2147/jir.s459999.
33. Segre, E.; Fullerton, J. N. Stimulated Whole Blood Cytokine Release as a Biomarker of Immunosuppression in the Critically Ill: The Need for a Standardized Methodology. Shock 2016, 45 (5), 490–494. https://doi.org/10.1097/shk.0000000000000557.
34. Patro, R.; Duggal, G.; Love, M. I.; Irizarry, R. A.; Kingsford, C. Salmon Provides Fast and Bias-Aware Quantification of Transcript Expression. Nat. Methods 2017, 14 (4), 417–419. https://doi.org/10.1038/nmeth.4197.
35. Soneson, C.; Love, M. I.; Robinson, M. D. Differential Analyses for RNA-Seq: Transcript-Level Estimates Improve Gene-Level Inferences. F1000Research 2016, 4, 1521. https://doi.org/10.12688/f1000research.7563.2.
36. Law, C. W.; Chen, Y.; Shi, W.; Smyth, G. K. Voom: Precision Weights Unlock Linear Model Analysis Tools for RNA-Seq Read Counts. Genome Biol. 2014, 15 (2), R29. https://doi.org/10.1186/gb-2014-15-2-r29.
37. McCarthy, D. J.; Smyth, G. K. Testing Significance Relative to a Fold-Change Threshold Is a TREAT. Bioinformatics 2009, 25 (6), 765–771. https://doi.org/10.1093/bioinformatics/btp053.
38. Ritchie, M. E.; Phipson, B.; Wu, D.; Hu, Y.; Law, C. W.; Shi, W.; Smyth, G. K. Limma Powers Differential Expression Analyses for RNA-Sequencing and Microarray Studies. Nucleic Acids Res. 2015, 43 (7), e47–e47. https://doi.org/10.1093/nar/gkv007.
39. Draghici, S.; Khatri, P.; Tarca, A. L.; Amin, K.; Done, A.; Voichita, C.; Georgescu, C.; Romero, R. A Systems Biology Approach for Pathway Level Analysis. Genome Res. 2007, 17 (10), 1537–1545. https://doi.org/10.1101/gr.6202607.
40. Donato, M.; Xu, Z.; Tomoiaga, A.; Granneman, J. G.; MacKenzie, R. G.; Bao, R.; Than, N. G.; Westfall, P. H.; Romero, R.; Draghici, S. Analysis and Correction of Crosstalk Effects in Pathway Analysis. Genome Res. 2013, 23 (11), 1885–1893. https://doi.org/10.1101/gr.153551.112.
41. Benjamini, Y.; Hochberg, Y. Controlling the False Discovery Rate: A Practical and Powerful Approach to Multiple Testing. J. R. Stat. Soc. Ser. B Stat. Methodol. 1995, 57 (1), 289–300. https://doi.org/10.1111/j.2517-6161.1995.tb02031.x.
42. Luan, L.; Patil, N. K.; Guo, Y.; Hernandez, A.; Bohannon, J. K.; Fensterheim, B. A.; Wang, J.; Xu, Y.; Enkhbaatar, P.; Stark, R.; Sherwood, E. R. Comparative Transcriptome Profiles of Human Blood in Response to the Toll-like Receptor 4 Ligands Lipopolysaccharide and Monophosphoryl Lipid A. Sci. Rep. 2017, 7 (1), 40050. https://doi.org/10.1038/srep40050.

43. Greenhill, C. J.; Rose-John, S.; Lissilaa, R.; Ferlin, W.; Ernst, M.; Hertzog, P. J.; Mansell, A.; Jenkins, B. J. IL-6 Trans -Signaling Modulates TLR4-Dependent Inflammatory Responses via STAT3. J. Immunol. 2011, 186 (2), 1199–1208. https://doi.org/10.4049/jimmunol.1002971.
44. Xia, J.; Chen, W.; Xu, C.; Wang, M.; Mo, G.; Zhang, X. CSF3 Enhances the Innate Immune Responses to ALV-J Infections via NF-κB and Interferon Pathways. Poult. Sci. 2025, 104 (11), 105648. https://doi.org/10.1016/j.psj.2025.105648.
45. Zhuang, J.; Ibarra, A.; Acosta, A.; Karns, A. P.; Aballi, J.; Nerenberg, M.; Sninsky, J. J.; Quake, S. R.; Toden, S. Survey of Extracellular Communication of Systemic and Organ-Specific Inflammatory Responses through Cell Free Messenger RNA Profiling in Mice. eBioMedicine 2022, 83, 104242. https://doi.org/10.1016/j.ebiom.2022.104242.
46. Ding, L.; Wang, X.; Hong, X.; Lu, L.; Liu, D. IL-36 Cytokines in Autoimmunity and Inflammatory Disease. Oncotarget 2018, 9 (2), 2895–2901. https://doi.org/10.18632/oncotarget.22814.
47. Queen, D.; Ediriweera, C.; Liu, L. Function and Regulation of IL-36 Signaling in Inflammatory Diseases and Cancer Development. Front. Cell Dev. Biol. 2019, 7, 317. https://doi.org/10.3389/fcell.2019.00317.
48. Wu, R.; Chen, F.; Wang, N.; Tang, D.; Kang, R. ACOD1 in Immunometabolism and Disease. Cell. Mol. Immunol. 2020, 17 (8), 822–833. https://doi.org/10.1038/s41423-020-0489-5.
49. Smiljanovic, B.; Grün, J. R.; Steinbrich-Zöllner, M.; Stuhlmüller, B.; Häupl, T.; Burmester, G. R.; Radbruch, A.; Grützkau, A.; Baumgrass, R. Defining TNF-α- and LPS-Induced Gene Signatures in Monocytes to Unravel the Complexity of Peripheral Blood Transcriptomes in Health and Disease. J. Mol. Med. 2010, 88 (10), 1065–1079. https://doi.org/10.1007/s00109-010-0648-8.
50. Akira, S. Toll-like Receptor Signaling. J. Biol. Chem. 2003, 278 (40), 38105–38108. https://doi.org/10.1074/jbc.R300028200.
51. Kim, H.-J.; Kim, H.; Lee, J.-H.; Hwangbo, C. Toll-like Receptor 4 (TLR4): New Insight Immune and Aging. Immun. Ageing 2023, 20 (1), 67. https://doi.org/10.1186/s12979-023-00383-3.
52. Moens, U.; Kostenko, S.; Sveinbjørnsson, B. The Role of Mitogen-Activated Protein Kinase-Activated Protein Kinases (MAPKAPKs) in Inflammation. Genes 2013, 4 (2), 101–133. https://doi.org/10.3390/genes4020101.
53. Liu, T.; Zhang, L.; Joo, D.; Sun, S.-C. NF-κB Signaling in Inflammation. Signal Transduct. Target. Ther. 2017, 2 (1), 17023. https://doi.org/10.1038/sigtrans.2017.23.
54. Bandow, K.; Kusuyama, J.; Shamoto, M.; Kakimoto, K.; Ohnishi, T.; Matsuguchi, T. LPS-induced Chemokine Expression in Both MyD88-dependent and -independent Manners Is Regulated by Cot/Tpl2-ERK Axis in Macrophages. FEBS Lett. 2012, 586 (10), 1540–1546. https://doi.org/10.1016/j.febslet.2012.04.018.
55. Chaiwut, R.; Kasinrerk, W. Very Low Concentration of Lipopolysaccharide Can Induce the Production of Various Cytokines and Chemokines in Human Primary Monocytes. BMC Res. Notes 2022, 15 (1), 42. https://doi.org/10.1186/s13104-022-05941-4.
56. Ngkelo, A.; Meja, K.; Yeadon, M.; Adcock, I.; Kirkham, P. A. LPS Induced Inflammatory Responses in Human Peripheral Blood Mononuclear Cells Is Mediated through NOX4 and Giα Dependent PI-3kinase Signalling. J. Inflamm. 2012, 9 (1), 1. https://doi.org/10.1186/1476-9255-9-1.
57. Xanthou, G.; Duchesnes, C. E.; Williams, T. J.; Pease, J. E. CCR3 Functional Responses Are Regulated by Both CXCR3 and Its Ligands CXCL9, CXCL10 and CXCL11. Eur. J. Immunol. 2003, 33 (8), 2241–2250. https://doi.org/10.1002/eji.200323787.
58. Ciesielski, C. J.; Andreakos, E.; Foxwell, B. M. J.; Feldmann, M. TNFα-Induced Macrophage Chemokine Secretion Is More Dependent on NF-κB Expression than Lipopolysaccharides-Induced Macrophage Chemokine Secretion. Eur. J. Immunol. 2002, 32 (7), 2037. https://doi.org/10.1002/1521-4141(200207)32:7<2037::AID-IMMU2037>3.0.CO;2-I.
59. Arger, N. K.; Ho, M. E.; Allen, I. E.; Benn, B. S.; Woodruff, P. G.; Koth, L. L. CXCL9 and CXCL10 Are Differentially Associated with Systemic Organ Involvement and Pulmonary Disease Severity in Sarcoidosis. Respir. Med. 2020, 161, 105822. https://doi.org/10.1016/j.rmed.2019.105822.

60. Proost, P.; Vynckier, A.; Mahieu, F.; Put, W.; Grillet, B.; Struyf, S.; Wuyts, A.; Opdenakker, G.; Damme, J. V. Microbial Toll-like Receptor Ligands Differentially Regulate CXCL10/IP-10 Expression in Fibroblasts and Mononuclear Leukocytes in Synergy with IFN-γ and Provide a Mechanism for Enhanced Synovial Chemokine Levels in Septic Arthritis. Eur. J. Immunol. 2003, 33 (11), 3146–3153. https://doi.org/10.1002/eji.200324136.
61. Proost, P.; Verpoest, S.; Van De Borne, K.; Schutyser, E.; Struyf, S.; Put, W.; Ronsse, I.; Grillet, B.; Opdenakker, G.; Van Damme, J. Synergistic Induction of CXCL9 and CXCL11 by Toll-like Receptor Ligands and Interferon-γ in Fibroblasts Correlates with Elevated Levels of CXCR3 Ligands in Septic Arthritis Synovial Fluids. J. Leukoc. Biol. 2004, 75 (5), 777–784. https://doi.org/10.1189/jlb.1003524.
62. Loos, T.; Dekeyzer, L.; Struyf, S.; Schutyser, E.; Gijsbers, K.; Gouwy, M.; Fraeyman, A.; Put, W.; Ronsse, I.; Grillet, B.; Opdenakker, G.; Damme, J. V.; Proost, P. TLR Ligands and Cytokines Induce CXCR3 Ligands in Endothelial Cells: Enhanced CXCL9 in Autoimmune Arthritis. Lab. Invest. 2006, 86 (9), 902–916. https://doi.org/10.1038/labinvest.3700453.
63. Metzemaekers, M.; Vanheule, V.; Janssens, R.; Struyf, S.; Proost, P. Overview of the Mechanisms That May Contribute to the Non-Redundant Activities of Interferon-Inducible CXC Chemokine Receptor 3 Ligands. Front. Immunol. 2018, 8, 1970. https://doi.org/10.3389/fimmu.2017.01970.
64. Eriksson, M.; Sartono, E.; Martins, C. L.; Balé, C.; Garly, M.-L.; Whittle, H.; Aaby, P.; Pedersen, B. K.; Yazdanbakhsh, M.; Erikstrup, C.; Benn, C. S. A Comparison of Ex Vivo Cytokine Production in Venous and Capillary Blood. Clin. Exp. Immunol. 2007, 150 (3), 469–476. https://doi.org/10.1111/j.1365-2249.2007.03515.x.
65. Kraaij, M. D.; Vereyken, E. J. F.; Leenen, P. J. M.; Van Den Bosch, T. P. P.; Rezaee, F.; Betjes, M. G. H.; Baan, C. C.; Rowshani, A. T. Human Monocytes Produce Interferon-Gamma upon Stimulation with LPS. Cytokine 2014, 67 (1), 7–12. https://doi.org/10.1016/j.cyto.2014.02.001.
66. Kanevskiy, L. M.; Telford, W. G.; Sapozhnikov, A. M.; Kovalenko, E. I. Lipopolysaccharide Induces IFN-γ Production in Human NK Cells. Front. Immunol. 2013, 4. https://doi.org/10.3389/fimmu.2013.00011.
67. Meredith, R. T.; Yarham, R. A. R.; Mills, H.; Oliver, M. A. Whole Blood Cytokine Release Assays Reveal Disparity between Capillary Blood Sampling Methods. Clin. Biochem. 2023, 120, 110648. https://doi.org/10.1016/j.clinbiochem.2023.110648.
68. Ni Lochlainn, M.; Cheetham, N. J.; Falchi, M.; Piazza, P.; Steves, C. J. Comparing Venous vs. Capillary Blood Collection Methods for Proteomic Measurement in Peripheral Blood. PROTEOMICS – Clin. Appl. 2025, 19 (4), e70007. https://doi.org/10.1002/prca.70007.
69. Toma, R.; Duval, N.; Pelle, B.; Parks, M. M.; Gopu, V.; Torres, P. J.; Camacho, F. R.; Shen, N.; Krishnan, S.; Hatch, A.; Tily, H.; Perlina, A.; Banavar, G.; Vuyisich, M. A Clinically Validated Human Capillary Blood Transcriptome Test For Global Systems Biology Studies. BioTechniques 2020, 69 (4), 289–301. https://doi.org/10.2144/btn-2020-0088.
70. Hameed, A.; Ferruzzi, M. G.; Kay, C. D.; Williams, D. K.; Rahbar, E.; Morris, A. J. Comparison of the Capillary and Venous Blood Plasma Lipidomes: Validation of Self-Collected Blood for Plasma Lipidomics. J. Lipid Res. 2025, 66 (3), 100755. https://doi.org/10.1016/j.jlr.2025.100755.
71. DiPasquale, C.; Christenson, R. H.; Donnelly, J. G.; Evans, S. A.; Wu, A. H. B.; Olson, E. G.; Barr, R.; Kosa, N.; McKenzie, H.; Abigania, M.; Jacobson, J. W. Equivalence between Capillary Blood and Venous Blood Test Results Using Miniaturized Assays and Novel Collection Methods to Support Routine Bloodwork. J. Appl. Lab. Med. 2025, jfaf059. https://doi.org/10.1093/jalm/jfaf059.

Chapter 6 | A Flexible and Responsive Remote Study Design to Assess Gene Expression Changes During Wildfire Smoke Exposure with homeRNA, an At-home Blood Sampling Kit

Reproduced in part from A. J. Haack, L. G. Brown*, Y. Zeng, T. Khan, I. H, Robertson, D. S. Kennedy, K. N. Adams, J. W. MacDonald, T. K. Bammler, F. Stefanovic, K. Moloney, J. E. Stolarczuk, M. G. Takezawa, M. Yunos Alizai, G. W. Hassan, F. Y. Lim, D. Chaussabel, E. G. Walker, N. A. Errett, E. Berthier, and A. B. Theberge, "A Flexible and Responsive Remote Study Design to Assess Gene Expression Changes During Wildfire Smoke Exposure with homeRNA, an At-home Blood Sampling Kit", In preparation.*
** Equal contribution*

AJH, EB and ABT contributed to the conception and design of the study. KNA, AJH, DSK EGW, NAE, EB and ABT designed and executed the human subjects study. AJH, DSK, FYL, EB, and ABT developed homeRNA and the protocols implemented in home sampling. AJH, IHR, DSK, KNA, FS, KM, JES, GWH and MGT conducted/contributed to the human subjects research and collection of samples. YZ and LGB performed the RNA extractions on samples and collected the RIN and yield data. AJH, LGB, YZ, JWM, TKB, IHR, MYA, JES, EB, DC, and ABT analyzed/interpreted the data. AJH, LGB, YZ, JES, IHR and ABT prepared the figures and wrote the chapter.

Abstract: Transcriptomic responses to wildfire smoke are difficult to study given the unpredictability of wildfires and the challenges of collecting blood during active disasters. To overcome these challenges, we developed a flexible study design leveraging homeRNA, our at-home blood collection and RNA stabilization kit. Between June 2021 and April 2022, 58 participants across 10 U.S. states collected 635 blood samples before, during, and after wildfire events. This responsive approach captured three exposure groups: high exposure in Okanogan County, Washington, medium exposure from transported smoke, and low exposure. During the 10-month study, 93% of participants (n=54/58) returned at least 6 samples. In a preliminary exploratory analysis, we analyzed 770 genes with a Nanostring panel from nine participants (6 high, 3 low-medium exposure) using the BloodGen3 framework. In the high exposure participants, we observed trends toward overexpression of inflammation (inflammation aggregates A33 and A35, and modules M13.1 and M13.12), with concurrent underexpression of adaptive immune responses (lymphocytic aggregates A1 and A6, B cell module M13.18, T cell modules M16.24 and M15.38). This study establishes that homeRNA enables flexible, responsive sampling during disasters, overcoming traditional logistical barriers to capture time-sensitive biological data across dispersed populations.

6.1 Introduction

The incidence and severity of wildfires have become a global concern, with many regions experiencing increases in fire season lengths and fire intensity.[1–3] A key pollutant present in wildfire smoke is $PM_{2.5}$, defined as particulate matter 2.5 μm in diameter or smaller, which comprises about 90% of wildfire smoke.[4–6] Between 2007 to 2018, wildfires have accounted for about 25% of $PM_{2.5}$ concentrations across the United States (U.S.) and up to 50% in the Western U.S.[7,8] Even in states where there are no wildfire burns in a given year, smoke from wildfires in other states or Canada can exacerbate $PM_{2.5}$ exposure due to transported smoke.[9] Wildfires are also increasingly prevalent globally, with major impacts documented in Australia, India, Indonesia, Brazil, Mediterranean Europe, Canada, and across African savannas.[10,11]

Wildfires not only have a severe impact on the environmental landscape but also are a contributor to adverse human health outcomes.[12–19] With the growing body of literature on the effects of wildfire smoke exposure on overall health, there has also been a push to understand the impacts of $PM_{2.5}$ exposure from a biomolecular mechanistic perspective, particularly on the respiratory tract and systemic inflammation.[20–23] Understanding the biological mechanisms involved in wildfire smoke exposure could enable biomarker discovery, targeted therapy development, and development of risk assessment tools for smoke exposure prevention and response. Moreover, understanding the transient immune response to wildfire smoke is critical as it can affect medical interventions ranging from vaccine efficacy[24] to reproductive health outcomes including sperm quality[25,26], potentially influencing both the timing and distribution of healthcare services during smoke events.

There have been multiple studies that have investigated acute inflammatory activation in wildland firefighters in response to occupational smoke exposure.[20,23,27–31] Most studies that capture wildfire smoke effects in the general population (i.e., smoke events unrelated to occupational exposure or controlled burns) are retrospective, where they take advantage of a separate study that happens to occur while a wildfire happens. Recently, Aguilera et al. designed a study to capture immune response to wildfire smoke exposure, where participants in an urban center came in for phlebotomy draws before, during, and after wildfire events. This study also found alterations in inflammatory protein prevalence in human blood in response to

wildfire smoke.[32] Johnson et al. recently examined immune responses in smoke-exposed individuals, demonstrating increased activation markers on memory T cells via mass cytometry and identifying 133 differentially methylated gene loci associated with smoke exposure[33] adding to other studies that have investigated the effects of wildfire smoke on DNA methylation[34,35], but there have been few studies that have investigated the transcriptomic immune response to wildfire smoke exposure in humans.

Understanding why such transcriptomic studies are rare requires examining the unique methodological challenges of wildfire smoke research. Typically, in person clinic-based blood draws are used to study longitudinal immune responses in blood transcriptomes. However, a similar study design for investigating the effects of wildfire smoke exposure is logistically challenging due to the unpredictable nature of wildfires and the low accessibility to healthcare and research centers in rural areas, where many fires occur. Running a clinic-based blood draw study on the general population experiencing wildfire smoke exposure would require either (1) relying on historical data to choose a location that has the infrastructure to support frequent clinic-based blood draws and a high prevalence of wildfire smoke[32], (2) setting up a multi-site clinic-based study to increase the chances that at least one site has a wildfire smoke event, or (3) relying on retrospective studies or capturing smoke exposure incidentally on a study investigating a different question where longitudinal blood samples are collected.[24,35,36] These factors make designing studies where blood is collected at multiple time points in response to wildfire smoke exposure logistically challenging and limit the number of participants included from rural areas.

To address this challenge, we employed a remote and flexible study design using homeRNA: a self-sampling kit comprising a commercially available blood collection device, Tasso-SST, and a custom engineered RNA stabilization tube we previously developed.[37] The homeRNA kit allows study participants to self-collect and stabilize blood by themselves in their own homes for shipment back to a centralized lab for downstream analysis. We have already demonstrated the ability to use homeRNA in high temperature settings[38,39] and to assess gene expression changes during acute respiratory infections from SARS-CoV-2.[40,41] Here, our primary objectives were to (1) evaluate the feasibility of a study design that allowed flexible responsive sampling during disasters, (2) demonstrate the usability of homeRNA across a 10-month

longitudinal study, and (3) assess the immediate and longitudinal effects of wildfire smoke exposure on gene expression in an initial cohort.

By facilitating self-sampling at home, homeRNA allows for a study design that includes a wider reach of participants living in remote locations who are traditionally inaccessible by mobile phlebotomists or clinic-based blood draws. Study kits can be mailed to participants within a day of a disaster warning or occurrence (such as a wildfire event), thus reducing the need to predict where the disaster would occur ahead of the study as would be required for a clinic-based blood draw study design. In contrast, in-clinic appointments need to be scheduled in advance and may not occur until days or up to a month after exposure, thereby missing the timescale of response that may be more immediate. Furthermore, multiple kits can be sent in one shipment that can be used by participants over several time points upon receiving, allowing for repeated sampling across different groups in response to an event as well as within a single individual throughout a repeated exposure. Here, we implemented homeRNA into a wildfire smoke exposure study to collect blood from 58 participants (635 total samples) across the Western and South Central U.S. before, during, and after wildfire smoke exposure from June 2021 to April 2022. We analyzed a subset of these samples with a targeted Autoimmune response gene panel followed by a gene-set enrichment visualization and interpretation repertoire known as BloodGen3. We analyzed high wildfire exposure response in six participants located in Okanogan County, Washington, which experienced two major wildfires during this time frame that resulted in Air Quality Index (AQI) categories ranging between very unhealthy ($PM_{2.5}$ 125.5 - 225.4 $\mu g/m^3$) and hazardous ($PM_{2.5} \geq 225.5$ $\mu g/m^3$) for two weeks in July 2021. We compared the immune response in participants who were being exposed during these dates (n=6) with the immune status of participants located elsewhere (California (n=2) and Western Washington (n=1)) during the same timeframe. The participants not located in Okanogan County (n=3) experienced low and moderate wildfire exposure throughout the study, with AQI categories ranging between good ($PM_{2.5} \leq 9.0$ $\mu g/m^3$) to unhealthy ($PM_{2.5}$ 55.5 - 125.4 $\mu g/m^3$) throughout the season.

6.2 homeRNA allows for investigating the effects of wildfire smoke exposure across a large geographic area (Western and South Central U.S.)

homeRNA is a kit that allows for the self-sampling and stabilization of whole blood RNA. It consists of a commercially available blood sampling device, the Tasso-SST and a custom designed stabilization tube. Study participants were mailed homeRNA kits throughout the study, where they sampled and stabilized their own blood in response to wildfire smoke exposure. Our study design consists of three stages of homeRNA sampling: 1) collecting baseline blood samples before wildfire smoke exposure, 2) collecting exposure samples during wildfire smoke exposure, and 3) collecting post-exposure samples three and six months after wildfire smoke exposure (Figure 6.1). At each stage, participants were sent three homeRNA kits and asked to self-collect and stabilize blood samples every 3-4 days. After each sample collection, the participant then shipped their homeRNA-stabilized blood sample back to the study team location (Seattle, Washington).

In the first stage of sampling, participants were sent homeRNA kits immediately after enrollment and collected up to three baseline samples that were collected every 2-4 days prior to wildfire smoke exposure (Figure 6.1A). Active enrollment occurred during the beginning of June to mid-July 2021. We note that for many participants this was a true baseline, as they did not experience wildfire smoke exposure, but for some participants, particularly those located in Okanogan County who experienced smoke earlier than expected, some of the three "baseline" samples (0-2 samples of the 3 baseline samples) were collected during a transported wildfire smoke event from a fire in Canada at the end of June that caused moderate AQI due to smoke exposure in the region. Even though there was some moderate exposure during this time we still considered these as baseline samples in our analysis, as the magnitude of difference between the exposure during this time (moderate $PM_{2.5}$ range from 9.1 - 35.4 $\mu g/m^3$) was substantially less than the exposure these participants experienced later in July 2021 (very unhealthy $PM_{2.5}$ 125.5 - 225.4 $\mu g/m^3$ to hazardous $PM_{2.5}$ $\geq$225.5 $\mu g/m^3$).

In the second stage of sampling, the study team monitored the daily average $PM_{2.5}$ level and wildfire occurrence in each participant's location using the Environmental Protection Agency (EPA) AirNow

website (https://fire.airnow.gov/). When the first wildfire was reported (located in Okanogan County), participants were immediately shipped a package containing three homeRNA kits to serve as wildfire smoke exposure samples (Figure 6.1B). In our particular study, a second wildfire was also reported in Okanogan County one week after the first event, so an additional package containing three homeRNA kits were sent to participants in Okanogan County. Each exposure sampling window lasted for about 1.5 weeks, thereby capturing multiple time points throughout a wildfire event (e.g., before, during, and after the wildfire-specific $PM_{2.5}$ spike). Participants who did not experience high exposure from the Okanogan County wildfires also received three homeRNA kits at similar time points to serve as low to moderate exposure comparison groups. Stage two sampling took place during mid-July to the end of September 2021.

Lastly, in the third stage of sampling, post-exposure samples were collected from all participants to assess the potential longitudinal effects of wildfire smoke exposure (Figure 6.1C). In this case, participants were sent a first set of three homeRNA kits three months (October to early November 2021) after the wildfire events in Okanogan County and a second set of three homeRNA kits six months (February to early April 2022) after the wildfire events. After completion of the study, each participant's daily average $PM_{2.5}$ exposure from wildfire smoke was recorded based on each participant's nearest EPA $PM_{2.5}$ monitor (see Methods for details) to assess overall exposure levels due to wildfire smoke exposure (Figure 6.1D).

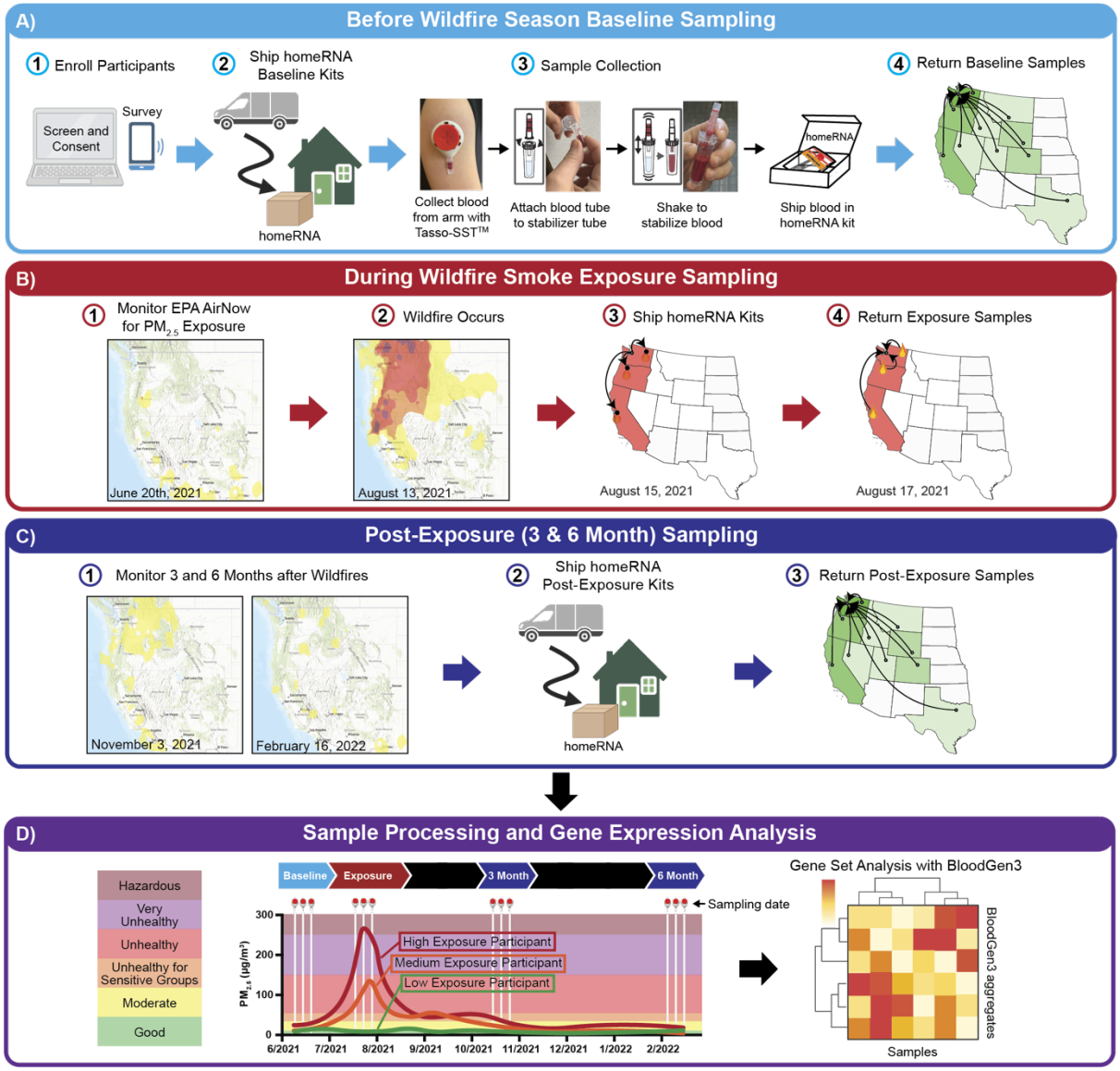

Figure 6.1. Study design for using homeRNA to investigate the effects of wildfire smoke exposure. A) Participants were enrolled across the Western and South Central United States and sent three homeRNA kits to collect baseline blood samples, which were then returned to the study team (Seattle, Washington). B) Throughout the 2021 wildfire season (June-September), wildfire occurrence and smoke exposure ($PM_{2.5}$) were monitored using the EPA AirNow site. When a wildfire occurred, three homeRNA kits were sent to participants experiencing wildfire smoke exposure to collect exposure samples. Eighteen participants were located in Okanogan County in Washington, where two severe wildfires occurred. A subset of participants located outside of Okanogan County were also sent three homeRNA kits and sampled at similar time to serve as low exposure controls. C) All participants were sent three homeRNA kits between October-early November (~3 months after wildfire events in Okanogan County), then again in February-April (~6 months after wildfire events in Okanogan County) to collect post-exposure samples. D) Representative $PM_{2.5}$ exposure timeline from a participant's nearest outdoor EPA $PM_{2.5}$ monitor. White vertical lines indicate blood sampling timepoints. Participants were categorized by exposure (High, Medium, or Low; see Methods). RNA from subset samples was analyzed using Nanostring gene panel coupled with BloodGen3 gene-set analysis.

In the present study, a total of 119 individuals were screened beginning in June 2021 (Figure 6.2); of these individuals screened, 10 were not eligible and 17 did not finish the screening process. Of the 92 eligible individuals, 63 participants were enrolled into the study for homeRNA sampling, with preference given to those located in Okanogan County, Washington (WA), as well as individuals who added to geographic diversity. Of the 63 enrolled participants, 5 did not collect any samples. In the end, 58 participants across 10 Western and South Central U.S. States completed the study (Washington, Oregon, California, Colorado, Idaho, Montana, Nevada, Utah, Wyoming, and Texas) and we captured two wildfire events that occurred in Okanogan County, WA (Figure 6.3A). We received a total of 635 homeRNA-stabilized samples before, during, and after the wildfire season. Of the 58 sampled participants, the median age was 41 (range 20-76), 71% (n=41) reported female sex at birth, 29% (n=17) reported male sex at birth, 50% (n=29) were from Washington, and 31% (n=18) were from Okanogan County (Figure 6.3B).

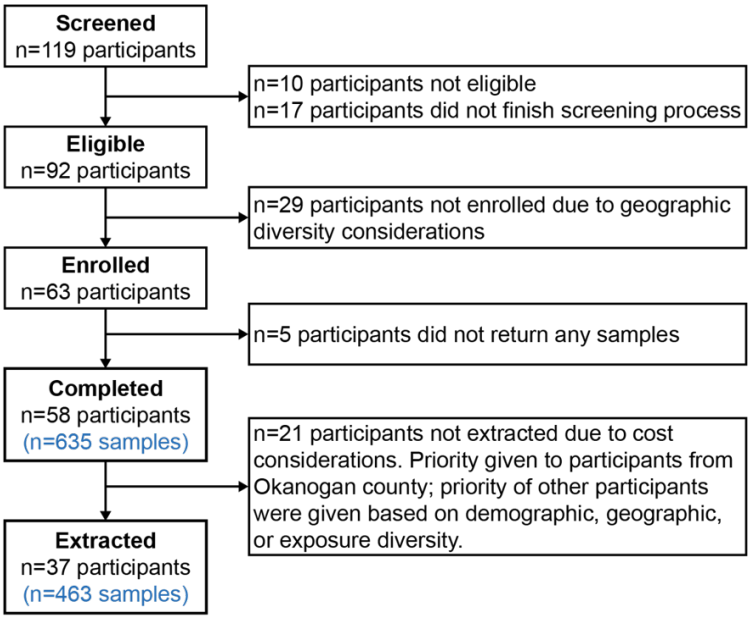

Figure 6.2. Study participant and sample flow chart. Participants were selected with a preference given to geographic diversity and those in highly wildfire-prone areas.

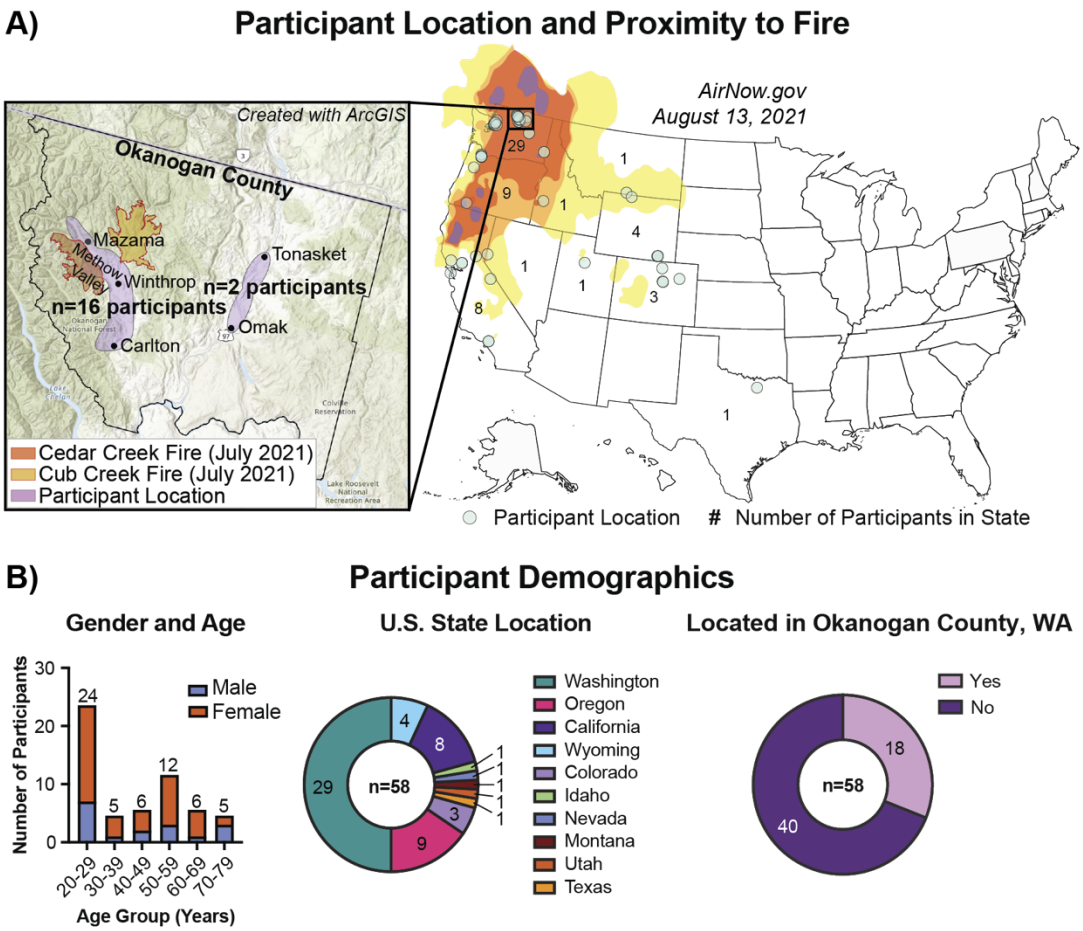

Figure 6.3. Location and demographics of study participants. A) Location of study participants in the Western and South Central United States. Each participant is represented by a circle and each state is numbered based on the number of participants located within the state. $PM_{2.5}$ levels from August 13, 2021 are shown as an overlay on the map, with colors representing the air quality index, available from the EPA AirNow interactive air quality map (airnow.gov/aqi/). Inset depicts Okanogan County in Washington state, where 18 total participants are located, with the burned area of two major wildfires, the Cedar Creek and Cub Creek fire, that started in July 2021. Inset map was generated with ArcGIS software, where each participant's reported zip code was used to generate coordinates (arcgis.com). Fire boundaries were provided by Central Washington Fire Recovery (centralwashingtonfirerecovery.info/wildfire-reports/). B) Demographics of all sampled participants who completed the study (n=58 participants), including gender, age, US state location, and number of participants located in Okanogan County, which was the area of the two major wildfires captured in this study.

6.3 homeRNA is an easy-to-use kit that allows high retention and flexibility across a 10-month long longitudinal study

Spanning 10 months (June 2021-April 2022), each participant collected up to 15 blood samples with the homeRNA kit before, during, and after the wildfire season; an average of 11 samples were self-collected from each participant. Despite the extended study duration and frequent sampling requirements,

we achieved remarkably high study retention. Of the 58 participants who completed at least one sample at the start of the study, 93% (n=54/58) collected at least 6 samples. All of the study participants were also asked to sample 3-months post wildfire smoke exposure (between October and November 2021), and 95% (n=55/58) completed at least one of the three requested samples (samples were scheduled to be every 2-4 days for each set of 3 samples). For the 6-month post exposure samples (between February to April 2022), 37 participants were asked to complete sampling and 95% (n=35/37) completed at least one of the three requested samples; this was at the end of 10 months total time after initial enrollment in June 2021 in the study. In the study conclusion survey, 93% of participants (n=50/54 participants who completed the closing survey) expressed interest in participating in a second year of the study during the 2022 wildfire season.

To assess the usability and practicality of using homeRNA in a 10-month longitudinal study, each participant completed a sample collection survey (see methods for details) that included questions regarding the usability of the homeRNA kit each time they sampled. As participants collected up to 15 samples in this study, we were first interested in participants' perceptions the first time they used the kit. After collecting their first blood sample, the majority of participants took a total of 5-10 minutes to sample and stabilize their blood with homeRNA and reported that the Tasso-SST device and the custom-engineered stabilizer tube were easy to use (Figure 6.4A). Additionally, all participants reported no or mild pain (n=35/58 reported no pain and n=23/58 reported mild pain) associated with the blood collection using homeRNA for the first time (Figure 6.4A). These initial responses suggest that the homeRNA kit was easy to use even during the first attempt.

We collected a total of 636 sampling surveys throughout the study. We note that while we collected 636 surveys, we received 635 homeRNA-stabilized blood samples; notably, throughout our 10-month study, only one sample was missing. When all the sampling surveys were assessed, the questions related to the homeRNA kit's usability showed similar responses as their first survey response (Figure 6.4B) The similar survey responses between the first sample collection and all sample collections demonstrate that homeRNA was easy to use in the beginning and stayed easy to use throughout the study. Overall, the survey

responses regarding the usability of homeRNA suggest the effectiveness of deploying homeRNA in a remote study design.

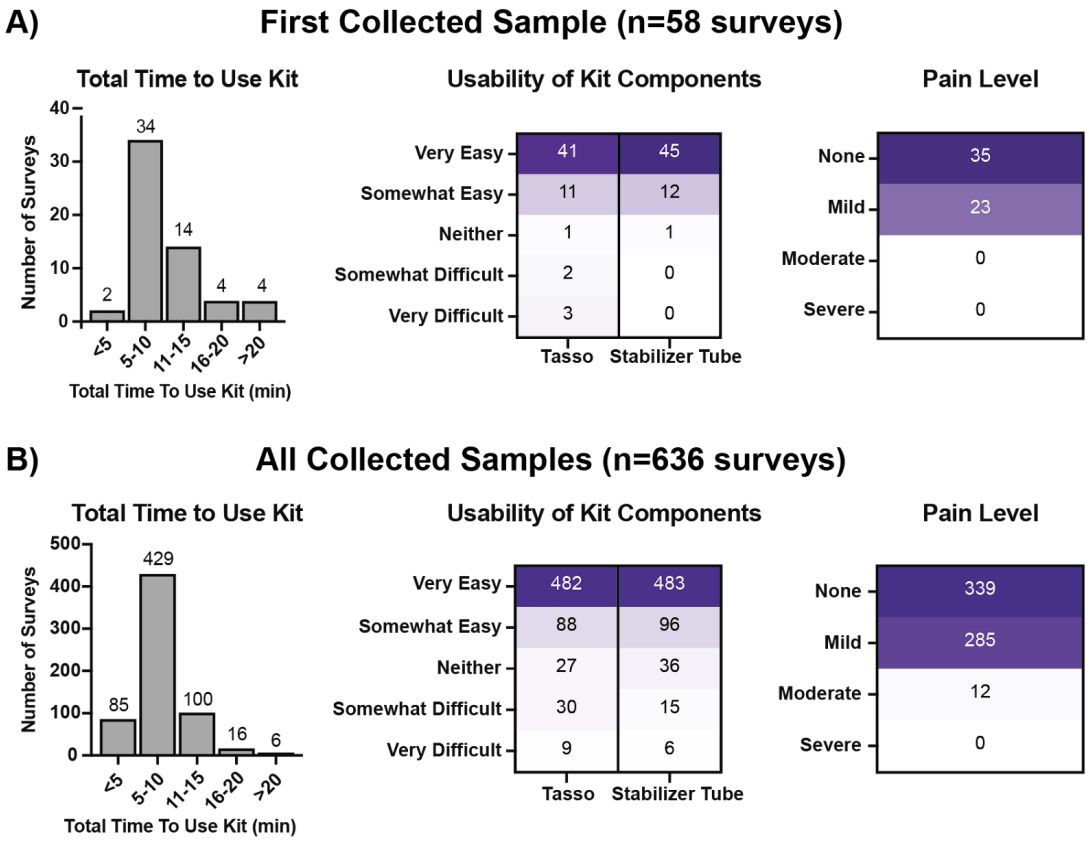

Figure 6.4. Usability survey responses for using the homeRNA kit to self-collect and stabilize blood throughout the study. Participant survey responses on the total time to use the homeRNA kit (left), the usability of the Tasso-SST blood collection device and the stabilizer tube (middle), and the pain level associated with blood collection (right) from A) first collected sample (n=58 surveys) and B) all collected samples (n=636 surveys) from 58 participants.

Apart from the kit being easy to use, the flexibility of the study design enabled by the remote self-blood sampling and stabilization further increased user's perception and willingness to be included in a study using homeRNA. A follow-up survey was administered in November 2023, 18 months after the completion of the study on the 2021 wildfire season, to assess participants' preference for the remote study design over a clinic-based blood draw study design and overall perception of a homeRNA-based remote study. In this survey, 93% of the respondents (n=28/30) considered participating in a remote blood sampling study (the current study) to be "significantly easier" or "somewhat easier" than an in-person blood sampling

study (e.g., clinic-based blood draw) (Figure 6.5A), reporting that length of commute to a clinic and difficulty fitting a clinic visit into their schedule was a barrier to in-person participation (Figure 6.5D). In contrast, 77% (n=23/30) reported that the flexibility in sampling time was an important factor in remote-sampling participation (Figure 6.5B). Given that this study design could be applied to investigate transcriptomic responses during various natural hazards (e.g., wildfires, earthquakes, extreme weather), we assessed participant comfort with using homeRNA kits during emergency situations. Notably, 83% (n=25/30) of respondents reported that they would be "very comfortable" or "somewhat comfortable" with using homeRNA during a disaster resulting from a natural hazard (Figure 6.5C). Lastly, almost all respondents (n=29/30) indicated that they would be willing to participate in this or a similar remote blood sampling study again (Figure 6.5E), with 70% (n=21/30) reporting that they would participate in a similar remote blood sampling study for up to 5 years (with this option being the longest period we provided in the survey) (Figure 6.5F).

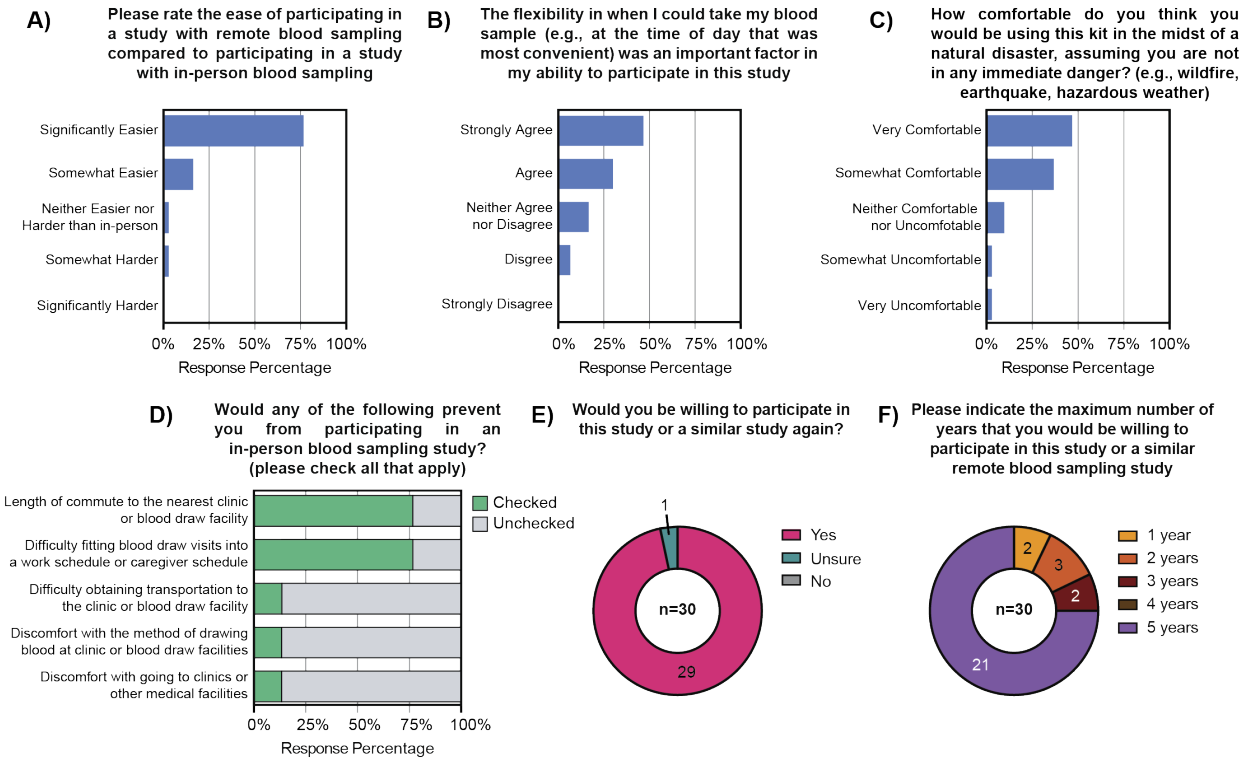

Figure 6.5. Follow-up survey responses from 30 participants (out of 40 participants invited) who were surveyed 18 months after the completion of the 10-month long wildfire smoke exposure study (June 2021-April 2022). A) Survey response on the A) ease of participating in a remote blood sampling study compared

to an in-person blood sampling study, B) flexibility provided by remote-based sampling, and C) comfortability of homeRNA-based sampling during a disaster. D) Checklist response on barriers to participating in an in-person blood sampling study. E) Survey response on willingness to participate in a similar remote blood sampling study again and F) maximum number of years willing to participate in a similar study again. Full survey questions are available in the Supplementary Information.

6.4 Our flexible study design captured a wide range of $PM_{2.5}$ exposure throughout wildfire season

Our study captured two major wildfires, both of which occurred in Okanogan County, WA in July 2021: the Cedar Creek Fire and the Cub Creek Fire (Figure 6.3A). Therefore, we will discuss the 58 sampled participants in the context of three groups based on their daily average $PM_{2.5}$ exposure: 1) high exposure participants (n=20 participants), which were 17 participants located in Okanogan County who were exposed to active wildfire smoke and three participants located in Nevada, Oregon, and California who were exposed to active wildfire smoke from the Caldor fire in Northern California and Nevada, 2) medium exposure participants (n=5 participants), which were participants who had elevated $PM_{2.5}$ levels in the unhealthy AQI category due to indirect wildfire smoke exposure (one participant was in Okanogan County farther away from the active wildfire, three participants were in Washington outside of Okanogan County, and one participant was in California who experienced a wildfire event later in the study), and 3) low exposure participants (n=32 participants) located in all other sampled states/counties who were not exposed to wildfire smoke and experienced good or moderate AQI categories based on our internal cut-off for how we defined $PM_{2.5}$ exposure (see extended details in Methods). The daily average $PM_{2.5}$ data (indoor and outdoor) of an example participant from each exposure group across the study timeline (June 2021 - April 2022) was plotted against their homeRNA sampling dates (Figure 6.6A); these graphs are color coded based on the EPA's AQI categories based on $PM_{2.5}$ exposures (Table 6.1). A subset of participants were selected to receive Indoor PurpleAir sensors to track indoor $PM_{2.5}$ concentrations. The daily average indoor Purple Air sensor data is plotted in grey on Figure 6.6A for three example participants, along with the outdoor EPA $PM_{2.5}$ monitors in black. The outdoor EPA $PM_{2.5}$ monitor data for the nine participants with samples analyzed with the Nanostring gene panel are plotted in Figure E3, with indoor PurpleAir $PM_{2.5}$ also plotted when available.

To visualize the $PM_{2.5}$ exposure for all participants throughout the wildfire season, we summarized the outdoor $PM_{2.5}$ data of all 58 sampled participants during June through September 2021 in a color coded heatmap based on the EPA's AQI categories (Figure 6.6B). In this heatmap, we grouped participants based on their wildfire exposure (high, medium, or low) to visualize the differences in $PM_{2.5}$ ranges captured in our study. This visualization helps illustrate temporal patterns in $PM_{2.5}$ exposure across the sampled cohort, highlighting the periods of elevated $PM_{2.5}$ levels during the Okanogan County Cedar Creek and Cub Creek wildfires in late July and early August 2021. The sporadic elevated $PM_{2.5}$ levels visible in the medium exposure group throughout August and September demonstrate the variable nature of indirect wildfire smoke exposure. White squares in the heatmap represent days where $PM_{2.5}$ concentrations were not reported by the EPA $PM_{2.5}$ monitor for that participant's location, which constitutes a potential limitation of this study as it may result in incomplete exposure characterization for some participants during certain time periods.

Table 6.1: AQI Categories and $PM_{2.5}$ Cutoffs as defined by the EPA (updated on February 2024)

AQI Category	**$PM_{2.5}$ (ug/m^3) Breakpoints for each AQI Category**
Good	0.0 - 9.0
Moderate	9.1 - 35.4
Unhealthy for Sensitive Groups	35.5 - 55.4
Unhealthy	55.5 - 125.4
Very Unhealthy	125.5 - 225.4
Hazardous	≥225.5

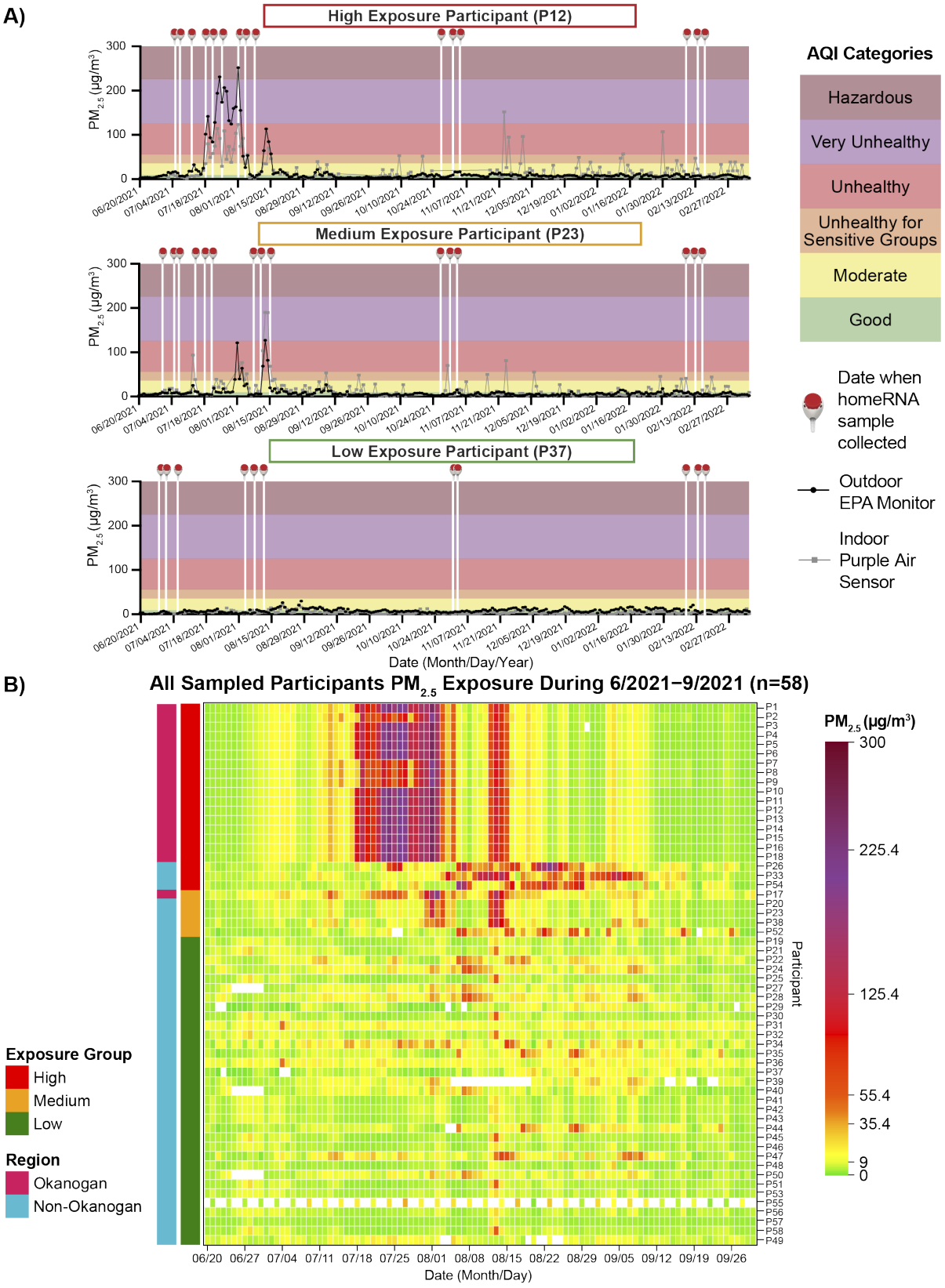
A)
High Exposure Participant (P12)
Medium Exposure Participant (P23)
Low Exposure Participant (P37)
PM2.5 (µg/m3)
300
200
100
0
06/20/2021
07/04/2021
07/18/2021
08/01/2021
08/15/2021
08/29/2021
09/12/2021
09/26/2021
10/10/2021
10/24/2021
11/07/2021
11/21/2021
12/05/2021
12/19/2021
01/02/2022
01/16/2022
01/30/2022
02/13/2022
02/27/2022
Date (Month/Day/Year)
AQI Categories
Hazardous
Very Unhealthy
Unhealthy
Unhealthy for Sensitive Groups
Moderate
Good
Date when homeRNA sample collected
Outdoor EPA Monitor
Indoor Purple Air Sensor
B)
All Sampled Participants PM2.5 Exposure During 6/2021−9/2021 (n=58)
Exposure Group
High
Medium
Low
Region
Okanogan
Non-Okanogan
Participant
PM2.5 (µg/m3)
300
225.4
125.4
55.4
35.4
9
0
06/20
06/27
07/04
07/11
07/18
07/25
08/01
08/08
08/15
08/22
08/29
09/05
09/12
09/19
09/26
Date (Month/Day)

Figure 6.6. homeRNA was able to capture a wide range of participant $PM_{2.5}$ exposures across the study period. A) Data from example participants exposed to high, medium, or low levels of wildfire smoke, plotted against the homeRNA sampling timepoints (white vertical lines with Tasso symbols on top), outdoor EPA $PM_{2.5}$ monitor (black lines with data points), indoor PurpleAir sensor (grey lines with data points), and AQI categories (colored background). B) Heatmap summarizing the outdoor $PM_{2.5}$ levels during the wildfire season (June 2021-September 2021) for all 58 sampled participants. Heatmap rows represent individual participants and columns represent daily average $PM_{2.5}$ concentrations for each participant throughout the 2021 wildfire season, with each $PM_{2.5}$ cell colored by the corresponding AQI category. Cells colored white represent days where no $PM_{2.5}$ concentrations were collected by the participant's nearest EPA $PM_{2.5}$ monitor. Participants are color-coded based on their geographic region (magenta: Okanogan County, teal: Non-Okanogan County) and exposure levels (red: high exposure, orange: medium exposure, green: low exposure).

6.5 homeRNA demonstrated sufficient RNA quality throughout study

At the end of the study, a total of 635 homeRNA samples were returned from 58 participants. Total blood cellular RNA was extracted from 463 samples for quality assessment. RNA integrity number (RIN) values were assessed across all participant samples to evaluate RNA quality from stabilized blood collections. Of the extracted samples, the average RIN value was 7.4 ± 1.3 with 92% of samples (n=426/463) above a RIN value of 6 (Figure 6.7A), which was the cutoff RIN value we used for downstream transcriptomic analysis; the 455 samples for which a RIN value was obtained are reflected in Figure 6.7A (eight samples did not yield a RIN value). Despite the presence of some degraded samples, the majority of samples yielding RIN values ≥ 6 indicates successful RNA preservation in our study, which is in concordance with our previous literature.[58–62] Collection efficiency was also high, with most participants collecting blood samples within 3-5 minutes and most samples had at least 300 μL of blood (n=412/636 surveys reported blood level 3 or 4) (Figure E1). Additionally, the distribution of RIN values varied both within and between participants, with low RIN values (< 6) occurring sporadically across the cohort rather than clustering within specific individuals, and participant age was also not predictive of RNA quality (Figure E2).

To assess potential confounding factors in our home-based sample collection protocol, we examined RIN values in relation to sampling date and $PM_{2.5}$ exposure levels. Sample collection occurred over a 10-month period and RIN values were consistently adequate throughout the sampling timeline, suggesting that seasonal variations did not systematically affect sample integrity (Figure 6.7B). Similarly,

$PM_{2.5}$ exposure levels, which varied across participants due to wildfire smoke events, did not negatively affect RNA stabilization and subsequent RIN values (Figure 6.7C). These findings demonstrate that our study successfully captured high-quality RNA samples across diverse temporal and environmental conditions, suggesting that homeRNA was robust to external factors that might otherwise introduce bias into RNA quality assessments. This further reinforces our previous studies where we found minimal effects of shipping time and temperature on homeRNA-stabilized samples.[38,39]

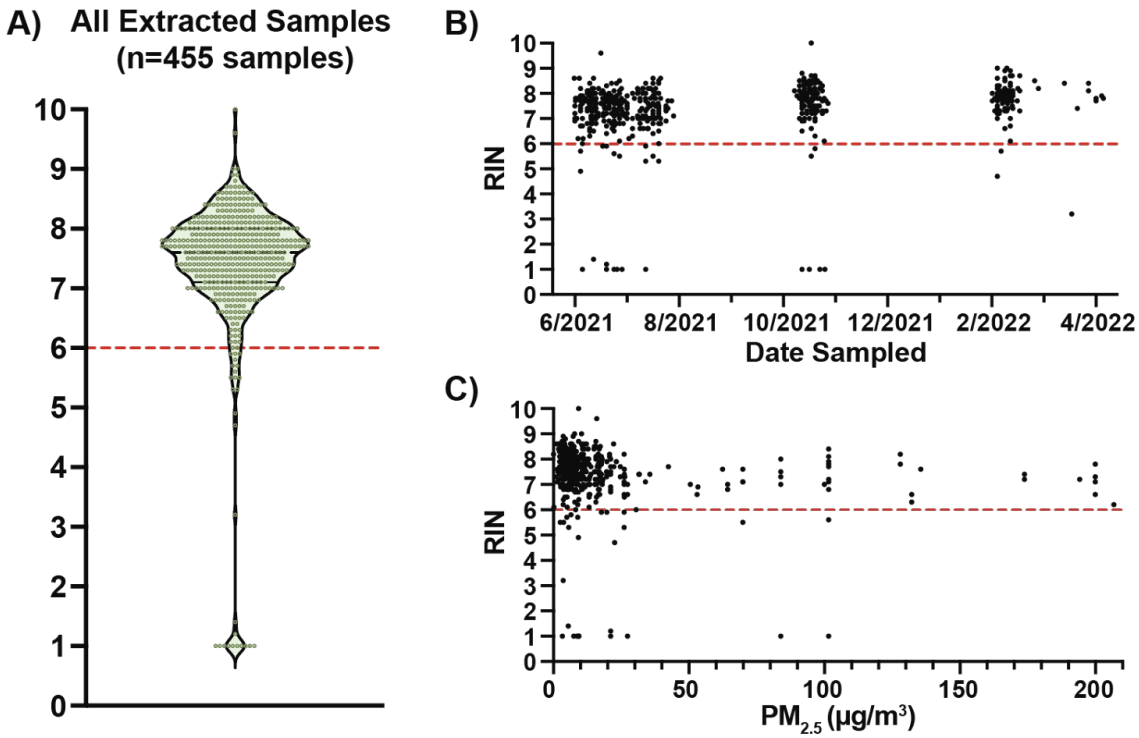

Figure 6.7. homeRNA was able to sufficiently stabilize RNA and preserve integrity throughout the 10-month long study regardless of sampling season and participant exposure. A) Resulting RNA Integrity Number (RIN) values of all extracted samples (n=455 samples). Eight samples did not yield a measurable RIN value. RIN values are given on a scale from 1 to 10, with a RIN of 1 representing the most degraded RNA and a RIN of 10 representing the most intact RNA. We used an internal quality control cutoff at RIN = 6 for downstream transcriptomic analysis. B) RIN values according to the date of sample collection and stabilization throughout the study period (June 2021 – April 2022). C) RIN values according to the corresponding average $PM_{2.5}$ exposure on the date of sampling.

6.6 Gene expression analysis of subset of participants shows preliminary patterns suggesting inflammatory changes with gene set analysis

In a preliminary analysis, we analyzed 107 samples from nine participants (out of 463 extracted samples from 37 participants) using a targeted Nanostring Autoimmune gene panel. The Autoimmune panel

includes 770 genes that encompass 35 pathways and processes associated with autoimmune disease and chronic inflammatory disorders; in particular, we were interested in capturing a wide array of inflammation markers, based on previous studies implicating an inflammatory-like response to wildfire smoke exposure.[21,28,29,31,36] Since there is no established transcriptional marker for wildfire smoke exposure, we chose to map the Nanostring gene expression data to the BloodGen3 repertoire framework, which contextualizes inflammatory signatures within broader immunological networks, rather than examining individual genes in isolation. BloodGen3 is a fixed repertoire of 382 transcriptional modules (which cluster into 38 module aggregates) derived from gene co-expression patterns across 985 blood samples from 16 diverse immunological and physiological states (including bacterial and viral infections, autoimmune diseases, COPD, cancer, and pregnancy).[42,43] This fixed repertoire provides a stable framework for analyzing and interpreting blood transcriptome data by grouping co-regulated genes into functionally annotated modules. Beyond the 16 cohorts used to construct the modules, this repertoire has since been applied to multiple independent datasets spanning diverse conditions and physiological states, providing a consistent reference for interpreting blood transcriptional profiling data and enabling cross-study comparisons.[44–49]

The nine participants for the preliminary analysis were chosen to include both participants from Okanogan County primarily (n=6, P5, P6, P8, P10, P12, P17), along with some participants with low exposure located in California (n=2, P31, P37) and medium exposure located in central Washington (n=1, P23), which experienced moderate smoke exposure from the Okanogan County fires. First, we performed a baseline correction on each participant's exposure timepoint samples by subtracting each participant's median gene module enrichment score calculated from their baseline timepoint samples. This correction allows for each participant to serve as their own control, thereby allowing us to identify changes in gene module activity relative to each participant's individual pre-exposure (i.e., baseline) state, this improves sensitivity for detecting exposure-related changes, while minimizing confounding effects of baseline differences We then compared the baseline-corrected enrichment scores between high-smoke-exposed participants (from Okanogan County) and low-medium-exposed participants during the active wildfire

period to identify modules that responded differently to smoke exposure. Of note, "exposure" timepoint samples from the low and medium smoke exposure participants (P23, P31, and P37) represent the time that they were collected, not the level of smoke exposure; these participants were sampled at the same time as the participants in Okanogan County who were the only group to actively experience wildfire smoke in the context of this analysis.

At the individual gene level, we identified 253 genes with differential expression (FDR < 0.05) between exposed and non-exposed groups. To determine biological significance, we also performed a minimum-effect test where the null hypothesis was $|\log_2 FC| \leq 0.5$.[50] No genes achieved FDR < 0.05 using this more stringent approach, indicating that while statistical differences exist, no genes showed fold changes greater than 1.4-fold with controlled false discovery rate. However, small transcriptional changes can still reflect biologically meaningful differences, particularly for regulatory genes and transcription factors that may not elicit large expression changes. Given our smaller panel (~770 genes) and limited sample size (n=6 vs 3), we present these findings as preliminary observations requiring further validation.

We next evaluated transcriptomic changes at the gene set level using the BloodGen3 framework. Of the 770 genes present in the Nanostring panel (20 of which are housekeeping genes), 567 genes were present in the BloodGen3 framework comprising 382 modules. These 382 modules are further organized into 38 higher-order module aggregates based on functional and expression similarities, providing both granular (module-level) and broader (aggregate-level) perspectives on immune system activity. At the module level, we evaluated enrichment across all 382 modules that comprise the BloodGen3 framework. We observed 10 modules representing distinct immune functions with differential expression patterns between the high-exposure wildfire exposed participants (i.e., Okanogan County participants, n=6) and the non-exposed participants (i.e., participants in other locations, n=3) (FDR < 0.05) (Figure 6.8A). These included modules associated with inflammation (M13.1 and M13.12 overexpressed in high exposure group), B cells (M13.18 underexpressed in high exposure group), T cells (M16.24 and M15.38 underexpressed in high exposure group), prostanoids (M8.2 overexpressed in high exposure group), and monocytes (M15.7 underexpressed in high exposure group). The overexpression of the prostanoid module

(M8.2) in the high exposure group suggests activation of cyclooxygenase-derived lipid mediators, which have been found to promote inflammation while suppressing adaptive immunity through prostaglandin E2 (PGE2) signaling[51]. The underexpression of the monocyte module (M15.7) in the high exposure group could potentially reflect monocyte redistribution rather than true suppression, as previous studies have demonstrated that particulate matter exposure can stimulate bone marrow release of monocytes with subsequent migration to lung tissue[52,53]. At the BloodGen3 aggregate level, we examined the 38 higher-order module aggregates that represent major immunological and physiological processes (Figure 6.8B). Of the 38 aggregates, we observed eight aggregates with differential expression patterns in the wildfire exposed participants compared to the non-exposed participants. Four of these aggregates did not have annotated functions. The other four aggregates had annotation functions of lymphocytic (aggregates A1 and A6, both underexpressed, suggesting potentially reduced adaptive immune cell activity or other mechanisms) and inflammation (aggregates A33 and A35, both overexpressed, possibly indicating increased innate immune activation and inflammatory mediator expression); in previous work, a similar expression pattern was found to be associated with psoriasis.[49] This pattern of decreased circulating lymphocyte-associated transcripts alongside increased inflammatory markers is consistent with complex stress-induced immune modulation, potentially involving lymphocyte redistribution and inflammatory activation[43,54]. Further, the presence of altered but functionally unannotated modules and aggregates is expected within the BloodGen3 framework, as modules are defined purely by co-expression patterns across diverse immunological states rather than by predetermined functional categories[43]. These unannotated modules and aggregates may represent novel coordinated transcriptional responses specific to environmental exposures like wildfire smoke or biological processes not yet well-characterized. Their alteration suggests wildfire smoke exposure may affect transcriptional networks beyond classical immune pathways, which warrants future investigation to determine their biological significance.

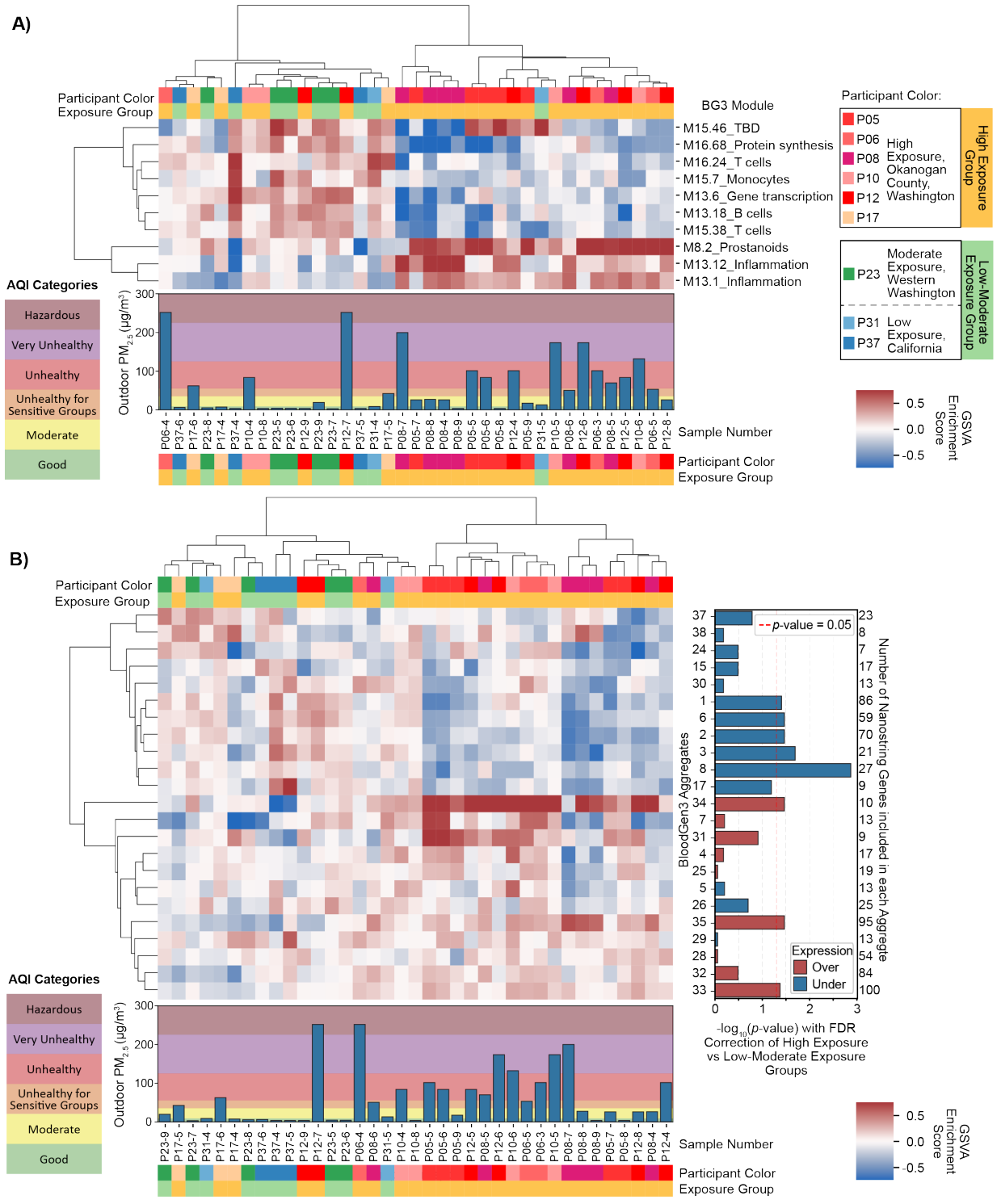

Figure 6.8. Heatmap of wildfire smoke exposure gene expression using BloodGen3 framework. Blood samples from nine participants (six high-exposure from Okanogan County, three low-moderate exposure from other locations; n=107 samples total) were analyzed using the Nanostring Autoimmune panel (770 genes), with 567 genes mapped to the BloodGen3 framework. A) Module-level and B) aggregate-level heatmaps show gene set variation analysis (GSVA) enrichment scores after baseline correction (participant-

specific median enrichment scores were subtracted from pre-exposure samples). Positive scores (red) indicate higher than average gene expression in a given module/aggregate; negative scores (blue) indicate lower than average gene expression in a given module/aggregate. Rows represent BloodGen3 A) modules or B) aggregates with hierarchical clustering; columns represent individual samples with hierarchical clustering. Sample labels indicate participant and sample number (e.g., P23-9 represents sample 9 from participant 23). Bar plots below heatmaps show average outdoor $PM_{2.5}$ concentrations from nearest EPA monitor on sampling dates, colored by EPA AQI categories. In B), statistical significance was assessed using two-sample Welch's t-tests comparing high vs. low-moderate exposure groups with Benjamini-Hochberg correction for multiple testing (FDR < 0.05). Significant aggregates are shown with $-\log_{10}$(p-values) on the right; red bars indicate overexpression, blue bars indicate underexpression.

6.7 Discussion

This study demonstrates that homeRNA technology enables flexible remote study logistics for investigating gene expression changes due to wildfire smoke exposure with geographically distributed participant recruitment. With homeRNA, participants can easily self-collect and stabilize blood samples in their homes throughout extended study periods, overcoming the inherent challenges of long-term, in-person blood collection studies. In this study, we employed a dual recruitment strategy: broad enrollment across the Western and South Central U.S., combined with targeted recruitment in Okanogan County, Washington, a region with historically severe wildfire seasons and active community wildfire preparedness efforts. This approach both allowed us to capture participants at similar time points who were either exposed or not exposed to wildfire smoke and to increase the likelihood of capturing a wildfire event in a subset of participants.

The utilization of a remote study design with homeRNA allowed for the study team to react to wildfire smoke exposure in real time, often sending out study kits within a day of the onset of a wildfire smoke event. Such flexibility would not have been possible in a more rigid study design requiring a physical location for blood draws. Moreover, once in participants hands, the homeRNA sampling could travel with the participants in the case of an evacuation. In fact, at one point in the study, some participants needed to evacuate, and a subset of these participants chose to take their homeRNA kits with them and continued sampling; such anecdotes exemplify the flexible nature of homeRNA study design and the potential utility of such tools for the study of disasters broadly. In this case, the study team used their evacuation address to assess their exposures and to schedule a UPS pick up of their samples for those days. Notably, despite the

psychological stress that wildfires and other disasters can impose on affected populations, the majority of surveyed participants reported being very or somewhat comfortable using homeRNA during such events, suggesting using the homeRNA kit does not cause additional burden during already challenging circumstances.

Further, it was easier for study participants to collect blood samples, both from the participant perspective (i.e., not needing to go to a physical location to have a blood draw) and also from a study logistics perspective (i.e., not needing to set up and staff a physical clinic or phlebotomy site for participants). These factors make collecting more samples in a longitudinal remote study simpler and less costly; thus, collecting up to 15 blood samples across 10 months with high participant retention and sample return rate to the last sampling time point is not only feasible, but demonstrated with this study. Additionally, the ability to collect baseline or pre-exposure samples allows for every participant to serve as their own control.

This study provides a rare window into real-world gene expression responses during an active wildfire season, with participants self-sampling throughout actual smoke exposure events in their home environments. By the nature of the remote study design, we sampled from the general population while they were being exposed to real-life smoke exposure in their own homes. Importantly, this includes the psychological stress inherent to experiencing a disaster, which is an inseparable component of wildfire smoke exposure. Some participants even needed to evacuate their homes during our study; such circumstances, including the associated stress, disrupted sleep patterns, and altered daily activities, are integral parts of how populations actually experience wildfire smoke events. Therefore, we cannot definitively determine whether the observed gene expression changes stem from the direct biological effects of $PM_{2.5}$ and other smoke components, or from the stress of experiencing a wildfire event. This inability to isolate specific causal mechanisms is inherent to studying disasters as they occur. However, understanding this holistic response may be more relevant for public health purposes as communities experiencing wildfire smoke, or other disasters, will often experience these stressors.

Beyond these inherent challenges of researching disasters, our study faces additional methodological limitations in quantifying exposure and controlling for temporal confounders, particularly in how we collected daily $PM_{2.5}$ averages. The distance between each participant's location and their nearest EPA $PM_{2.5}$ monitor varies amongst the study participants, with many participants, particularly those in Okanogan County, sharing the same monitor despite potentially different actual exposures. To look at differences in outdoor versus indoor $PM_{2.5}$ exposures, we also sent a subset of participants Purple Air sensors as part of the Clean Air Methow program. We observed discrepancies between indoor and outdoor $PM_{2.5}$ levels, with some participants experiencing higher indoor $PM_{2.5}$ at times possibly due to other indoor environmental sources such as cooking, candles, or differences in home ventilation; participants were asked to place the PurpleAir sensors away from indoor stoves, but the ventilation and layout of homes can vary. Individual behaviors further affect effective exposure assessment depending on time spent indoors versus outdoors and protective measures such as wearing N95 masks or using HEPA filters. For the purposes of this initial analysis, we chose to not include the indoor PM2.5 levels collected by the PurpleAir sensors due to incomplete coverage across all participants and the additional complexity of modeling indoor exposure, which we plan to address in future analyses with subset comparisons. Additionally, since our study lasted 10 months, there are other potentially confounding immune response factors such as the seasonal flu and allergies, which fluctuate in severity across different seasons. While all of these combined factors are inherent in most human subject-based research, they are important confounding variables to consider when designing a remote study with homeRNA and interpreting the transcriptomic results. These challenges with using proximal outdoor monitors as surrogate exposures may be overcome with the recent advent of more affordable, wearable personal exposure monitors for $PM_{2.5}$ (e.g., Atmotube) or other emerging wildfire-specific $PM_{2.5}$ exposure modeling frameworks.[55,56]

In the 2021 wildfire season, Okanogan County experienced one of its worst summers for wildfire smoke; smoke from nearby wildfires caused several days of hazardous AQI category (hazardous air quality is a $PM_{2.5} \geq 225.5$ $\mu g/m^3$; for reference, good air quality is $PM_{2.5} \leq 9.0$ $\mu g/m^3$). As such, the participants located in Okanogan County served as our "high exposure" group. Concurrently sampled participants

enrolled elsewhere that did not experience wildfire smoke were categorized into "low exposure", and participants that experienced transported smoke exposure from the Okanogan County fires were categorized into “moderate exposure” groups. Due to cost, this initial analysis was small (n=107 samples), with only six participants experiencing significant wildfire smoke exposure and three participants experiencing low-moderate levels of $PM_{2.5}$ exposure; additional analysis on over 300 samples from 29 participants is forthcoming.

The demographic composition of our analyzed cohort and broader study population reflects both the strengths and limitations of our remote recruitment approach. Our participants were predominantly female (71%) and had a median age of 41 years. While we attempted to match controls for age and sex when selecting the three participants with low and moderate exposure for our initial transcriptomic analysis, this matching was constrained by the limited control participant pool. Comprehensive demographic data on race/ethnicity was not collected in initial enrollment surveys, a limitation we addressed in follow-up surveys but that prevented our enrollment process from being responsive to balancing demographics. Our recruitment through word-of-mouth and existing community networks, particularly the Clean Air Ambassador Program led by Clean Air Methow, a community-based organization in Okanogan County, WA, likely contributed to demographic homogeneity, with overrepresentation of groups already engaged in community air quality initiatives. These demographic limitations should be considered when interpreting results, as wildfire smoke exposure impacts may vary across different demographic groups.

Despite the small sample size, our preliminary transcriptomic analysis in nine participants (n=6 exposed, n=3 non-exposed) identified patterns of inflammatory activation characterized by overexpression of inflammatory module aggregates (A33, A35) and inflammation-associated modules (M13.1 and M13.12). Concurrently, we observed reduced adaptive immune cell activity characterized by underexpression of lymphocytic aggregates (A1, A6), modules associated with T cells (M16.24 and M15.38), modules associated with B cells (M13.18), and monocyte modules (M15.7). While our sample size limits definitive conclusions, these initial observations using the BloodGen3 framework demonstrate its sensitivity in detecting coordinated transcriptional responses to environmental exposures. It is

noteworthy that these patterns involve modules relevant to immune competence and vaccine responses. Interestingly, a recent study by Sanghar et al. documented compromised COVID-19 vaccine immunity in individuals exposed to wildfire smoke.[24] Although we cannot directly link our preliminary observations to their clinical findings, the involvement of similar adaptive immune pathways in both studies warrants further investigation with larger cohorts to understand potential mechanisms underlying immune alterations during environmental exposures. These preliminary findings, while requiring validation in our full cohort and independent studies, suggest that homeRNA technology can overcome logistical challenges of disaster research while potentially capturing biologically relevant gene expression signatures.

Currently, we are employing bulk RNA-sequencing on over 300 samples from 29 participants from this study to further investigate wildfire-related transcriptomic response. This follow up analysis will have greater statistical power and will include a greater number of genes than were included in the Nanostring panel, strengthening the aggregate analysis. With this larger data set, we will also be able to employ additional investigations into the temporal component of the sampling data with time course gene set analysis, utilizing the 3- and 6-month timepoint samples to further understand the time course of the gene expression response to wildfire smoke.

The demonstrated feasibility and flexibility of homeRNA technology in this study opens new avenues for population-scale research on environmental exposures and natural disasters. The remote nature of homeRNA sampling addresses key barriers that have traditionally limited disaster-related health research: the ability to deploy studies quickly, maintain geographic flexibility, and preserve study continuity when communities experience disruption. Future applications could extend beyond wildfire smoke to investigate gene expression changes during other environmental exposures such as extreme weather events or infectious disease outbreaks, where traditional clinic-based sampling would be logistically challenging. Furthermore, the preliminary transcriptomic findings from this study could inform the development of more targeted, cost-effective gene panels specifically designed for wildfire smoke exposure research, enabling larger studies with greater statistical power at reduced costs. The scalability and flexibility of remote sampling technologies like homeRNA represent valuable tools for advancing our understanding of how

populations respond biologically to environmental exposures, ultimately informing public health research and intervention strategies across diverse geographic regions and populations.

6.8 Materials and methods

homeRNA kit components

homeRNA is a self-sampling kit for the collection and stabilization of whole blood RNA.[37] The kit uses a commercially available Tasso-SST™ blood collection device for the self-collection of peripheral blood and a specially engineered stabilizer tube containing RNA*later*™ for immediate stabilization of cellular RNA. The Tasso-SST™ blood collection device was purchased from Tasso, Inc (Seattle, WA). The stabilizer tube was injection molded out of polycarbonate (PC: Makrolon 2407) by Protolabs, Inc (Maple Plain, MN) and was designed to hold an RNA stabilization solution and connect to the Tasso-SST™ blood collection tube. The stabilizer tube was filled with 1.4 mL RNA*later*™ (Thermo Fisher) stabilization solution and capped. The stabilizer tube insert was injection molded out of polycarbonate (PC: Makrolon 2407) by Protolabs, Inc (Maple Plain, MN) and was designed to hold the stabilizer tube containing blood in a 50 mL conical tube during shipping. All components were cleaned via sonication in 70% ethanol (v/v) for 30 min and air dried prior to assembly. Finally, all kit components were placed in a rigid custom-designed mailer box (The BoxMaker, Inc.). Detailed design files and the workflow of assembling and using the homeRNA kit can be found in an initial pilot study in which we characterized the feasibility of using homeRNA for remote blood collection and RNA.[37]

homeRNA kit use workflow

The workflow of the homeRNA kit is described in detail in Haack, Lim, et al.[37] Briefly, to use the homeRNA kit, participants first collected capillary blood from their upper arm using the Tasso-SST™ device. The authors note that the serum separator tube (SST) gel (included in the Tasso-SST collection tube) is not necessary for RNA stabilization and analysis. At the time of the study, the Tasso-SST was the only available Tasso device for purchase. Next, participants were asked to estimate the volume of the blood collected based on a reference photo of the Tasso-SST™ tube in the sample collection survey (Figure E1C). The participants then stabilized the blood in RNA*later*™ by interfacing the RNA stabilizer tube with the Tasso-

SST™ blood tube and shaking vigorously to mix the blood with the stabilizing solution. Finally, after mixing, the stabilized blood sample was placed inside a 50 mL conical tube containing an insert to hold the sample tube in place, which was then packaged within a custom homeRNA cardboard box and UPS LabPak and mailed back to the lab for downstream analysis.

Participant recruitment and enrollment

The study was approved by the University of Washington (UW) Institutional Review Board (IRB) under protocol STUDY00012463. All study procedures were performed after informed consent was obtained. All samples were collected remotely by study participants and online surveys were administered through Research Electronic Data Capture (REDCap). Participants were recruited via social media, community outreach (e.g., through Clean Air Methow, a community air quality program[57,58]), and word of mouth between June and September 2021. After completing a screening survey online, individuals were invited to complete the informed consent and enrollment by the study team. To be eligible for the study, participants had to be: (1) 18 years old or older; (2) living in an area prone to wildfire including the states of Alaska, Arizona, California, Colorado, Florida, Idaho, Montana, Nevada, New Mexico, Oklahoma, Oregon, Texas, Utah, Washington, and Wyoming; (3) not pregnant (upon enrollment); (4) not residing in a correctional facility; and (5) not a friend or family member of researchers conducting study. Participants were enrolled with preference given to: (1) those located in Okanogan County, Washington (WA) (a historically wildfire-prone area) and (2) those with diverse geographic locations outside of Okanogan County.

Sample collection timeline

Throughout the study, participants were sent a package containing three homeRNA kits, and given a schedule for when to use each kit. Typically, each of the three samples was taken 3 to 4 days apart, and returned immediately via overnight shipping, if available. Depending on the smoke exposure conditions, participants were sometimes sent an additional set of three kits if there was continued wildfire smoke exposure in their area.

Before wildfire season: Immediately upon enrollment, participants were sent three samples to serve as baseline time-point samples before the start of wildfire season (June 2021). Samples were collected 2-4 days apart from each other.

During wildfire season: The location of wildfires, smoke plumes, and $PM_{2.5}$ values were monitored throughout the wildfire season (July-September 2021). If smoke was present in a participant's area, participants were immediately sent a box with three kits and asked to sample every 2-4 days. During the wildfire smoke events in Okanogan County, WA, participants outside of this region who were not experiencing smoke exposure were also asked to sample at similar times to match participants located in Okanogan County.

After wildfire season: All participants were sent an additional set of three homeRNA kits between October - November 2021 (3 months after the wildfire events in Okanogan County), then again in late February - early April 2022 (approximately 6 months after the wildfire events in Okanogan County). For each timepoint, samples were collected every 2-4 days.

$PM_{2.5}$ data collection

The average daily concentration of $PM_{2.5}$ that each participant was exposed to during the study period was taken from each participant's nearest outdoor EPA $PM_{2.5}$ monitor. A subset of participants were also provided an indoor PurpleAir monitor to collect indoor $PM_{2.5}$ data

Outdoor $PM_{2.5}$: Daily average $PM_{2.5}$ data collected by the closest EPA $PM_{2.5}$ monitor to each participant's home address was downloaded from the EPA website.[59] The closest monitor was determined by using the equirectangular approximation to calculate the shortest distance between the coordinates of each participant's home address and the reported coordinates of EPA $PM_{2.5}$ monitors. If no average $PM_{2.5}$ data were available on a certain day with a participant's calculated nearest monitor, then $PM_{2.5}$ data were taken from the calculated second nearest EPA $PM_{2.5}$ monitor. If the second nearest EPA monitor did not have available data, then data were taken from the calculated third nearest $PM_{2.5}$ monitor. For a few cases, there were no data from the nearest three monitors, and these particular days were excluded from the analysis.

Indoor $PM_{2.5}$: A subset of participants (n=15) were provided with indoor PurpleAir monitors, and the study team was provided with the sensor ID. Indoor $PM_{2.5}$ data collected by participant's PurpleAir sensors were downloaded from the PurpleAir website[60], and the daily average $PM_{2.5}$ from the PurpleAir sensor was calculated for each day of the study period.

Exposure level categorization: Participant exposure levels were categorized as high, medium, and low based on the standard deviation of the mean of their total outdoor $PM_{2.5}$ values throughout the study period (June 2021 - April 2022). Those with a standard deviation >20 $\mu g/m^3$ were considered high exposure participants; those with a standard deviation between 10 and 19 $\mu g/m^3$ were considered medium exposure participants; those with a standard deviation <10 $\mu g/m^3$ were considered low exposure participants. Given that ambient air quality was generally good throughout most of the study period, with $PM_{2.5}$ spikes concentrated during the 3 month wildfire season, we used standard deviation rather than mean $PM_{2.5}$ as our primary metric for classifying participants into exposure groups. This approach specifically identifies individuals who experienced high-magnitude episodic exposures, which would be obscured by time-averaged means in a population with uniformly low baseline exposures.

Survey data collection

Participants were surveyed throughout the study period through REDCap. Specific surveys are described below.

Enrollment Survey: This survey was given immediately after informed consent was acquired. It collects information about participant demographics, home addresses (for sending samples and tracking $PM_{2.5}$ data), as well as underlying health conditions, recent vaccinations, and medications that may affect immune activation.

Baseline Survey: This survey was given with the first blood sample collected, whether it was before the first wildfire smoke exposure or not. The baseline survey collects information on exposures a participant may have experienced in the past year, the participant's occupation (specifically if their profession involves working outside), and the participant's typical daily activities. Questions on daily activities and stress were adapted from standardized surveys on stress assessment available on PhenX.[61] The baseline survey also

includes all the questions in the Sample Collection Survey (below), and if the participant was experiencing smoke exposure for the first sample, they were asked additional questions that are specific to smoke exposure listed in the Smoke Exposure Survey (below).

Sample Collection Surveys: This survey was given with every blood sample collected. It includes questions about the date and time of the sample collection, sample collection metrics (e.g., blood volume estimation, time used for the collection), and homeRNA usability (e.g., ease of use with the kit, pain level using the Tasso device). The survey also included questions about any symptoms related to smoke exposure (the list of symptoms was adopted from a CDC website on health effects of wildfire smoke[62]), they were asked to rate their stress levels compared to normal, they were asked to estimate hours of sleep, and they were asked about whether or not they were able to engage in their normal daily activities. If a participant received an indoor PurpleAir monitor, they were asked to report the $PM_{2.5}$ value on the air monitor at the time of collection.

Smoke Exposure Surveys: This survey was given if a study participant was using the homeRNA kit during wildfire smoke exposure. It contains all the questions in the Sample Collection Survey (above) with additional questions specifically about behaviors in response to wildfire smoke exposure. These questions included how much time the participants spent outdoors, in a car or bus, and the amount of time spent indoors. It also asked if they utilized any mitigation strategies, such as using an air filter, wearing masks, avoiding outside activities, or keeping windows closed.

Closing Survey: This survey was given at the end of the study period. It included demographic and behavior questions, including if a participant had a major change in behavior, health status, or location (e.g., on vacation) during the study.

Follow-up Survey: This survey was given in November 2023, which was 18 months after the study was concluded in April 2022. Of the 40 participants invited to complete the survey, 30 participants provided responses and completed the follow-up survey. This survey asked for the participant's motivation to enroll in the study, comparisons between remote blood sampling and in-person blood draws, feedback on using the homeRNA kit, and willingness to participate again.

Sample processing

After the homeRNA kit was mailed back to the lab, it was stored immediately in a -20°C freezer on campus. Within a week, the 50 mL conical tube containing the homeRNA-stabilized blood sample was removed from the kit, and transferred to -80°C until ready for further processing. Total cellular RNA was isolated from samples using the Ribopure™ - Blood RNA Isolation Kit (Thermo Fisher) according to the manufacturer's protocol and eluted in two 50 µL aliquots. Isolated RNA was stored at -80°C until ready for further analysis.

Assessment of total cellular RNA integrity and yield

The RNA Integrity Number (RIN) scores of the first 50 µL elution were obtained on a Bioanalyzer 2100 (Agilent) using the Agilent RNA 6000 Pico Kit (Agilent 5067-1513). All RNA samples were diluted 1:20 in nuclease-free water before RIN measurement to ensure the RNA concentration of the loaded sample was in the qualitative range for the Agilent RNA 6000 Pico Kit. The RNA concentrations of the first 50 µL elution were measured using the Qubit Flex Fluorometer (Thermo Fisher) using the Qubit RNA High Sensitivity Assay Kit (Invitrogen Q32855).

Participant and sample selection for Nanostring analysis

For an initial exploratory analysis using a Nanostring panel, nine participants were selected from the total 58 participants who completed the study. As Okanogan County experienced the most profound smoke exposure during the study period, six of the nine selected participants were located in this region. We also selected three additional participants; one was located in central Washington who experienced a moderate amount of smoke exposure due to their proximity to Okanogan County, and the other two were located in California, who experienced little to no smoke exposure in the 2021 wildfire season.

Participant selection preference was given to participants if they had (1) at least five samples collected with associated surveys and if (2) at least one of the five samples collected was collected during wildfire smoke exposure (if located in Okanogan County) or with a similar time point (if not located in Okanogan County). In total, we submitted 107 samples from nine participants for gene expression analysis using the nanoString nCounter Autoimmune Profiling Panel. Additional RNA processing was performed

on a subset of these samples; these RNA samples were treated with DNase I (RNase-free) (New England Biolabs, M0303S) to remove contaminating genomic DNA and/or Monarch® RNA Cleanup Kit (New England Biolabs, T2030L) to purify and concentrate the RNA according to the manufacturer's protocols. The final cutoff RIN value for samples after processing was >6. Most samples used an input of 100 ng, but a handful of samples had inputs less than 100 ng. Input volumes ranged from 8-10 μL.

Gene Expression Analysis

nCounter data quality control and normalization: Raw nCounter RCC files were processed using custom Python scripts. Quality control metrics were evaluated for all samples prior to normalization following established nCounter guidelines[63,64]. Imaging quality required a minimum of 75% fields of view (FOV) successfully registered, while binding density was assessed with acceptable ranges of 0.05-2.25 spots/μm². Positive control linearity was evaluated through correlation analysis with expected synthesis RNA concentrations (0.125-128 fM), requiring $R^2 > 0.95$ to ensure proper hybridization efficiency. Negative control probes were assessed for background levels, with mean plus two standard deviations used as detection thresholds. Housekeeping gene variability was evaluated using coefficient of variation, with sample showing CV > 50% flagged for potential exclusion due to high technical variability.

Gene expression normalization was performed using a sequential pipeline combining standard nCounter procedure with additional variance stabilization methods. The process began with positive control normalization utilizing the geometric mean of synthetic positive control probes to adjust for technical variation in hybridization and detection across samples. Codeset content normalization followed, employing eight reference genes (*TUBB, MRPS7, TBP, SDHA, GUSB, HRPT1, NMT1, PGK1*) selected based on low variance and moderate expression levels across the dataset. Background subtraction was performed using negative control statistics, with gene showing expression below detection threshold flagged accordingly. Following these standard steps, data underwent counts per million (CPM) transformation to normalize for library size differences, then trimmed means of m-values (TMM) normalization with 30% trimming to address compositional bias between samples. Final normalized values

were log2-transformed for downstream analyses. All data processing was performed using custom Python scripts with numpy (v1.22.3) and pandas (v.1.4.2) libraries.

Differential expression analysis: To control for intra-individual baseline variation, participant-specific median expression values for each gene were calculated from pre-exposure baseline samples (timeline category "before") and subsequently subtracted from exposure timepoint measurements corresponding to that participant. This yielded baseline-corrected gene expression values that reflect changes relative to each participant's pre-exposure state. At the individual gene level, we identified 253 genes with differential expression (FDR < 0.05) between exposed and non-exposed groups. To determine biological significance, we also performed a minimum-effect test where the null hypothesis was $|\log_2 FC| \leq 0.5$.[50] No genes achieved FDR < 0.05 using this more stringent approach, indicating that while statistical differences exist, no genes showed fold changes greater than 1.4-fold with controlled false discovery rate.

Gene set enrichment of wildfire smoke exposure samples using BloodGen3

BloodGen3 module enrichment analysis: Gene set variation analysis (GSVA) was performed to calculate enrichment scores for each of the 38 BloodGen3 module aggregates across all samples using normalized expression.[42,43] GSVA enrichment scores were computed using the GSVA R package (v1.46.0) with default parameters, generating a per-sample enrichment score (from -1 to +1) for each module, where values represent the degree of coordinated down- or up-regulation of genes within each functional module.[42,43]

Baseline correction: To control for intra-individual baseline variation, participant-specific median enrichment scores were calculated from pre-exposure samples (timeline category "before") and subsequently subtracted from each of the following timepoint measurements corresponding to that participant. This yielded baseline-corrected enrichment scores that reflect changes relative to each participant's pre-exposure state.

Group comparisons: Differential enrichment between wildfire smoke exposed and non-exposed participants was assessed using two-tailed Student's t-tests on baseline-corrected enrichment scores during exposure period (timeline category “during”). P-values were adjusted for multiple comparisons by

controlling the false discovery rate (FDR) using the Benjamini-Hochberg procedure. Bloodgen3 modules and aggregates with adjusted p-values < 0.05 were considered statistically significant.

Data visualization: Hierarchical clustering was performed using Ward's method with Euclidean distance to organize samples and module aggregates based on similarity in enrichment patterns. Heatmaps were generated to visualize baseline-corrected enrichment scores, with red indicating increased enrichment and blue indicating decreased enrichment relative to baseline. Statistical significance of between-group differences was visualized using bar plots of -log10(FDR-corrected p-values), with a threshold line at p = 0.05. To contextualize exposure level, outdoor $PM_{2.5}$ concentrations were displayed as bar plots aligned with sample collection timepoints to contextualize exposure levels.

Software and computational tools: All statistical analyses were performed using Python 3.9 and R 4.2.0. Data manipulation employed pandas (v1.4.2) and numpy (v1.22.3). Statistical testing and multiple comparison correction (FDR) were implemented using scipy.stats (v1.8.1) and statsmodels (v0.13.2). Data visualizations were generated using matplotlib (v3.5.2) and seaborn (v0.11.2). Complex heatmaps with hierarchical clustering were created using the ComplexHeatmap R package.

6.9 References

1. Senande-Rivera M, Insua-Costa D, Miguez-Macho G. Spatial and temporal expansion of global wildland fire activity in response to climate change. *Nat Commun* 2022; **13**: 1208.
2. Doerr SH, Santín C. Global trends in wildfire and its impacts: perceptions versus realities in a changing world. *Philos Trans R Soc B Biol Sci* 2016; **371**: 20150345.
3. Jones MW, Abatzoglou JT, Veraverbeke S, *et al.* Global and Regional Trends and Drivers of Fire Under Climate Change. *Rev Geophys* 2022; **60**: e2020RG000726.
4. Vicente A, Alves C, Calvo AI, *et al.* Emission factors and detailed chemical composition of smoke particles from the 2010 wildfire season. *Atmos Environ* 2013; **71**: 295–303.
5. Groß S, Esselborn M, Weinzierl B, Wirth M, Fix A, Petzold A. Aerosol classification by airborne high spectral resolution lidar observations. *Atmospheric Chem Phys* 2013; **13**: 2487–505.
6. Zhang Y, Obrist D, Zielinska B, Gertler A. Particulate emissions from different types of biomass burning. *Atmos Environ* 2013; **72**: 27–35.
7. Zhang D, Wang W, Xi Y, *et al.* Wildland Fires Worsened Population Exposure to PM2.5 Pollution in the Contiguous United States. *Environ Sci Technol* 2023; **57**: 19990–8.
8. Burke M, Driscoll A, Heft-Neal S, Xue J, Burney J, Wara M. The changing risk and burden of wildfire in the United States. *Proc Natl Acad Sci* 2021; **118**: e2011048118.
9. Hartnett N, Jing P, Zhang B, Stuart M, Wang J. Wildfire smoke and PM2.5 pollution in Chicago: Evidence from 2019 to 2023. *Urban Clim* 2025; **61**: 102472.
10. Chen Y, Hall J, Van Wees D, *et al.* Multi-decadal trends and variability in burned area from the fifth version of the Global Fire Emissions Database (GFED5). *Earth Syst Sci Data* 2023; **15**: 5227–59.
11. Xu R, Ye T, Huang W, *et al.* Global, regional, and national mortality burden attributable to air pollution

from landscape fires: a health impact assessment study. *The Lancet* 2024; **404**: 2447–59.
12. Lopes M, Monteiro A, Mouzourides P, Kouis P. The health burden of wildfire smoke in a changing climate: Exposure, risks, and strategies for mitigation. *Curr Opin Environ Sci Health* 2025; **46**: 100631.
13. Reid CE, Brauer M, Johnston FH, Jerrett M, Balmes JR, Elliott CT. Critical Review of Health Impacts of Wildfire Smoke Exposure. *Environ Health Perspect* 2016; **124**: 1334–43.
14. Jegasothy E, Hanigan IC, Van Buskirk J, *et al.* Acute health effects of bushfire smoke on mortality in Sydney, Australia. *Environ Int* 2023; **171**: 107684.
15. Chowdhury S, Hänninen R, Sofiev M, Aunan K. Fires as a source of annual ambient PM2.5 exposure and chronic health impacts in Europe. *Sci Total Environ* 2024; **922**: 171314.
16. Ma Y, Zang E, Liu Y, *et al.* Long-term exposure to wildland fire smoke $PM_{2.5}$ and mortality in the contiguous United States. *Proc Natl Acad Sci* 2024; **121**: e2403960121.
17. Qiu M, Li J, Gould CF, *et al.* Wildfire smoke exposure and mortality burden in the US under climate change. *Nature* 2025; published online Sept 18. DOI:10.1038/s41586-025-09611-w.
18. Humphreys A, Walker EG, Bratman GN, Errett NA. What can we do when the smoke rolls in? An exploratory qualitative analysis of the impacts of rural wildfire smoke on mental health and wellbeing, and opportunities for adaptation. *BMC Public Health* 2022; **22**. DOI:10.1186/S12889-021-12411-2.
19. Eisenman DP, Galway LP. The mental health and well-being effects of wildfire smoke: a scoping review. *BMC Public Health* 2022; **22**: 2274.
20. Swiston JR, Davidson W, Attridge S, Li GT, Brauer M, Van Eeden SF. Wood smoke exposure induces a pulmonary and systemic inflammatory response in firefighters. *Eur Respir J* 2008; **32**: 129–38.
21. Jia H, Liu Y, Guo D, He W, Zhao L, Xia S. PM2.5-induced pulmonary inflammation via activating of the NLRP3/caspase-1 signaling pathway. *Environ Toxicol* 2021; **36**: 298–307.
22. Huttunen K, Siponen T, Salonen I, *et al.* Low-level exposure to ambient particulate matter is associated with systemic inflammation in ischemic heart disease patients. *Environ Res* 2012; **116**: 44–51.
23. Hejl AM, Adetona O, Diaz-Sanchez D, *et al.* Inflammatory effects of woodsmoke exposure among wildland firefighters working at prescribed burns at the Savannah River Site, SC. *J Occup Environ Hyg* 2013; **10**: 173–80.
24. Sanghar GK, Teuber M, Ravindran R, *et al.* Real-life observation of wildfire smoke–impaired COVID-19 vaccine immunity. *J Allergy Clin Immunol* 2025; **155**: 1371-1377.e6.
25. Rubin ES, Kornfield M, Parker P, *et al.* Poor air quality from wildfire smoke is associated with decrease in total motile sperm count at time of intrauterine insemination. *Fertil Steril* 2024; **121**: 881–3.
26. Lindell LX, Holt SK, Petersen E, *et al.* Wildfire Smoke Exposure is Associated with Decreased Sperm Concentration and Total Motile Sperm Count. 2025; published online March 11. DOI:10.1101/2025.03.09.25323436.
27. Navarro KM, Kleinman MT, Mackay CE, *et al.* Wildland firefighter smoke exposure and risk of lung cancer and cardiovascular disease mortality. *Environ Res* 2019; **173**: 462–8.
28. Adetona AM, Adetona O, Gogal RM, DIaz-Sanchez D, Rathbun SL, Naeher LP. Impact of Work Task-Related Acute Occupational Smoke Exposures on Select Proinflammatory Immune Parameters in Wildland Firefighters. *J Occup Environ Med* 2017; **59**: 679–90.
29. Cherry N, Beach J, Galarneau J-M. Are Inflammatory Markers an Indicator of Exposure or Effect in Firefighters Fighting a Devastating Wildfire? Follow-up of a Cohort in Alberta, Canada. *Ann Work Expo Health* 2021; **65**: 635–48.
30. Esteves F, Madureira J, Barros B, *et al.* Impact of occupational exposure to wildfire events on systemic inflammatory biomarkers in Portuguese wildland firefighters. *Environ Res* 2025; **277**: 121608.
31. Main LC, Wolkow AP, Tait JL, *et al.* Firefighter's Acute Inflammatory Response to Wildfire Suppression. *J Occup Environ Med* 2020; **62**: 145–8.
32. Aguilera J, Kaushik A, Cauwenberghs N, *et al.* Granzymes, IL-16, and poly(ADP-ribose) polymerase 1 increase during wildfire smoke exposure. *J Allergy Clin Immunol Glob* 2023; **2**: 100093.
33. Johnson MM, Kaushik A, Kline OA, *et al.* Immune impacts of fire smoke exposure. *Nat Med* 2025; **31**: 3110–20.
34. Prunicki M, Miller S, Hopkins A, *et al.* Wildfire smoke exposure is associated with decreased

methylation of the PDL2 gene. *J Immunol* 2020; **204**: 146.17-146.17.
35. Xu R, Li S, Wu Y, *et al.* Wildfire-related PM2.5 and DNA methylation: An Australian twin and family study. *Environ Int* 2023; **171**. DOI:10.1016/j.envint.2022.107704.
36. Parenteau AM, Alen NV, La J, *et al.* Associations of air pollution with peripheral inflammation and cardiac autonomic physiology in children. *New Dir Child Adolesc Dev* 2022; **2022**: 125–54.
37. Haack AJ, Lim FY, Kennedy DS, *et al.* home RNA: A Self-Sampling Kit for the Collection of Peripheral Blood and Stabilization of RNA. *Anal Chem* 2021; **93**: 13196–203.
38. Brown LG, Haack AJ, Kennedy DS, *et al.* At-home blood collection and stabilization in high temperature climates using homeRNA. *Front Digit Health* 2022; **4**: 903153–903153.
39. Stefanovic F, Brown LG, MacDonald J, *et al.* Your Blood is Out for Delivery: Considerations of Shipping Time and Temperature on Degradation of RNA from Stabilized Whole Blood. *Anal Chem* 2025; **97**: 1635–44.
40. Lim FY, Lea HG, Dostie AM, *et al.* homeRNA self-blood collection enables high-frequency temporal profiling of presymptomatic host immune kinetics to respiratory viral infection: a prospective cohort study. *eBioMedicine* 2025; **112**: 105531.
41. Lim FY, Kim S-Y, Kulkarni KN, *et al.* High-frequency home self-collection of capillary blood correlates IFI27 expression kinetics with SARS-CoV-2 viral clearance. *J Clin Invest* 2023; **133**. DOI:10.1172/jci173715.
42. Rinchai D, Roelands J, Toufiq M, *et al.* BloodGen3Module: Blood transcriptional module repertoire analysis and visualization using R. *Bioinformatics* 2021; **37**: 2382–9.
43. Altman MC, Rinchai D, Baldwin N, *et al.* Development of a fixed module repertoire for the analysis and interpretation of blood transcriptome data. *Nat Commun* 2021; **12**: 4385.
44. Rinchai D, Brummaier T, A Marr A, *et al.* A data browsing application for accessing gene and module-level blood transcriptome profiles of healthy pregnant women from high- and low-resource settings. *Database* 2024; **2024**: baae021.
45. Subba B, Toufiq M, Omi F, *et al.* Human-augmented large language model-driven selection of glutathione peroxidase 4 as a candidate blood transcriptional biomarker for circulating erythroid cells. *Sci Rep* 2024; **14**: 23225.
46. Syed Ahamed Kabeer B, Subba B, Rinchai D, *et al.* From gene modules to gene markers: an integrated AI-human approach selects CD38 to represent plasma cell-associated transcriptional signatures. *Front Med* 2025; **12**: 1510431.
47. Brummaier T, Rinchai D, Toufiq M, *et al.* Design of a targeted blood transcriptional panel for monitoring immunological changes accompanying pregnancy. *Front Immunol* 2024; **15**: 1319949.
48. Bettacchioli E, Chiche L, Chaussabel D, Cornec D, Jourde-Chiche N, Rinchai D. An interactive web application for exploring systemic lupus erythematosus blood transcriptomic diversity. *Database* 2024; **2024**: baae045.
49. Rawat A, Rinchai D, Toufiq M, *et al.* A Neutrophil-Driven Inflammatory Signature Characterizes the Blood Transcriptome Fingerprint of Psoriasis. *Front Immunol* 2020; **11**: 587946.
50. McCarthy DJ, Smyth GK. Testing significance relative to a fold-change threshold is a TREAT. *Bioinformatics* 2009; **25**: 765–71.
51. Kalinski P. Regulation of Immune Responses by Prostaglandin E2. *J Immunol* 2012; **188**: 21–8.
52. Goto Y, Ishii H, Hogg JC, *et al.* Particulate Matter Air Pollution Stimulates Monocyte Release from the Bone Marrow. *Am J Respir Crit Care Med* 2004; **170**: 891–7.
53. Hiraiwa K, Van Eeden SF. Contribution of Lung Macrophages to the Inflammatory Responses Induced by Exposure to Air Pollutants. *Mediators Inflamm* 2013; **2013**: 1–10.
54. Dhabhar FS. Effects of stress on immune function: the good, the bad, and the beautiful. *Immunol Res* 2014; **58**: 193–210.
55. Wen J, Heft-Neal S, Baylis P, Boomhower J, Burke M. Quantifying fire-specific smoke exposure and health impacts. *Proc Natl Acad Sci U S A* 2023; **120**. DOI:10.1073/pnas.2309325120.
56. Considine EM, Hao J, deSouza P, Braun D, Reid CE, Nethery RC. Evaluation of Model-Based $PM_{2.5}$ Estimates for Exposure Assessment during Wildfire Smoke Episodes in the Western U.S. *Environ Sci*

Technol 2023; **57**: 2031–41.
57. Durkin A, Gonzalez R, Isaksen TB, Walker E, Errett NA. Establishing a Community Air Monitoring Network in a Wildfire Smoke-Prone Rural Community: The Motivations, Experiences, Challenges, and Ideas of Clean Air Methow's Clean Air Ambassadors. *Int J Environ Res Public Health 2020 Vol 17 Page 8393* 2020; **17**: 8393–8393.
58. Clean Air Methow. https://www.cleanairmethow.org/about.
59. Outdoor Air Quality Data. EPA. https://www.epa.gov/outdoor-air-quality-data/download-daily-data.
60. Download Sensor Data. PurpleAir. 2021; published online Oct. https://community.purpleair.com/t/download-sensor-data/100.
61. Hamilton CM, Strader LC, Pratt JG, *et al.* The PhenX Toolkit: Get the Most From Your Measures. *Am J Epidemiol* 2011; **174**: 253–60.
62. How Wildfire Smoke Affects Your Body. CDC. 2024; published online April 19. https://www.cdc.gov/wildfires/risk-factors/index.html (accessed May 27, 2024).
63. Bhattacharya A, Hamilton AM, Furberg H, *et al.* An approach for normalization and quality control for NanoString RNA expression data. *Brief Bioinform* 2021; **22**: bbaa163.
64. Veldman-Jones MH, Brant R, Rooney C, *et al.* Evaluating Robustness and Sensitivity of the NanoString Technologies nCounter Platform to Enable Multiplexed Gene Expression Analysis of Clinical Samples. *Cancer Res* 2015; **75**: 2587–93.

Appendix

A. Appendix for Chapter 2

Reproduced in part from A. J. Haack, L. G. Brown*, A. J. Goldstein, P. Mulimani, J. Berthier, A. R. Viswanathan, I. Kopyeva, J. M. Whitten, A. Lin, S. N. Nguyen, T. P. Leahy, E. E. Bouker, R. M. Padgett, N. A. Mazzawi, J. C. Tokihiro, R. C. Bretherton, A. Wu, S. J. Tapscott, C. A. DeForest, T. E. Popowics, E. Berthier, N. J. Sniadecki#, A. B. Theberge#. "Suspended Tissue Open Microfluidic Patterning (STOMP)." Advanced Science, 2025, 2501148.*
**Equal contribution*
#Co-corresponding authors

Extended Technical Details of Methods

Immunofluorescent imaging of periodontal tissues: PTCs on posts were fixed in 4% PFA at room temperature for 1 hour. PTCs were then dismounted from the posts for the immunofluorescence staining process. In short, PTCs were permeabilized with 0.2% Triton-X for 10 min followed by blocking with 10% normal goat serum (Invitrogen) for 10 min at room temperature. Samples were then incubated for 1 hour with Alexa Fluor 647 phalloidin (Invitrogen A22287, 1:400), and Hoechst 33342 (ThermoFisher, 1:1000). After 1 hour, PTCs were rinsed three times in PBS for 10 min each on a room temperature shaker. Whole PTCs were mounted between glass slides and coverslips using VECTASHIELD mounting medium and allowed to dry overnight. A Leica SP8 confocal microscope was used for imaging. Three to four images per PTC were obtained under 10X objective at 2X zoom and 1024 x 1024 resolution. Since three independent experiments were carried out and each experiment was conducted in triplicate, we ensured a minimum of 30 images per condition for analysis. Laser strength and gain were kept constant between all samples and fields of view (Figure A12).

Synthesis of poly(ethylene glycol)-bicyclononyne (PEG-BCN:. 4-arm poly(ethylene glycol)-bicyclononyne (PEG-BCN) was synthesized as described in previous publications [1-3]. 4-arm poly(ethylene glycol) tetraamine (MW 20kDa, 1.143 g, 0.0571 mmol, 0.2 mol NH_2 groups, 1x; JenKem Technology USA; Plano, TX), (1R,8S,9s)-bicyclo[6.1.0]non-4-yn-9-ylmethyl (2,5-dioxopyrrolidin-1-yl) carbonate (BCN-OSu) (Sigma Aldrich; St. Louis, MO) (100 mg, 0.343 mmol, 1.5x to NH_2 groups), and N,N-Diisopropylethylamine (DIEA, 159µL, 8 mmol, 4x to NH_2 groups) were dissolved in anhydrous

dimethylformamide (DMF, 5 mL) and stirred overnight. The next day, the mixture was diluted with DI H_2O (10x volume) and dialyzed overnight in DI H_2O (molecular weight cutoff ~ 2kDa; SpectraPor, Repligen; Waltham, MA) and lyophilized over three days to yield a white powder. The powder was resuspended in sterile PBS at a 10 mM stock concentration and stored at -80°C until further use. ^{1}H NMR confirmed functionalization to be >95% by comparing integral values for characteristic BCN peaks (δ 2.24, 1.57, 1.34, 0.92) with those from the PEG backbone (δ 3.63).

Peptide Synthesis of eSrtA(4S9)- and eSrtA(2A9)-sensitive Crosslinkers: The eSrtA(4S9)- and eSrtA(2A9)-sensitive diazide peptide crosslinkers H-RGPQGIWGQLPESGGRK(dde)-NH_2 and H-RGPQGIWGQLAETGGRK(dde)-NH_2, respectively, were synthesized on rink amide ProTide resin (CEM Corporation; Charlotte, NC) following induction heating-assisted Fmoc solid-phase techniques with HCTU activation (Gyros Protein Technologies PurePep Chorus; Tucson, AZ) at a 0.4 mmol scale. Deprotection of the 1-(4,4-dimethyl-2,6-dioxacyclohexylidene)ethyl (dde) group was accomplished by treating with 2% hydrazine monohydrate in DMF (3x10 min). For azide modification of the both the N-terminal amine and the ε-amino group of the C-terminal lysine, 4-azidobutanoic acid (227 µL, 2 mmol, 4x to NH_2 groups), hexafluorophosphate azabenzotriazole tetramethyl uronium (HATU, 750 mg, 1.97 mmol, 3.95x to NH_2 groups) and DIEA (1.38 mL, 8 mmol, 16x to NH_2 groups) were prereacted for 5 minutes and then reacted with the peptide for 1.5 hours. For peptide cleavage and deprotection, the resin was treated with trifluoracetic acid/triisopropylsilane/water (95:2.5:2.5) for 3 hours, then crashed out and washed in ice-cold diethyl ether (2 x 150mL). The crude peptides were purified via semi-preparative reversed-phase high performance liquid chromatography with a linear gradient of 5-100% acetonitrile and 0.1% TFA for 45 minutes and then lyophilized to yield white powders of the final peptides N_3-RGPQGIWGQLPESGGRK(N_3)-NH_2 and N_3-RGPQGIWGQLAETGGRK(N_3)-NH_2. Peptide mass was verified via ESI-LCMS.

eSrtA(4S9) and eSrtA(2A9) Expression and Purification: The pET29B expression plasmids for eSrtA(4S9) and eSrtA(2A9) were a generous gift from Dr. David Liu at Harvard University (Addgene plasmids #75146 and #75145). The sortase variants were expressed and purified as previously described

[3]. Electrically competent BL21 cells were transfected with the eSrtA(4S9) and eSrtA(2A9) plasmids and selected on kanamycin-containing agar plates. 5 mL of Luria Broth (LB) with kanamycin (50µg/mL) was inoculated with a plasmid-containing colony and grown overnight at 37ºC shaking at 200 rpm. The following day, 1 L of LB broth, including 40 mL of autoinduction sugars (60% v/v glycerol, 10% w/v glucose, 8% w/v lactose) as well as kanamycin, was inoculated with the 5mL overnight culture and allowed to incubate at 37ºC, 200 rpm overnight. The following day, cells were pelleted via centrifugation (4000g, 20 mins), resuspended in lysis buffer (20 mM Tris, 50 mM NaCl, 10 mM imidazole; pH 7.5) with 1 mM phenylmethylsulfonyl (PMSF; TCI, Portland, OR) protease inhibitor, and lysed by sonication (6x, 3 min cycle, 30% amplitude; Fisher Scientific; Waltham, MA). The lysate was clarified via centrifugation (20 mins, 11000g). The clarified lysate was then purified using an ÄKTA Pure 25 L FPLC (Cytiva; Marlborough, MA) equipped with a 5 mL HisTrap HP column at a flow rate of 5 mL min^{-1}. The column was equilibrated with 5 column volumes (CV) of lysis buffer, followed by loading the sample and washing with 8 CV of endotoxin removal buffer (20 mM Tris, 50 mM NaCl, 20 mM imidazole, 0.1% Triton-X 114; pH = 7.5) and 8 CV of wash buffer (20 mM Tris, 50 mM NaCl, 20 mM imidazole; pH = 7.5). His-tagged protein was eluted over an 8 CV gradient of imidazole (20 mM Tris, 50 mM NaCl, 5-250 mM imidazole; pH = 7.5) into a 96 well plate; protein-containing fractions were pooled and dialyzed with SnakeSkin dialysis tubing (10 kDa cut off; ThermoFisher, Waltham, MA) in PBS over two days. Purified sortase was spin-concentrated using an Amicon Ultra 15 centrifugation filter (10,000 Da cut off; Sigma Aldrich; St. Louis, MO). The final stocks were diluted with PBS containing 10% glycerol to a concentration of 100 µM. Sortase purity was evaluated with sodium-dodecyl sulfate-polyacrylamide gel electrophoresis and identity was confirmed with electrospray ionization mass spectrometry on an AB SCIEX 5600 QTOF instrument (SCIEX; Framingham, MA).

Extended Technical Descriptions of Results

1. Full details on theoretical characterization of pinning in STOMP channels.

In this study, we investigate the successive pinning of the two liquids in the STOMP device shown in Figure A3. The “green” liquid represents a hydrogel (e.g., cell-ECM mixture) first pipetted into the outer

cylindrical regions of the STOMP device. The "orange" liquid represents a second hydrogel (cell-ECM mixture) pipetted later in the center region. In this analysis, we assume both hydrogels (green and orange regions) are 5 mg/mL collagen, but this analysis can be extended to any hydrogel by utilizing that specific hydrogel's properties (e.g., density, contact angle on patterning device surface, etc.).

It is assumed that liquid #1 (green in Figure A3) is pipetted first, so it is the pinning of this liquid that is investigated here. In a first approach, we follow a 2D approach, neglecting the effect of the horizontal free surfaces at bottom and top. We shall justify this approximation later in the text. Here, we analyze two pinning feature designs we refer to as convex "vampire" pins and concave "cavity" pins.

We first address the case of the convex "vampire" pinning features (Figure A4). The design is constituted by two facing reliefs resembling two "teeth". We note that α is the angle formed by the triangular-shaped relief, θ the contact angle of the hydrogel with the channel wall, and w is the distance between the two facing reliefs of the convex "vampire" pins. The Laplace pressure ΔP of the liquid is given by equation (A.1), where r is the curvature radius of the pinned interface (in the horizontal plane) and denotes the surface tension of the liquid.

$$\Delta P = \frac{\gamma}{r} \qquad \text{A.1}$$

At the pinning limit (i.e., the maximum interface the fluid bulges before pinning is broken), the bulging fluid front forms the angle θ with the external side of the triangular edge [4-8]; its complement is noted in Figure A4. Any additional bulging results in a capillary flow passing over the pinning feature. Let us denote the points A and B the tip of the "teeth", O the center of the circular arc formed by the interface, and C the middle of the segment AB. Using the construction in Figure A4, the angle {AC,AO} is simply given by the expression $\pi/2-\Theta+\alpha/2$. Then considering the rectangular triangle ACO, we find

$$\cos\left(\frac{\pi}{2} - \theta + \frac{\alpha}{2}\right) = \frac{w}{2r} \qquad \text{A.2}$$

or

$$\sin\left(\theta - \frac{\alpha}{2}\right) = \frac{w}{2r} \quad \text{A.3}$$

Remark that we have considered Θ>α/2. When Θ=α/2, the fluid interface is flat, and r is infinite. Substituting equation (A.3) into equation (A.1) yields the threshold Laplace pinning pressure, above which pinning is lost in the convex "vampire" pinning feature design (Eq. A.4).

$$\Delta P = \frac{\gamma}{r} = \frac{2\gamma\sin\left(\theta - \frac{\alpha}{2}\right)}{w} \quad \text{A.4}$$

Second, we analyze the case of the concave "cavity" pinning features (Figure A5). The Laplace pressure is still given by equation (A.1). Let us note β as the angle of solid at the ridge. Let us separate two cases: β > θ and β < θ. The first case is the usual case, because θ is generally small and the cavity angle β cannot be too small due to the 3D printing fabrication process of the STOMP device. The first case (β > θ) corresponds to the configuration used here in this work.

Case β > θ: Again, at the limit, the bulging angle forms the angle θ with the external side of the tooth [4–8]; its complement is noted as π-θ in Figure A5. Any additional bulging results in a capillary flow passing over the ridge. Let us denote the points A and B the tip of the ridges, O the center of the circular arc formed by the interface, and C the middle of the segment AB. Using the construction in Figure A5, the angle {AC,AO} is simply β-θ. Then considering the rectangular triangle ACO, we find

$$\cos(\theta - \beta) = \frac{w}{2r} \quad \text{A.5}$$

Substituting equation (A.5) into (A.1) yields the threshold Laplace pinning pressure, above which pinning is lost in the concave "cavity" pinning feature design (Eq. E6).

$$\Delta P = \frac{\gamma}{r} = \frac{2\gamma\cos(\theta - \beta)}{w} \quad \text{A.6}$$

Case β < θ: While this case is not the usual case, we mention it for completion of the study. In this case, the fluid front creates a bulging curvature, where the center of the curvature (point O in Figure A6) formed is located past the pinning ridge (line segment AB in Figure A6). The threshold Laplace pinning pressure is still the same as Eq. A.5, but this equation reaches its maximum value when β is equal to θ, which is 30° in

our theoretical model (the average contact angle of 5 mg/mL collagen on 3D printed resin treated with 1% BSA). Therefore, the maximum Laplace pinning pressure that can be experienced in the concave "cavity" pinning feature is given below in equation (A.7) and is visualized as the solid green line in Figure A6.

$$\Delta P = \frac{2\gamma}{w} \quad \text{A.7}$$

Lastly, because gravity has a small, but not negligible effect, we must also consider the hydrostatic pressure at the pinning interface. For both pinning feature designs, the hydrostatic pressure at the bottom of the channel is given below in equation (A.8), where ρ is the density of the hydrogel, g is the gravitational constant, and h is the height of the channel.

$$\Delta P = \rho g h \quad \text{A.8}$$

2. Analyzing the 3D effect of gravity in theoretical approach to pinning in STOMP

In our theoretical pinning model for STOMP, we used a 2D approach where we neglected the effect of the horizontal free air-liquid interfaces at the bottom and top of the open channel. To justify this approach, we also analyzed the potential 3D effects, which are twofold: 1) gravity effects that may distort the bottom air-liquid interface of the open channel and 2) corner effects from the rounded vertical air-liquid interface along the height of the open channel.

First, to analyze the effect of gravity, the Bond number has to be calculated. For testing the pinning in STOMP, devices with a channel height of 3.5 mm and width of 1.2 mm were used. The equation for bond number Bo is given below in equation (A.9), where ρ is the density of the 5 mg/mL collagen hydrogel, g is the gravitational constant, h is the height of the channel, R is the radius of the outer cylinders, and γ is the surface tension of the liquid (estimated to be water here).

$$Bo = \frac{\rho g h R}{\gamma} \quad \text{A.9}$$

In the case of the outer cylinders, the radius is 1.5 mm. Therefore, the bond number for the outer cylinders can be approximately calculated, as shown below in equation (A.10).

$$Bo_{\,outer\ cylinders} = \frac{958\,\frac{kg}{m^3} \times 10\frac{m}{s^2} \times 3.5 \cdot 10^{-3} m \times 1.5 \cdot 10^{-3} m}{72 \cdot 10^{-3}\frac{N}{m}} \approx 0.7 \qquad \text{A.10}$$

In the case of the central region of the open channel, the radius R is replaced by the semi-width, w/2. When experimentally testing the pinning, we used the STOMP devices with a channel height of 3.5 mm and a width of 1.2 mm. Therefore, the bond number for the central region can be approximately calculated with a semi-width of 0.6 mm, as shown below in equation (A.11).

$$Bo_{\,central\ region} = \frac{958\frac{kg}{m^3} \times 10\frac{m}{s^2} \times 3.5 \cdot 10^{-3} m \times 0.6 \cdot 10^{-3} m}{72 \cdot 10^{-3}\frac{N}{m}} \approx 0.3 \qquad \text{A.11}$$

In both cases of the outer cylinders that surround the posts and the central region of the open channel where flow occurs, we calculated that Bo < 1, which means surface tension forces dominates in the open channel. In both cases, gravity has a small effect on the horizontal free air-liquid interface at the bottom and top of the open channel. While the effect of gravity is not negligible, it is small enough that we can justify using a 2D approach in our theoretical characterization of the pinning in the STOMP devices.

The corner effects of the vertical air-liquid interface along the height of the open channel are more difficult to predict. We used Brakke's software Surface Evolver to determine the shape of these interfaces [9]. The results are plotted in Figure A7, which demonstrates that some corner effects do exist in our STOMP system.

3. Experimentally testing different volumes and pinning feature angles in STOMP

To understand the sensitivity of our system to changes in volume, we tested pinning in five different pinning angles of both pinning feature designs (i.e., α=10°, 20°, 30°, 45°, and 60° for the convex "vampire" pins and β=40°, 60°, 90°, 100°, and 120° for the concave "cavity" pins, n=3 devices for each pin angle) at four different volumes (20, 22, 23, and 24 μL). These results are illustrated in Figure A2.

Every volume tested exhibited different pinning results, where increasing the volume resulted in less successful pinning. At every volume, the concave "cavity" pinning feature with pins β=120° resulted in failed pinning; this matches what we would expect from the theoretical results (see Figure 2.2d).

Generally, in all volumes tested, the concave "cavity" pinning feature was more consistent than the convex "vampire" pinning feature. This phenomenon may be explained by the large range in the pinning Laplace pressure for the convex pinning features (see Figure 2.2c). We observed that a volume of 23 μL best fitted our theoretical model.

When 23 μL was pipetted into the convex "vampire" pinning features, we observed successful pinning of the collagen solution when α=10°, 20°, 30° (n=3/3 devices pinned). These experimental results match what would be expected from the average theoretical maximum Laplace pinning pressure (Figure 2.2c). Further, there was less successful pinning when α=45° and 60° (n=2/3 devices did not pin). We note that one out of the three devices for both the angles α=45° and 60° had successful pinning, but these angles have conditions of success and failure within the pinning range of the maximum Laplace pinning pressure (Figure 2.2c, green shading showing successful conditions and magenta shading showing failure conditions), suggesting that those devices had variable BSA adsorption onto the channel walls that may have changed the contact angle of the collagen on the channel surface.

When 23 μL was pipetted into the concave "cavity" pinning features, we observed successful pinning of the collagen solution when β=40° and 60° (n=3/3 devices pinned) and no pinning when β=90°, 100°, and 120° (n=3/3 devices did not pin). While successful pinning at β=40° and 60° experimentally matches the theory, loss of pinning was observed in all three replicates in devices with β=90° which was expected, even within the contact angle range, to successfully pin (Figure 2.2d). It is possible that the contact angle was towards the lower bound of the possible threshold Laplace pressure (Figure 2.2d), where the line does cross below the hydrostatic pressure at β=90°. There could also be additional reasons for fluid de-pinning when not predicted. In some cases, a fluid may initially pin, but then lose that pinning if there are deformities present on the pinning feature (i.e., rough surface, inconsistency in 3D printing, etc.).

4. Influence of liquid volume in pinning

Since we observed differences in pinning as the pipetted volume changed, we wanted to look at two possible factors that could influence pinning: 1) change in the horizontal interface of the liquid in the

channel (i.e., change in volume of liquid bulging at the top and bottom of the channel) and 2) change in the vertical interface of the pinned fluid front (i.e., change in the pinned fluid angle).

First, we will estimate the volume bulging at the bottom of the channel due to the weight of the precursor liquid hydrogel in the STOMP channel. At the bottom of the channel, the air-liquid interface bends due to hydrostatic pressure, as depicted in Figure A8. If we consider the bending of the horizontal bottom surface to be a cylinder, then the curvature of the surface is $\kappa = 1/R$. Therefore, the bending of the surface by hydrostatic pressure can be modeled by equation (A.12), where R is the curvature radius of the bulging surface.

$$\Delta P = \rho g h = \frac{2\gamma}{R} \tag{A.12}$$

If a denotes the radius of the cylinder, the volume of the liquid in the spherical cap bulging below the cylinder is given below in equation A.13 [4].

$$V_{horizontal\ bulging} = \frac{\pi}{6}\left(R - \sqrt{R^2 - a^2}\right)\left[3a^2 + \left(R - \sqrt{R^2 - a^2}\right)^2\right] \tag{A.13}$$

From Berthier and Brakke [4], the negative bulging height can be deduced as

$$R = \frac{a^2 + h^2}{2h} \tag{A.14}$$

or

$$h = R - \sqrt{R^2 - a^2} \tag{A.15}$$

If ρ is 958 kg/m3 (density of 5 mg/mL collagen), g is 9.8 m/s^2, h is 3.5 mm (the height of the open channel), γ is 72 mN/m, and a is 1.5 mm (the radius of the outer cylinders of the STOMP device), then we find that the curvature radius R is 4.38 mm, giving a bulging volume of 0.945 μL (or 0.945 mm^3) with a bulging height of 0.265 mm (or 265 μm). Thus, if the volume of the precursor hydrogel is equal to exactly the volume of the cylinder plus the inner channel walls (unto the pinning features), then the bottom surface bulges out 265 μm below the channel.

Next, we will calculate the surface area of the pinned fluid's vertical interface as a function of the pinning angle. Figure A9 shows a top-down cross section of the STOMP channel, where R is the curvature

radius of the bulging vertical interface, w is the width of the open channel, δ is the bulging distance of the pinned fluid's vertical interface, ϕ is the pinning angle of the fluid front, and S is the vertical surface denoted with a dark green line. In a 2D approximation, a change in volume delimited by the surface S can be modeled as

$$V_{vertical\ bulging} = h \times S \tag{A.16}$$

where h is the height of the open channel. Geometrical considerations give us the curvature radius R, denoted below in equation (A.17).

$$R = \frac{w}{2\sin(\phi)} \tag{A.17}$$

Modeling the vertical bulging surface as a circular segment, the surface area of the arc (denoted as S) can be modeled by equation (A.18).

$$S = \frac{R^2}{2}\left[2\phi - \sin(2\phi)\right] \tag{A.18}$$

Substituting equation (A.17) and (A.18) into (A.16), we obtain an equation that calculates the change in volume of the vertical surface S as a function of the bulging pinning angle ϕ.

$$V_{vertical\ bulging} = h \times \frac{R^2}{2}\left[2\phi - \sin(2\phi)\right] = h \times \frac{w^2}{8} \times \frac{2\phi - \sin(2\phi)}{\sin^2(\phi)} \tag{A.19}$$

Additionally, the bulging distance δ is given by equation (A.20).

$$\delta = R\left[1 - \cos(\phi)\right] = \frac{w(1 - \cos(\phi))}{2\sin(\phi)} \tag{A.20}$$

As more liquid is added to the channel, the vertical interface of the pinned fluid will continue to bulge past the pinning features, thus changing the angle of the pinned liquid. Let us now assume that an additional liquid volume, denoted as dV, is added to the initial volume V (Figure A10). The surface area of the vertical interface now becomes S + dS. To find the effect of the increase of volume dV on the bulging angle ϕ, we can calculate the derivative of equation (E19) to find dV/dϕ. This derivatization gives us equation (A.21)

$$\frac{dV}{d\phi} = h \times \frac{w^2}{4} \times \frac{\left[\sin(\phi) + 2\phi + \cos(3\phi)\right]}{\sin^3(\phi)} \tag{A.21}$$

which gives us $d\phi/dV$ in equation (A.22).

$$\frac{d\phi}{dV} = \frac{4\sin^3(\phi)}{h \times w^2 \times \left[\sin(\phi) + 2\phi + \cos(3\phi)\right]} \quad \text{A.22}$$

The values of the increased bulging angle ϕ with an increase of liquid volume of only 1 μL (or 1 mm^3) for 4 initial pinning angles ϕ_0 (20°, 30°, 40°, and 50°) are listed in Table A2. We find that adding 1 μL of additional volume can change the bulging angle; for example, an initial pinning angle of 40° or 50° can increase by 17° or 28°, respectively, with the addition of only 1 μL. This calculation can help explain why experimentally we observed changes in successful pinning of the fluid front at different pipetted volumes.

1. R. C. Bretherton, A. J. Haack, I. Kopyeva, F. Rahman, J. D. Kern, D. Bugg, A. B. Theberge, J. Davis, C. A. DeForest, User-Controlled 4D Biomaterial Degradation with Substrate-Selective Sortase Transpeptidases for Single-Cell Biology. *Adv. Mater.* **35**, 2209904 (2023).
2. C. A. DeForest, D. A. Tirrell, A photoreversible protein-patterning approach for guiding stem cell fate in three-dimensional gels. *Nat. Mater.* **14**, 523–531 (2015).
3. I. Kopyeva, E. C. Goldner, J. W. Hoye, S. Yang, M. C. Regier, K. R. Vera, R. C. Bretherton, C. A. DeForest, Stepwise Stiffening/Softening of and Cell Recovery from Reversibly Formulated Hydrogel Double Networks. [Preprint] (2024). https://doi.org/10.1101/2024.04.04.588191.
4. J. Berthier, K. A. Brakke, "Sessile Droplets" in *The Physics of Microdroplets* (Wiley, ed. 1, 2012; https://onlinelibrary.wiley.com/doi/book/10.1002/9781118401323), pp. 105–142.
5. A. Buguin, L. Talini, P. Silberzan, Ratchet-like topological structures for the control of microdrops. *Appl. Phys. A* **75**, 207–212 (2002).
6. T. Ondarçuhu, Total or Partial Pinning of a Droplet on a Surface with a Chemical Discontinuity. *J. Phys. II* **5**, 227–241 (1995).
7. J. Bico, C. Marzolin, D. Quéré, Pearl drops. *Europhys. Lett. EPL* **47**, 220–226 (1999).
8. J. Bico, C. Tordeux, D. Quéré, Rough wetting. *Europhys. Lett. EPL* **55**, 214–220 (2001).
9. K. A. Brakke, The Surface Evolver. *Exp. Math.* 1, 141–165 (1992).

Table A1. Experimental contact angle measurements of 5 mg/mL collagen on 1% BSA treated 3D printed resin.

Experiment number	1% BSA treated 3D printed surface number	Number of technical measured replicates from Krüss drop shape analyzer goniometer	Mean contact angle (degrees) from Krüss drop shape analyzer goniometer	Standard deviation (degrees) of contact angle from Krüss drop shape analyzer goniometer	Overall Average of mean contact angles (degrees)	Average standard deviation of contact angle (degrees)
1	1	10	34.73	0.98	29.62	3.51
	2	6	28.69	4.13		
	3	9	48.41	2.07		
2	4	6	18.11	2.55		
	5	5	26.01	2.7		
	6	10	36.31	2.46		
	7	7	23.18	2.15		
	8	5	20.82	1.36		
	9	9	22.38	2.77		
3	10	5	19.80	11.96		
	11	7	41.85	1.93		
	12	7	30.75	2.26		
	13	8	39.64	3.6		
	14	9	35.74	4.04		
	15	5	21.75	2.62		
	16	9	32.36	2.3		
	17	5	39.81	2.81		
	18	7	28.28	2.98		
	19	6	29.06	4.45		
	20	5	14.62	2.93		

Table A2. Change in the bulging angle of the pinned fluid's vertical interface as a function of change in volume.

w (mm)	h (mm)	ϕ_0 (°)	ϕ_0 (rad)	δ_0 (μm)	S_0 (mm^2)	V_0 (mm^3)	$dV/d\phi$ (mm^3/rad)	$d\phi/dV$ (°/mm^3)	dV (mm^3)	ϕ (°)	δ (μm)
0.8	3.5	20	0.35	70.5	0.04	0.13	21.56	2.66	1.0	23	80.1
0.8	3.5	30	0.52	107.2	0.06	0.20	6.93	8.27	1.0	38	138.8
0.8	3.5	40	0.70	145.6	0.08	0.28	3.25	17.66	1.0	57	220.2
0.8	3.5	50	0.87	186.5	0.10	0.36	2.05	27.95	1.0	78	323.6

Table A3. Parameters considered in the vampire and cavity pinning feature design in STOMP.

Parameter	Convex "Vampire" Pinning Feature	Concave "Cavity" Pinning Feature
Width between pins, w_1, w_2 (mm)	0.8	1.2
Vampire angle, α (degrees)	5 to 80	–
Cavity angle, β (degrees)	–	25 to 130
Channel height, h (mm)	3.5	
Collagen density (kg/m^3)	958	
Surface tension (mN/m)	72	
Average static contact angle of collagen on 3D printed resin, θ (degrees)	30 ± 3.5	
Lowest measured contact angle (degrees)	15	
Highest measured contact angle (degrees)	48	
Gravitation constant (m/s^2)	10	

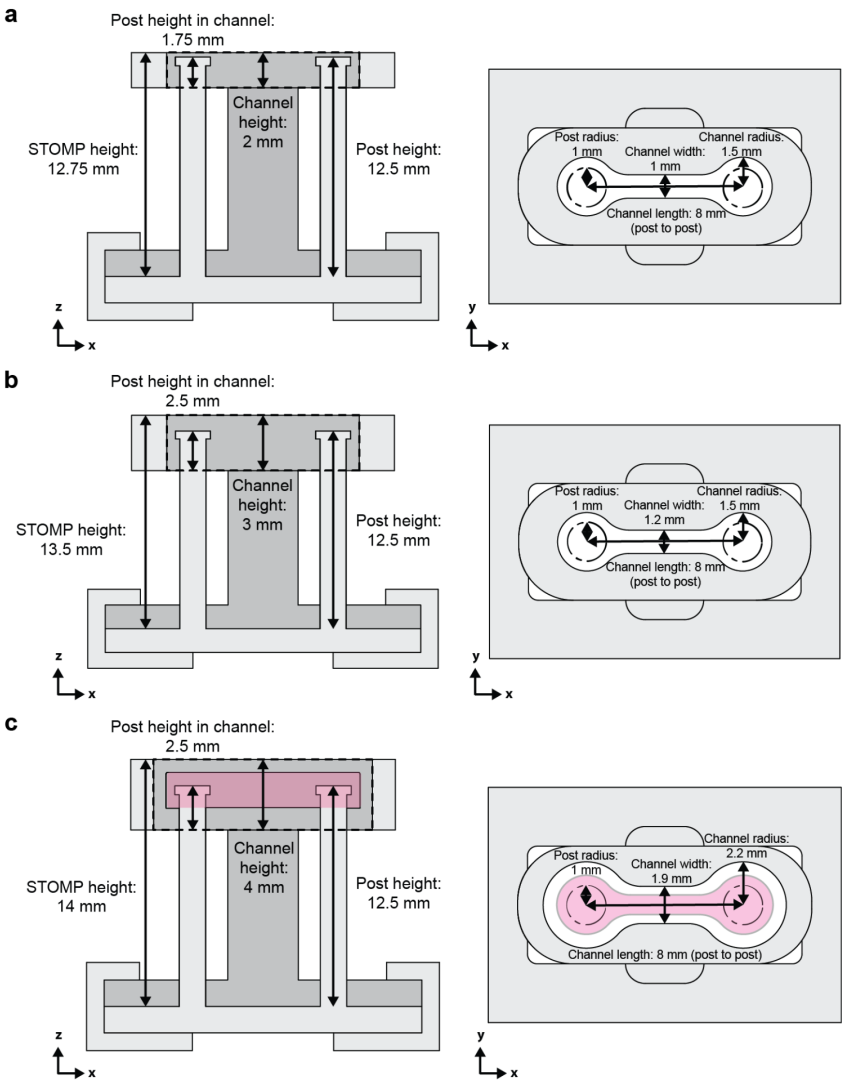

Figure A1. Dimensions of STOMP devices used in this work. a) 2 mm height device, b) 3.5 mm height device, and c) outer region patterning device surrounding previously patterned hydrogel (in pink), featured in Fig. 2.5

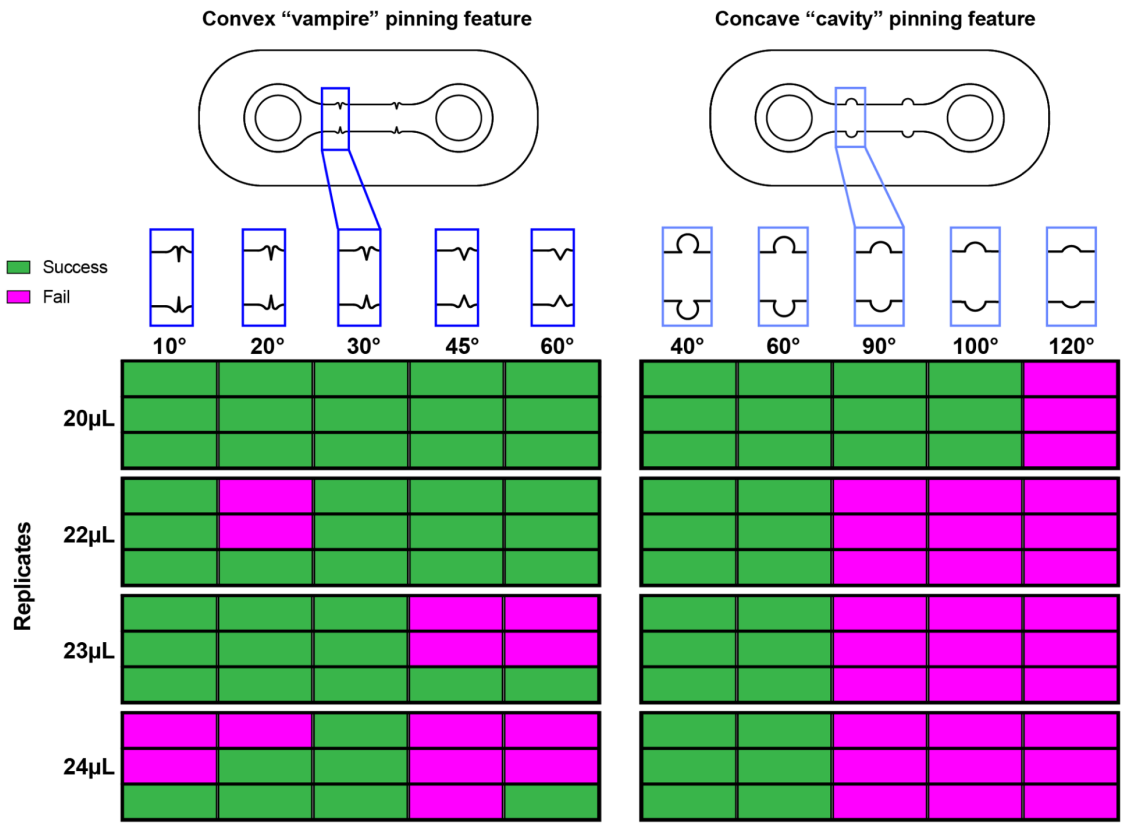

Figure A2. Experimental results of pinning of the 5 mg/mL collagen precursor fluid front at different pipetted volumes. For both the convex “vampire” and concave “cavity” pinning features, five different pinning feature angles were tested to observe either success (green) or failure (magenta) of pinning at the pinning feature. For the convex “vampire” pinning features, the angle of the pinning feature refers to the vertex angle of the triangular pinning feature. For the concave “cavity” pinning features, the angle of pinning feature refers to the angle between the line tangent to the semicircular pinning feature to the straight channel wall.

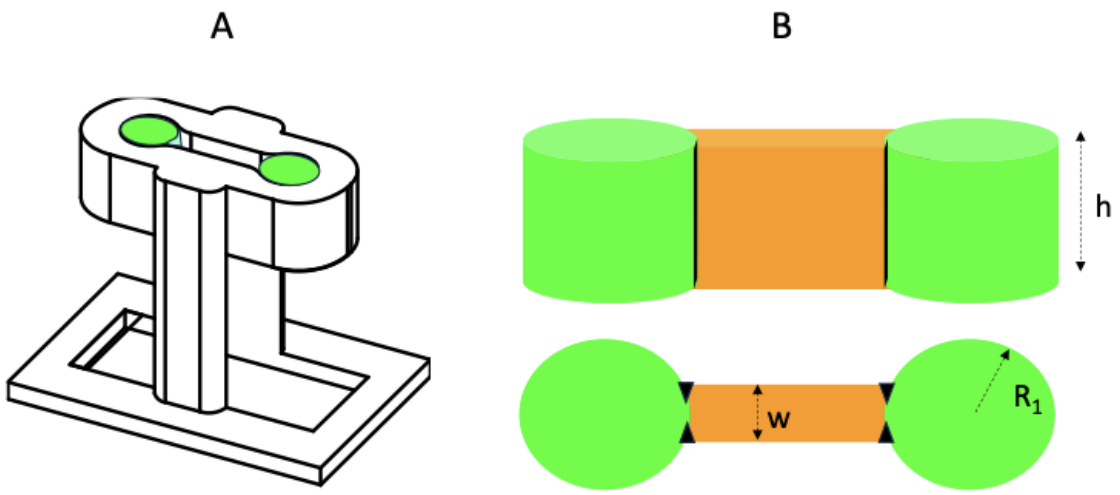

Figure A3. Modeling fluid in the multi region STOMP device. A) isometric view of the device. B) top: side view of the filled device; bottom: top view of the filled device. The black lines and arrows symbolize the relief/design that pins the liquids during the filling.

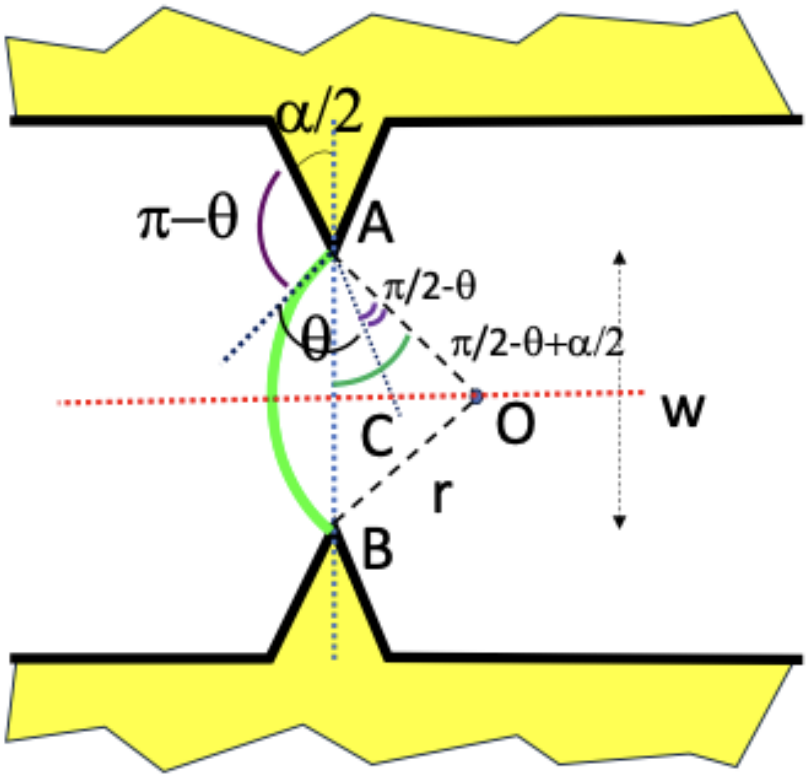

Figure A4. Geometrical analysis of convex "vampire" pinning features. Green line is the fluid front, where the hydrogel precursor was pipetted first into the region on the right, so the fluid front is bulging to the left at the Laplace pinning threshold.

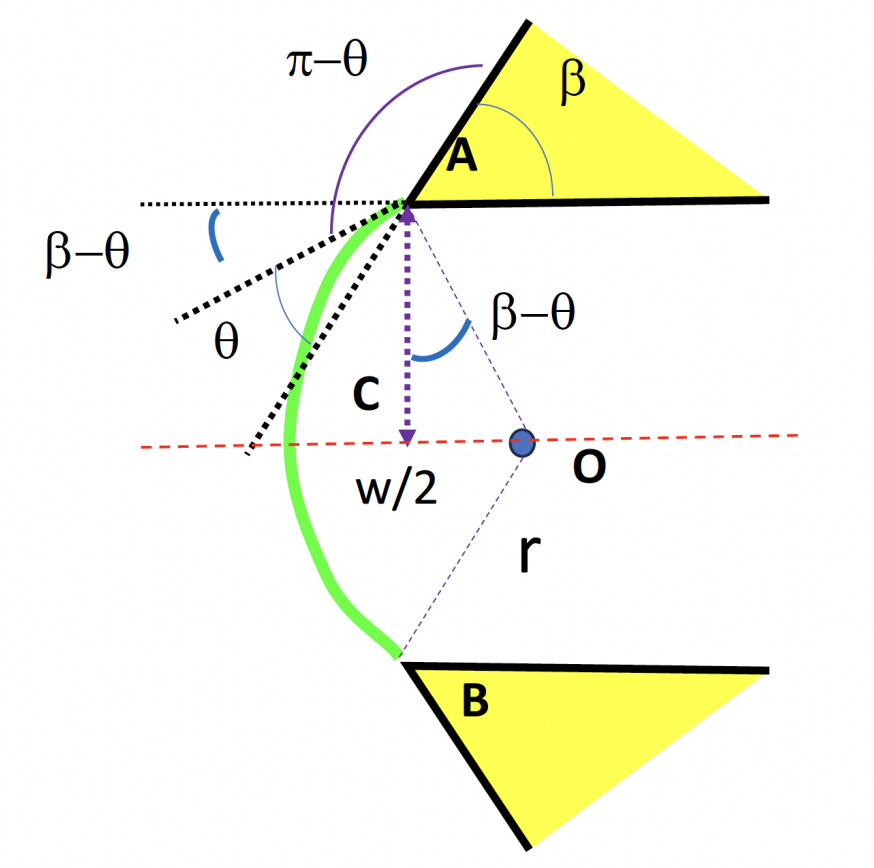

Figure A5. Geometrical analysis of concave "cavity" pinning features when $\beta > \theta$. Green line is the fluid front, where the hydrogel precursor was pipetted first into the region on the right, so the fluid front is bulging to the left at the Laplace pinning threshold.

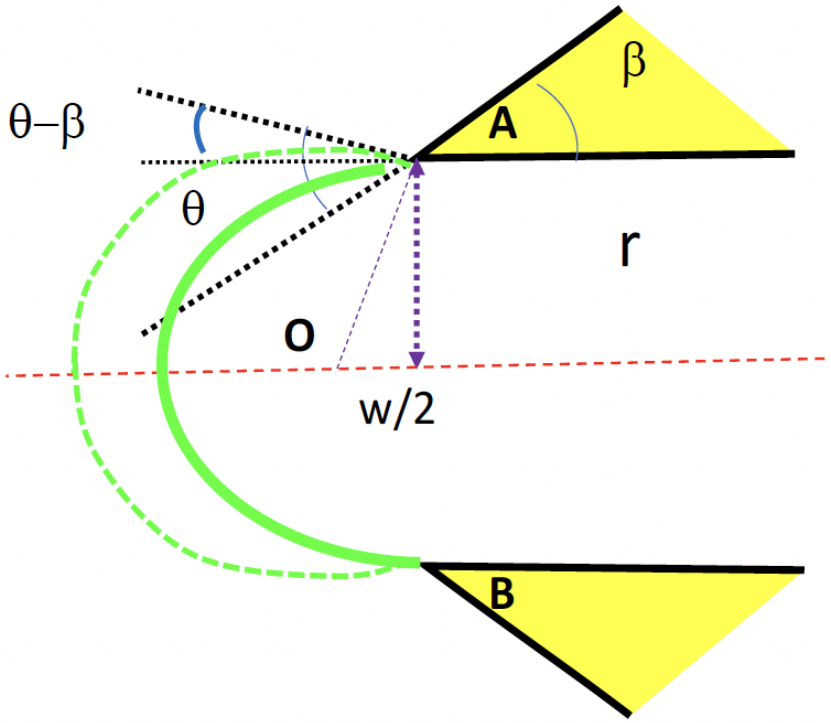

Figure A6. Geometrical analysis of concave "cavity" pinning features when $\beta < \theta$. The dotted green line is the expected fluid front, where the hydrogel precursor was pipetted first into the region on the right, so the fluid front is bulging to the left. However, the actual fluid front is the solid green line, which is the maximum Laplace pinning threshold.

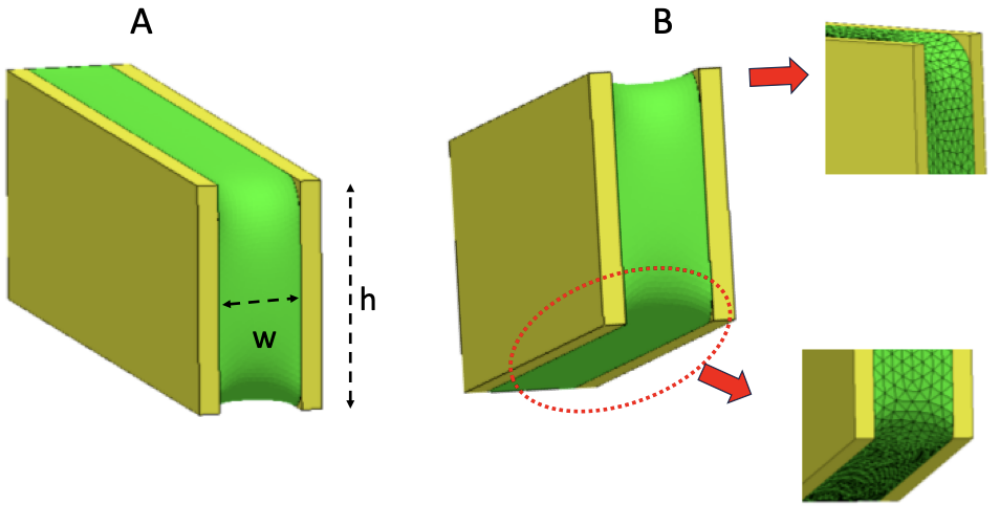

Figure A7. 3D calculation of the free air-liquid interface of a liquid between two vertical walls with a width of 1.2 mm and a height of 3.5 mm. A) Isometric view of a fluid (green) within an open channel with two walls and no ceiling or floor. B) Closer view of the top and bottom corners of the vertical interface, showing the plots obtained using the Surface Evolver software.

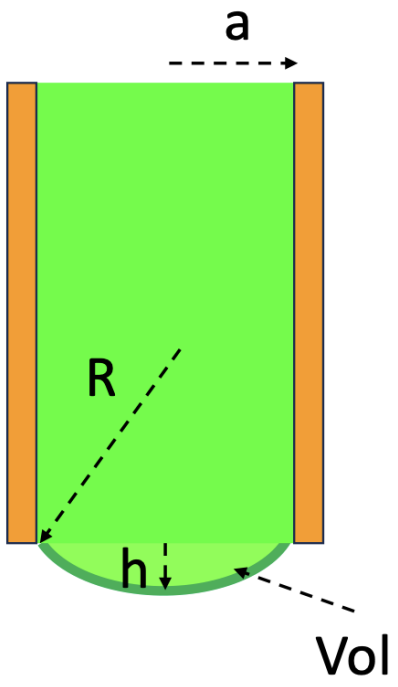

Figure A8. Schematic of the fluid (green) bulging below the suspended channel walls (orange).

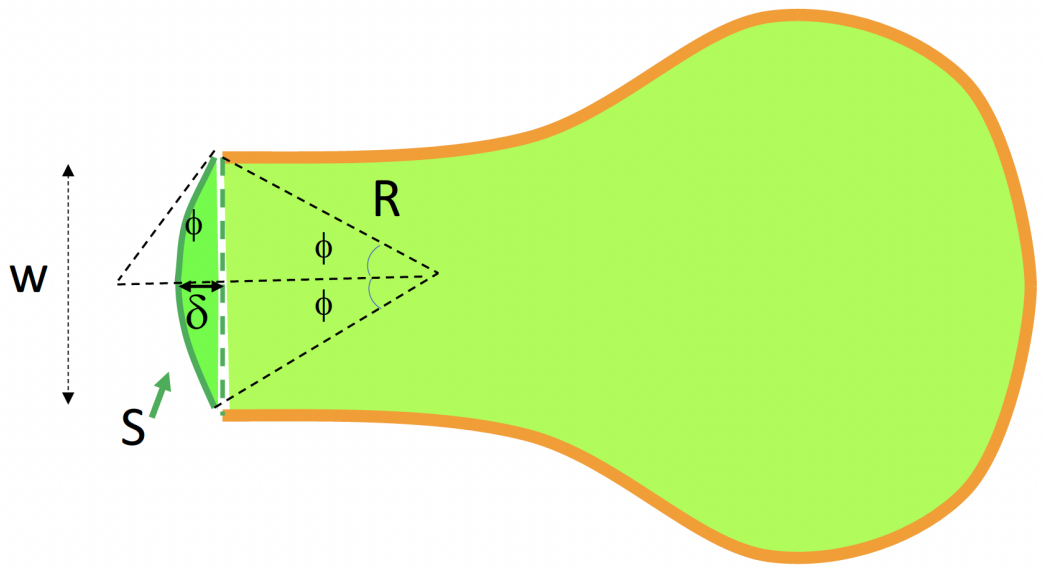

Figure A9. Top-down schematic of the fluid (green) filling the outer regions of the suspended channel (walls denoted in orange) before reaching the pinning features (location marked by dotted green line). After reaching the pinning feature, the fluid will bulge some distance δ along the vertical interface, with the bulging angle denoted as ϕ. The surface area S (dark green) is the surface area of the bulging liquid along the vertical interface.

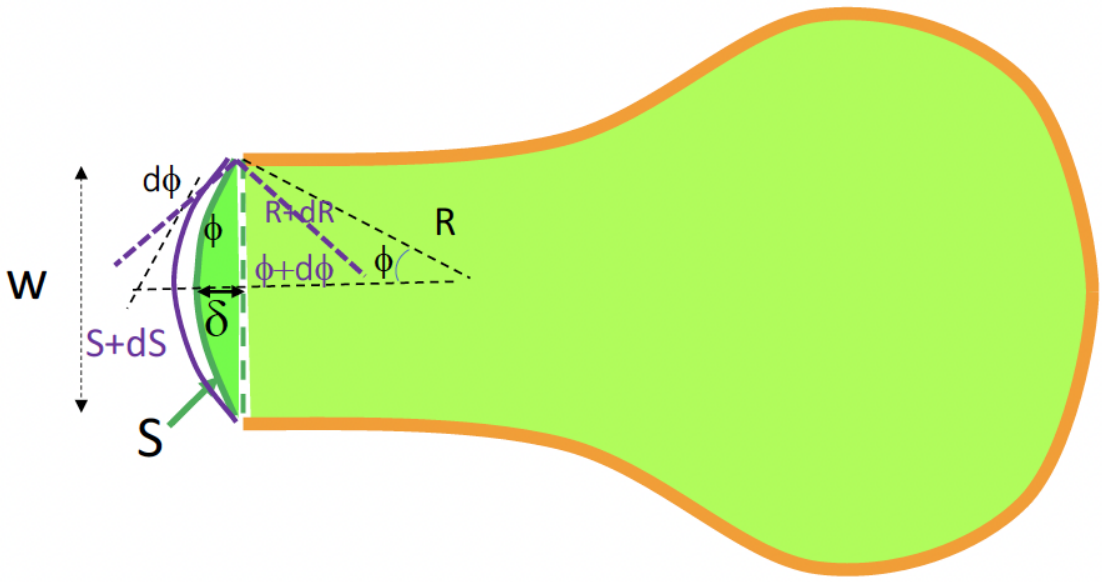

Figure A10. Top-down schematic of how the bulging fluid (dark green) along the vertical interface changes after pipetting additional volume into the suspended channel.

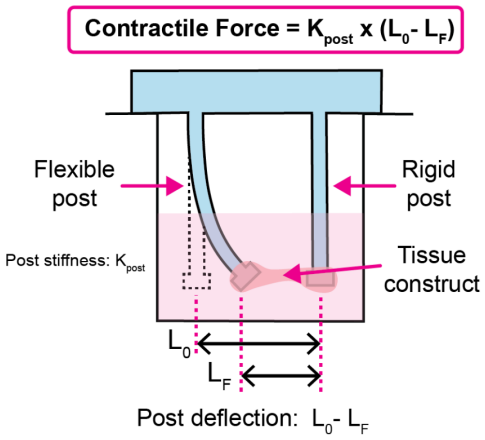

Figure A11. Tissue contractile force calculation using post deflection. Deflection of post is measured by initial length of tissue, L_0, minus the final length of tissue, L_F.

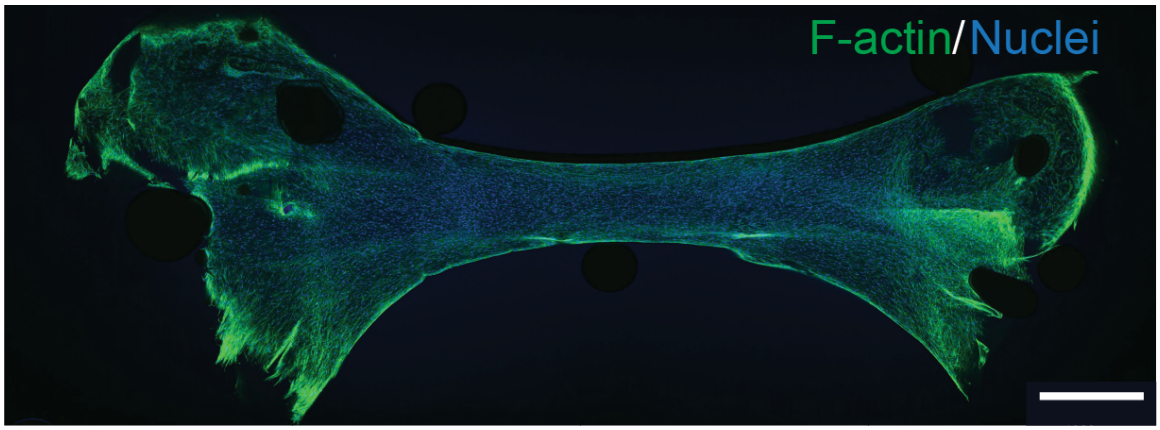

Figure A12. Fluorescent image of a patterned PTC stained for F-actin (green) and nuclei (blue). Scale bar is 1 mm.

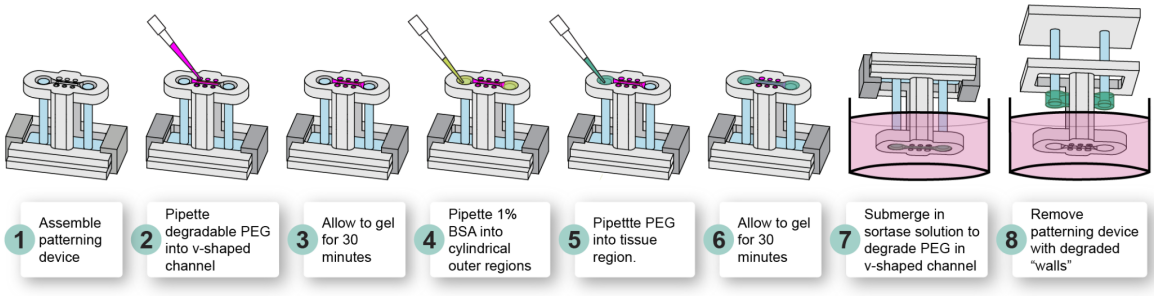

Figure A13. Schematic showing process for patterning a degradable hydrogel channel wall and middle tissue region. The hydrogel depicted in magenta uses a sortase degradable crosslinker allowing for selective degradation of the channel wall with the addition of sortase.

B. Appendix for Chapter 3

Reproduced in part from L.G. Brown, A. J. Haack*, D. S. Kennedy, K. N. Adams, J. E. Stolarczuk, M. G. Takezawa, E. Berthier, S. Thongpang, F. Y. Lim, D. Chaussabel[#], M. Garand[#], and A. B. Theberge[#], "At-home blood collection and stabilization in high temperature climates using* home*RNA" Frontiers in Digital Health, 2022, **4**, 903153.*
**Equal contribution*
[#]Co-corresponding author

Table B1: Experimental timeline and external temperature conditions for Doha, Qatar pilot study

Time (h)	Event / Procedure	External Temperature (℃)	Location
0	Overnight hold at room temperature	21	Lab, Research
27	Start in lab	21	Lab, Research
27.25	Transport outside to car	26	Outside
27.3	In car - A/C started	35.5	Indoor parking
27.4	In car - A/C on	27	Indoor parking
27.5	In car - driving with some sun exposure	33	Driving
28	In car - A/C stopped	31	Outdoor parking - moderate sun exposure
28.1	In car - A/C restarted	37	Outdoor parking - moderate sun exposure
28.25	Car stopped - A/C off	30	Outdoor parking - covered
29	Car restarted - A/C on	41	Outdoor parking - covered
29.19	Car stopped - A/C off	32	Home parking - covered
29.42	Car restarted - A/C on	40	Home parking - covered
29.49	Car stopped - A/C off - Walking to Lab	32	Indoor parking
29.54	Enter building	36	Research
29.56	Office	32	Office, Research
30	Transferring blood from stabilizer tube to store	21	Lab, Research
30.3	Storing sample	-80	Lab, Research

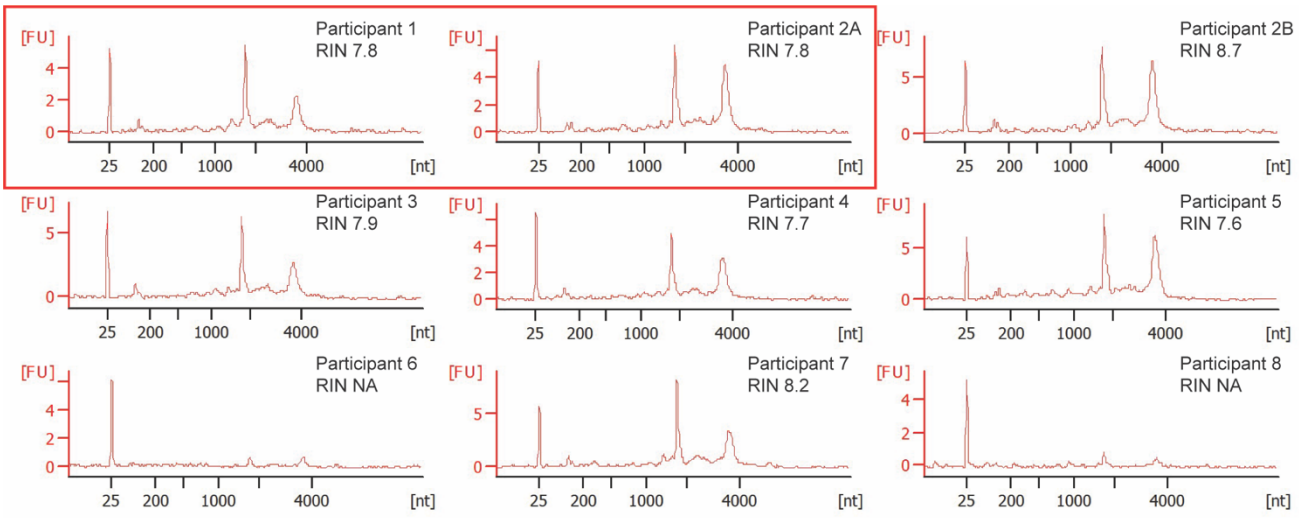

Figure B1. Electropherograms of isolated RNA from stabilized *home*RNA samples in Doha, Qatar. Electropherograms were obtained as raw data using a RNA 6000 Nano Kit on an Agilent 2100 bioanalyzer, which uses fluorescence to detect the marker (~25 nt), 18S rRNA fragments (~1900 nt), and 28S rRNA fragments (~3900 nt). The RIN algorithm then uses these peaks to assign a RIN value to the corresponding sample. The electropherograms are used to generate a gel image, as seen in Figure 3.2B. Samples 1 and 2A in the red box correspond to control samples.

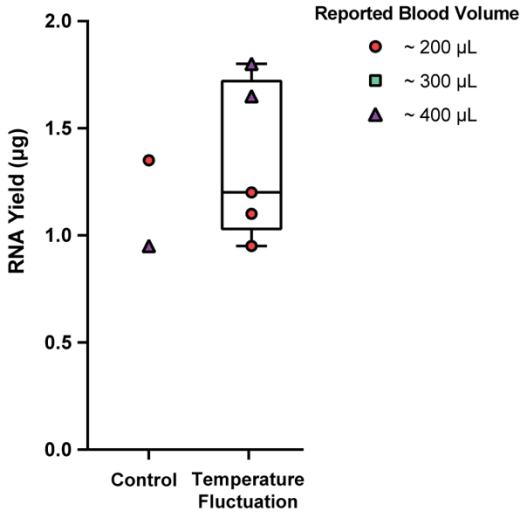

Figure B2. Yield of isolated RNA from stabilized *home*RNA samples in Doha, Qatar. Reported yields were obtained from bioanalyzer measurements by taking the reported concentration from the first 50 µL elution. For the two samples (from participant 6 and 8) that did not have scorable RIN values, yields were not included on the graph since their concentrations were below the lower limit of the qualitative range of the RNA 6000 Nano kit (5 ng/µL). However, for reference, the bioanalyzer reported 4 ng/µL for participants 6 and 8. While concentrations from the Agilent 2100 Bioanalyzer are not typically used for obtaining yield, a threshold value of 200-500 ng total yield is typically needed for downstream analysis such as RNA sequencing. Therefore, an exact value is less important and the bioanalyzer can be used to obtain approximate RNA concentration ranges.

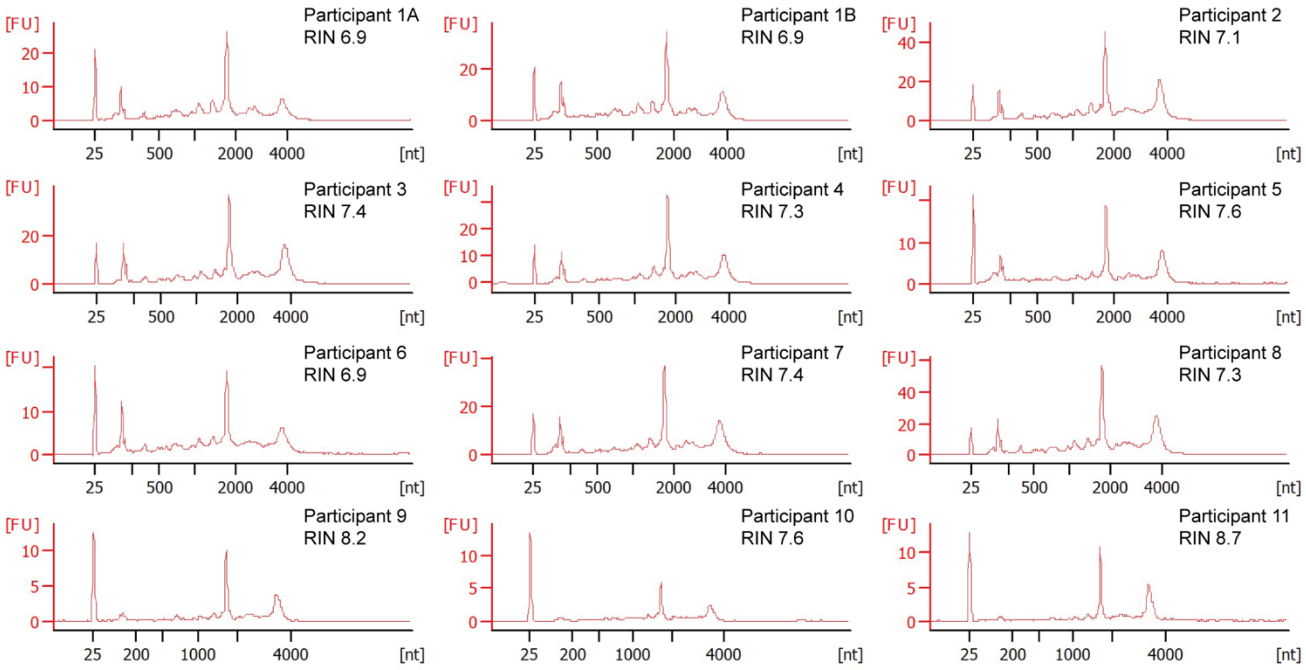

Figure B3. Electropherograms of isolated RNA from stabilized *home*RNA samples in the Western and South Central USA. Electropherograms were obtained as raw data using a RNA 6000 Pico Kit for samples 1-8 and a RNA 6000 Nano Kit for samples 9-11 on an Agilent 2100 bioanalyzer. For samples 1-8, the RNA 6000 Pico kit uses fluorescence to detect the marker (~25 nt), 5S rRNA fragments (~150 nt), 18S rRNA fragments (~1900 nt), and 28S rRNA fragments (~3900 nt). The RNA 6000 Nano kit detects the same peaks with the exception of the 5S rRNA fragment peaks. The RIN algorithm then uses these peaks to assign a RIN value to the corresponding sample. The electropherograms are used to generate a gel image, as seen in Figure 3.3A.

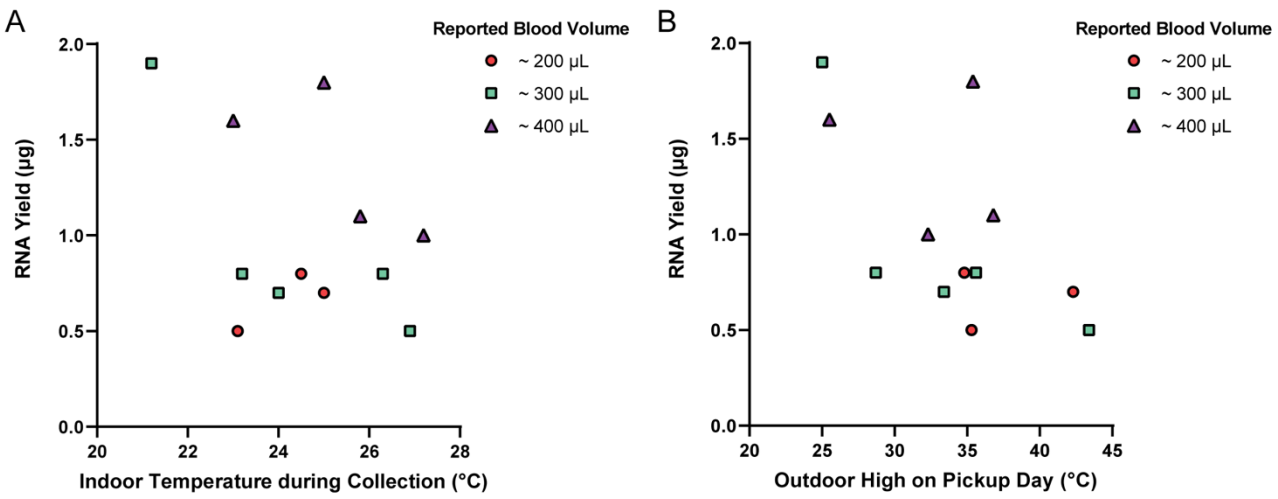

Figure B4. Total yield of isolated RNA from stabilized *home*RNA samples collected, stabilized, and shipped at high temperatures in Western and South Central USA. Reported total yields were obtained by measuring both 50 µL elutions from the RNA isolation protocol (see Methods and Materials) on Cytation 5 Multi-Mode Reader and adding them together to obtain a total yield. Each total yield is reported with the corresponding A) indoor ambient temperature at the time of collection and B) reported outdoor temperature high on the pickup day.

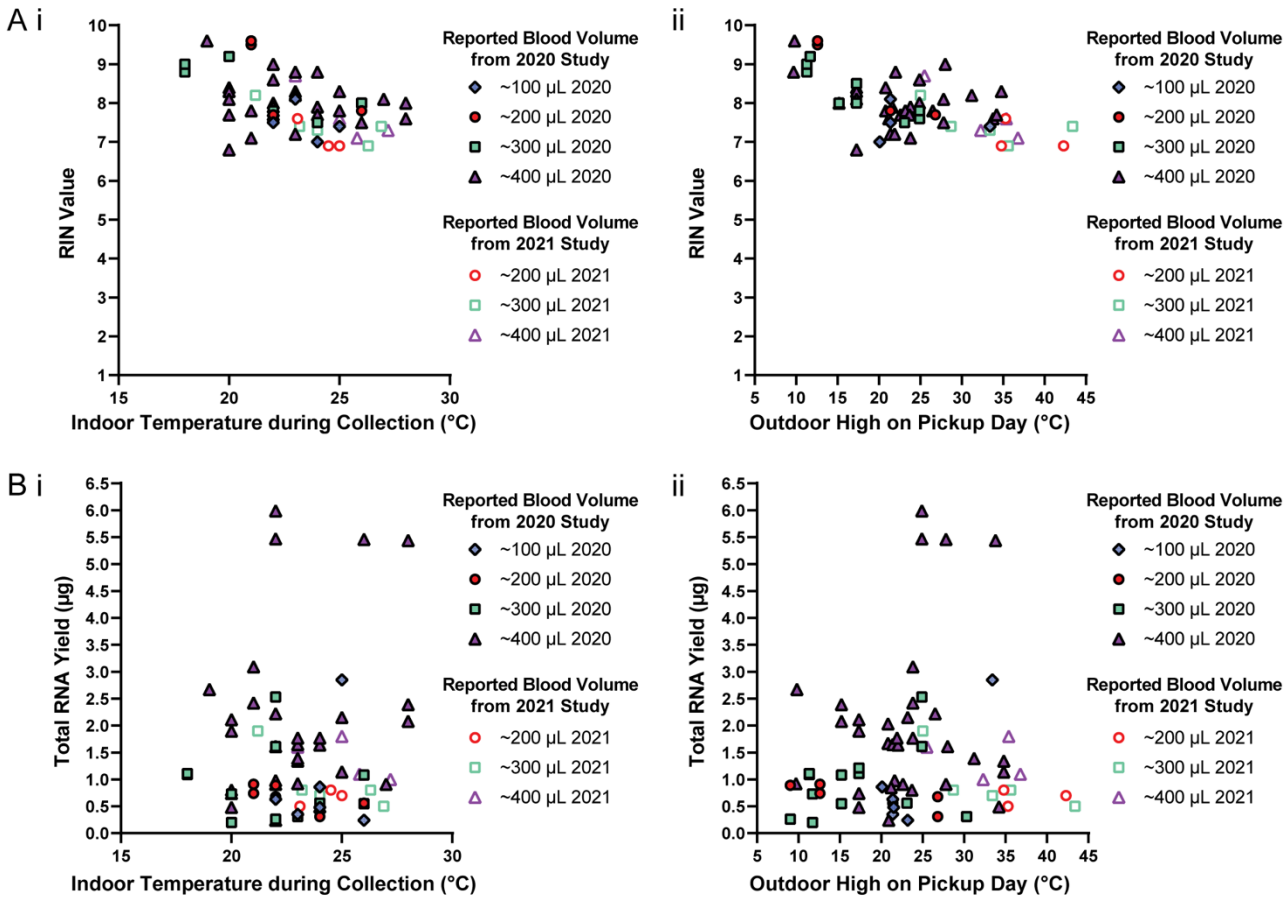

Figure B5. RNA quality and quantity versus temperature, combining data from the present study (summer 2021) from our previous pilot study (summer 2020, Haack, Lim, et al. 2021) [1]. A) RIN values versus i) indoor temperature and ii) outdoor high on pickup day. B) Total RNA yield versus i) indoor temperature and ii) outdoor high on pickup day.

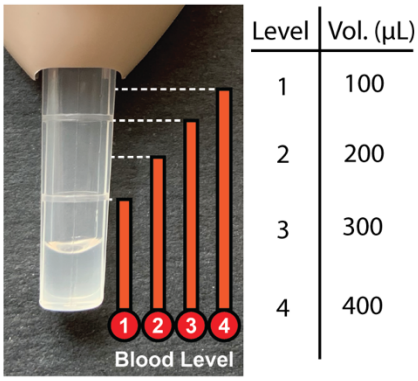

Level	Vol. (µL)
1	100
2	200
3	300
4	400

Figure B6. Reported blood level volumes. Study participants for both the Qatar and Western and South Central USA groups were asked to report the approximate volume with each blood collection with the Tasso-SST™ based on this picture provided in the survey that they completed with sampling. Image was reprinted with permission from Haack, Lim, et al. *home*RNA: A Self-Sampling Kit for the Collection of Peripheral Blood and Stabilization of RNA**.** *Anal. Chem.* 2021, 93, 39, 13196–13203. Copyright 2021 American Chemical Society. [1]

References

1. Haack AJ, Lim FY, Kennedy DS, Day JH, Adams KN, Lee JJ, Berthier E, Theberge AB. *home*RNA: A Self-Sampling Kit for the Collection of Peripheral Blood and Stabilization of RNA. *Anal Chem* (2021) **93**:13196–13203. doi: 10.1021/acs.analchem.1c02008

PREPARE DEVICES AND APPLICATION SITE

FIRST TIME USERS

Please watch the instructional video provided at

https://www.youtube.com/watch?v=iV3GZ8SmmuM

1. Wash hands and get a timer.

You will use a timer in Steps 2 and 10.

2. Apply hot pack to upper arm for 2 minutes.

Warming helps your blood flow better.

3. Clean arm with alcohol wipe.

4. Open the stabilizer tube by twisting off the purple cap.

5. Open Tasso pouch by pulling apart white and clear layers.

Discard cap in pouch.

COLLECT BLOOD USING TASSO-SST

6. Remove clear plastic cover over the red button.

7. Peel paper tab behind the red button.

Keep the tube pointing down.

8. Stick device to shoulder.

Do not remove once it is on.

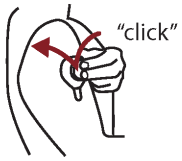

9. Press button quickly and firmly until it can't go any farther. Wait 2 seconds then let go.

10. Start a 5 minute timer.

Keep arm at your side. You wont see blood right away. It can take up to a minute for blood to flow.

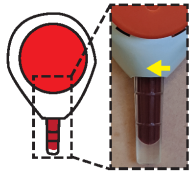

11. After 5 minutes or when the tube fills, *whichever comes first*, peel off the device.

12. Remove tube by firmly twisting a quarter turn and pulling down.

This may take a bit of finger strength.

MIX AND PACKAGE

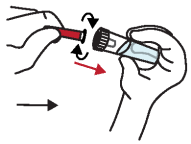

13. Bring together the blood tube and stabilizer tube and screw these together tightly.

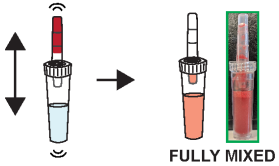

14. With the stabilizer tube on the bottom, shake hard up and down to mix. Stop when mixed.

Some fluid may remain in blood tube. When mixed, the color is the same. See insert for details.

DO NOT DISCONNECT TUBES.

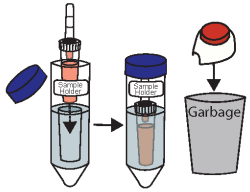

15. Place sample in sample holder. Throw away used Tasso device.

16. Place blood sample in the specimen bag. Wash your hands with soap and water

17. Fill out the online Collection Survey that was emailed to you.

You will need the Unique Code on the box.

18. After filling out the survey, place your sample back in the box, and return using the provided shipping return bag.

Figure B7. Instructions for use for *home*RNA

For research use only

INSTRUCTIONS FOR USE

Home Blood Collection Kit

INTENDED USE

TASSO-SST is a single use blood collection device that is intended for the self collection of capillary blood from the upper arm of adults (18 years or older). The stabilizer tube contains liquid that is intended for stabilizing the collected blood. The home blood sampling kit is for academic research use.

STORAGE

Store at 15 - 30ºC (60 - 80ºF) in a dry place.

WARNINGS

- The TASSO-SST is a sterile device. Do not open until use.
- The TASSO-SST device contains sharps. Handle with care.
- For external use only.
- Keep out of reach of children.
- Use while seated as fainting may occur during blood sampling procedure.
- Do not activate the red button until device is firmly on skin.
- Wipe application site with alcohol wipe to reduce infection risk.
- Always use a new unopened pouch of Tasso-SST. Do not re-use.

ONLINE SYMPTOM AND COLLECTION SURVEY

Please check your e-mail or text message based on the preference you has listed for a link to fill out the daily use online survey.
If you cannot find the link, e-mail us at [redacted]

If you need assistance please contact us at bcmeresearch@uw.edu or call [redacted]

Thank you for participating in our study!

KIT CONTENTS

Make sure your kit contains all components listed below

1) Tasso-SST device
2) Stabilizer tube
3) Alcohol wipes
4) Hot pack
5) Bandage
6) Specimen bag
7) Sample Holder
8) Mail return bag

C. Appendix for Chapter 4

Reproduced in part from F. Stefanovic, L.G. Brown*, J. MacDonald, T. Bammler, D. Rinchai, S. Nguyen, Y. Zeng, V. Shinkawa, K. Adams, D. Chaussabel, E. Berthier, A.J. Haack[#], and A.B. Theberge[#], ``AYour Blood is Out for Delivery: Considerations of Shipping Time and Temperature on Degradation of RNA from Stabilized Whole Blood." Anal Chem. 2025 Jan 28;97(3):1635-1644.*
** Equal contribution*
[#]Co-corresponding authors

Table C1: Summary of temperature probe data

Location	RUCA	Time (h)	Tavg (°C)	Tmed (°C)	Tmax (°C)	Tsd (°C)	Hours above 30°C
AZ	1	168	26.8	26.9	40	4.2	38.3
CA	1	72	26.5	25.4	44.4	4.9	11.1
CO	4	96	24.3	24.1	39.5	4.4	7.6
GA	1	72	24.8	24.3	41.9	4.4	7.4
HI	4	193	26.1	25.5	38.5	3.7	22.8
IL	1	72	23.7	22.6	38	1.9	4.5
In-Lab	1	200	25.5	25.5	25.7	0.4	0
KS	1	71	25.8	24.0	43.3	4.9	10.4
MA	1	72	26.4	26.5	40.9	3.5	8.2
ME	5	72	24.0	23.4	35.4	3.2	3.8
MN	1	71	25.4	23.3	39.3	5.6	14.4
NC	5	72	27.7	28	38.8	4.1	18
NE	10	168	28.5	27.2	45.1	5.5	55
NM	1	72	26.4	26.1	39.3	3.9	9.5
WA	1	71	23.8	23.1	36.6	3.1	3.7

Table C1. Summary of temperature probe data. This table summarizes the shipping conditions of each state where samples were shipped. The Rural-Urban Commuting Area (RUCA) codes are designations made by the United States Department of Agriculture to quantify how rural or urban a location is. A RUCA value of 1 represents the most urban area where a value of 10 represents the most rural area. The time and temperature values are all calculated from the data measured by the Elitech RC-5+ continuous temperature probes. Here, we report the average (Tavg), median (Tmed), maximum (Tmax), and standard deviation (Tsd) of temperatures experienced by the samples sent to each location. We also calculate the total number of hours the samples spent above a temperature of 30ºC, which we classify as “elevated” or “high” temperature conditions**.**

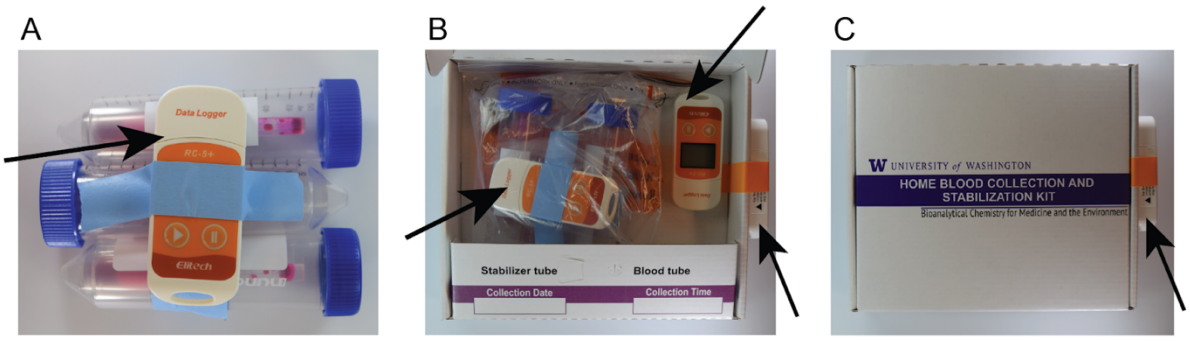

Figure C1. Shipping experiment continuous temperature probe setup. (A) Each homeRNA-stabilized sample is placed in a 50 mL conical tube with a custom insert to prevent excessive movement in the shipping process. Three such replicates are taped together, and a temperature monitor (indicated by black arrows) is attached directly to this construct. (B) The samples are sealed in a biohazard bag and are then placed in the homeRNA box. Another temperature probe is placed inside of the box as a backup. (C) Then an additional temperature probe is attached to the outside as a final backup; the entire box is placed into a UPS LabPak and shipped to the participants. These samples are kept indoors overnight at which point a pre-printed return label (in a label pouch on the outside of the LabPak) is attached. The LabPak is placed on the volunteers' front porch or mailroom and picked up by UPS to be returned to the lab.

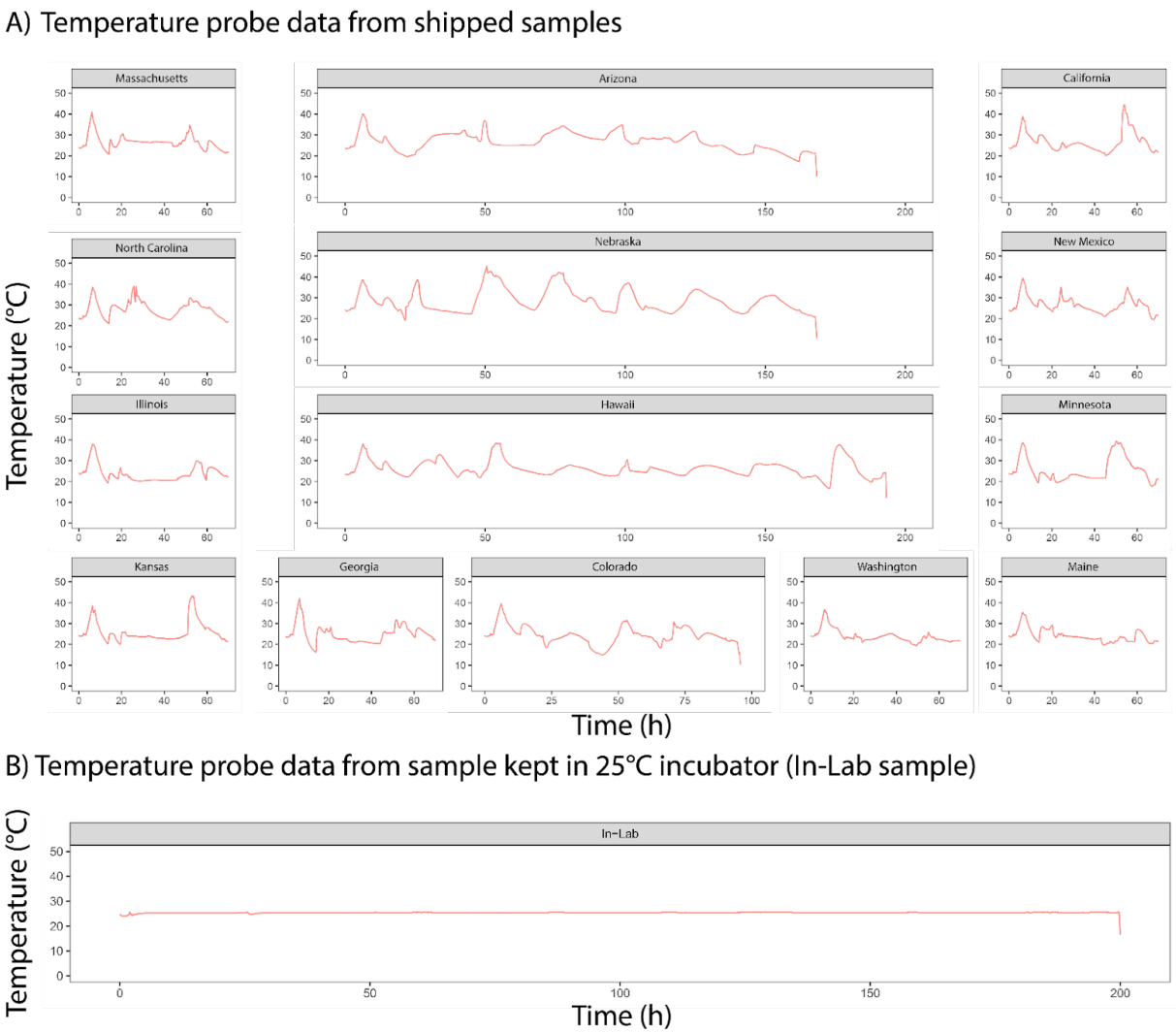

Figure C2. (A) Visual summary of temperature probe data from each location. The shipping locations are states within the United States. Before the packages were picked up by the courier service and shipped to the participant, all packages were placed in a UPS box. During this time in the UPS box, the temperature monitors in the packages showed a peak, with an average maximum temperature of 38.6°C (over 14 temperature probes) and reaching up to 41.9°C (one temperature probe). B) Temperature probe data from the In-Lab sample kept in a 25°C incubator until last shipped sample (Hawaii, 8 days) was returned to lab.

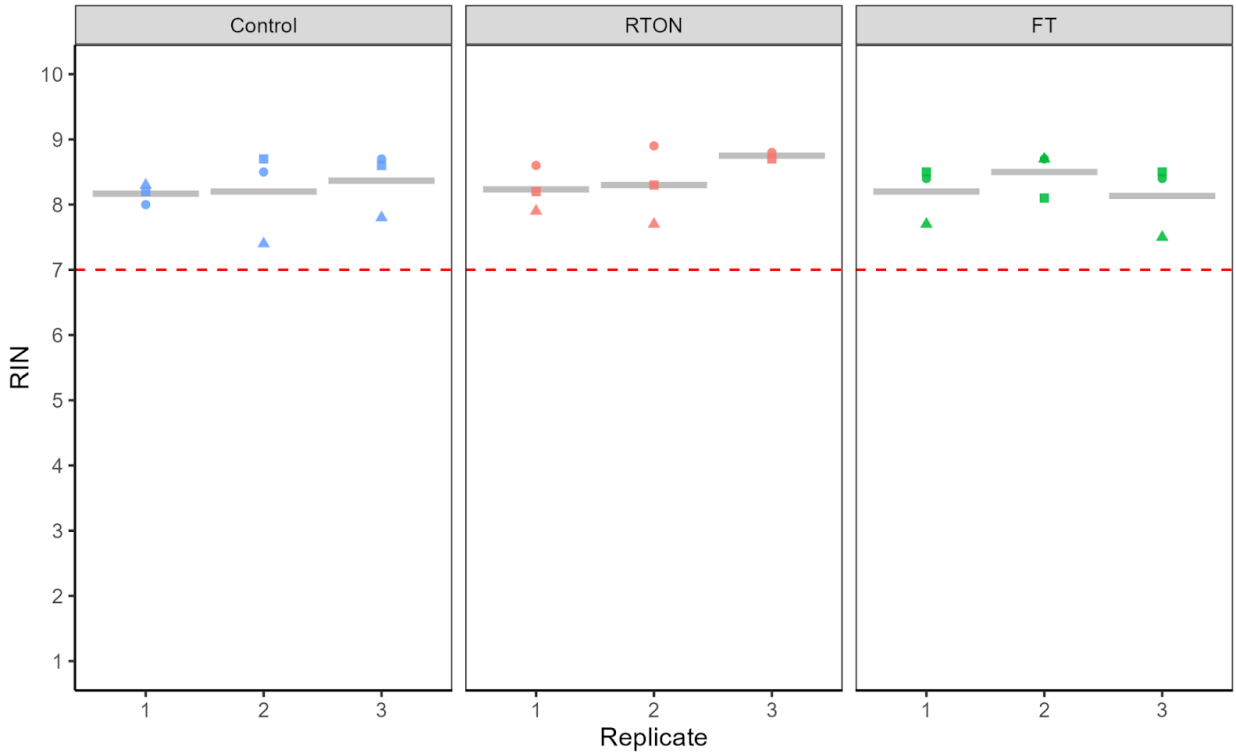

Figure C3. Effects of freeze-thaw on RNA integrity in homeRNA-stabilized blood samples. The resulting RINs are plotted here where each column represents the condition, with the gray crossbars indicating average values for each replicate. Overall, the data did not suggest that there were any adverse effects on RNA integrity as a result of a freeze-thaw cycle of homeRNA-stabilized blood samples.

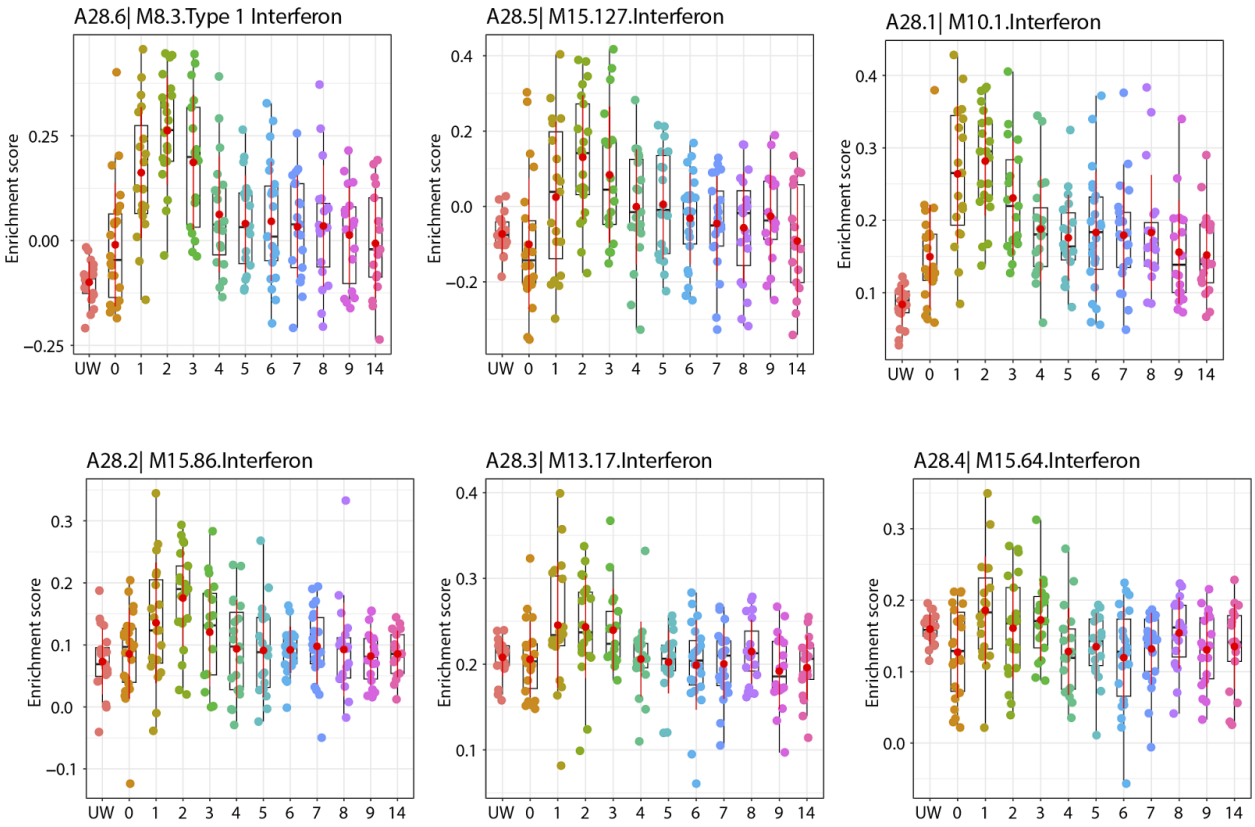

Figure C4: Analysis of Interferon Modules Enrichment Scores of Subjects Pre- and Post- Vaccination. The dot plots show the enrichment scores for six interferon response modules (M8.3, M10.1, M13.17, M15.64, M15.86, and M15.127) for the current study (UW) and at different days before and after administration of COVID-19 mRNA vaccine (COVAX study – day 0 = pre-vaccination sample). Following the UW (shipping) samples, the y-axis represents days of sampling from the COVAX study.

Supplementary discussion of Figure C5

In addition to the BloodGen3 analysis, we also fit a model that includes the time spent above a temperature of 30°C, RIN, and 4 surrogate variables (generated using the Bioconductor sva package) to account for any unobserved technical variability [1]. After fitting this model, we selected genes with a false discovery rate (FDR) of <0.05, which estimates the maximum number of false positives in a set of significant results, as well as requiring at least a 1% change in expression. This resulted in only two genes (MMP9 and ADGRG3) that had a decrease in expression as a function of time spent at 30°C or higher (Figure S5). While both genes appear to be affected by storage at high temperatures, they also exhibit a notable amount of noise mainly due to the small sample size. Moreover, linear regression is not resistant to outliers; in our data, we propose that there are some (3 for MMP9 and 4 for ADGRG3) high-leverage points that are multiple orders of magnitude greater than the rest of the points and are not representative of the rest of the samples. This suggests that the two genes MMP9 and ADGRG3 potentially could be affected by shipping conditions, but future work with more sensitive methods could potentially capture differences in the transcriptome not detected here.

1. Leek, J. T. & Storey, J. D. Capturing Heterogeneity in Gene Expression Studies by Surrogate Variable Analysis. *PLOS Genetics* **3**, e161 (2007).

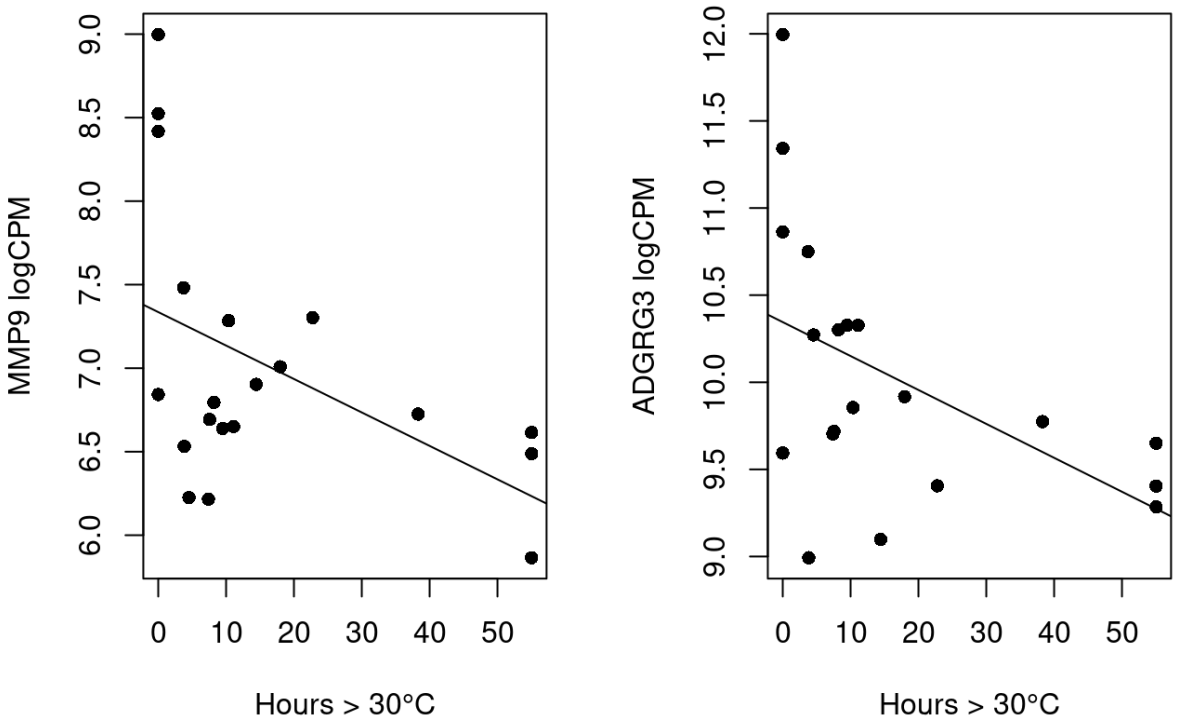

Figure C5. Expression levels of MMP9 and ADGRG3 as a function of time in excess of 30°C. The slope for both genes correspond to an approximate 34% reduction in transcript for each 10 hours > 30°C.

Supplementary discussion of Figures C6 and C7

Further, we fit linear regressions with "time in transit" or "time above 30°C" against RIN scores to better understand the effects these variables have on RNA degradation (Figures C6 and C7). All samples that spent below 100 hours in transit had RIN scores at or above 7. The samples that were in transit the longest were AZ (168 h), HI (193 h), and NE (168 h) and had mean RINs of 6.1, 6.2, and 5.5. Here, the data show that the time in transit alone is not representative of RIN since HI had a higher RIN score than NE even though it was in transit for longer. If we consider time spent over 30°C, AZ was exposed to temperatures above 30°C for only 38.3 hours, HI was exposed for 22.8 hours, while NE was exposed for a total of 55 hours. When the time spent above 30°C is considered, the corresponding RIN scores seem to follow a more sensible pattern with longer exposures leading to lower RIN values.

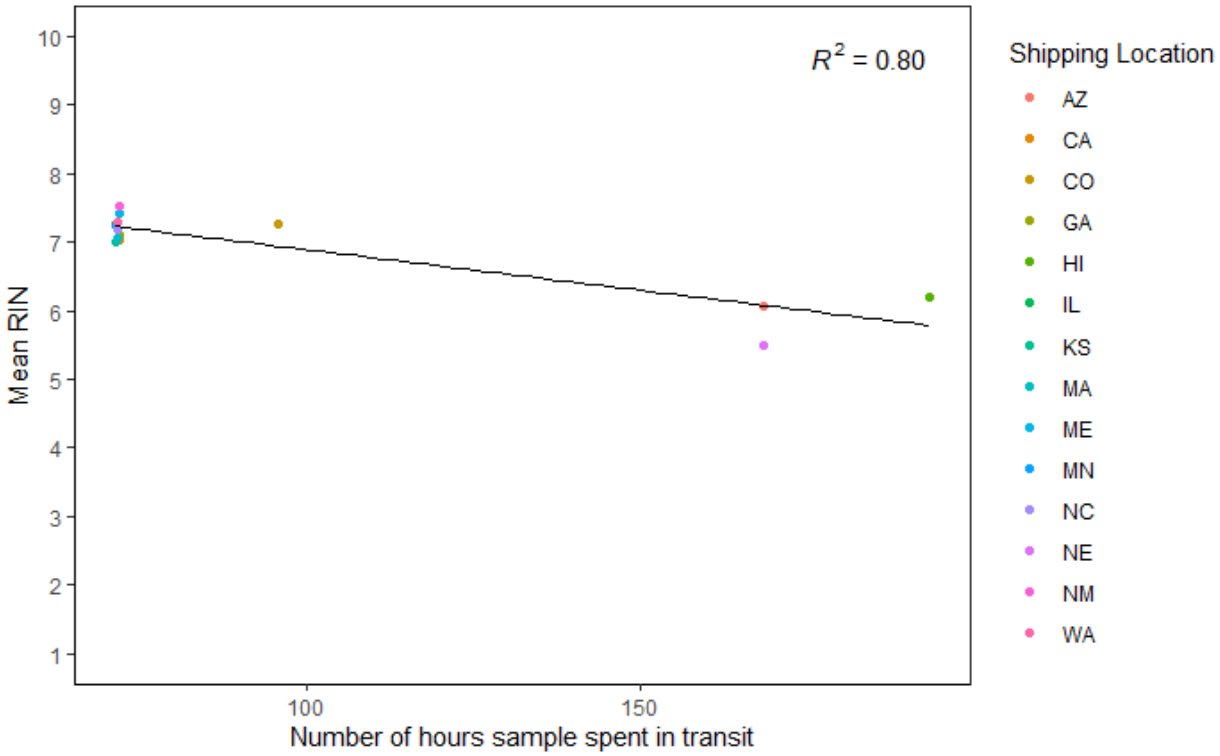

Figure C6. Effects of transit time on RNA integrity in homeRNA-stabilized blood samples. Mean RIN scores for each location are plotted against the times in transit for each location which are extrapolated from the temperature probe data visualized above. Though a trend of lower RINs with longer times in transit is observed, the R^2 value is only 0.57, indicating that there is not a strong correlation between the two variables suggesting that increased time in transit minimally affects the RNA integrity of homeRNA-stabilized blood samples. Despite this trend, all RIN values are well within the acceptable range for 3' mRNA sequencing.

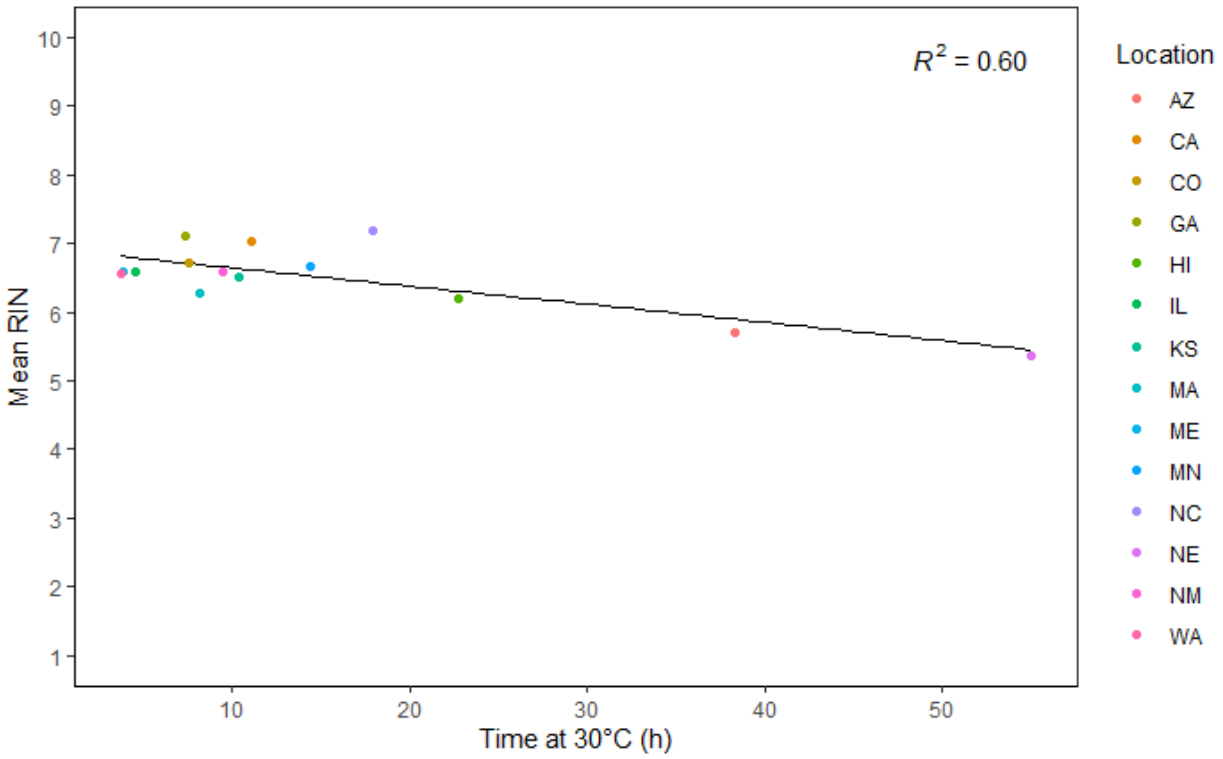

Figure C7. Effects of time spent above 30°C on RNA integrity in homeRNA-stabilized blood samples. Mean RIN scores for each location are plotted against the number of hours a sample experienced a temperature of 30°C or higher. Longer times spent at or above 30°C correspond to lower mean RIN values, however, there is not a strong correlation between the two variables (R^2= 0.60), suggesting that longer times spent above 30°C minimally affect the RNA integrity of homeRNA-stabilized blood samples.

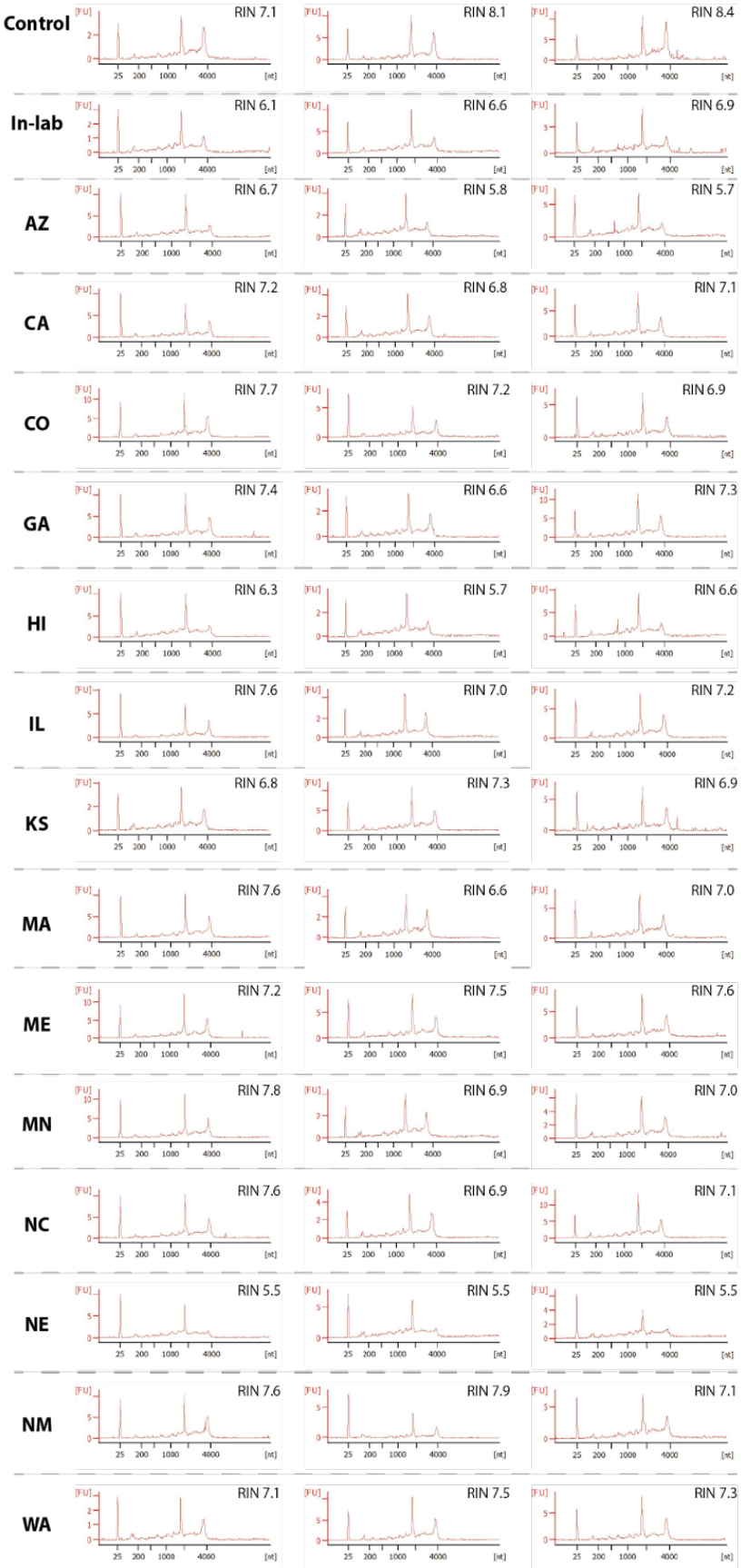

Figure C8. Electropherograms of isolated RNA from RNA*later*-stabilized blood samples shipped to 14 different US states. Electropherograms were obtained as raw data using a RNA 6000 Nano Kit on an Agilent 2100 bioanalyzer, which uses fluorescence to detect the marker (~25 nt), 18S rRNA fragments (~1900 nt), and 28S rRNA fragments (~3900 nt). The RIN algorithm then uses these peaks to assign a RIN value to the corresponding sample. Each state was shipped blood samples in triplicate (left, middle, and right columns are replicates 1, 2, and 3, respectively). Samples from the third replicate (right column) were sequenced with 3'mRNA-seq. All three replicates from the Control and Nebraska (NE) samples were also sequenced with 3'mRNA-seq.

D. Appendix for Chapter 5

Reproduced in part from Lauren G. Brown, Xiaofu Wei, Laura A. Milton, M. Yunos Alizai, James W. MacDonald, Theo K. Bammler, Yuting Zeng, Ingrid H. Robertson, Karen N. Adams, Damien Chaussabel, Erwin Berthier, Amanda J. Haack#, and Ashleigh B. Theberge#, "From Home to Transcriptome: Comparing the transcriptomic profile of induced immune response via lipopolysaccharide stimulation in homeRNA and venous blood" In preparation.
#Co-corresponding authors

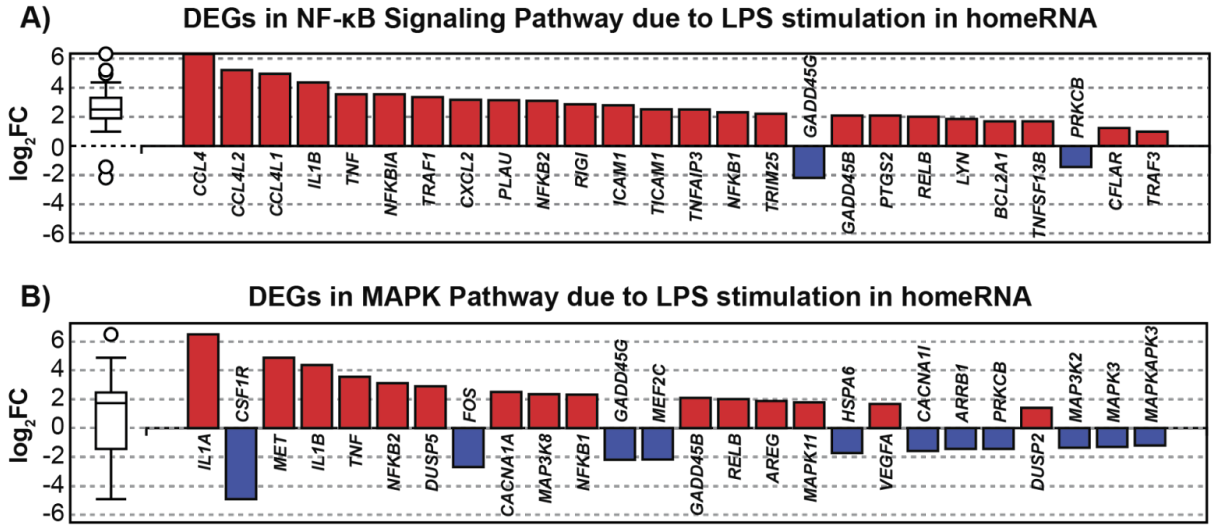

Figure D1. Differentially expressed genes (DEGs) in downstream MAPK and NF-kB pathways initiated by LPS stimulation in homeRNA-collected and -stabilized samples. A) All up- and down-regulated DEGs (n=26 DEGs) in the NF-kB signaling pathway (KEGG: 04064) ranked based on their absolute value of log2 fold change. B) All up- and down-regulated DEGs (n=26 DEGs) in the mitogen-activated protein kinase (MAPK) pathway (KEGG: 04010) ranked based on their absolute value of log2 fold change. Up-regulated genes are shown in red; down-regulated genes are shown in blue. The box and whisker plot on the left summarizes the distribution of all DEGs in this pathway with outliers represented by circles.

Supplementary discussion of Figures D2, D3, and D4

In addition to LPS stimulation, we compared the baseline gene expression profiles between unstimulated homeRNA-stabilized blood (capillary) and unstimulated venous blood stabilized with RNAlater (the same stabilization reagent used in homeRNA). We identified 1489 DEGs between unstimulated capillary and venous blood samples (Figure D2), with many of the up-regulated genes in the capillary samples being cytokines and chemokines associated with inflammatory responses (e.g., CCL2, CXCL2, CXCL3, and IL1A). This baseline inflammatory signature in capillary samples likely reflects methodological differences in blood collection. Specifically, the Tasso-SST blood collection tubes used for the homeRNA samples contain no anticoagulant, whereas the venous blood samples were collected in EDTA-coated vacutainers. Consequently, we observed visible coagulation in the Tasso-collected capillary samples immediately following blood collection but not in the venous samples. This coagulation process may have triggered a baseline inflammatory response in the capillary samples, accounting for the elevated expression of inflammatory mediators even without LPS stimulation.

Importantly, in this study the collected blood samples were incubated for six hours prior to stabilization so that they could serve as controls for LPS, which were stimulated for six hours. However, in typical homeRNA-based studies, collected capillary blood samples would immediately be stabilized. Therefore, the increased inflammatory gene expression response observed over hours would not necessarily translate to typical conditions used in homeRNA studies.

Despite these differences, genome-wide analysis revealed strong concordance between collection methods. The gene expression profiles between unstimulated homeRNA-stabilized samples and unstimulated venous RNAlater-stabilized showed a high Pearson correlation of 0.95 (Figure D2), with 15% of detectable genes showing differential expression (Figure D2). We also performed a similar comparison between stabilization methods (RNAlater and PAXgene) in the venous blood samples, which showed strong correlation (r=0.95) with 1% of genes demonstrating differential expression (Figure D3), demonstrating that stabilization has minimal impact on the transcriptomic profile of venous blood.

While this gene expression difference in homeRNA-stabilized samples can be partially attributed to differences in collection methodology, we wanted to probe further if we are observing internal variance or between group variance in our samples. We compared technical replicates of RNAlater-stabilized venous blood from the same donor and these replicates showed a Pearson correlation of 0.93 with no significant DEGs (Figure D4). Since the correlations are similar between the unstimulated homeRNA and Venous RNAlater samples (r=0.95) and the technical replicates of the Venous RNAlater samples (r=0.93), there is limited evidence to indicate substantial differences between the capillary (homeRNA) and venous blood samples within the expected error of RNA-sequencing.

These findings demonstrate that while homeRNA-stabilized samples exhibit a baseline baseline inflammatory signature compared to RNAlater-stabilized venous blood, the two collection methods have highly correlated transcriptomic profiles. Notably, despite this baseline difference, we were still able to detect similar levels of LPS-induced inflammatory response in the stimulated homeRNA samples compared to stimulated venous blood samples (Figure 5.3), suggesting that the systematic nature of these differences could be accounted for through appropriate normalization strategies in future transcriptomic studies with homeRNA (e.g., normalizing an exposure or targeted response sample with a baseline sample). Further, this baseline inflammatory signature could also be reduced by incorporating an anticoagulant into the Tasso blood collection tube, which has already been incorporated in other Tasso devices such as the Tasso+, which interfaces with any commercially available BD microtainer (including EDTA-coated tubes). Lastly, the high correlation between the unstimulated homeRNA and venous RNAlater samples observed in this study (r=0.95) is consistent with other comparisons on the gene and protein expression between capillary blood and venous blood[1-5], supporting the potential of homeRNA to be used in remote transcriptomic studies in place of clinic-based phlebotomy draws.

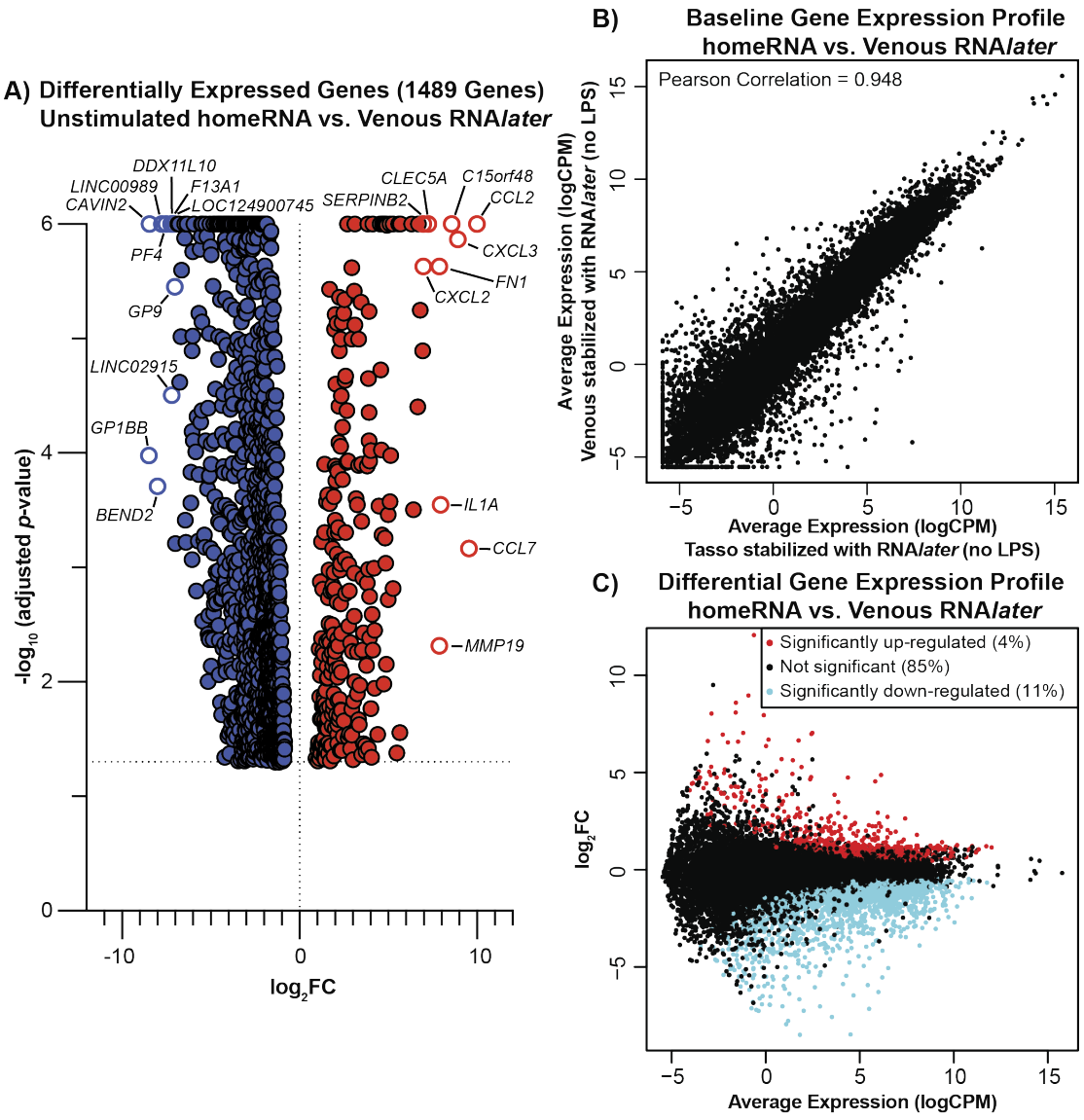

Figure D2. Unstimulated homeRNA blood samples exhibit some baseline inflammatory signatures absent in unstimulated RNAlater-stabilized venous samples while still having highly correlated gene expression profiles. A) Volcano plot of differentially expressed genes (DEGs) between unstimulated homeRNA-stabilized samples and venous blood stabilized with RNAlater. All DEGs (n=1489 DEGs) are represented by adjusted p-value on the y-axis and log2fold change on the x-axis. Red scatter dots represent up-regulated genes with $p \leq 0.05$ and log2fold change ≥ 1.3. Blue scatter dots represent down-regulated with $p \leq 0.05$ and log2fold change ≤ -1.3. The top 10 up-regulated and top 10 down-regulated genes are labeled. B) Pearson correlation plot comparing gene expression profiles between homeRNA (Tasso blood stabilized with RNAlater) and venous RNAlater-stabilized blood in unstimulated samples. Each point represents a gene, with x-axis showing log counts per million (logCPM) expression in homeRNA samples and y-axis showing logCPM expression in venous RNAlater-stabilized samples. C) MA-plot showing differential gene expression between homeRNA and venous RNAlater collection methods. The x-axis represents average expression (logCPM) across samples, and the y-axis shows log2fold change (homeRNA vs. Venous RNAlater). Red points indicate significantly up-regulated genes (4%) with $p \leq 0.05$; blue points indicate significantly down-regulated genes (11%) with $p \leq 0.05$; and black points represent non-significant genes (85%).

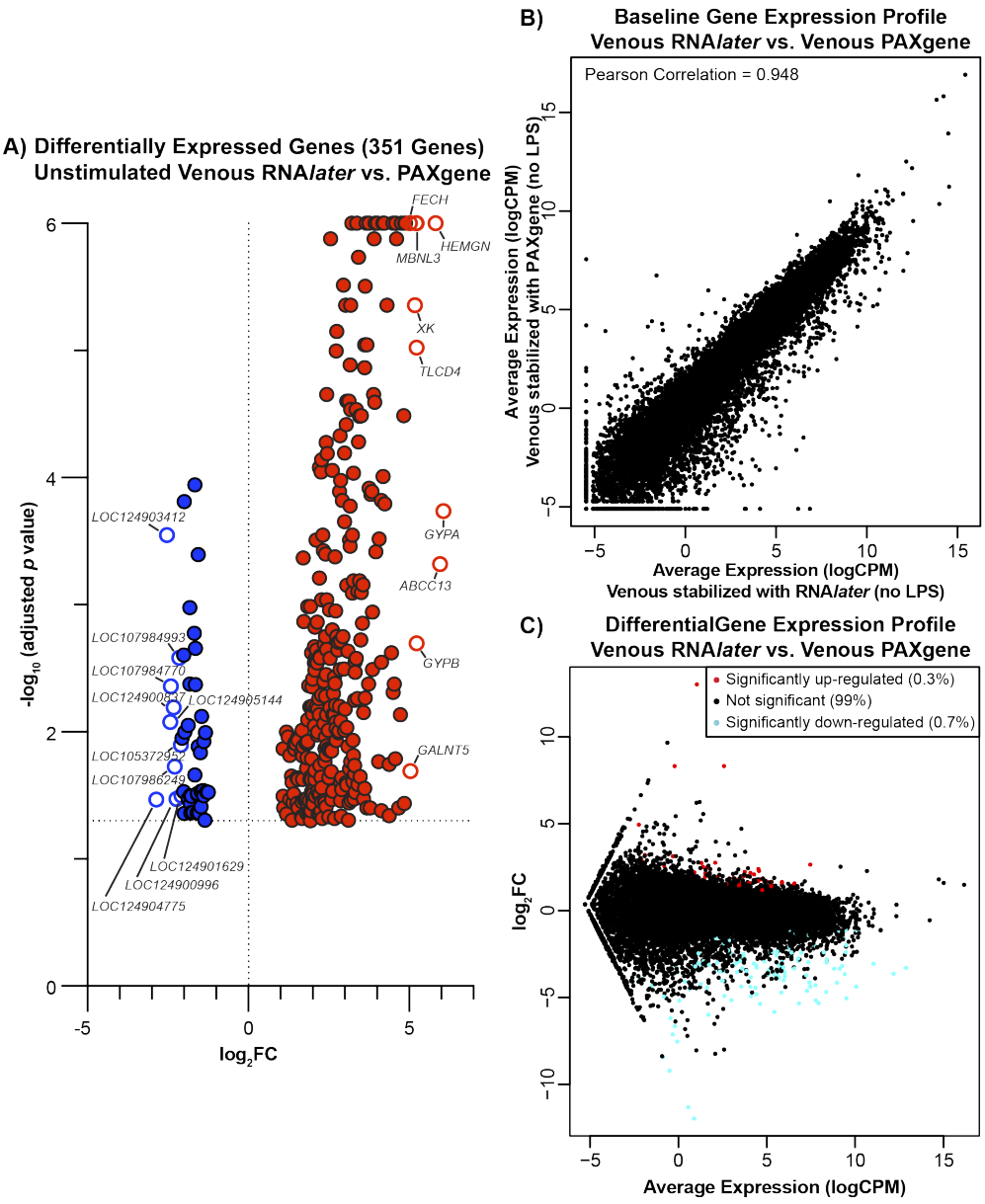

Figure D3. Comparison of gene expression signature in unstimulated (no LPS) venous blood stabilized with RNAlater and PAXgene. A) Volcano plot of differentially expressed genes (DEGs) between unstimulated venous RNAlater-stabilized samples and venous PAXgene-stabilized samples. All DEGs (n=351 DEGs) are represented by adjusted p-value on the y-axis and fold change on the x-axis. Red scatter dots represent up-regulated genes with $p \leq 0.05$ and log2fold change ≥ 1.3. Blue scatter dots represent down with $p \leq 0.05$ and log2fold change ≤ -1.3. The top 10 up-regulated and top 10 down-regulated genes are labeled. B) Pearson correlation plot comparing gene expression profiles between venous blood stimulated with RNAlater and PAXgene in unstimulated samples. Each point represents a gene, with x-axis showing log counts per million (logCPM) expression in venous RNAlater-stabilized samples and y-axis showing logCPM expression in venous PAXgene-stabilized samples. C) MA-plot showing differential gene expression between RNAlater and PAXgene stabilization methods. The x-axis represents average logCPM across samples, and the y-axis shows log2fold change (venous RNAlater vs. venous PAXgene). Red points indicate significantly upregulated genes (0.3%) with $p \leq 0.05$; blue points indicate significantly downregulated genes (0.7%) with $p \leq 0.05$; black points represent non-significant genes (99%).

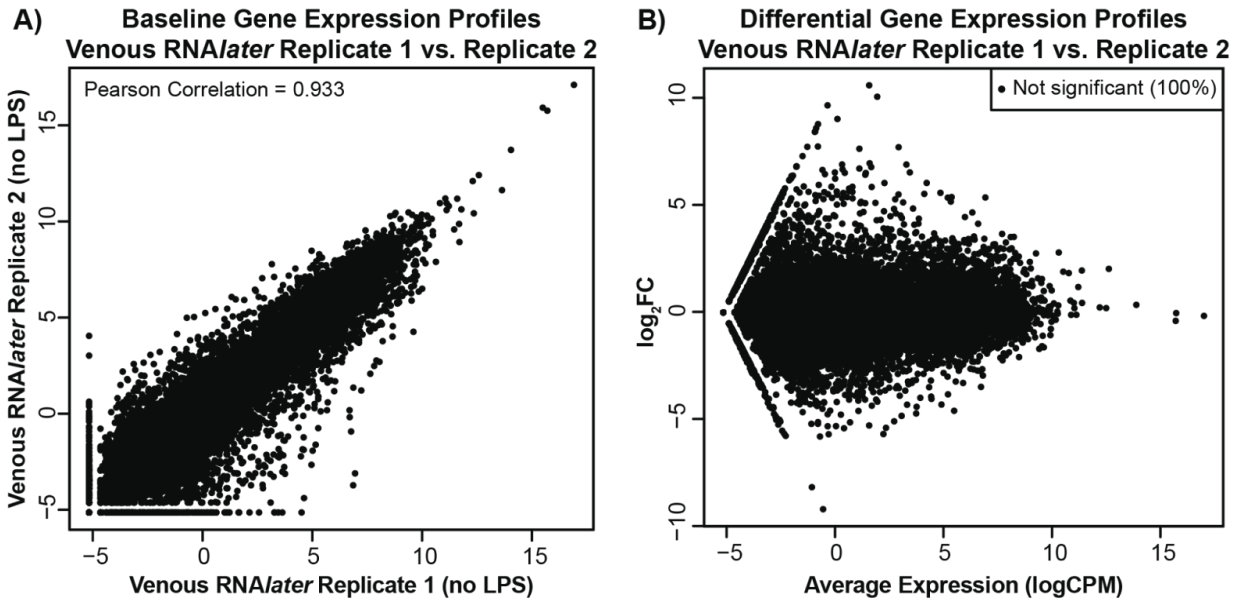

Figure D4: Technical variability in venous RNAlater-stabilized blood samples. A) Pearson correlation plot comparing gene expression profiles between two unstimulated technical replicates of venous RNAlater-stabilized samples from all three donors. Each point represents a gene, with x-axis showing log counts per million (logCPM) expression in replicate 1 and y-axis showing logCPM expression in replicate 2. C) MA-plot showing differential gene expression between replicates 1 and 2 in venous RNAlater-stabilized blood samples from the all three donor. The x-axis represents average expression (logCPM) across samples, and the y-axis shows $\log_2$fold change (replicate 1 vs. replicate 2). Black points represent non-significant genes (100%).

References

1. Meredith, R. T.; Yarham, R. A. R.; Mills, H.; Oliver, M. A. Whole Blood Cytokine Release Assays Reveal Disparity between Capillary Blood Sampling Methods. *Clin. Biochem.* **2023**, *120*, 110648. https://doi.org/10.1016/j.clinbiochem.2023.110648.
2. Ni Lochlainn, M.; Cheetham, N. J.; Falchi, M.; Piazza, P.; Steves, C. J. Comparing Venous vs. Capillary Blood Collection Methods for Proteomic Measurement in Peripheral Blood. *PROTEOMICS – Clin. Appl.* **2025**, *19* (4), e70007. https://doi.org/10.1002/prca.70007.
3. Toma, R.; Duval, N.; Pelle, B.; Parks, M. M.; Gopu, V.; Torres, P. J.; Camacho, F. R.; Shen, N.; Krishnan, S.; Hatch, A.; Tily, H.; Perlina, A.; Banavar, G.; Vuyisich, M. A Clinically Validated Human Capillary Blood Transcriptome Test For Global Systems Biology Studies. *BioTechniques* **2020**, *69* (4), 289–301. https://doi.org/10.2144/btn-2020-0088.
4. Hameed, A.; Ferruzzi, M. G.; Kay, C. D.; Williams, D. K.; Rahbar, E.; Morris, A. J. Comparison of the Capillary and Venous Blood Plasma Lipidomes: Validation of Self-Collected Blood for Plasma Lipidomics. *J. Lipid Res.* **2025**, *66* (3), 100755. https://doi.org/10.1016/j.jlr.2025.100755.
5. DiPasquale, C.; Christenson, R. H.; Donnelly, J. G.; Evans, S. A.; Wu, A. H. B.; Olson, E. G.; Barr, R.; Kosa, N.; McKenzie, H.; Abigania, M.; Jacobson, J. W. Equivalence between Capillary Blood and Venous Blood Test Results Using Miniaturized Assays and Novel Collection Methods to Support Routine Bloodwork. *J. Appl. Lab. Med.* **2025**, jfaf059. https://doi.org/10.1093/jalm/jfaf059.

E. Appendix for Chapter 6

Reproduced in part from A. J. Haack, L. G. Brown*, Y. Zeng, T. Khan, I. H, Robertson, D. S. Kennedy, K. N. Adams, J. W. MacDonald, T. K. Bammler, F. Stefanovic, K. Moloney, J. E. Stolarczuk, M. G. Takezawa, M. Yunos Alizai, G. W. Hassan, F. Y. Lim, D. Chaussabel, E. G. Walker, N. A. Errett, E. Berthier, and A. B. Theberge, "A Flexible and Responsive Remote Study Design to Assess Gene Expression Changes During Wildfire Smoke Exposure with homeRNA, an At-home Blood Sampling Kit", In preparation.*

** Equal contribution*

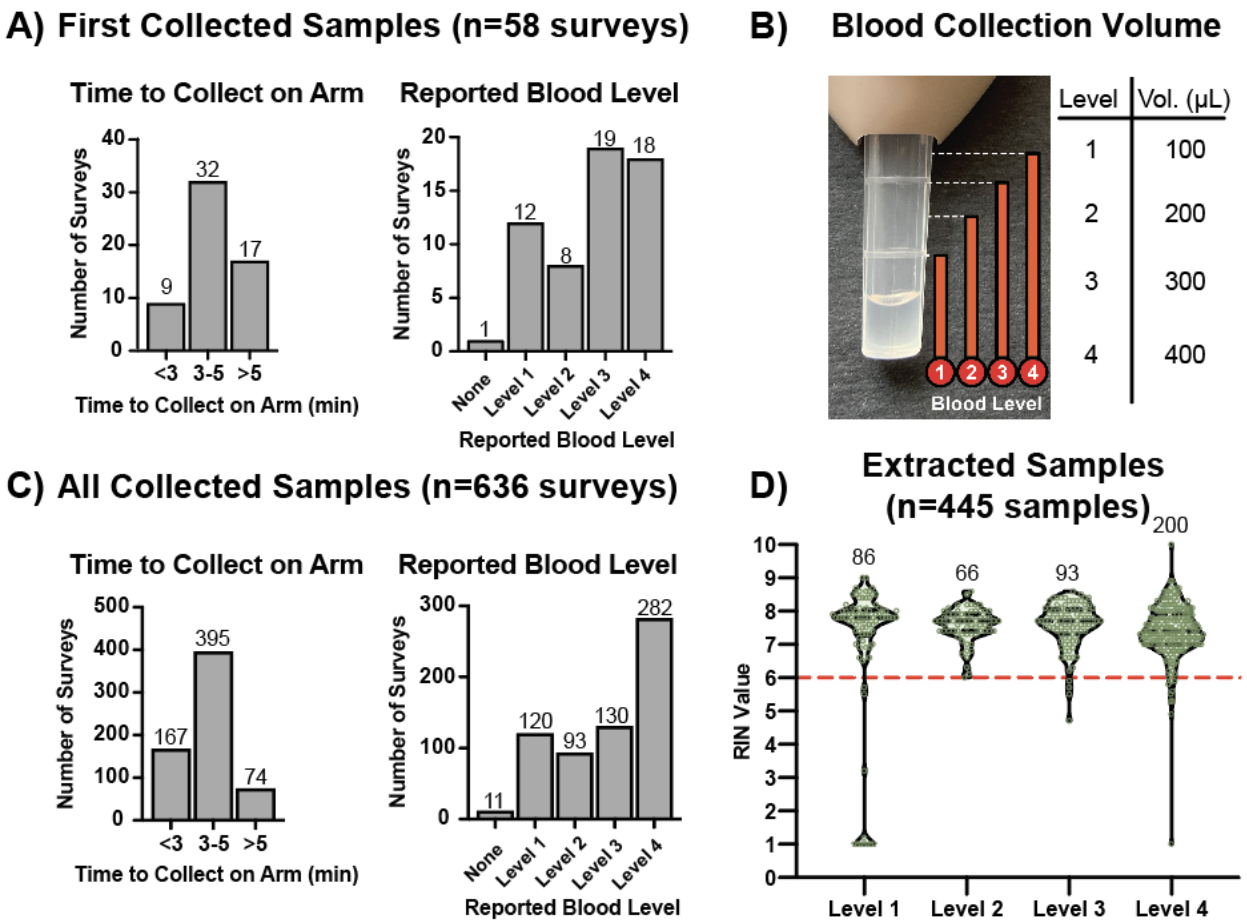

Figure E1. Blood collection volume associated with the Tasso-SST device had little effect on resulting RNA Integrity (RIN) values. Participant survey responses on the total time to collect blood on the upper arm with the Tasso-SST device (left) and the reported blood level collected (right) from A) first collected sample (n=58 surveys) and C) all collected samples (n=636 surveys) from 58 participants. B) Image of Tasso-SST blood collection device with approximate volume levels marked. Participants were asked to report blood level by eye after blood collection based on this image. D) Distribution of RIN values from reported blood collection levels (n=455 samples from the 37 participants that had samples extracted). Seven samples were reported to have no blood collected, so those were excluded here. RIN values are given on a scale from 1 to 10, with a RIN of 1 representing the most degraded RNA and a RIN of 10 representing the most intact RNA.

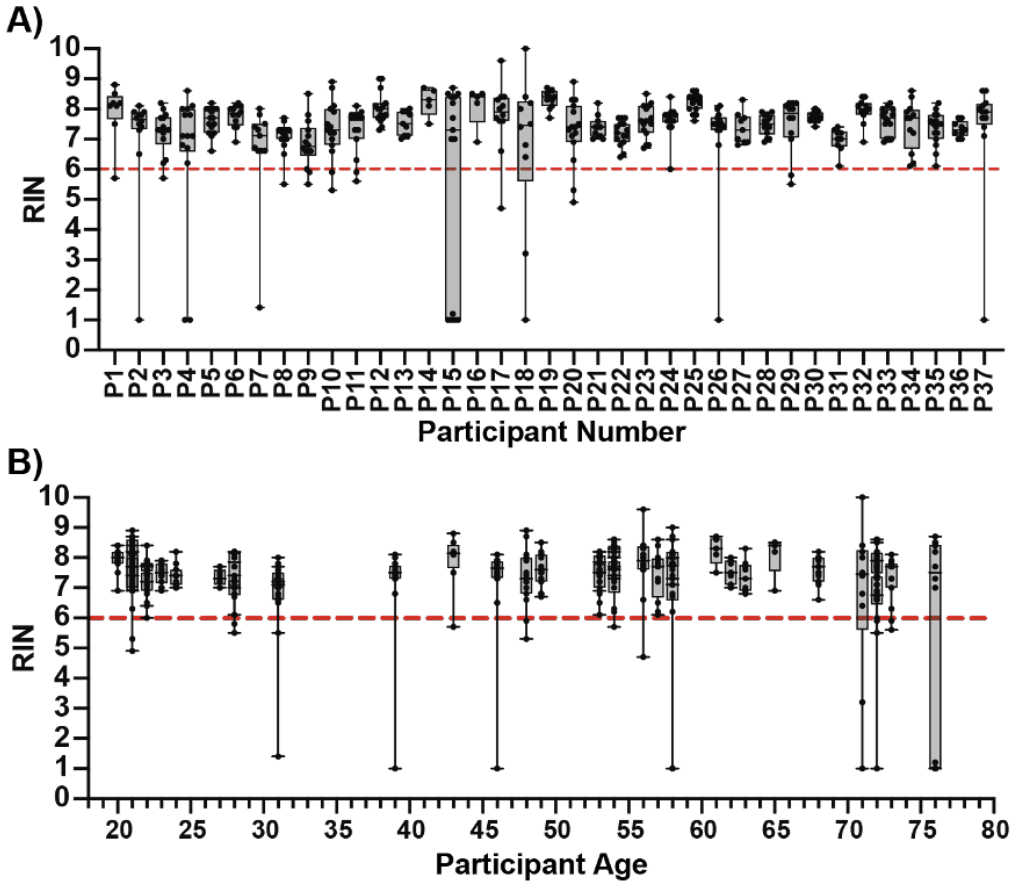

Figure E2. RNA stability of extracted homeRNA-stabilized samples based on each individual participant and participant age. A) Distribution of RNA Integrity Number (RIN) values from each participant (n=37 participants) from which samples were extracted. B) Distribution of RIN values according to participant age (n=37 participants). RIN values are given on a scale from 1 to 10, with a RIN of 1 representing the most degraded RNA and a RIN of 10 representing the most intact RNA.

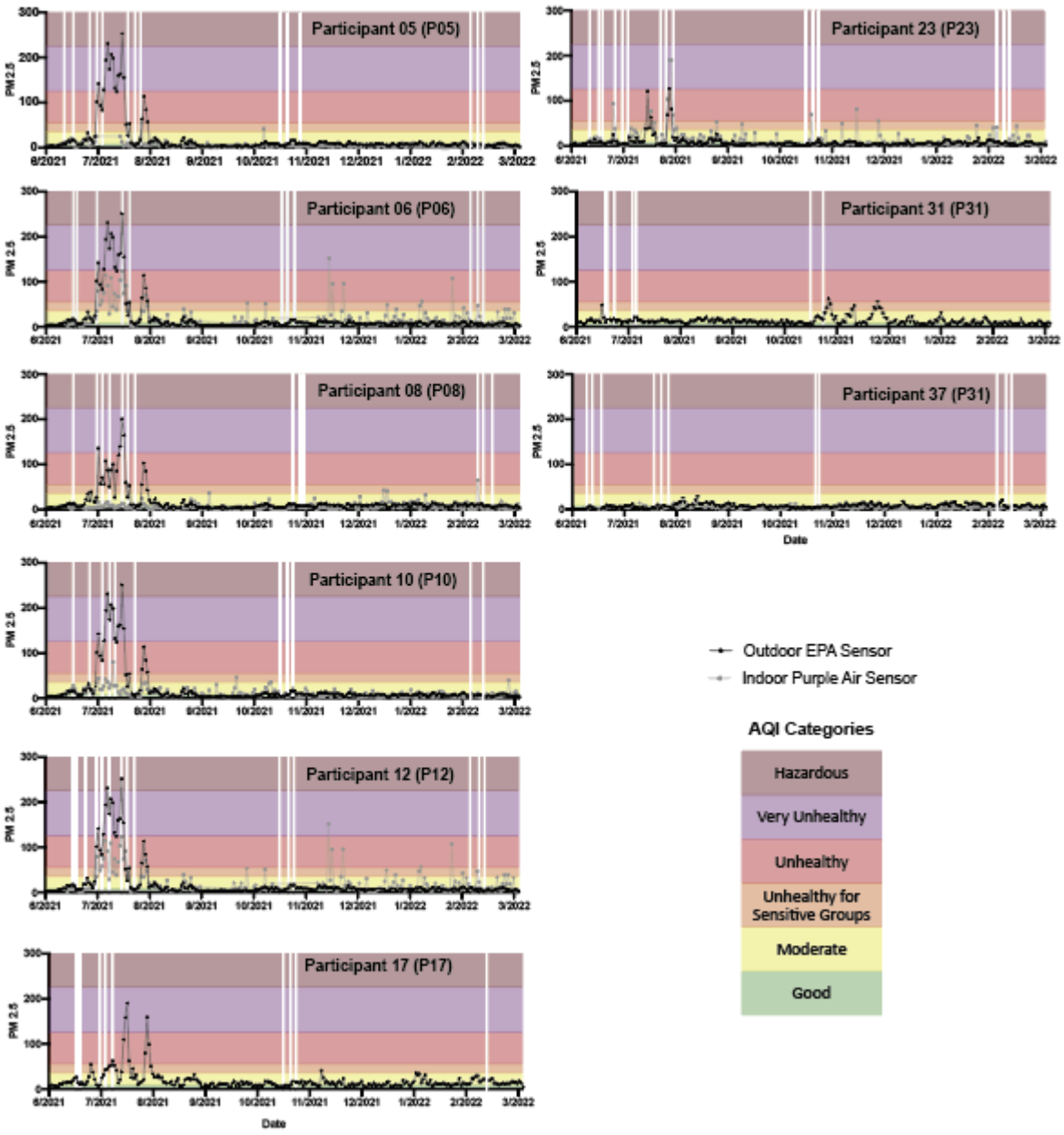

Figure E3. PM2.5 data for participants that were analyzed with the Nanostring Autoimmune gene panel. Data from participants exposed to high (left), medium (right, top), or low (right, bottom two) levels of wildfire smoke, plotted against the homeRNA sampling timepoints (white vertical lines with Tasso symbols on top), outdoor EPA sensor (black lines with data points), indoor PurpleAir sensor (grey lines with data points), and AQI categories as defined in Table 6.1.